

UNIVERSITÀ DEGLI STUDI DI FIRENZE
DIPARTIMENTO DI ASTRONOMIA E SCIENZA DELLO SPAZIO

DOTTORATO DI RICERCA IN ASTRONOMIA
CICLO XVIII
(COD. FIS/05)

**UV Spectroscopy of Coronal
Plasmas and its application to
different structures**

Alessandro Bemporad

FIRENZE, DECEMBER, 2005

Supervisors: Prof. Giannina Poletto
Dr. Marco Romoli

Coordinator: Prof. Mario Perinotto

A mia madre e mio padre.

*Forsitan et rosea sol alte lampade lucens
possideat multum caecis fervoribus ignem
circum se, nullo qui sit fulgore notatus
aestifer ut tantum radiorum exaugeat ictum.*

And possibly the sun, a gleam on high with rosy lampion,
possesses about him with invisible heats
a plenteous fire, by no effulgence marked,
so that he maketh, he, the Fraught-with-fire,
increase to such degree the force of rays.

(Lucretius, *De Rerum Natura*, V, 610–613;
transl. by William Ellery Leonard)

Abstract.

Over the last ten years experiments onboard the Solar and Heliospheric Observatory (SOHO) acquired XUV data of the solar corona (from ~ 165 to 1600 \AA) which provided us with a comprehensive data set covering all phenomena occurring in this region. Striking new results were obtained from these observations on the morphological and physical properties of small and large-scale static and dynamic coronal features, covering a complete solar activity cycle from its minimum in 1996, through the last maximum on 2001 and its declining phase towards the next minimum expected in 2007.

In this Thesis we present the results we obtained from an analysis of coronal spectroscopic observations acquired with the UltraViolet Coronagraph Spectrometer (UVCS) aboard the SOHO spacecraft. After a brief historical introduction on UV coronal observations and a summary of the main properties of coronal plasmas, in the first part of this Thesis we review the most important physical processes which give rise to the observed coronal UV spectrum and illustrate the spectroscopic diagnostic techniques used to derive informations on the thermodynamic state of the emitting plasma. A description of the UVCS instrument – together with an outline of the characteristics of the other SOHO experiments whose data have been analyzed for a better and more thorough interpretation of data – concludes the first part.

In the second part of the Thesis we focus on results from the analysis of four UVCS datasets. In the first work we study the temporal evolution of a streamer complex observed in June 2000 at the time of a SOHO-Ulysses quadrature. We examine in particular two streamers, which were slowly evolving, for which we derive densities, temperatures and elemental abundances: these turned out to be different in different structures. This possibly depends on the streamer “age” at the time observations have been acquired. In spite of the change in abundance values, both streamers have the same FIP (First Ionization Potential) bias (i.e. the same overabundance of low to high FIP elements, with respect to the photospheric value of the ratio). We conclude that the process responsible for the FIP effect is independent of the absolute values of abundances. The Fe/O ratio, which may be considered a proxy for the FIP effect, was also measured *in situ* by the Solar Wind Ion Composition Spectrometer (SWICS) aboard the Ulysses spacecraft, with the aim of comparing coronal and *in situ* values and identify the coronal source of the plasma sampled *in situ*. As we will show, data do not allow us to come to a definite conclusion on this issue.

The second and third work analyze UVCS data from transient phenomena, the Coronal Mass Ejections (CMEs), in their early and late stage

of evolution. In particular, our second work concentrates on the UVCS observations of a CME which occurred on 31 January 2000. Purpose of our analysis is to infer the structure of the CME in the early stage of its development and derive physical parameters of plasma in different parts of the CME. These are not well known: measurements of densities, temperatures and other physical parameters may help us identify the mechanisms that lead to the CME phenomena and serve as guidelines for a theoretical model of CMEs. With the support of data from the Magnetic Doppler Imager (MDI) the active region (AR) where the CME originates is identified and, combining white light data from the Mauna Loa Observatory and UVCS data, we reconstruct the CME configuration. To our knowledge this is the first time that the CME three-part structure has been identified at this low coronal levels. A comparison of the observed structure with that predicted by the Lin & Forbes (2000) CME model shows the two to be quite similar. Plasma densities and temperatures in the expanding CME front and core are also given but their distribution does not fully agree with the Lin & Forbes predictions; this result may help theoreticians to better define their models. A tentative estimate of the mass in different parts of the CME, and of its overall mass, indicates that at the heliocentric distance of our data (1.6 solar radii) the CME has not yet reached its final mass.

In our third work we report on UVCS observations of the coronal restructuring following a CME which occurred in November 2002 at the time of a SOHO-Ulysses quadrature campaign. These observations cover, with occasional gaps, a time interval of more than 2 days giving us the possibility to study the evolution of the coronal plasma parameters in the CME late stage. The observed UV emission indicates plasma temperatures above 6×10^6 K: a comparison of the site of hot UV plasma with images from the Extreme UV Imaging Telescope (EIT) aboard SOHO shows the high temperature emission to overlie a growing post-flare loop system formed in the aftermath of the CME. This emission most likely originates in the current sheet (CS) overlying the arcade, for which we infer densities and give the temperature vs. time profile. Although this does not represent the first identification of a CS in a CME event, it is the first time that the evolution in time of its physical parameters has been given. Because, at the time of the quadrature, Ulysses was directly above the location of the CME, its instrumentation intercepted the ejecta. High ionization state Fe was detected by the Ulysses Solar Wind Ion Composition Spectrometer (SWICS) throughout the magnetic cloud associated with the CME: this is the first unambiguous identification of the coronal source of the highly ionized plasma measured *in situ* by Ulysses. Hence, the SOHO-Ulysses data set provided us with the unique opportunity of analyzing a current sheet structure from its lowest

coronal levels out to its *in situ* properties. Both the remote and *in situ* observations are compared with predictions of theoretical CME models. In the fourth and last work of this Thesis we analyze UVCS observations of a sungrazing comet observed on February 2001; in particular we show how from UV data it is possible to estimate the physical parameters of the coronal plasma encountered by the comet. This gives us the opportunity of illustrating briefly atomic processes which occur at the time of the interaction between the cool cometary and hot coronal plasmas and are usually not discussed when dealing with coronal spectroscopy. We also derived some cometary properties such as the water outgassing rate, the nucleus size and the number density of dust particles in the tail. This comet apparently went through sequential fragmentation events along its path and it is the first time that UVCS identified two cometary fragments and their size has been evaluated.

A concise description of future work is given at the end of the Thesis.

Contents

Abstract	i
I Diagnostics and Instrumentations	1
1 Introduction	3
1.1 Observations of the solar corona: an hystorical overview	3
1.2 Purposes of the Thesis	5
2 A summary of morphological and physical properties of the corona	7
2.1 Coronal magnetic fields	7
2.2 Coronal electron densities	10
2.3 Coronal electron temperatures	11
2.4 Coronal elemental abundances	12
3 Coronal plasma diagnostics	13
3.1 The observed coronal emission	13
3.2 UV Spectral line emission	15
3.2.1 The validity of thermodynamic equilibrium	15
3.2.2 Spectral lines formation	17
3.2.3 Atomic levels population	19
3.2.4 Atomic ionization balance	23
3.2.5 The validity of ionization equilibrium	25
3.2.6 Emission line intensity	26
3.2.7 Line broadening	32
3.3 Plasma diagnostics from EUV observations	34
3.3.1 Separation of radiative and collisional components	36
3.3.2 Plasma electron temperature	37
3.3.3 Plasma electron density	38
3.3.4 Elemental abundances	40
3.3.5 Oxygen elemental abundance	40
3.3.6 Plasma outflow speed	41
3.4 White light continuum emission	42

4	Instrumentation and Data Reduction	47
4.1	The SOHO mission	47
4.2	The SOHO/UVCS instrument	48
4.2.1	The spectrometer UV and WL channels	48
4.2.2	Instrument description	50
4.2.3	Stray light suppression	52
4.3	UVCS data reduction	53
4.4	Other SOHO instruments	55
4.4.1	LASCO	55
4.4.2	EIT	55
4.4.3	MDI	56
II	Observations & Results	59
5	Temporal evolution of a streamer complex	61
5.1	Introduction	61
5.2	The goal of our observations	62
5.3	Streamer evolution from LASCO C2 images	63
5.4	UVCS observations and data analysis	64
5.5	Streamers physical properties	66
5.5.1	Electron temperatures	67
5.5.2	Electron densities	71
5.5.3	Elemental abundances: FIP effect	73
5.6	Abundances measured <i>in situ</i> and their coronal counterparts	79
5.7	Conclusions	83
6	Early evolution of a CME in the low corona	85
6.1	Introduction	85
6.2	The goal of our observations	87
6.3	The January 2000 CME scenario	88
6.4	UVCS observations	90
6.5	Mark IV observations	95
6.6	Density diagnostics from white light observations	96
6.7	Estimate of the CME electron density	98
6.8	Estimate of the CME outflow speed	100
6.9	Estimate of the CME electron temperature	101
6.10	Mass of the CME	105
6.11	Uncertainties in the CME parameters	105
6.12	Discussion and conclusion	108

7	Post-CME current sheet evolution	111
7.1	Introduction	111
7.2	The goal of our observations	112
7.3	The November 2002 CME scenario	113
7.4	UVCS observations	116
7.5	Physical parameters in the corona and the CS	120
7.6	Results	124
7.6.1	Elemental abundances in the CS and adjacent regions	129
7.6.2	Densities in the CS and ambient corona	131
7.7	Ulysses observations	132
7.8	Discussion and conclusions	136
8	Coronal & cometary parameters from sungrazer observations	141
8.1	Introduction: sungrazer observations	141
8.2	UVCS data	144
8.2.1	The observed emission	145
8.2.2	Ly α line profiles	149
8.3	Physics of cometary and coronal Ly α emission	152
8.4	A model for the observed Ly α emission	154
8.4.1	Cometary and coronal parameters	156
8.4.2	Effect of Pyroxene dust grains	160
8.5	Summary	162
9	Summary and Future Perspectives	163
	Acknowledgements	I
	Bibliography	II

Part I

Diagnostics and Instrumentations

Chapter 1

Introduction

1.1 Observations of the solar corona: an historical overview

The optical emission from the outer atmosphere of the Sun, the solar corona, is ≈ 6 orders of magnitude weaker than the emission from its visible “surface”, the photosphere. Hence, historically, first observations of the corona have been possible only during solar eclipses, when the solar surface is occulted by the moon. Regular observations of solar eclipses started only in 1842 (by P. A. Secchi in Italy and C. A. Young of Princeton University), while the first photographic records have been made in 1851 (by Berkowski, in Königsberg, on a daguerrotype). It is interesting to note, though, that drawings of coronal structures at eclipses have long been preferred to photographic records, because of difficulties in setting appropriate exposure times: short exposures, convenient for low-lying structures, were insufficient for higher, fainter structures while long times led to overexposures of the brighter low structures.

Whether the corona was a solar or an atmospheric phenomenon (terrestrial or lunar) was long debated and only in the second half of the 19th century the concept of a solar corona started developing. Observations of the solar corona outside eclipses became possible only after the first coronagraph was built (B. Lyot, 1930). Spectroscopic observations started with the pioneering works of J. Janssen (and J. N. Lockyer) at the 1868 eclipse, which led to the discovery of Helium in prominences. The puzzling observations, in the coronal spectrum, of unidentified lines (and in particular of a strong green line observed at $\lambda = 5303\text{\AA}$), led Young, in 1895, to postulate the existence of an element, called *coronium*, not found on the Earth. The problem was solved in 1942 by the Swedish scientist Bengt Edlén who identified the observed lines with forbidden lines from highly ionized atoms (such as Fe XI, Ca XII, Ca XIII). This – together with the large width of the green line and the observation of only a small depression at the position where the H and K lines of Ca should be – led to the concept of a million-degree temperature of the solar corona.

Because of the very high temperature of the coronal plasma (see Chapter 2), emission from coronal regions is highest in the EUV and soft X-ray ranges, which are almost entirely absorbed by the Earth atmosphere. Then, it became evident that, in order to increase our knowledge of coronal structures, space observations were mandatory. With the beginning of the space era with its rocket flights and spacecraft missions (in the second half of the 20th century) the number of coronal observations raised tremendously.

Space observations of the corona had started by the *Naval Research Laboratory* (NRL) in 1946, when the first far UV spectra were obtained by a spectrograph mounted aboard a rocket. The first X-ray photograph of the Sun was obtained in 1963 (by Friedman) with a pinhole camera on a NRL rocket flight. However, these flights allowed only very short (about 7 minutes) observations of the solar corona that provided only a “snapshot” over a very limited time interval, hence hiding its extremely dynamic nature.

Long-term observations were obtained for the first time with the satellite series *Orbiting Solar Observatory* (*OSO-1* to *OSO-8*), launched between 1962 and 1975. Data acquired by the non-imaging EUV, soft X-ray and hard X-ray spectrometers and spectroheliographs aboard these satellites led to the first studies of the temporal variability of the electron temperature and density above active regions, the first detection of very high temperature emission ($T \sim 1.5\text{--}2.0 \cdot 10^7\text{K}$) during a flare and other relevant scientific achievements such as the first indication of temporal fluctuations in chromospheric and transition region lines.

A new era of multi-wavelength coronal observations from space started in 1973 with the launch of the ATM package aboard the *Skylab* mission. The ATM package included a white-light coronagraph, two X-ray telescopes, EUV spectroheliometers/spectroheliographs and an UV spectrograph. The *Skylab* mission has been the most productive mission in the history of solar observations from space, thanks to the quality and quantity of data, its nine-month duration and the level of funding provided for data analysis. The most significant progresses were made in our understanding of coronal holes, of the structure, activity and energy balance of active regions and in the observation and prediction of solar flares.

The first space mission that operated over nearly a full solar cycle (1980–1989) was the *Solar Maximumn Mission* (SMM). The SMM satellite, the first to be completely dedicated to solar observations, focussed on spectroscopy over a broad range of wavelengths rather than on the predominantly imaging activities of *Skylab* experiments. The mission payload included a *Gamma Ray Spectrometer* (GRS), hard X-ray instruments (HXRBS and HXIS), an *UV Spectrometer & Polarimeter* (UVSP, which provided a higher resolution imaging of the transition region plasma in flares than previously achieved) and a coronagraph (which observed several hundred *coronal mass ejections* and discovered 10 new sungrazing comets).

In 1991 the *Compton Gamma-Ray Observatory* (CGRO), designed to detect bursts from cosmological objects, recorded more γ -ray and X-ray photons from solar flares than from the rest of the universe providing crucial measurements of γ -ray

lines and contributing to a precise localization of the source of particle acceleration in solar flares. The great breakthrough in soft X-ray imaging of the solar corona and flares came with the *Yohkoh* mission, launched in 1991 and operating through 2001. The spacecraft carried a payload of four scientific instruments: the *Hard X-ray Telescope* (HXT) with four energy channels in the 14–93 keV range, the *Soft X-ray Telescope* (SXT) with multiple filters sensitive to temperatures of $T \geq 1.5 \cdot 10^6 \text{K}$, the *Wide-Band Spectrometer* (WBS) and a *Bragg Crystal Spectrometer* (BCS). The *Yohkoh* mission provided 10 years of soft X-ray images of the solar disk as well as of flares, increasing our knowledge about magnetic reconnection and field reconfiguration processes.

The next major solar mission was the *Solar and Heliospheric Observatory* (SOHO), launched in 1995 and still fully operational at the time of this writing. This is a cooperative mission between the U.S. *National Aeronautics and Space Administration* (NASA) and the *European Space Agency* (ESA). All the results described in this Thesis are obtained from an analysis of SOHO data: a short description of its instrumentation is given in Chapter 4.

Recent space missions are the *Transition Region And Coronal Explorer* (TRACE) and the *Ramaty High Energy Solar Spectroscopic Imager* (RHESSI). TRACE is a NASA/ESA mission launched in 1998, with a single, high resolution ($\sim 1''$) EUV telescope and was designated to explore the connections between plasma structures observed in the solar outer atmosphere and the fine-scale photospheric magnetic field. High resolution images from the TRACE telescope have revealed intriguing details about coronal heating and cooling, magnetic reconnection processes and the dynamic of coronal plasma structures. RHESSI is a NASA mission launched in 2002: its telescope provides images in hard X-ray with the highest spatial resolution ($\sim 2.3''$) ever achieved and was designed to explore the energy release in solar flares and the basic physics of particle acceleration.

1.2 Purposes of the Thesis

The aim of this Thesis is twofold: in the first part atomic processes leading to coronal emission will be illustrated and spectroscopic techniques that allow us to derive the physical parameters (temperature, density, velocity, elemental abundances) of coronal plasma will be described. In the second part we will show the results obtained by applying these techniques to the analysis of data acquired by the SOHO experiments. The data we analyze refer to different structures of the solar corona, such as streamers and Coronal Mass Ejections (CME), and the significance of the problem we study will be preliminarily illustrated and put in a wider context, via a concise description of the state-of-the-art in the field.

Chapter 2

A summary of morphological and physical properties of the corona

Since the time of the first eclipse observations the solar corona appeared to have a highly *inhomogeneous structure*. This because atoms, at the high coronal temperature, are partially or fully ionized (i.e. they are in the “plasma” state) and their motion follows the magnetohydrodynamic laws. The 2D configuration of coronal fields is revealed by XUV and white light images; the magnetic field dictates the topology and evolution of coronal structures and makes the solar corona dramatically different from a simple gravitationally stratified atmosphere. The single parameter that illustrates the influence of the magnetic field on the coronal plasma is the so called plasma- β , which is the ratio of the thermal p_{th} to the magnetic pressure p_{mag} . In the solar corona the magnetic pressure dominates over the thermal pressure preventing the horizontal stratification across the magnetic field.

As we said in Chapter 1, the coronal temperature is on the order of 10^6 K, i.e. temperature increases moving outwards from the photosphere (which is at 5000–6000 K). The transition from photospheric to coronal temperatures occurs in a thin layer, known as the “transition region”, where density drops by about two orders of magnitude and the gas temperature has a sharp rise in a region between 2000 km and 3000 km above the solar surface (Figure 2.1). At typical coronal temperatures ($T \approx 10^6$ K) and densities ($N_e \approx 10^8$ cm $^{-3}$) plasma in a 10 Gauss field has a $\beta \ll 1$, justifying our previous statement that the corona is magnetically dominated. In the following Sections we briefly describe the coronal magnetic field properties and give a representative profile of density and temperature vs. the heliocentric distance.

2.1 Coronal magnetic fields

Observations over extended periods of time revealed that the activity cycle has an 11 year periodicity. The total magnetic flux reaches a maximum during the peak of a cycle (hence at the maximum of solar activity) and drops to a low level during the solar minimum. The fact that the Sun magnetic field changes dramatically

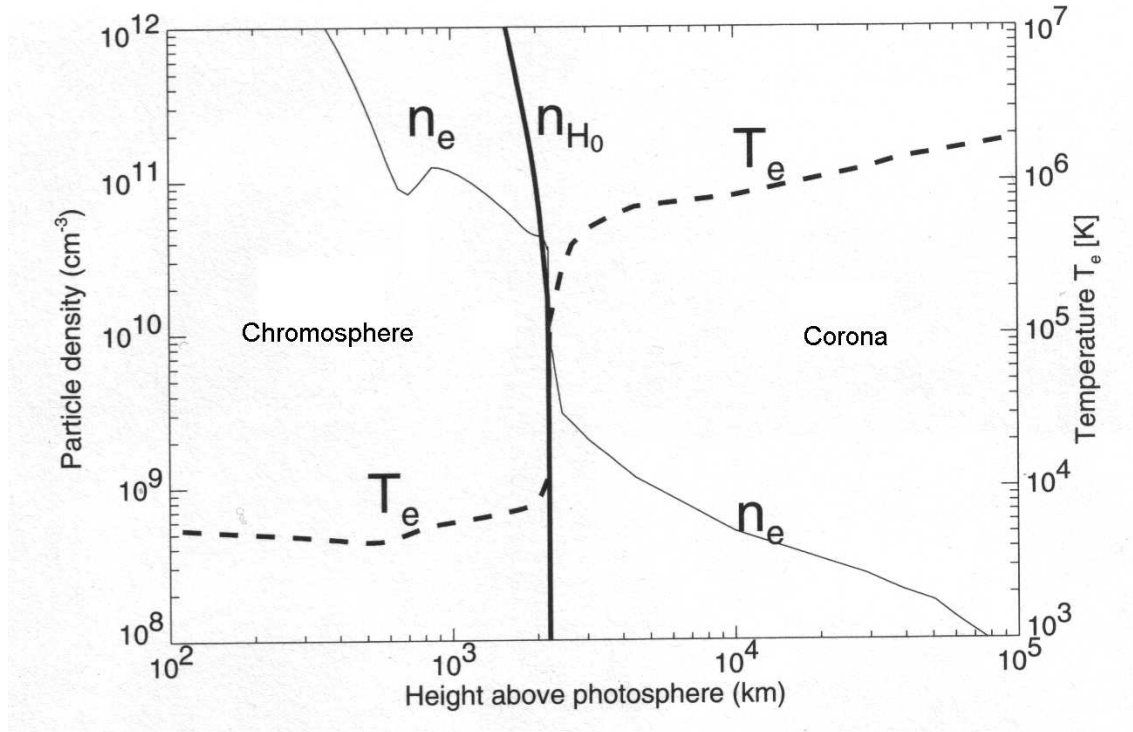


Figure 2.1: Electron temperature (T_e , dashed line) and density (n_e , solid thin line) model of the chromosphere (Fontenla et al., 1990; Model FAL-C) and lower corona (Gabriel, 1976). In the transition region the neutral hydrogen density (n_{H_0} , solid thick line) decreases below the electron density because the plasma becomes fully ionized (from Aschwanden, 2004).

in just a few years in a cyclical pattern hints to a continuous generation of the magnetic field inside the Sun. Because photospheric and coronal magnetic fields are strongly coupled, all the chromospheric and coronal phenomena have also an 11 year periodicity.

The appearance on the Sun of vast, low-brightness, unipolar regions - the coronal holes - where the so-called *open* fieldlines originate, is related to the phase of the activity cycle: the largest unipolar regions appear at solar minimum, are centered around the poles and extend down to low latitudes. At this times, the corona has a typical shape, with large, dark coronal holes that occupy a high percentage of the total surface, while bright areas are concentrated in an equatorial belt, where streamers are located. Streamers are approximately radial structures, which consist of an arcade of closed field lines that open up at the top of the structure, where a current sheet forms.

At the time of maximum activity, coronal holes, if any, shrink in size and are limited to polar areas, while streamers appear also at high latitudes. In this phase the clear distinction between open and closed fieldline regions disappears and the

magnetic field structure becomes more complicated than in the simple dipole-like configuration at the minimum of the activity cycle. At this time, the number of transient phenomena, like flares or coronal mass ejections (CME) maximizes: a description of these events invokes the restructuring/opening/and subsequent closing down of magnetic fields.

The observed shape of all the structures typical of the “static” corona (i.e. phenomena with variation times on the order of days or months) is determined by closed and/or open field configurations. This happens for instance for the coronal loops (closed configuration), holes (open), plumes (open) and streamers (closed configuration surmounted by an open one). Moreover, all the observed variable features typically included in the “dynamic” corona class (i.e. phenomena with variation times on the order of few days to minutes) may be described in terms of opening (e.g. flares, plasma blowout) and/or closing (e.g. magnetic reconnection) processes of the magnetic field.

Measurements of photospheric magnetic fields are made by solar magnetographs which take advantage of the Zeeman effect, i.e. the splitting of the atomic energy levels induced by an external magnetic field whose intensity is proportional to the amount of splitting. These instruments measure the radial component of the magnetic field, while more sophisticated equipment - the vector magnetographs - can measure also the normal component of the field (it is beyond the scope of this thesis to give a detailed description of these instruments). These measurements demonstrated that the the strongest magnetic fields (2000 – 3000 G) are found in sunspots, while active regions and plages have an average photospheric field of 100 – 300 G containing small-scale pores with typical fields of ~ 1100 G. Network fields are believed to be located mainly in between granules and to have a high field strengths (1000 – 2000 G), concentrated in slender flux tubes (typical size $\approx 100 - 330$ km). Unipolar regions, like coronal holes, have average fields on the order of a few gauss. During the solar cycle, the magnetic flux varies by a factor ≈ 8 in active regions and by a factor ≈ 2 in ephemeral regions.

Direct measurements of coronal magnetic fields are still in their infancy: the only estimate we have comes from radio measurements or refer to prominences. Dulk & McLean (1978) gave an empirical formula for the decrease of the magnetic field $B(r)$ with height¹:

$$B(r) = (0.5 \text{ G}) \left(\frac{r}{R_{\odot}} - 1 \right)^{-1.5} \quad (2.1)$$

which is valid for the equatorial corona at the sunspot minimum between 1.02 and $10 R_{\odot}$. This profile yields values of about 1 G at an heliocentric distance of $1.5 R_{\odot}$, decreasing to ~ 0.02 G at $10 R_{\odot}$. Of course, this curve does not include the variations (by $1 - 2$ orders of magnitude) of the magnetic field strength caused by the solar cycle.

¹This formula has been derived from a compilation of different magnetic field measurements such as *in situ* measurements, extrapolation from photospheric fields measured with the Zeeman effect and radio bursts.

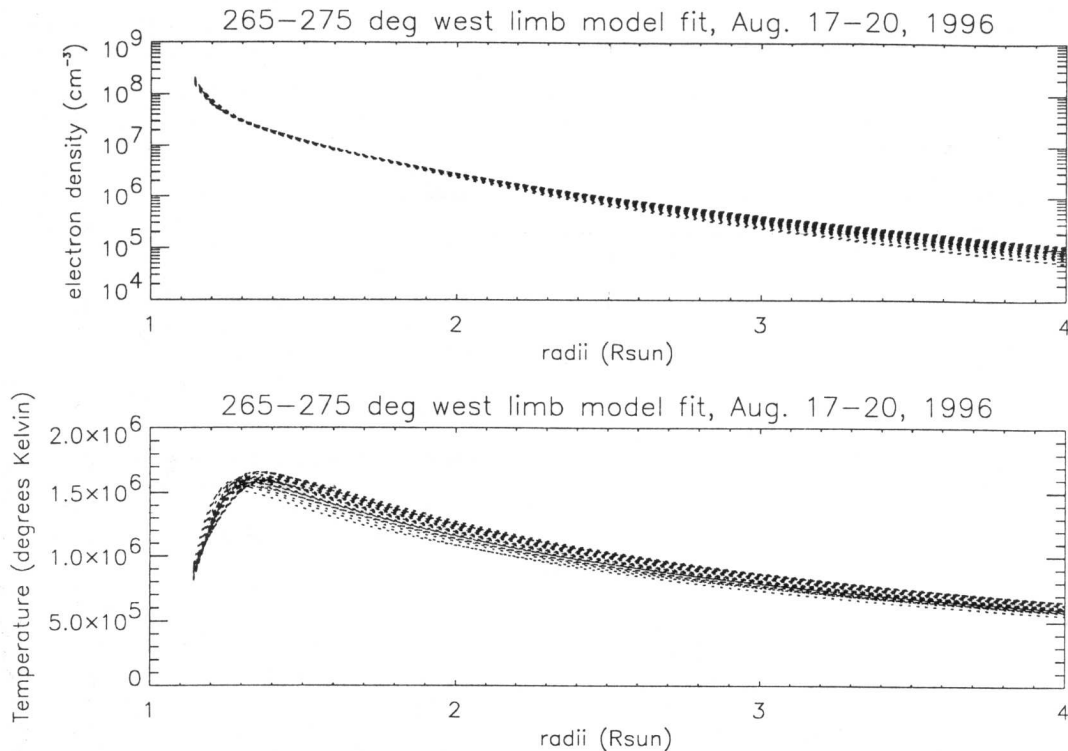


Figure 2.2: Top: radial profiles of the electron density as derived via van de Hulst inversion from various white light measurements in an equatorial streamer. Bottom panel: radial profiles of electron temperature as derived (see text) from the above density measurements assuming hydrostatic equilibrium (from Gibson et al., 1999). Different curves in these plots refer to profiles from different measurements during the Whole Sun Month campaign in August 1996.

There is a number of numerical techniques, based on the magnetic field measurements at photospheric levels, that give values of the field at coronal altitudes. These are based on different assumptions, the simplest being the “potential” approximations. More sophisticated techniques assume the field to be force-free (i.e. $\nabla \times B = \alpha B$) with a constant or non constant α value. These are widely used, their weakness being that the derived values depend obviously on the a priori assumptions on which they are based.

2.2 Coronal electron densities

Coronal electron densities were first measured from white light using the van de Hulst (1950) inversion technique (see later, § 3.4). In Figure 2.2 (top panel) we show the electron density N_e as a function of the heliocentric distance as derived with this technique in an equatorial streamer (Gibson et al., 1999) at the minimum

of the solar activity. This can be represented by a radial power law:

$$N_e^{str}(r) = 10^8 \cdot (77.1 \cdot r^{-31.4} + 0.954 \cdot r^{-8.3} + 0.55 \cdot r^{-4.63}) \quad (\text{cm}^{-3}) \quad (2.2)$$

where r is the heliocentric distance in solar radii. A similar analysis applied at different latitudes shows that, at a nominal height of ≈ 2500 km above the solar limb (hence at the base of the corona, see Figure 2.1), the electron density decreases from a value of $(3 - 5) \cdot 10^8 \text{ cm}^{-3}$ in coronal streamers to $(0.5 - 1) \cdot 10^8 \text{ cm}^{-3}$ in coronal holes.

Coronal densities have been determined in the last years with different techniques from frequency of radio bursts propagating through the corona, and from analysis of EUV spectral line emission using coronal forbidden lines, emission measure and density sensitive lines. A brief description of these techniques will be given in § 3.3.3; however, we anticipate here that densities inferred from UV diagnostics may depend on other parameters like temperature, velocity and ion abundances (as we show in Chapter 3) and sometimes it is difficult to estimate the uncertainties in the inferred values. On the other hand, white light measurements, which depend only on the geometry and the electron density distribution, yield results that are more easily interpreted (see later, § 3.4).

2.3 Coronal electron temperatures

A major and still unsolved problem in solar physics is the identification of the mechanism leading to the sudden temperature rise from the chromosphere to the corona (Figure 2.1). The total power emitted in x-rays by the corona is only $\approx 10^{-6}$ of the Sun's bolometric luminosity, and even taking into account all of the possible coronal energy loss mechanisms, the total energy budget of the corona is still only $\approx 10^{-4}$ of the Sun's total output. Hence, the issue is not the source of the coronal energy, but the mechanism which converts this small fraction of the total solar output into heating and this problem is still debated.

For its solution, reliable measurements of coronal temperatures at different heights and in different coronal structures are mandatory. In Figure 2.2 we show the results obtained for the $T_e(r)$ profile inside a coronal streamer from white light data; these temperatures have been derived from equation 2.2 assuming hydrostatic equilibrium to hold locally at each altitude r . It turns out that in coronal streamers T_e continuously rises between $0.001 - 0.003$ and $0.3 - 0.4 R_\odot$, and decreases at higher altitudes. Similar profiles have been obtained also from EUV observations of coronal holes showing mainly the same general behaviour shown in Figure 2.2 for coronal streamers (see e.g. Kohl et al., 1997; Ko et al., 1997).

Before concluding this Section we point out that temperatures have been derived in the hypothesis that plasma along the LOS is isothermal. However, because the coronal plasma is optically thin (as we discuss in § 3.1) at all wavelengths, whenever different structures are present along the LOS this assumption is not tenable and a further factor of uncertainty affects the derived values.

2.4 Coronal elemental abundances

Elemental abundances can be derived both from *remote sensing* technique (as we describe in the next Chapter) and *in situ* measurements. In the last years it has been found that some elements appear to be overabundant with respect to the photospheric abundances, while other elements are possibly depleted. The main parameter which seems to separate elements with different behaviour is the *First Ionization Potential* (FIP): elements with a low FIP (i.e. $\leq 10 - 10.5$ eV) seem to be depleted with respect to elements with a high FIP ($\geq 10 - 10.5$ eV). This phenomenon (referred to as *FIP-effect*) is typically unobserved in coronal holes and is characteristic of coronal streamers. In particular, in these structures a center-to-limb effect has been observed (i.e. a larger FIP effect in the streamer limbs with respect to the center; see e.g. Raymond et al, 1997) at $1.5 R_{\odot}$. This effect becomes very important when streamer abundances are compared with *in situ* measurements: from the ratio between the abundances of low to high FIP elements (such as Mg/O or Fe/O, where Mg and Fe are low FIP, while O is a high FIP element) it has been found an anti-correlation between the solar wind speed and the FIP-effect (see e.g. Aellig et al., 1999). Hence these observations may lead to conclude that the slow wind source lies in the coronal streamer boundaries. However, observations in coronal streamers at higher heliocentric distances ($3.6 R_{\odot}$) led to conclude that slow wind may originate also from the streamer cusps (Strachan et al., 2002), while other works indicate the low latitude branches of coronal holes as another possible source of slow wind (Poletto et al., 2002); as a consequence, this subject is up to now debated.

Chapter 3

Coronal plasma diagnostics

In this Chapter we briefly discuss the origin of the coronal spectral line emission in the extreme ultra-violet range (EUV; $\lambda \sim 100 - 1000\text{\AA}$). The observed properties of the radiative emission from the solar corona strongly depend on the physical parameters of the emitting plasma. In order to extract, from the coronal data, information about the plasma temperature, density, elemental abundances and velocity field we need to know all the main processes responsible for this emission, that we briefly review in § 3.2. We then concentrate on the plasma diagnostic techniques to estimate the plasma parameters from EUV observations (§ 3.3). At the end of this Chapter (§ 3.4) we also give a concise discussion of the physical processes originating the coronal continuum emission in the white light range (WL; $\lambda \sim 3000 - 7000\text{\AA}$). As we will show, this information complements those derived from UV lines, allowing a better exploitation of data whenever both observations are available.

3.1 The observed coronal emission

The spectrum of the solar corona spans over at least 14 orders of magnitude, from the shortest wavelengths in γ -rays to hard X-rays, soft X-rays, ultraviolet, visible, infrared and radio, with each wavelength regime revealing different physical processes. From the observational point of view, typically 4 different components to the coronal spectrum (formed by different mechanisms) are distinguished, namely:

- the *K-corona* (Kontinuierlich): shows a strongly polarized continuum spectrum, where the photospheric Fraunhofer lines are not visible because have been completely smeared out. This component arises from the scattering of the photospheric light by the fast moving electrons of the coronal gas (described in § 3.4);
- the *F-corona* (Fraunhofer): shows the Fraunhofer absorption lines of the photospheric spectrum. This component arises from the scattering of the photospheric light by small dust particles;

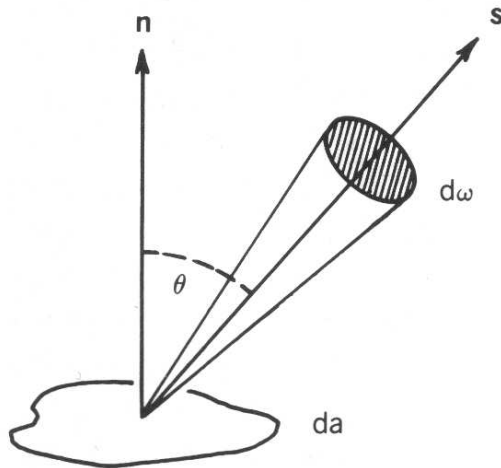


Figure 3.1: Geometry of the radiation transport from the source region to the observer: the specific intensity I_ν is defined in the text.

- the *E-corona* (Emission): is made of line emission from various atoms and ions in the high temperature coronal ambient (described in § 3.2): the strongest line in the visible range is the 530.3 nm line of Fe XIV (green line);
- the *T-corona* (Thermal): is a barely visible component in the infrared spectrum caused by the thermal emission of interplanetary dust.

Because of its high temperature, the primary coronal emission is in the UV and soft X-ray spectral range, where emission lines of the E-corona are strong relative to the background level of K- and F- continuum emission. At any frequency ν , the *specific intensity* I_ν ($\text{erg s}^{-1} \text{sr}^{-1} \text{cm}^{-2} \text{Hz}^{-1}$) is defined (see Figure 3.1) as the energy per time interval dt in the frequency between ν and $\nu + d\nu$ flowing within a solid angle $d\omega$ through an area da in the direction of the vector \mathbf{s} oriented at an angle θ with respect to the normal \mathbf{n} to the surface. We can then write

$$dE_\nu = I_\nu da \cos \theta d\omega d\nu dt \quad (\text{erg}) \quad (3.1)$$

The variation of this quantity dI_ν as it passes through intervening material depends on the intensity increase $dI_\nu^{em}(s) = \epsilon_\nu(s) ds$ (where $\epsilon_\nu(s)$ is the *local emission coefficient* due to atomic emission processes at the position s along the path through the solar source) and the intensity decrease $dI_\nu^{ab} = -k_\nu(s) I_\nu(s) ds$ (where $k_\nu(s)$ is the *specific* (i.e. function of ν) *absorption coefficient*) due to the atomic absorption processes. Combining these two contributions we can write the *radiative transfer*

equation:

$$\frac{dI_\nu(s)}{ds} = -k_\nu(s) I_\nu(s) + \epsilon_\nu(s)$$

This equation written in terms of the so-called *source function* $S_\nu = \epsilon_\nu(s)/k_\nu(s)$ and of the *optical depth* $\tau_\nu(s) = \int_{s_0}^s k_\nu(s') ds'$ (where s_0 is the remotest source location along the line of sight s) has approximate solutions in the optically thick ($\tau_\nu \gg 1$) and optically thin ($\tau_\nu \ll 1$) limits:

$$\begin{aligned} I_\nu(\tau_\nu) &\approx S_\nu && \text{if } \tau_\nu \gg 1 \\ I_\nu(\tau_\nu) &\approx I_0 + S_\nu \tau_\nu && \text{if } \tau_\nu \ll 1 \end{aligned}$$

where $I_0 = I_\nu(s_0)$ is the background intensity in absence of any intervening material. Mainly because of the low coronal density, the transfer equation for the coronal plasma holds in the optically thin limit. Moreover, because $I_0 \sim 0$, the coronal specific intensity I_ν is proportional to the opacity τ_ν , which for a constant absorption coefficient is proportional to the depth L of the source ($k_\nu = \text{const}$ implies $\tau_\nu(s) = \int_0^L k_\nu ds = k_\nu L$).

As we said, this Thesis (apart from a brief Section on WL emission) focusses on the analysis of the UV spectrum. We note, in passing, that in an optically thin plasma, because L increases from the disk center outwards, there is a center-to-limb effect, which is fairly visible in UV. Because our UV data are taken at heliocentric distances $> 1.5 R_\odot$, we do not have such effect and we will not discuss this issue any further. After this brief introduction on the general characteristics of the coronal spectrum, we proceed to review the physical processes leading to coronal UV emission.

3.2 UV Spectral line emission

In this Section we start illustrating the ambient where the processes leading to UV line formation occur (§ 3.2.1). After a general introduction on the spectral line formation (§ 3.2.2), we describe the main processes leading to the atomic levels population (§ 3.2.3) and to different ionization stages (§ 3.2.4). We conclude deriving an expression for the observed line intensities (§ 3.2.6) and reviewing the processes responsible for the observed line profiles (§ 3.2.7).

3.2.1 The validity of thermodynamic equilibrium

A gas is in *thermodynamic equilibrium* at a temperature T if the energy transfer between the particles is dominated by collisions. The process that leads to thermodynamic equilibrium is called thermalisation (characteristic of high density gases) and is the basic requirement for the validity of the Saha equation (which controls the ratio between ionization states of the same element), the Boltzmann equation (which controls the atomic level population within a specific ion) and the Planck

function (which gives the energy density of the radiation field). In thermodynamic equilibrium a single temperature T can be assumed and the velocity distribution of ions can be described by a *Maxwellian distribution* at that temperature. Global thermodynamic equilibrium requires that no temperature gradients exist in the plasma and this condition is practically never achieved in real plasmas. However, when the gas parameters (temperature, pressure, etc...) are varying in space and time so slowly that one can assume thermodynamic equilibrium to hold in the neighborhood of any point, we are in the condition of *local thermodynamic equilibrium* (LTE). In other words, LTE is valid whenever the thermalization length is (much) shorter than the distance over which the gas parameters vary. In the transition region and corona, the plasma is optically thin and the emitted photons are free to escape without further interactions with the ambient: hence there is no LTE. The very concept of “temperature” breaks down, the thermodynamic equilibrium laws mentioned above are not valid and the velocity distributions of coronal protons and electrons are not expected to be Maxwellian. However, it can be shown that in some coronal regions it is still possible to consider the protons and electrons in thermal equilibrium, if the collisional processes which thermalize the gas are more efficient than the processes preventing the equilibrium. To this end we evaluate the most important parameters for thermalization which are the proton-proton (τ_{pp}), electron-proton (τ_{ep}) and electron-electron (τ_{ee}) collision times, and compare these with the characteristic time for coronal expansion (τ_{exp}), assumed to be representative of characteristic time over which plasma conditions change. Estimates for these times as a function of the ambient electron temperature and density are given by (Mariska, 1992):

$$\tau_{pp} \approx (0.313 \text{ s cm}^{-3} \text{ K}^{-\frac{3}{2}}) \cdot \left(\frac{m_p}{m_e}\right)^{1/2} \frac{T_p^{3/2}}{N_p \ln \Lambda}$$

$$\tau_{ee} \approx (0.313 \text{ s cm}^{-3} \text{ K}^{-\frac{3}{2}}) \cdot \frac{T_e^{3/2}}{N_e \ln \Lambda}$$

$$\tau_{ep} \approx (13.0 \text{ s cm}^{-3} \text{ K}^{-\frac{3}{2}}) \cdot \frac{T_e^{3/2}}{N_e}$$

where T_p and N_p are the proton kinetic temperature and density, T_e and N_e are the electron kinetic temperature and density, and $\ln \Lambda = 23 - \ln(N_e^{1/2} T_e^{-3/2})$ is the Coulomb logarithm ($\ln \Lambda \sim 20$ in solar transition region and corona). In an equatorial coronal streamer ($N_e \sim N_p \sim 7 \cdot 10^7 \text{ cm}^{-3}$, $T_e \sim T_p \sim 1.3 \cdot 10^6 \text{ K}$ at $1.2 R_\odot$; Gibson et al., 1999) we obtain values of $\tau_{pp} = 14\text{s}$, $\tau_{ee} = 0.33\text{s}$, $\tau_{ep} = 270\text{s}$. Because in equatorial coronal streamers the outflow speed is negligible up to an heliocentric distance of $\sim 3.6 R_\odot$ (see Strachan et al., 2002), there is no coronal expansion ($\tau_{exp} \sim \infty$) and the assumption of a single temperature plasma governed by a Maxwell-Boltzmann distribution is justified up to this distance. However, even assuming that the plasma is outflowing at a speed $v_{exp} = (2.5 \cdot 10^8 \text{ cm}^{-2} \text{ s}^{-1} / N_e) \times [215.4 / h(R_\odot)]^2 \simeq$

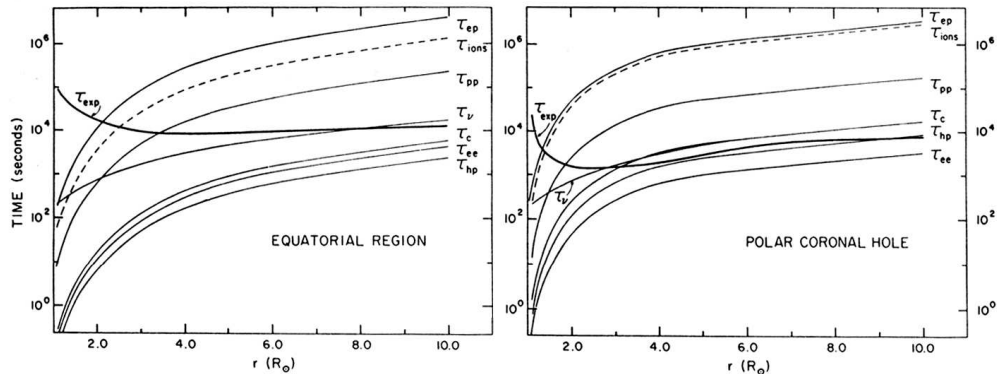


Figure 3.2: Characteristic times τ as a function of the heliocentric distance in a typical equatorial region (left panel) and in a coronal hole (right panel). This Figure compares time scales for different processes: the ionization equilibrium time τ_{ion} for heavy ions, H I collisional ionization times τ_c , H I photoionization time τ_ν , electron thermalization time τ_{ee} , proton thermalization time τ_{pp} , time for hydrogen-proton charge exchange τ_{hp} and time for electron and proton temperatures equalization τ_{ep} . These times have to be lower than the coronal expansion times τ_{exp} in order to maintain LTE condition and ionization equilibrium (adapted from Withbroe et al., 1982).

1.1 km/s given by the mass flux conservation, we have $\tau_{exp} = [(v/n) dn/dr]^{-1} \simeq 1.6 \cdot 10^5$ s and the thermodynamic equilibrium hypothesis is still valid. By using the same formulas in a coronal hole ($N_e \sim N_p \sim 5 \cdot 10^7$ cm $^{-3}$, $T_e \sim T_p \sim 8.5 \cdot 10^5$ K at 1.2 R_\odot ; Cranmer et al., 1999) we obtain values of $\tau_{pp} = 10$ s, $\tau_{ee} = 0.24$ s, $\tau_{ep} = 200$ s, while $\tau_{exp} \simeq 780$ s with $v_{exp} \sim 110$ km/s (Cranmer et al., 1999) and the LTE condition is also justified. Values at different heliocentric distances are given in Figure 3.2 (adapted from Withbroe et al., 1982) which shows that for τ_{exp} values computed with the above formula (assuming the mass flux conservation in the equatorial region and using the v_{exp} given by Munro & Mariska, 1977 for the polar region) the LTE condition is justified below $\sim 3 R_\odot$ and $\sim 2 R_\odot$ respectively in the equatorial and polar regions.

3.2.2 Spectral lines formation

The coronal spectrum is generated by the superposition of all the bound-bound (i.e. from an energy level to another within an ion/atom), bound-free and free-free emissions processes occurring among the coronal electrons and ions/atoms. The emission in a coronal spectral line of an element X with m electrons removed (X^{+m}) occurs via a bound-bound transition from a higher energy level X_j^{+m} to a lower level X_i^{+m} whereby the photon is emitted at a frequency $\nu_{ij} = \Delta E_{ij}/h$. The photon may be emitted via *spontaneous emission* (when an electron in a bound state spontaneously falls to the lower energy level) or *stimulated emission* (when an electron in a bound excited state is stimulated by a passing photon from the ambient radia-

tion field). From the same transition, photons are emitted over a small range of frequencies around ν_{ij} and this spread leads to the formation of the *emission profile* $\psi(\nu)$ (which, however, is by far less broad than the observed profile, whose origin is discussed in § 3.2.7). As mentioned above, the solar corona is optically thin, hence we can assume that the probability that the emitted photon interacts with other atoms/ions before leaving the corona is negligible. As a consequence, the process of stimulated emission can be neglected with respect to the spontaneous emission, which dominates, and we do not need to solve the radiative transfer equation. In this case, the specific emissivity $P_{ij}(\nu)$ (given in $\text{erg cm}^{-3} \text{s}^{-1} \text{Hz}^{-1}$) in the transition $j \rightarrow i$ of a unit volume of plasma is given by:

$$P_{ij}(\nu) = N_j(X^{+m}) A_{ji} h\nu_{ij} \psi(\nu) \quad (3.2)$$

where $N_j(X^{+m})$ is the number density (cm^{-3}) of atoms m times ionized X^{+m} which are in level j and A_{ji} (s^{-1}) is the spontaneous radiative transition probability. The total power P_{ij} (typically referred to as the *line emissivity*) emitted in the transition $j \rightarrow i$ is then given by:

$$P_{ij} = \int_0^\infty P_{ij}(\nu) d\nu = N_j(X^{+m}) A_{ji} h\nu_{ij} \quad (\text{erg cm}^{-3} \text{s}^{-1}) \quad (3.3)$$

In the literature an alternative definition of the line emissivity independent of the ion number density $N(X^{+m})$ is

$$\epsilon_{ij} \equiv \frac{P_{ij}}{N(X^{+m})} = \frac{N_j(X^{+m})}{N(X^{+m})} A_{ji} h\nu_{ij} \quad (\text{erg s}^{-1}) \quad (3.4)$$

which is referred to as the *normalized line emissivity*. The intensity I_{ij} ($\text{erg cm}^{-2} \text{s}^{-1} \text{sr}^{-1}$) detected at Earth in the observed emission line (in the optically thin limit) is given by:

$$I_{ij} = \frac{1}{4\pi} \int_{-\infty}^{+\infty} P_{ij} dz \quad (3.5)$$

where the integration is made along the line of sight (LOS) z .

The largest source of uncertainty in the latter equations is the number density $N_j(X^{+m})$, because of the unknown coronal abundance of the element X and of the many processes possibly modifying the particular ionization state $+m$ and the j -level population of the X atom. Each element may be found in one or several different stages of ionization at any given plasma temperature and the computation of any transition probability often depends upon having many other transitions already calculated. Moreover, depending on the behaviour of the excited level population, spectral lines may be distinguished between those from *allowed transitions* and those from metastable levels referred to as *forbidden* or *intersystem lines*. Hence, in order to evaluate F_{ij} , it is necessary to introduce some approximations. Typically plasma is assumed to be in a *steady state*: locally the thermodynamic plasma conditions are

not time-dependent. This assumption is valid whenever the time scales for energy input to the coronal gas and/or for the changes in the gas thermodynamic state are short with respect to the time scales for the other physical processes involved. The plasma steady state holds in "stable" coronal structures such as streamers and coronal holes, while its validity has to be verified in transient or impulsive phenomena such as Coronal Mass Ejections (CMEs) or flares. In the next sections we describe the other assumptions typically introduced to compute the atomic level population (§ 3.2.3) and the atomic ionization state (§ 3.2.4).

3.2.3 Atomic levels population

The electron of an m times ionized atom may be in the ground level g of that stage or in any of the excited levels j . In general, any given level j may be populated by radiative and collisional excitation from lower levels and by collisional de-excitation and both spontaneous and stimulated radiative decay from upper energy levels. Hence the same atomic processes may depopulate the j -th level via excitation to higher levels or de-excitation to lower levels. The population density of each level must be calculated by summing in a statistical manner (i.e. taking into account all the different statistical weights) over a number of adjacent levels considering all the excitation and de-excitation mechanisms for each level. Moreover, the j -th level may be depopulated by ionization (if the electron is removed) or populated by recombination (if an electron is captured) processes. A selection of the most important atomic processes that contribute to the atomic levels population (and to the atom distribution among different ionization stages) is shown in Figure 3.3. In practice, carrying out a calculation that takes into account all these processes is an enormously complicated task that is solved by introducing some approximations which we list hereafter.

- First, we point out that in the chromosphere and the lower corona ionization and recombination processes (occurring on time scales on the order of tens to thousands of seconds) are much slower than excitation and de-excitation processes (fractions of a second). This allows us to compute the population of a j -th level for a given ionization stage $+m$, independently of the ionization/recombination processes (discussed separately in § 3.2.4).
- Second, the steady state condition corresponds, as far as atomic processes are concerned, to the *statistical equilibrium* hypothesis: if the plasma does not evolve on time scales faster than the characteristic time scale for excitation/de-excitation processes (on the order of $10^{12}/N_e$ s, see e.g. Harrison & Thompson, 1992; Mariska, 1992), we can assume that the level population is not time-dependent (i.e. $dN_j(X^{+m})/dt = 0$), because the atomic processes populating and depopulating that level balance each other.
- Third, under conditions usually found in the solar corona ($T < 10^7$ K and $N_e < 10^8$ cm⁻³), the computation of the atomic level population can be simplified

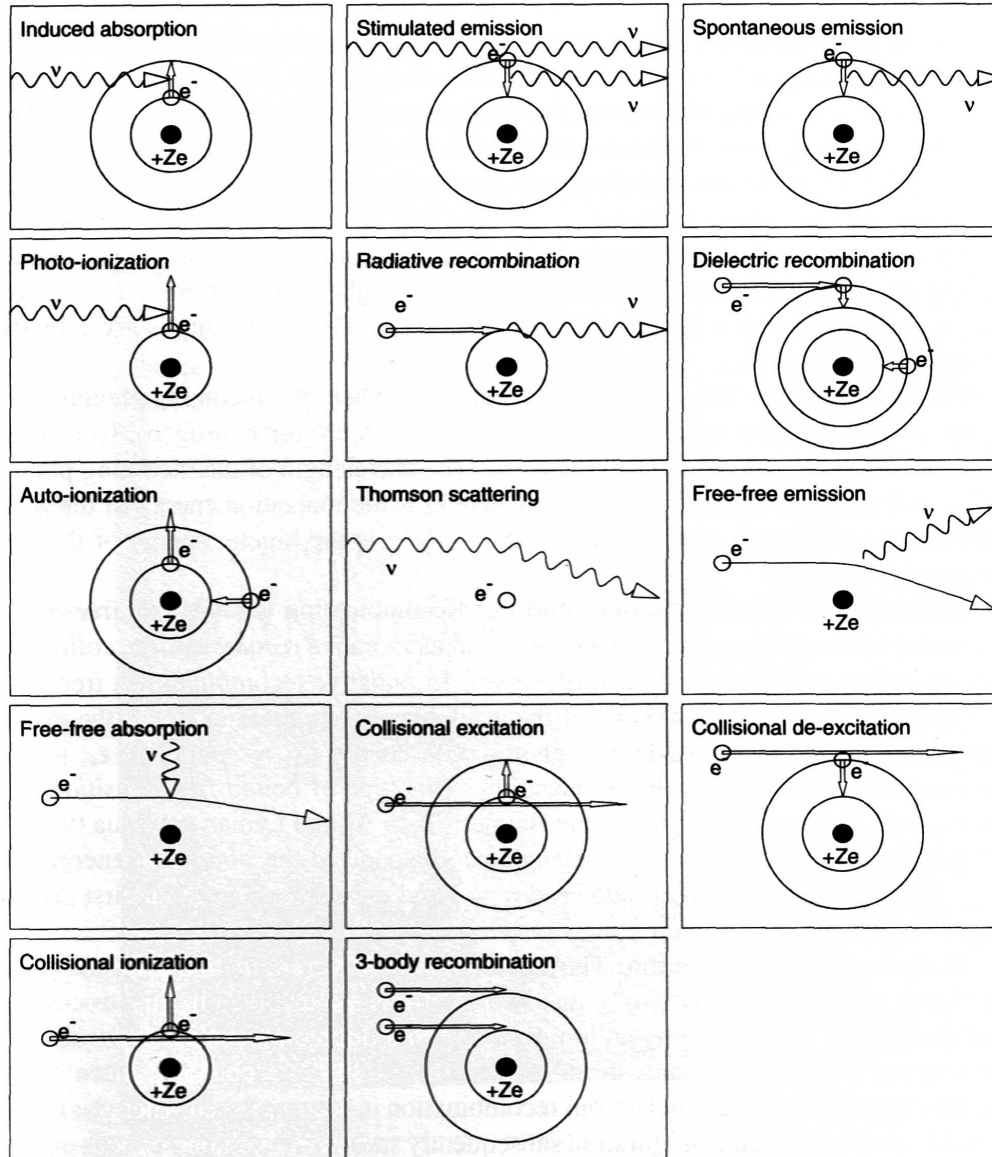


Figure 3.3: A diagram showing the main physical processes involved in the excitation/de-excitation and ionization/recombination of coronal atoms. Atoms and ions are marked with filled dots, electron with open dots, electron orbits with circles, electron transitions with arrows and photons with a wiggly arrow (from Aschwanden, 2004).

even more by assuming that the j -th level is populated/depopulated exclusively from/to the ground level g , hence that $N_j(X^{+m}) \ll N_g(X^{+m}) \simeq N(X^{+m})$ (where $N(X^{+m})$ is the number density (cm^{-3}) of the m times ionized element X). The latter condition (usually referred to as the *two level atomic model*) holds for allowed transitions from the ground level of ions without metastable levels (such as the Li-like ions) and is justified by the higher efficiency in the corona of the spontaneous emission (populating the g level) with respect to all the excitation processes (depopulating the g level) shown in Figure 3.3.

- Fourth, a comparison among the computed time scales for all the different atomic processes possibly involved in the level population changes, shows that in coronal conditions the excitation to the upper level j occurs mainly by collisions with thermal electrons (*collisional excitation*), while the level depopulation occurs mainly by *spontaneous emission*. The collisional de-excitation is negligible because of the low coronal density, while the stimulated emission does not occur because of the low (in the EUV range) background radiation field and the optical thinness of the coronal plasma; hence, these processes can be neglected (this is sometimes referred as the *coronal approximation*). Moreover, the collisional excitation by protons is less important than excitation by electrons and can also be neglected.

We note that for ions with metastable levels j for which the radiative decay rate A_{jg} is small, the collisional de-excitation becomes an important depopulating mechanism and the above approximations are not valid. As we mentioned at the beginning of this section, any given level j may be populated also by radiative excitation. This occurs for those atoms/ions which emit in lines whose chromospheric emission is high. In this case, absorption of photons from the background radiation (*induced absorption*, called also *radiative excitation*) is also important. In the following we concentrate only on electron collisional excitation, radiative excitation and spontaneous emission and we give for each of these processes an expression for the number of transitions occurring per cm^3 per second assuming that all the above approximations are valid.

Electron collisional excitation

Collisions of ions with free coronal electrons may excite an ion from its ground level g to an upper j -th level (depending on the kinetic energy E_e of the impacting electron). The number of collisional excitation processes (in units of $\text{cm}^{-3}\text{s}^{-1}$) is given by $N_g(X^{+m}) N_e C_{gj}^e$ where $N_g(X^{+m}) \simeq N(X^{+m})$ is the number density (cm^{-3}) of the ion X^{+m} in the ground state g , N_e (cm^{-3}) is the electron density and C_{gj}^e is the electron collisional excitation coefficient (cm^3s^{-1}). The latter can be computed, once the collisional cross section σ_{gj} (cm^{-2}) is known, as

$$C_{gj}^e = \int_0^{+\infty} \sigma_{gj}(v) f(v) v dv \quad (3.6)$$

where $f(v)$ is the velocity distribution of the impacting electrons. The collisional cross section is given by:

$$\sigma_{gj} = \frac{\pi a_0^2 I_H \Omega_{gj}(E_e)}{\omega_g E_e} \quad (3.7)$$

where a_0 is the Bohr radius, I_H is the ionization potential of the hydrogen atoms, $\Omega_{gj}(E_e)$ is the *collision strength* and $\omega_g = (2J + 1)$ is the statistical weight of the ground state. Assuming (because of thermodynamic equilibrium) $f(v)$ to be Maxwellian, C_{gj}^e can be expressed as a function of the electron temperature T_e as:

$$C_{gj}^e = \frac{8.63 \cdot 10^{-6}}{\omega_g T_e^{1/2}} \int_{\Delta E_{gj}} \Omega_{gj}(E) \exp\left(-\frac{E_e}{k_B T_e}\right) d\left(-\frac{E_e}{k_B T_e}\right) \quad (3.8)$$

where ΔE_{gj} is the threshold energy for the transition, k_B is the Boltzmann's constant and the collision strength $\Omega_{gj}(E)$ is obtained from theoretical calculations.

Radiative excitation

Absorption of a photon at frequency ν may excite an ion from its ground level g to an upper level j provided the photon energy $h\nu$ is equal or larger than the energy difference between the two levels ΔE_{gj} . If \bar{J} (erg cm⁻²) is the mean intensity of the exciting disk radiation absorbed by the scattering ions and B_{gj} (erg⁻¹ cm² s⁻¹) is the Einstein absorption coefficient, then the number of radiative excitation processes (in units of cm⁻³s⁻¹) is given by $N_g(X^{+m}) B_{gj} \bar{J}$. The general expression for the coefficient B_{gj} is:

$$B_{gj} = \frac{\omega_g}{\omega_j} \frac{8\pi^2 e^2 f_{gj}}{2h\nu_{gj} m_e c} \quad (3.9)$$

where $e = 4.8 \cdot 10^{-10}$ esu is the electron charge, ω_g is the statistical weight of the ground level g , m_e is the electron mass and f_{gj} is the oscillator strength of the considered transition. \bar{J} can be evaluated once the exciting spectrum (typically originating in the underlying chromosphere), the atomic absorption profile and the velocity distribution of the absorbing atoms are known.

Spontaneous emission

As already mentioned, in the solar corona the spontaneous emission dominates over the stimulated emission and the collisional de-excitation. If $A_{jg} = B_{gj} 2h\nu^3/c^2$ (s⁻¹) is the Einstein coefficient for the spontaneous emission from the j -th level to the ground level g , then the number of processes per unit volume and per second (cm⁻³s⁻¹) is given by $N_j(X^{+m}) A_{jg}$.

We note, however, that radiative excitation is important only for spectral lines which have a high exciting radiation, hence lines which form also in the underlying chromosphere transition region. For spectral lines observed only in the solar corona

only the collisional component is important. In order to evaluate $N(X^{+m})$, we write the *statistical equilibrium equation* for the population of the atomic level j of the ion X^{+m} ; taking into account the three processes mentioned above (and recalling that $N_g(X^{+m}) \simeq N(X^{+m})$), this equation can be written as:

$$N(X^{+m}) (N_e C_{gj}^e + B_{gj} \bar{J}) = N_j(X^{+m}) \sum_{i < j} A_{ji} \quad (\text{cm}^{-3} \text{s}^{-1}) \quad (3.10)$$

This simple relationship gives the number density $N_j(X^{+m})$ for the X^{+m} ion excited to the j -th level as a function of the number density $N(X^{+m})$ of the ion it self: the determination of the latter parameter is discussed in the next Section.

3.2.4 Atomic ionization balance

The ion number density $N(X^{+m})$ is often given as a chain of ratios:

$$N(X^{+m}) \equiv \frac{N(X^{+m})}{N(X)} \frac{N(X)}{N(H)} \frac{N(H)}{N_e} N_e$$

This expression separates the dependence of $N(X^{+m})$ on the electron temperature T_e (given by the ratio $R_X(T_e) = N(X^{+m})/N(X)$ defined by the *ionization balance*) and on the abundance of the element X relative to hydrogen (given by the ratio $A_X = N(X)/N(H)$). In the corona usually $N(H)/N_e \simeq N(H)/[N(H) + 2N(He)] \simeq 0.83$ assuming that both hydrogen and helium are fully ionized and that $N(He)/N(H) \simeq 0.1$. Hence, the term $N(X^{+m})$ is typically written as:

$$N(X^{+m}) = 0.83 \cdot R_X(T_e) A_X N_e \quad (3.11)$$

and the number $N(X^{+m})$ can be evaluated by the ionization balance equations. The ionization stage X^{+m} of a given element depends on many different ionization and recombination processes (see Figure 3.3). However, as we did for the determination of the atomic levels population, it is possible to identify the predominant phenomena in the coronal plasma.

Ionization processes for astrophysical plasmas include, among others, photoionization, collisional ionization and auto-ionization. In the low density, high temperature coronal plasma the photoionization (i.e. the bound-free transition due to the absorption of a photon carrying an energy higher than the ionization energy), three-body recombination (i.e. the inverse process of collisional ionization) and charge exchange recombination (i.e. the capture by an ion of a neutral hydrogen electron) processes are negligible. Hence, in the following we describe the most important processes determining the ionization stage of each element in the corona, namely the collisional ionization, radiative recombination, dielectronic recombination and auto-ionization.

Collisional ionization

Collisional ionization occurs whenever free electrons colliding with an atom/ion remove one of its bound electrons. This process requires the speed of the ambient electrons to be comparable with that of the bound electrons. Because in each ion the binding energy gets progressively larger from the outer to the inner electrons, higher plasma temperature corresponds to higher ionization stage species. The abundance curve of any given atomic ionization stage X^{+m} as a function of temperature has a minimum both at low temperatures (because free electrons have not enough energy to ionize the atom) and at very high temperatures (because the “average” degree of ionization is much greater). In between these two minima there is a temperature $T_{max}(+m)$ of maximum efficiency for the ionizing process (depending on the selected ionization stage $+m$ and the considered atomic species) called *temperature of maximum formation*. In spite of the low coronal densities, this is the dominant ionization process because of the weak radiation field where the corona is immersed.

Radiative recombination

The radiative (or two-body) recombination is the capture of a free electron by an ion into one of the available energy states followed by the emission of a photon; this is the inverse process of the photoionization.

Dielectronic recombination and auto-ionization

In these two processes a free electron is captured by the ion and lands in an excited state, while also one of the bound electrons becomes excited; both electrons are excited and we end up with a doubly excited state. Hence, the process can follow two different ways: if the highly unstable doubly excited configuration stabilizes (with one or both excited electrons falling to the lowest available state) we have the dielectronic recombination. On the contrary, if the ion spontaneously ionizes ejecting an highly excited electron, while an excited bound electrons falls to a lower state, we have the auto-ionization process. The net result of the latter reaction is equivalent to an elastic collision between an electron and the ion.

The assumption of balance between opposing processes made for bound-bound transitions determining the population of the j -th level, can also be extended to the bound-free transitions to include ionization processes. Hence, for a plasma in thermodynamic equilibrium at a given temperature T , a balance is generally assumed between all processes causing the stripping of electrons from atoms of a given element and all the recombination processes leading to lower ionization stages. This approximation is used to calculate the *ionization equilibrium*: that is, under this hypothesis, given a plasma temperature T , we can write a system of equations for the ionized stages of a given element from which the number density of each ion X^{+m} can be evaluated. Once the ionization balance $R_X(T_e)$ is computed, from the statistical

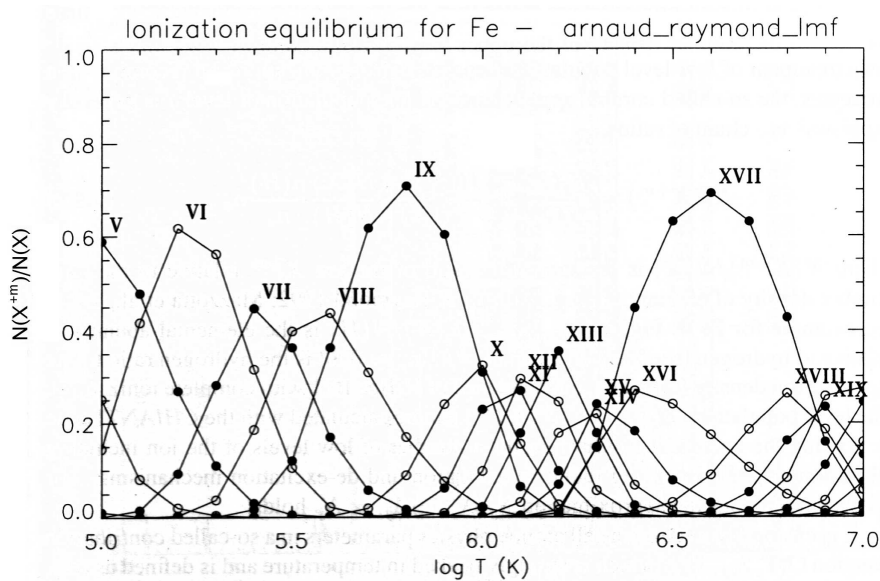


Figure 3.4: Ionization equilibrium calculations for different Fe ionizations stages (from Fe v to Fe XIX) in the temperature range $T = 10^5 - 10^7$ as calculated by Arnaud & Raymond (1992) using the CHIANTI code.

equilibrium (equation 3.10) it is possible to compute, for each ionization stage, the population of different levels j . Ionization equilibrium and levels population can be computed with spectral codes available on the web; an useful code is the *Arcetri Spectral code* (Landi & Landini, 1998; Landini & Monsignori Fossi, 1990) accessible also the web¹. This code computes the contribution function for different spectral lines as a function of temperature; moreover, the CHIANTI database allows the user to evaluate the normalized emissivity ϵ_{ij} (see equation 3.4) for a given plasma temperature and electron density (see Figure 3.4).

3.2.5 The validity of ionization equilibrium

In order to determine the coronal regions where the ionization equilibrium can be considered a valid hypothesis it is necessary (similar to our discussion for the validity of thermodynamic equilibrium in § 3.2.1) to compare the time scales for ionization τ_{ions} and recombination τ_{rec} processes with the coronal expansion time τ_{exp} . For an ion X^{+m} the collisional ionization time $\tau_{ions}(m)$ to reach the ionization state $m + 1$ and the recombination time $\tau_{rec}(m)$ from the state $m + 1$ to m can be written as

$$\tau_{ions}(m) = (N_e q_m)^{-1} \quad ; \quad \tau_{rec}(m) = (N_e \alpha_{m+1})^{-1} \quad (3.12)$$

where q_m and α_{m+1} are the ionization and recombination rates ($\text{cm}^3 \text{s}^{-1}$). In order to estimate these times, it is necessary to assume a coronal model that gives tem-

¹See <http://wwwsolar.nrl.navy.mil/chianti/othercodes.html> for a list of spectral codes available on the web.

peratures, densities and outflow speeds at different heliocentric distances. Results from these computations are given in Figure 3.2 (from Withbroe et al., 1982) that shows the ionization equilibrium time for heavy ions τ_{ions} vs. the coronal expansion time at different heliocentric distances. From this Figure we can see that, because the density drops and the outflow speed increases with distance, above ~ 1.5 and $\sim 2.5 R_{\odot}$ respectively at the polar and equatorial region, the lifetime of the ions is longer than the coronal expansion time and there is no ionization balance. In these conditions, no further ionization/recombination processes have time to occur and the atomic ionization state becomes “frozen-in”, i.e. is conserved into the outflowing solar wind. For the hydrogen atoms, time scales involved in the ionization equilibrium are the photoionization time τ_{ν} and the collisional ionization τ_c in Figure 3.2, which overcome the coronal expansion time above ~ 3 and $\sim 8 R_{\odot}$ respectively at the polar and equatorial region.

3.2.6 Emission line intensity

We can now compute the intensity of coronal emission lines. The observed emission is the sum of the collisional (I_{col}) and the radiative (I_{rad}) components: in the following we give the general expressions for the radiative and collisional components of the observed line intensities and we will show in § 3.3.1 how in the data analysis we can separate these two contributions.

Collisional component

As we already discussed, the number of collisional excitation processes n_c occurring per second and cubic centimeter is given by $n_c = N(X^{+m}) N_e C_{gj}^e$ ($\text{cm}^{-3} \text{s}^{-1}$) where $N(X^{+m}) = 0.83 \cdot R_X(T_e) A_X N_e$, hence

$$n_c = 0.83 \cdot R_X(T_e) A_X C_{gj}^e(T_e) N_e^2 \quad (3.13)$$

The collisional line emissivity P_{gj}^{col} ($\text{erg cm}^{-3} \text{s}^{-1}$) is then given by

$$P_{gj}^{col} = 0.83 \cdot h\nu_{gj} R_X(T_e) A_X C_{gj}^e(T_e) N_e^2 \quad (3.14)$$

The photons emitted from collisional excitations spread over a solid angle of 4π , hence the expression for the observed collisional line intensity I_{gj}^{col} is obtained by integrating the emissivity along the line of sight:

$$I_{gj}^{col} = \frac{1}{4\pi} \int_{-\infty}^{+\infty} P_{gj}^{col} dz \quad (\text{erg cm}^{-2} \text{sr}^{-1} \text{s}^{-1}) \quad (3.15)$$

We note that the above equations have been written by assuming that $N(H)/N_e \simeq 0.83$. In general, $N(X^{+m}) = R_X(T_e) A_X N(H)$, hence equation 3.13 has to be written as

$$n_c = R_X(T_e) A_X C_{gj}^e(T_e) N_e N(H) \quad (3.16)$$

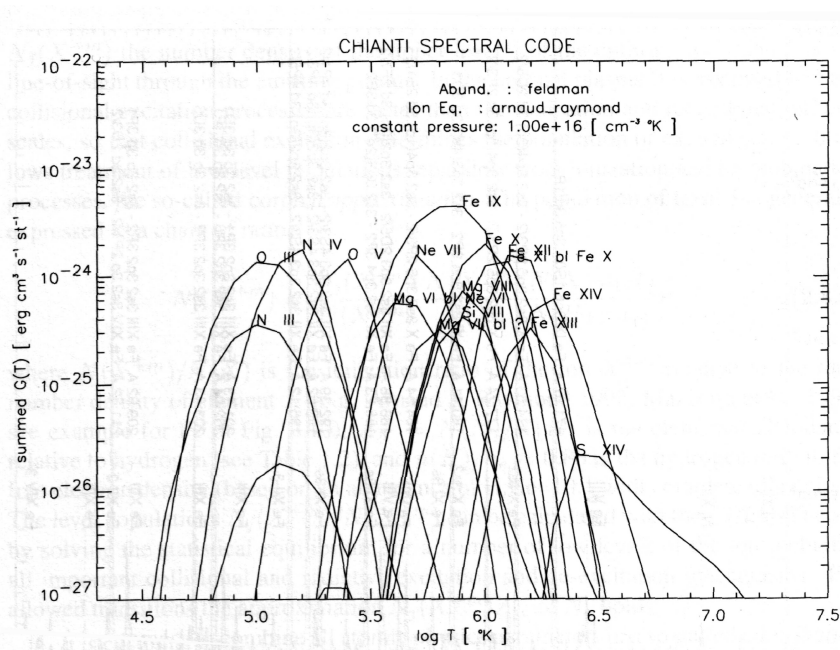


Figure 3.5: The contribution functions $G(T_e, A_X)$ (multiplied by a factor $h\nu_{gj}/4\pi$) for different spectral lines in the temperature range $T = 10^{4.3} - 10^{7.5}$. The curves showed in this Figure have been calculated with the CHIANTI code using elemental abundances from Feldman (1992), ionization equilibrium values from Arnaud & Raymond (1992) and Mazzotta et al. (1998) and a constant pressure $p = N_e T = 10^{16} \text{ cm}^{-3}\text{K}$.

From the latter equation we can define the so called *contribution function* C_{line} (which is useful to combine all the atomic physical parameters involved)

$$C_{line}(T_e, N_e) = \frac{N(H)}{N_e} R_X(T_e) C_{gj}^e(T_e) \quad (\text{cm}^3 \text{s}^{-1}) \quad (3.17)$$

With the approximation $N_H/N_e \simeq 0.83$ the contribution function is only temperature dependent ($C_{line} = C_{line}[T_e]$); as we better explain in § 3.3.3 this is true only for *allowed* transitions, while for *intercombination* or *forbidden* transitions the C_{line} function may be density-sensitive. In the literature there is an alternative definition of the contribution function including also the abundance factor:

$$G_{line}(T_e, A_X) = A_X C_{line}(T_e) \quad (\text{cm}^3 \text{s}^{-1}) \quad (3.18)$$

With the above definitions the collisional line intensity can be simply written as:

$$I_{gj}^{col} = \frac{h\nu_{gj}}{4\pi} \int_{-\infty}^{+\infty} G_{line}(T_e, A_X) N_e^2 dz \quad (3.19)$$

Often the collisional intensity is written by introducing the *differential emission measure* $dEM(T)/dT$ defined as:

$$\frac{dEM(T)}{dT} = N_e N(H) \frac{dz}{dT} \quad (\text{cm}^{-5} \text{K}^{-1}) \quad (3.20)$$

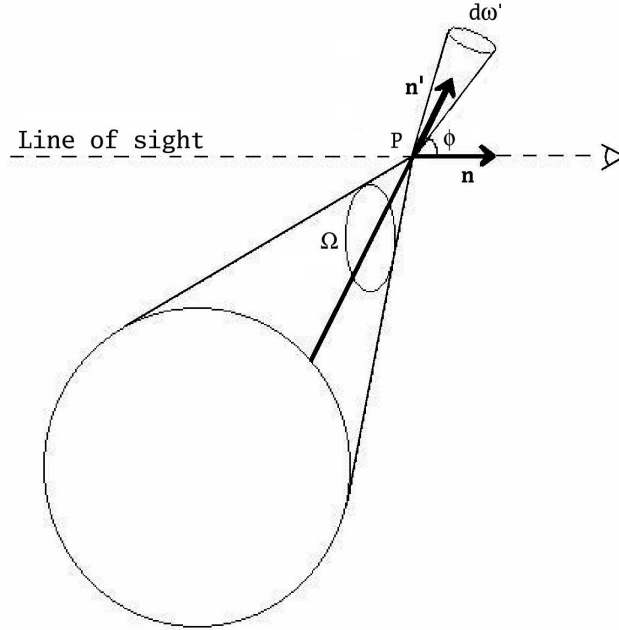


Figure 3.6: Geometry of the radiative excitation process and following diffusion of the absorbed radiation in the direction of the observer (see text).

hence we have:

$$I_{gj}^{col} = \frac{h\nu_{gj}}{4\pi} \int_T G_{line}(T_e, N_e, A_X) \frac{dEM(T)}{dT} dT \quad (3.21)$$

The $dEM(T)/dT$ function gives an indication of the amount of plasma along the line of sight in the interval between T and $T + dT$ that contributes to the emitted radiation. From the $dEM(T)/dT$ function it is possible also to define the *emission measure* EM as:

$$EM = \int_T \frac{dEM(T)}{dT} dT \simeq \int_{LOS} N_e^2 dz \quad (\text{cm}^{-5}) \quad (3.22)$$

which measures the amount of emitting plasma along the line of sight. As we will see later on (§ 3.3.3) this expression is useful for plasma density diagnostics.

Radiative component

As mentioned in § 3.2.3, the number n_r of radiative excitation processes occurring per second and cubic centimeter is given by:

$$n_r = N(X^{+m}) B_{gj} \bar{J} = 0.83 \cdot R_X(T_e) A_X N_e B_{gj} \bar{J} \quad (\text{cm}^{-3}\text{s}^{-1}) \quad (3.23)$$

where \bar{J} (erg cm^{-2}) is the mean intensity absorbed from the disk by the scattering ions. For the geometry of the scattering process we refer to Figure 3.6, where \mathbf{n}'

is the unit vector along the direction of the incident photon, \mathbf{n} is the unit vector parallel to the LOS (hence, the direction of propagation of the observed photon), Ω is the solid angle under which the solar disk is seen by the source of the scattered radiation and $d\omega'$ is the infinitesimal solid angle around \mathbf{n}' . The mean intensity \bar{J} absorbed by the scattering ion depends on the normalized absorption profile $\Psi(\nu - \nu_0)$ ($\int_0^\infty \Psi(\nu - \nu_0) d\nu = 1$) of the ion (in a frame of reference at rest with the ion where $\nu_0 \equiv \nu_{gj}$) as follows:

$$\bar{J} = \int_0^\infty J_\nu \Psi(\nu - \nu_0) d\nu \quad (\text{erg cm}^{-2}) \quad (3.24)$$

where J_ν is the average disk intensity $I_{disk}(\nu, \mathbf{n}')$ (at a given frequency ν) impinging from the whole disk on the scattering ion and is given by:

$$J_\nu = \frac{1}{4\pi} \int_\Omega I_{disk}(\nu, \mathbf{n}') d\omega' \quad (\text{erg cm}^{-2}) \quad (3.25)$$

By using equations 3.23, 3.24 and 3.25 we can write the emissivity P_{gj}^{rad} of a radiatively excited spectral line as:

$$P_{gj}^{rad} = 0.83 h\nu_{gj} B_{gj} \int_\Omega R_X(T_e) A_X N_e \int_0^\infty \Psi(\nu - \nu_0) I_{disk}(\nu, \mathbf{n}') d\nu \frac{d\omega'}{4\pi} \quad (\text{erg cm}^{-3} \text{s}^{-1}) \quad (3.26)$$

However, the latter equation holds only for scattering ions at rest with respect to the source of the exciting radiation. In a more general expression we have also to take into account that the scattering ions can be in motion with respect to the source of the exciting radiation, hence the absorbed spectrum is seen Doppler shifted in the ion frame of reference. In particular, if \mathbf{w} is the outflow speed of the absorbing ion, an incident photon emitted by the source at the frequency ν in the direction \mathbf{n}' is seen by the ion at a frequency ν' given by:

$$\nu' = \nu \sqrt{\frac{1 - \frac{\mathbf{w} \cdot \mathbf{n}'}{c}}{1 + \frac{\mathbf{w} \cdot \mathbf{n}'}{c}}} \simeq \nu \left(1 - \frac{\mathbf{w} \cdot \mathbf{n}'}{c} \right) \quad (3.27)$$

where c is the speed of light. Hence, in order to write the correct expression for the observed line intensity it is necessary to integrate equation 3.26 over the velocity distribution function $f(\mathbf{w})$ of the scattering ions. Moreover, the photons scattering is in general not isotropic: if ϕ is the angle between the directions \mathbf{n} and \mathbf{n}' (see Figure 3.6), the probability that a photon arriving from all the possible directions around \mathbf{n}' in $d\omega'$ is scattered in the direction \mathbf{n} is written as $p(\phi) d\omega'$, where $p(\phi)$ is the so-called *redistribution phase function*. Hence, this function has to be added in the integration over the solid angles $d\omega'$ in equation 3.26. Finally, the resulting expression for the line emissivity due to the radiative excitation is

$$P_{gj}^{rad} = 0.83 h\nu_{gj} B_{gj} \int_\Omega p(\phi) \int_{\mathbf{v}} f(\mathbf{v}) R(T_e) A_X N_e \int_0^\infty \Psi(\nu - \nu_0) I_{disk}(\nu', \mathbf{n}') d\nu d^3v \frac{d\omega'}{4\pi} \quad (\text{erg cm}^{-3} \text{s}^{-1}) \quad (3.28)$$

The intensity detected at Earth I_{gj}^{rad} ($\text{erg cm}^{-2} \text{s}^{-1} \text{sr}^{-1}$) is then given by and integration of the line emissivity along the line of sight:

$$I_{gj}^{rad} = \frac{1}{4\pi} \int_{-\infty}^{+\infty} P_{gj}^{rad} dz \quad (\text{erg cm}^{-2} \text{sr}^{-1} \text{s}^{-1}) \quad (3.29)$$

The expression for the $p(\phi)$ function depends on the spectral line; in particular, for the lines most frequently used here is (House, 1970; Beckers & Chipman, 1974; Noci et al., 1987):

$$\begin{aligned} &\text{Lyman-}\alpha \lambda 1216\text{\AA}, \\ &\text{Lyman-}\beta \lambda 1025\text{\AA} \text{ and} \quad 4\pi p(\phi) = \frac{11+3\cos^2\phi}{12} \end{aligned} \quad (3.30)$$

$$\begin{aligned} &\text{Lyman-}\gamma \lambda 973\text{\AA} \\ &\text{O VI } \lambda 1032\text{\AA} \quad 4\pi p(\phi) = \frac{7+3\cos^2\phi}{8} \end{aligned} \quad (3.31)$$

$$\text{O VI } \lambda 1037\text{\AA} \quad 4\pi p(\phi) = 1 \quad (3.32)$$

Assuming the ions to have a Maxwellian velocity distribution (if the plasma is in the LTE condition), the absorption profile $\Psi(\nu - \nu_0)$ along the direction \mathbf{n}' of the incident radiation can be written as a Gaussian function with a $1/e$ half width $\Delta\nu$ given by:

$$\Delta\nu = \frac{c}{\lambda^2} \Delta\lambda = \frac{\nu}{c} \sqrt{\frac{2k_B T_{\mathbf{n}'}}{m_i}} \quad (3.33)$$

where m_i is the mass of the emitting ion and $T_{\mathbf{n}'}$ is its kinetic temperature along the direction \mathbf{n}' . Hence, the normalized absorption profile (i.e. $\int_0^\infty \Psi(\nu - \nu_0) d\nu = 1$) is given by:

$$\Psi(\nu - \nu_0) = \frac{c}{\nu} \sqrt{\frac{m_i}{2\pi k_B T_{\mathbf{n}'}}} \exp \left[-\frac{m_i c^2}{2 k_B T_{\mathbf{n}'}} \left(1 - \frac{\nu}{\nu_0} \right)^2 \right] \quad (\text{Hz}^{-1}) \quad (3.34)$$

Equation 3.28 states that the component I_{rad} to the line intensity arises from a convolution integral between the atomic absorption profile $\Psi(\nu - \nu_0)$ and the incident lower atmosphere intensity $I_{disk}(\nu', \mathbf{n}')$, where $\nu' = \nu - \delta\nu$ with $\delta\nu = \nu (\mathbf{w} \cdot \mathbf{n}')/c$. In particular, the radiative excitation rate of a coronal line depends on the quantity:

$$F(\delta\nu) = \int_0^\infty I_{disk}(\nu - \delta\nu) \Psi(\nu - \nu_0) d\nu \quad (3.35)$$

(which differs from equation 3.24 for \bar{J} in that $F(\delta\nu)$ do not include an integration over the solid angles and here the I_{disk} function depends on the Doppler shifted frequency $\nu - \delta\nu$). Because, typically, the coronal plasma is outflowing, $\mathbf{w} \cdot \mathbf{n}' > 0$, hence $\nu' < \nu$, $\lambda' = c/\nu' > c/\nu = \lambda$ and the incident profile is seen by the scattering ion red-shifted by Doppler effect. If the $I_{disk}(\nu - \delta\nu)$ intensity profile originates from an emission line², the convolution integral maximizes when the central frequency of

²i.e. is the superposition of all the emission profiles of spectral lines emitted from the lower atmosphere layers

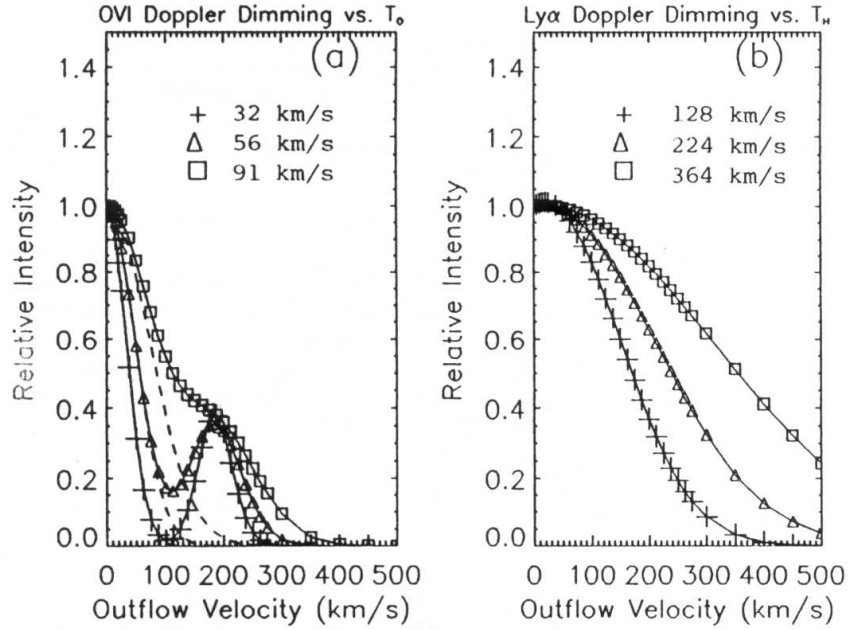


Figure 3.7: Left: the Doppler dimming factor $D(\mathbf{w})$ as a function of the plasma outflow velocity \mathbf{w} (km/s) for the O VI $\lambda 1032\text{\AA}$ (dashed lines) and O VI $\lambda 1037\text{\AA}$ (solid) spectral lines for different ion kinetic temperatures. Right: the same for the Ly α line for different proton temperatures (from Kohl et al., 1997).

the exciting line coincides with the centroid position ν_0 of the coronal absorption profile Ψ , and its value decreases as $|\delta\nu|$ (hence $|\mathbf{w}|$) gets larger. For high enough outflow speed \mathbf{w} , the Doppler shift between the emission and the absorption profiles is such that the convolution integral is zero and the scattered component I_{rad} vanishes. This effect is known as *Doppler dimming*; we will come back to this in § 3.3.6. The amount of Doppler dimming of the radiative component of a line is characterized by the parameter D (called Doppler dimming factor) defined as

$$D = \frac{\int_{\Omega} F(\delta\nu) p(\phi) d\omega'}{\int_{\Omega} F(0) p(\phi) d\omega'} \quad (3.36)$$

which corresponds (from the observative point of view) to the ratio between the actual intensity of a line and the intensity that should be seen in absence of any Doppler dimming effect. Figure 3.7 shows the factor D computed for several spectral lines as a function of the coronal outflow speed \mathbf{w} . Typically the full width at half maximum (FWHM) of the Ly α spectral line is on the order of $\sim 0.9 - 1 \text{\AA}$, while the O VI $\lambda 1032\text{\AA}$ has a smaller FWHM on the order of $\sim 0.16 - 0.18 \text{\AA}$. As a consequence, for a given outflow speed the Doppler dimming is more effective for the latter spectral line, as shown in Figure 3.7. A comparison between D factors computed for the Ly α line with different kinetic temperatures T_k shows also that, given the same outflow velocity, the Doppler dimming decreases as T_k (hence the

kinetic temperature) increases, as expected. The D curves for the O VI $\lambda 1037.6\text{\AA}$ line (left panel, solid) are more complicated because, for outflow speeds larger than ~ 100 km/s, the shift in wavelength is large enough to allow the O VI $\lambda 1037.6\text{\AA}$ line to be excited by the nearby C II $\lambda 1037.0\text{\AA}$ and 1036.3\AA spectral lines. This effect (called *line pumping*) is shown in Figure 3.7³ by the increase in the factor D for the O VI $\lambda 1037.6\text{\AA}$ line (solid curve) for $w > 100$ km/s. Doppler dimming and line pumping can affect the radiative component of the observed O VI line intensities and have to be taken into account in the data analysis.

3.2.7 Line broadening

The specific emissivity $P_{gj}(\nu)$, as defined in equation 3.2, ($\text{erg cm}^{-3} \text{ s}^{-1} \text{ Hz}^{-1}$) is given by:

$$P_{ij}(\nu) = N_g(X^{+m}) A_{ji} h\nu_{ij} \psi(\nu)$$

where $\psi(\nu)$ is the emission line profile normalized to unity. The shape of the observed profile derives from the convolution of all the emission profiles generated by different broadening mechanisms:

$$\psi(\nu) = \psi(\nu)_{nat} * \psi(\nu)_{col} * \psi(\nu)_{th} * \psi(\nu)_{tur} \quad (3.37)$$

where $\psi(\nu)_{nat}$ is the natural broadening, $\psi(\nu)_{col}$ the collisional broadening, $\psi(\nu)_{th}$ the thermal Doppler broadening and $\psi(\nu)_{tur}$ is the broadening due to unresolved turbulent micro- and macroscopic motions of the gas. In the following we briefly discuss the importance of each of these terms.

The $\psi(\nu)_{nat}$ broadening is a consequence of the Heisenberg uncertainty principle: as we discussed above, each atomic level j is depopulated through spontaneous decay to the ground level g at a rate A_{jg} (s^{-1}), hence the lifetime of the j level is $\Delta t_j = 1/A_{jg}$. Defining ΔE_j as the uncertainty in the energy of the j level, from the uncertainty principle we have:

$$\Delta E_j \Delta t_j = h \frac{c}{\lambda_{gj}^2} \Delta \lambda_{gj} \frac{1}{A_{jg}} \sim \frac{h}{2\pi} \quad (3.38)$$

hence the natural line broadening (in wavelength) is given by:

$$\Delta \lambda_{gj} = \frac{A_{jg} \lambda_{gj}^2}{2\pi c} \quad (3.39)$$

However, $\Delta \lambda_{gj} < 10^{-3} \text{\AA}$ and is thus completely negligible in observed lines.

Atoms in a cloud of gas experience two types of perturbations from their neighbors: they collide directly with some, and are affected by the electric fields of particles passing close by. The energy levels of the atom are then perturbed by collisions or close encounters with other atoms or ions. These two effects lead to collisional

³in these curves the authors did not include the pumping from C II $\lambda 1036.3\text{\AA}$.

and pressure broadening, respectively. Most simply, we may suppose that the atoms are unaffected by other particles if the relative distance is larger than the mean free path l_0 of the interacting particles

$$l \equiv \frac{1}{N\sigma} = \sqrt{\frac{2k_B T}{m}} \tau_0 \quad (3.40)$$

where N (cm^{-3}) is the number density of the colliding particles with mass m and σ is the collision cross section. Hence, the width $\Delta\lambda_{col}$ of the collisional broadening (i.e. its full width at half maximum FWHM) by assuming a Maxwellian distribution can be written as:

$$\Delta\lambda_{col} = \frac{\lambda^2}{c} \frac{1}{\pi \tau_0} = \frac{\lambda^2}{c} \frac{N\sigma}{\pi} \sqrt{\frac{2k_B T}{m}} \quad (3.41)$$

where, in our case, $N \equiv N_e$ and $T \equiv T_e$. Because the width increases linearly as the number density N and the square root of the temperature T , at the densities and temperatures typical of the solar corona this effect can be neglected (Mariska 1992), and becomes important only in relatively dense plasmas ($N \geq 10^{11} \text{ cm}^{-3}$).

Emission lines from H atoms and hydrogen-like atoms, can be also broadened by the Stark effect (i.e. the splitting of a spectral line into several components in the presence of an external electric field interacting with the atomic electric dipole). The Stark components of the hydrogen lines are symmetrically distributed around the position λ_0 of the line centroid and photons emitted by these splitted levels result in an overall line broadening. An expression for the width $\Delta\lambda_S$ of the Stark broadening in hydrogen-like C, N and O ions has been derived e.g. by Gonzalez et al. (1998) who give:

$$\Delta\lambda_S = 0.48 \frac{\lambda^2}{c} N_e^{2/3} \frac{n_u^{2.3}}{Z} \quad (3.42)$$

where n_j is the principal quantum number of the upper j level of the transition and Z is the ion atomic number. For instance, for the H Ly α line is $n_j = 3$ and assuming $N_e = 10^7 \text{ cm}^{-3}$ we get $\Delta\lambda_S \sim 10^{-6} \text{ \AA}$, hence this effect in the corona is negligible.

The main effect that dominates the line broadening in the solar corona is the thermal broadening. Photons emitted at a wavelength λ_0 in the atomic reference frame by atoms moving at a thermal velocity v_{th} , because of Doppler effect, will be observed at a wavelength $\lambda = \lambda_0 (1 \pm v_{th}/c)$, red or blue shifted depending on the v_{th} component along the direction to the observer. Because the directions of the atomic velocities are randomly distributed, the overall resulting line profile is a superposition of all the red and blue shifted atomic emissions, resulting in a line broadening. Assuming a Maxwellian distribution of velocities $f(v)$, the thermal line broadening $\Delta\lambda_{th}$ (i.e. its FWHM) is:

$$\Delta\lambda_{th} = 2\sqrt{\ln 2} \frac{\lambda_0}{c} \sqrt{\frac{2k_B T_k}{m}} \quad (3.43)$$

where m is the mass of the emitting ion or atom with kinetic temperature T_k . For instance, by using equation 3.43 for the Ly α spectral line, with a typical coronal

temperature of $T = 10^6$ K, we get $\Delta\lambda_{th} \simeq 0.87$ Å; hence the thermal broadening is the main physical process affecting the observed line shape. Because lines emitted by a steady isothermal plasma with a Maxwellian particle velocity distribution have a Gaussian profile, any time the observed line profiles are well represented by a Gaussian shape (Mariska, 1992), we may assume that the LTE approximation holds. This is often the case for coronal plasmas: hence, from a Gaussian fit of the line profile it is possible to evaluate the kinetic temperature.

An additional component to the Doppler broadening can be due to turbulent plasma motions. Assuming (for simplicity) that this additional velocity field is also Maxwellian with a root mean square velocity ξ , we have:

$$\Delta\lambda_{th} = 2\sqrt{\ln 2} \frac{\lambda_0}{c} \sqrt{\frac{2k_B T_k}{m} + \xi^2} \quad (3.44)$$

Usually the thermal and turbulent line broadening components are identified by comparing the widths of lines emitted by at least two atoms of different atomic weight.

Before concluding this Section, we recall that the observed line profile it is not the “true” profile of the line. If $\psi(\nu - \nu_0)$ is the true emission profile formed by the superposition of all the processes mentioned above and $G(\nu)$ is the instrumental profile, the observed line profile $O(\nu)$ is given by the convolution integral:

$$O(\nu_0) = \int_0^\infty \psi(\nu - \nu_0) G(\nu) d\nu \quad (3.45)$$

The instrumental profile $G(\nu)$ represent the smoothing by the spectrometer of an infinitely narrow spectral line and can be determined in laboratory by observing spectral lines emitted by a heavy element (such as mercury) to minimize the thermal Doppler broadening. It can be shown that, if $\psi(\nu - \nu_0)$ and $G(\nu)$ are both Gaussian profiles with halfwidth $\Delta\nu_{line}$ and $\Delta\nu_{inst}$ respectively, then the observed profile will also be a Gaussian with halfwidth

$$\Delta\nu_{obs} = \sqrt{\Delta\nu_{line}^2 + \Delta\nu_{inst}^2} \quad (3.46)$$

This equation is commonly used to correct the observed line profiles for the instrumental broadening, once $\Delta\nu_{inst}$ is known. The latter depends also on the slit width of the spectrometer used for the observations: the full expression for the $\Delta\nu_{inst}$ term is given in § 4.3.

3.3 Plasma diagnostics from EUV observations

A number of techniques allow us to derive, from the observed UV spectral line intensities and line profiles, the plasma electron density N_e and electron temperature T_e , the kinetic temperatures T_k for different atomic species, the elemental abundances $N(X)$ and the outflow speed \mathbf{w} . In the following we will describe these

techniques: to this end, it is necessary to derive a simplified form for equations 3.15 and 3.28 (§ 3.2.6) which gives a general expression for the radiative and collisional line intensities as a function of the physical parameters of the emitting plasma.

Equation 3.15 gives the collisional line intensity I_{col} as an integral along the line of sight (LOS). In the integrand function, only the electron density N_e typically changes by many order of magnitudes along the LOS, while the rate of change for the $C(T_e, N_e)$ and A_X functions is significantly lower. This implies that, in first approximation, it is possible to rewrite equation 3.15 as:

$$\begin{aligned} \langle I_{col} \rangle &= \frac{1}{4\pi} \langle A_X \rangle \langle C_{line}(T_e) \rangle \int_{LOS} N_e^2 dz = \\ &= \frac{1}{4\pi} \langle A_X \rangle \langle C_{line}(T_e) \rangle EM \end{aligned} \quad (3.47)$$

where $\langle A_X \rangle$ and $\langle C(T_e) \rangle$ are, respectively, the average value along the LOS of the elemental abundance and the contribution function. Because in general temperature varies along the LOS, the critical factor in this approximation is the contribution function $C(T_e)$, which depends strongly on the electron temperature T_e . Usually we assume that the ion emission originates in a narrow region around the temperature of maximum ion formation, i.e. the average value of $C(T_e)$ is given by

$$\langle C(T_e) \rangle = \frac{\int_{T_e}^{T_e+\Delta T_e} C(T_e) dT_e}{\Delta T_e} \quad (3.48)$$

and the approximation is valid when $\Delta T_e \ll T_e$. It is important to note that, because (as we described in § 2.2), the electron density typically decreases rapidly moving away from the plane of the sky (for instance it decreases by more than 1 order of magnitude between the heliocentric distances of $\sim 1.1 R_\odot$ and $\sim 1.6 R_\odot$) and because I_{col} in equation 3.47 is multiplied by $\int_{LOS} N_e^2 dz$, the observed I_{col} originates mainly in a narrow ($L < 1 R_\odot$) region along the LOS over which, because of its limited extension, the above approximation is tenable. However, the above considerations are valid only for quiet coronal structures (such as streamers and coronal holes), while more sophisticated techniques may be necessary for dynamic phenomena such as CMEs and flares.

Following similar arguments the radiative component I_{rad} of the observed line intensity (equation 3.28) may be written in an approximate form for a Maxwellian velocity distribution $f(\mathbf{v})$, assuming the function $p(\phi)$ to be independent of the considered atomic transition. From equations 3.28, 3.29, 3.35 and 3.36 we can write

$$\langle I_{rad} \rangle \simeq k \frac{h\nu_{gj}}{4\pi} \langle p(\phi) \rangle \langle \Omega \rangle \langle F(0) \rangle \langle D \rangle \int_{LOS} N_e dz \quad (3.49)$$

where $k = 0.83 \cdot B_{gj} \langle R(T_e) \rangle \langle A_X \rangle$. The above average functions are given by:

$$\langle p(\phi) \rangle = 1/4\pi \quad (3.50)$$

$$\langle \Omega \rangle = \pi h(r) = 2\pi \left(1 - \sqrt{1 - \frac{R_\odot^2}{r^2}} \right)$$

$$\langle F(0) \rangle = \frac{1}{\sqrt{\pi}} \frac{\int_0^\infty I_{disk}(\nu) d\nu}{\Delta\nu} = \frac{\lambda/\nu}{\sqrt{\pi}} \frac{\int_0^\infty I_{disk}(\lambda) d\lambda}{\Delta\lambda}$$

where r (R_\odot) is the heliocentric distance of observation, $\Delta\lambda = \sqrt{\Delta\lambda_{cor}^2 + \Delta\lambda_{disk}^2}$, $\Delta\lambda_{cor}$ and $\Delta\lambda_{disk}$ are, respectively, the $1/e$ half-widths of the coronal absorption and of the chromospheric exciting line profiles (assumed to have a Gaussian shape) and $\langle D \rangle$ is the average Doppler dimming factor. The resulting approximate expression for the I_{rad} component is then:

$$\langle I_{rad} \rangle = k \frac{h\lambda_{gj}}{16\pi\sqrt{\pi}} \frac{\int_0^\infty I_{disk}(\lambda) d\lambda \int_{LOS} N_e dz}{\sqrt{\Delta\lambda_{cor}^2 + \Delta\lambda_{disk}^2}} \langle D \rangle h(r) \quad (3.51)$$

We note here that, while the collisional component I_{col} is proportional to $\sim N_e^2$, the radiative component is proportional to $\sim N_e$. As a consequence, the coronal region responsible for the observed I_{rad} component has a larger extension along the LOS than the region where I_{col} originates.

3.3.1 Separation of radiative and collisional components

The coronal intensity of strong spectral lines which are emitted also by the underlying chromosphere and transition region is due both to radiative and collisional excitation processes. This is the case for the Lyman- α $\lambda 1216\text{\AA}$ (in the following, Ly α), Lyman- β $\lambda 1025\text{\AA}$ (Ly β) and Lyman- γ $\lambda 973\text{\AA}$ (Ly γ) lines of neutral Hydrogen and for the O VI $\lambda\lambda 1032\text{--}1037\text{\AA}$ doublet lines. In order to derive informations on the plasma state it is necessary to separate the contributions I_{rad} and I_{col} of the observed line intensity $I_{tot} = I_{rad} + I_{col}$. Assuming we observed the line intensities of 2 spectral lines emitted by the same ion/atom (as in the case of Ly α and Ly β lines), the radiative and collisional components can be computed by solving the following linear system:

$$\begin{aligned} I_{rad}(\text{Ly}\alpha) + I_{col}(\text{Ly}\alpha) &= I_{tot}(\text{Ly}\alpha) \\ I_{rad}(\text{Ly}\beta) + I_{col}(\text{Ly}\beta) &= I_{tot}(\text{Ly}\beta) \\ I_{rad}(\text{Ly}\alpha)/I_{rad}(\text{Ly}\beta) &= R_{\alpha\beta r} \\ I_{col}(\text{Ly}\alpha)/I_{col}(\text{Ly}\beta) &= R_{\alpha\beta c} \end{aligned}$$

where $R_{\alpha\beta r}$ and $R_{\alpha\beta c}$ are, respectively, the expected ratios between the radiative and the collisional components of the Ly α and Ly β lines. From these equations we have

$$\begin{aligned} I_{rad}(\text{Ly}\alpha) &= \frac{I_{tot}(\text{Ly}\alpha) - R_{\alpha\beta c} I_{tot}(\text{Ly}\beta)}{1 - R_{\alpha\beta c}/R_{\alpha\beta r}} \\ I_{col}(\text{Ly}\alpha) &= \frac{I_{tot}(\text{Ly}\alpha) - R_{\alpha\beta r} I_{tot}(\text{Ly}\beta)}{1 - R_{\alpha\beta r}/R_{\alpha\beta c}} \\ I_{rad}(\text{Ly}\beta) &= \frac{I_{tot}(\text{Ly}\beta) R_{\alpha\beta c} - I_{tot}(\text{Ly}\alpha)}{R_{\alpha\beta c} - R_{\alpha\beta r}} \\ I_{col}(\text{Ly}\beta) &= \frac{I_{tot}(\text{Ly}\beta) R_{\alpha\beta r} - I_{tot}(\text{Ly}\alpha)}{R_{\alpha\beta r} - R_{\alpha\beta c}} \end{aligned} \quad (3.52)$$

The collisional and radiative ratios are given by:

$$R_{\alpha\beta r} = \frac{b_{\text{Ly}\alpha} f_{\text{Ly}\alpha} \nu_{\text{Ly}\beta} I_{disk}(\text{Ly}\alpha)}{b_{\text{Ly}\beta} f_{\text{Ly}\beta} \nu_{\text{Ly}\alpha} I_{disk}(\text{Ly}\beta)} \quad (3.53)$$

$$R_{\alpha\beta c} = \frac{b_{Ly\alpha} q_{Ly\alpha}}{b_{Ly\beta} q_{Ly\beta}}$$

where $b_{Ly\alpha}$ and $b_{Ly\beta}$ are the Ly α and Ly β branching ratios, $f_{Ly\alpha}$ and $f_{Ly\beta}$ are the corresponding oscillator strengths, and $q_{Ly\alpha}$, $q_{Ly\beta}$ are the corresponding collisional excitation rates $q_{gj} = N_e C_{gj}^e$ (s^{-1}). Hence, the radiative ratio $R_{\alpha\beta r}$ is known, once the disk intensities $I_{disk}(Ly\alpha)$ and $I_{disk}(Ly\beta)$ have been measured. The collisional ratio $R_{\alpha\beta c}$ depends on the electron temperature

$$\frac{q_{Ly\alpha}}{q_{Ly\beta}} = \frac{E_{Ly\beta} f_{Ly\alpha}}{E_{Ly\alpha} f_{Ly\beta}} \exp\left(-\frac{E_{Ly\alpha} - E_{Ly\beta}}{k_B T_e}\right) \quad (3.54)$$

where $E_{Ly\alpha}$ and $E_{Ly\beta}$ are the energies involved in the transition. Because of the high coronal temperature, the value of the exponential factor is ~ 1 independently on the precise value of the unknown electron temperature. We note that, because in the particular case of Lyman lines is often $I_{col}(Ly\alpha) \sim 0$, the procedure described above is better suitable for the other spectral line of the Lyman series or for the O VI $\lambda\lambda$ 1032–1037 Å doublet. Moreover, in the latter case the expected ratio between the radiative and the collisional components, for negligible plasma outflows, is (Noci et al., 1987)

$$\begin{aligned} \frac{I_{rad}(1032)}{I_{rad}(1037)} &= 4 \\ \frac{I_{col}(1032)}{I_{col}(1037)} &= 2 \end{aligned} \quad (3.55)$$

Hence, for the O VI doublet the expected ratios are constant and independent of the disk intensity.

We now proceed to describe the techniques to derive plasma parameters from UV line intensities.

3.3.2 Plasma electron temperature

Traditionally, temperatures in coronal streamers are calculated from the density vs. height profile, under the assumption that the streamer is in radial hydrostatic equilibrium. The profile of the electron density (N_e) vs. the heliocentric distance r is usually deduced via a Van de Hulst inversion technique (Van de Hulst, 1950) from measurements of the white light coronal polarized brightness (pB) (see § 3.4). This method allows “temperatures” to be derived over an extended altitude range and has been applied also recently by Gibson et al. (1999) to derive streamers’ temperatures (see Figure 2.2): we refer the reader to that paper for a concise description of the results.

Over a more limited altitude range (assuming ionization equilibrium and all the approximations described in the previous Sections), electron temperatures can be derived from the line-ratio technique, when different ions from the same element are

available, or from temperature-sensitive line ratios from lines of the same ion (see, e.g., Wilhelm et al., 2002). These ratios are independent of elemental abundances and emission measures. From equations 3.47 and 3.48 we have that the ratio between spectral line intensities (formed only by collisional excitation) of 2 different ionization stages X^{+m} and X^{+n} of the same element X is simply:

$$\frac{I(X^{+m})}{I(X^{+n})} = \frac{\langle C_{X^{+m}}(T_e) \rangle}{\langle C_{X^{+n}}(T_e) \rangle} \quad (3.56)$$

which depends on the plasma temperature T and is independent of the unknown elemental abundance A_X and the unknown emission measure EM (assuming that the observed line intensities arises from the same element of isothermal plasma along the LOS). The plasma temperature can be estimated simply from a comparison between the observed and the expected line ratio computed as a function of T .

A more accurate determination of electron temperature involves the intensity ratio of two spectral line emitted from the same ion. Indicating with j and k the two excited levels, which (in the two level approximation) are populated only from (and radiatively decay to) the ground level g , the ratio between the corresponding line intensities I_{gj} and I_{gk} is given by (see equations 3.47 and 3.8):

$$\frac{I_{gj}}{I_{gk}} = \frac{\Delta E_{gj} \Omega_{gj}}{\Delta E_{gk} \Omega_{gk}} \exp\left(\frac{\Delta E_{gk} - \Delta E_{gj}}{k_B T_e}\right) \quad (3.57)$$

where Ω_{gj} and Ω_{gk} are thermally averaged collision strengths. This ratio is sensitive to the change in electron temperature if $(\Delta E_{gk} - \Delta E_{gj})/k_B T_e \gg 1$, hence, for an appropriate use of the technique, it is necessary to observe spectral lines from an ion whose excited levels are well separated in energy, hence lines which are far apart in wavelength.

Because, as we describe in the next Chapter, the spectral intervals covered by the UVCS instrument include spectral lines from different ionization stages of many elements such as *Fe*, *S*, *Ar*, *Si*, *Ca* and *Ni*, in this work electron temperatures have been estimated with the line ratio technique.

3.3.3 Plasma electron density

Once the electron temperature is known, we can make an evaluation of the plasma electron density from oxygen lines, for a static plasma, taking advantage of the N_e and N_e^2 dependence of, respectively, the line radiative and collisional components. Following Noci et al. (1987), the ratio between the intensities of the O VI $\lambda 1032\text{\AA}$ and the O VI $\lambda 1037\text{\AA}$ spectral lines can be written (considering the ratio between the emissivities) as:

$$\frac{I(1037)}{I(1032)} = \frac{q_{1037} N_g + 4\pi \frac{P_{gj}}{h\nu_{gj}}}{q_{1032} N_g + 4\pi \frac{P_{gk}}{h\nu_{gk}}} \quad (3.58)$$

where g, j, k indicate, respectively, the ground, lower and upper level of the transition from which the lines originate, P_{gj}, P_{gk} are, respectively, the emissivities of the resonantly scattered component of the 1037 and 1032 doublet lines, N_g is the population of the ground level, $q_{1037} = N_e C_{gj}^e$ and $q_{1032} = N_e C_{gk}^e$ are the collisional excitation rates (s^{-1}) from the ground level and the other symbols have their usual meaning. Equation 3.58 can be rewritten as:

$$\frac{I(1037)}{I(1032)} = \frac{\omega_j}{\omega_k} \frac{1 + \frac{\omega_j}{\omega_k} \theta}{1 + \theta} \quad (3.59)$$

where ω are the statistical weights of the levels and θ , which represents the ratio between the collisional and radiative components of the 1032 Å line, is given by

$$\theta \equiv \frac{I_{rad}(1032)}{I_{col}(1032)} = 5.75 \cdot 10^2 \frac{\lambda_{gk}^2 \exp \frac{E_{gk}}{k_B T_e} \sqrt{T_e} \int_{gk} I_{disk}(\nu) d\nu}{\bar{g} N_e (\Delta \lambda_{cor}^2 + \Delta \lambda_{disk}^2)^{\frac{1}{2}}} \left(\frac{R_{sun}}{r} \right)^2 h(r) \quad (3.60)$$

where I_{disk} is the intensity of the exciting chromospheric line with a $1/e$ half-width $\Delta \lambda_{disk}$; $\Delta \lambda_{cor}$ is the $1/e$ half-width of the coronal absorption profile; \bar{g} is the Gaunt factor; $h(r)$ is the geometrical factor given in equation 3.50 and other symbols have their usual meaning. We point out that densities derived with these relationships are crudely evaluated because we made the assumptions that a) the plasma is static and b) emission originates mainly from the same isothermal plasma.

Another technique often used to estimate the plasma electron density takes advantage of the peculiar behaviour of spectral lines formed from metastable levels. As we already mentioned, for these lines the collisional de-excitation becomes an important depopulating mechanism: if the electron densities are small ($N_e \ll A_{jj}/C_{gj}^e$) the line intensity I_{gj} has the same dependence on the electron density as an allowed line ($I_{gj} \propto N_e^2$), while for larger N_e values ($N_e \gg A_{jj}/C_{gj}^e$) the metastable levels are in Boltzmann equilibrium with the ground level and $I_{gj} \propto N_e$. For intermediate N_e values we have $I_{gj} \propto N_e^\alpha$ with $1 < \alpha < 2$. As a consequence, these lines are density-sensitive and from the ratio of forbidden or intersystem line to allowed line intensities it is possible to estimate the electron density. In particular, by applying this technique to different spectral lines from the same ion it is not necessary to make assumptions about the element abundance, the ionization ratio and the size of the emitting volume.

However, the most widely used technique to derive electron densities is via the emission measure analysis: for each observed spectral line intensity I_{gj} it is possible, by assuming a priori the elemental abundance A_X and the ionization equilibrium curve $R_X(T_e)$ from predefined catalogues, to compute (for instance with the CHIANTI code) the contribution function G_{line} , hence the differential emission measure $dEM(T)/dT$ (see equation 3.21). By computing the contribution function for all the observed spectral lines it is possible to determine the best-fitting $dEM(T)/dT$ distribution, i.e. the differential emission measure which gives the best agreement between the observed and predicted line intensities. Because

$dEM(T)/dT = \int N_e N_H dz \approx N_e^2 L$, by assuming a typical value for the depth L of the source along the LOS, the average plasma density can be estimated for a range of temperatures T . In order to obtain the best $dEM(T)/dT$ distribution it is important to select spectral lines which are relatively density-insensitive (hence no metastable levels are involved), and covering a wide range of temperatures. Large indeterminations may occur in temperature intervals poorly constrained by the available data.

3.3.4 Elemental abundances

The so called ‘‘absolute abundances’’ $A_X = N(X)/N(H)$ (i.e. the abundance relative to hydrogen) can be derived from spectral lines formed solely by collisional excitation, via a comparison between the observed and the predicted line intensities. Given the electron temperature T_e (estimated as described in § 3.3.2) and the observed line intensity $I_{col}(X^{+m})$ from an atom m times ionized, the only unknown parameters in equation 3.47 are the abundance A_X and the emission measure EM . Once the observed collisional component $I_{col}(H)$ of an hydrogen spectral line (typically the Ly β line) has been derived (§ 3.3.1), the dependence from the EM can be eliminated (assuming that the observed emission in the two lines arises from the same volume of isothermal plasma) evaluating the ratio:

$$\frac{I_{col}(X^{+m})}{I_{col}(H)} = \langle A_X \rangle \frac{C_{X\ line}(T_e)}{C_{H\ line}(T_e)} \quad (3.61)$$

From the estimated T_e value one can evaluate the contribution functions $C(T_e)$ of the two lines (for instance using the CHIANTI code) and from the latter equation the elemental abundance A_X . In the next Section we describe how, with a different technique, it is possible to estimate the oxygen abundance independently (in first approximation) of the knowledge of the electron temperature. We note that with this technique it is possible, as already mentioned, to compute absolute elemental abundances, while in general only relative abundances (e.g. $N(Fe)/N(O)$) are known.

3.3.5 Oxygen elemental abundance

The absolute oxygen abundance (i.e. the oxygen to hydrogen abundance ratio) can be calculated with the method first described by Raymond et al. (1997). The authors point out that, once the collisional and radiative contributions to the intensities of the oxygen lines are identified, it is possible to derive 2 different estimate for the oxygen abundance. If R is the ratio of the disk intensities in the Lyman- β and O VI 1032 radiation ($R = I_{disk}(Ly\beta)/I_{disk}(1032)$), the value of the oxygen abundance from the radiative $(\frac{N(O)}{N(H)})_{rad}$ and the collisional components $(\frac{N(O)}{N(H)})_{col}$ is given, respectively,

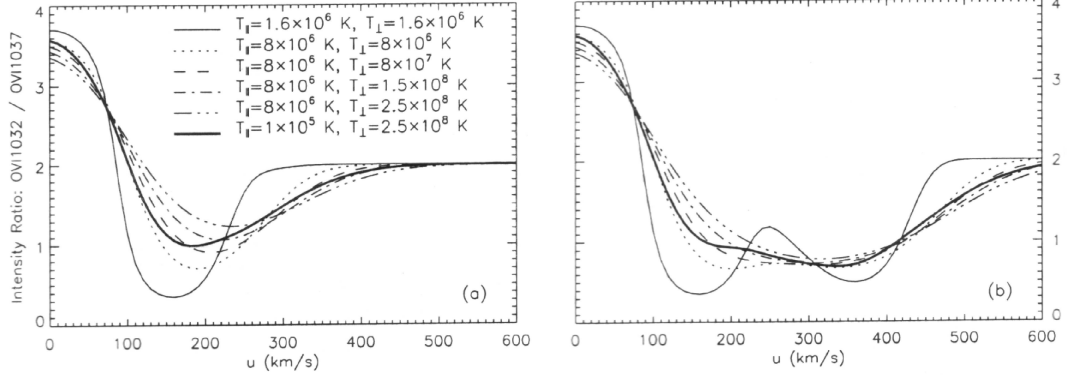


Figure 3.8: The computed ratio between O VI $\lambda 1032\text{\AA}$ and O VI $\lambda 1037\text{\AA}$ line intensities as a function of the outflow plasma speed for different combinations of T_{\parallel} and T_{\perp} obtained by computing the integral along the LOS at $3 R_{\odot}$ with the electron density profile of Fischer & Guhatakurta (1995). In the left panel the curves have been calculated including line pumping only by C II $\lambda 1037\text{\AA}$, while in the right panel both C II $\lambda 1037$ and $\lambda 1036.3$ have been included (from X. Li et al., 1998).

by

$$\left(\frac{N(O)}{N(H)}\right)_{rad} = R \frac{I_{rad}(1032)}{I_{rad}(Ly\beta)} \frac{C_{HI}}{C_{OVI}} \frac{b_{Ly\beta}}{b_{OVI}} \frac{f_{Ly\beta}}{f_{1032}} \frac{\delta\nu_{OVI}}{\delta\nu_{HI}} \quad (3.62)$$

and:

$$\left(\frac{N(O)}{N(H)}\right)_{col} = \frac{I_{col}(1032)}{I_{col}(Ly\beta)} \frac{C_{HI}}{C_{OVI}} \frac{b_{Ly\beta}}{b_{OVI}} \frac{q_{Ly\beta}}{q_{1032}} \quad (3.63)$$

where $\delta\nu$ are the line widths and q the excitation rates. We point out that the ratio of ion concentrations C_{OVI}/C_{HI} over the $\log T$ interval 6.0 – 6.2 (appropriate for coronal plasma conditions) changes by only $\leq 10\%$: hence (opposite to what happens for the abundance estimate of other elements), the oxygen abundance can be evaluated from equations 3.62 and 3.63 even if the precise value of T_e is not known.

3.3.6 Plasma outflow speed

As we already mentioned in § 3.2.6, the radiative component of a spectral line is strongly dependent on the outflow speed of the scattering ions because of the Doppler dimming and the line pumping processes. An important consequence of equation 3.51 is that the ratio between the radiative components of two lines emitted from the same ion (such as the O VI doublet lines) depends only on the ratio between the correspondent Doppler dimming factors, hence is a function solely of the outflow speed. In particular, the ratio between the total (i.e. radiative plus collisional)

intensities of the O VI $\lambda 1032$ over $\lambda 1037$ lines is expected to be $\simeq 2$ (i.e. equal to the ratio between the collisional components, see equation 3.55) for very high outflow speeds, because the radiative components are completely smeared out by Doppler dimming; on the contrary, for negligible outflow speeds we expect to observe a higher ratio, closer to the upper limit 4 (i.e. the ratio between the radiative components). By taking into account also the line pumping, it is possible to compute the expected ratio as a function of the outflow speed (Figure 3.8). These curves can be used to estimate, from the observed ratio, a possible value for the outflow speed: for instance, ratios larger than ~ 2.5 typically implies an outflow speed smaller than 100 km/s, while values smaller than 1 are reached only at larger speeds. However, as shown in Figure 3.8, temperature anisotropies can significantly affect the Doppler dimming and pumping and subsequently increase the observed line ratio expected for a given velocity.

3.4 White light continuum emission

As we anticipated in § 3.1, the observed solar corona continuum emission arises from the superposition of two different components: the K-corona and the F-corona. In this Section we focus on the formation and properties of the observed K-corona. The K component is observed at all position angles and decreases much more rapidly with height than the F-corona, which is concentrated toward the plane of the ecliptic. The mechanism that produces the K-corona emission is the Thomson scattering by coronal electrons: the classical Thomson differential cross section σ_T ($\text{cm}^2 \text{sr}^{-1}$) for the elastic scattering of plane polarized photons is:

$$\frac{d\sigma_T}{d\Omega} = r_e^2 (1 - \sin^2 \chi \cos^2 \phi) \quad (3.64)$$

where ϕ is the angle between the plane of the incident electric vector and the scattering plane, χ is the photon scattering angle and $r_e = e^2/(m_e c^2)$ (cm) is the classical electron radius. The above expression maximizes when the photon scatters in the plane normal to the polarization plane. The total Thomson cross section σ_T integrated over all angles, is:

$$\sigma_T = \frac{8\pi}{3} \left(\frac{e^2}{m_e c^2} \right)^2 = \frac{8\pi}{3} r_e^2 \quad (3.65)$$

The electric fields of the incoming and of the observed beams can be divided into the “radial” components (i.e. those in the plane defined by the incoming and observed beams) and those normal to that plane referred to as “tangential” components. The scattering electron is accelerated in the direction of the oscillating electric field and the resulting dipole radiation (mainly emitted in the direction perpendicular to its motion) is then polarized (see Figure 3.9). In particular, if $\epsilon dt dV d\Omega d\lambda$ is the energy scattered by a volume element dV in time dt into a solid angle $d\Omega$ between

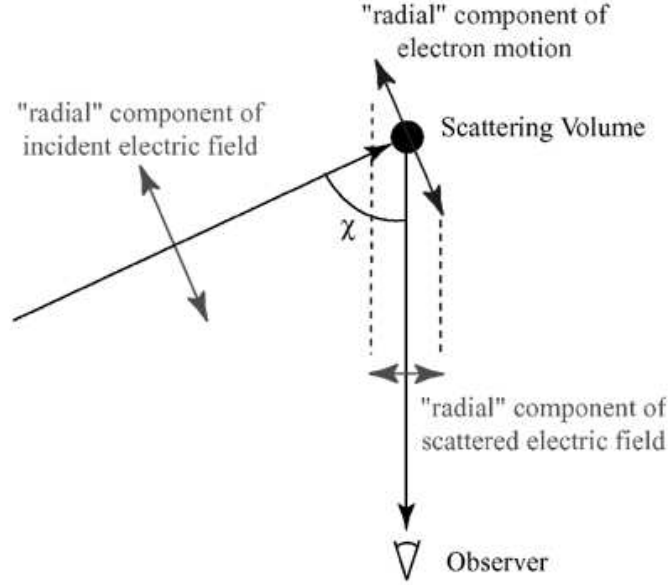


Figure 3.9: Geometry of the formation by Thomson scattering of the radial component of the scattered electric field.

wavelengths λ and $\lambda + d\lambda$ (where ϵ is the *emission coefficient*), the observer can define two emission coefficients, ϵ_r and ϵ_t , corresponding, respectively, to radially and tangentially polarized light (Figure 3.9). For unpolarized incident light, these are given by:

$$\begin{aligned}\epsilon_t &= \frac{\pi}{2} I_0 r_e^2 N_e \\ \epsilon_r &= \frac{\pi}{2} I_0 r_e^2 N_e \cos^2 \chi\end{aligned}\quad (3.66)$$

where I_0 ($\text{erg cm}^{-2} \text{ s}^{-1} \text{ \AA}^{-1}$) is the incident flux (center disk intensity). As a consequence, there are a tangentially and a radially polarized brightness component I_t and I_r which are given by:

$$\begin{aligned}I_t &= \frac{\pi}{2} \sigma_T I_0 N_e [(1-u)C(r) + uD(r)] \\ I_t - I_r &= \frac{\pi}{2} \sigma_T I_0 N_e \sin^2 \chi [(1-u)A(r) + uB(r)]\end{aligned}\quad (3.67)$$

where A , B , C and D are functions of the solid angle Ω subtended by the solar disk at the scattering point and $u = 0.63$ is the limb darkening coefficient in the visible wavelength of interest. The polarized and unpolarized brightness (I_p and I_u) are given by:

$$\begin{aligned}I_p &= I_t - I_r \\ I_u &= 2 I_r\end{aligned}\quad (3.68)$$

hence I_p is the difference between the intensity of white light radiation polarized along the radial to the sun (I_r) and the tangential (I_t) to the solar limb. Finally,

the observed polarized brightness pB (usually normalized to the mean solar surface brightness \bar{B}_\odot) at an heliocentric distance of observation ρ is given by an integration of I_p along the LOS (Cranmer et al., 1999):

$$pB(\rho) = \frac{\pi}{2} \sigma_T \bar{B}_\odot \int_{-\infty}^{+\infty} N_e(z) \left[\frac{(1-u)A(r) + uB(r)}{1-u/3} \right] \frac{\rho^2}{r^2} dz \quad (3.69)$$

where $z = \sqrt{r^2 - \rho^2}$ and the expressions for function $A(r)$ and $B(r)$ are given later on (see § 6.6, equations 6.2 and 6.3). The factor $1/(1-u/3)$ arises from an average, over the solid angle subtending the solar disk, of a disk luminosity function $I = I_0(1-u+u\cos\phi)$ (which takes into account of the limb darkening), where ϕ is the angle between the radial to the disk source point and the radial to the scattering point.

The pB at a given point ρ on the plane of the sky is measured by acquiring three white light intensities at that point (I_α , I_β and I_γ) with three different orientations (α , β and γ) of a linear polarizer; the solution of a set of three linear equations expressing the unknown components (I, Q, U) of the Stokes vector as a function of the intensities I_α , I_β and I_γ gives the observed $pB = \sqrt{Q^2 + U^2}$. From the pB values it is possible to estimate the coronal electron density N_e with the advantage, with respect to the techniques which use EUV spectral lines, that the pB depends *solely* on the electron density distribution N_e . However, in order to invert the above integral we need an a priori expression for the dependence of N_e on latitude and longitude. This can be done in several ways, from simple spherical symmetric model (Van de Hulst, 1950), to axisymmetric model, to more complex models which take into account large scale structures such as coronal streamers or polar plumes (Romoli et al., 1993; Romoli et al., 1997; Strachan et al., 1993). For instance, by assuming a spherically symmetric density distribution $N_e(r)$, the pB integral may be written as an Abel's integral equation (Strachan et al., 1993); assuming a polynomial expression

$$pB(\rho) = \sum_{i=1}^m a_i \rho^{-b_i} \quad (3.70)$$

for the observed pB , the electron density can be written as a simple polynomial function of the (a_i, b_i) coefficients (see e.g. Strachan et al., 1993; Guhathakurta et al., 1996), of $A(r)$, $B(r)$ and u . The coefficients (a_i, b_i) are evaluated by fitting the measured pB vs. ρ curve, leading to an estimate of the $N_e(r)$ profile. Measurements of the $pB(\rho)$ vs. ρ profiles at different coronal latitudes can be used to find, in a similar way, an axisymmetric 2-dimensional profile $N_e = N_e(r, \theta)$ which gives also the density variations with latitudes θ .

The techniques described above are valid only at the minimum of solar activity, when the corona typically shows large loop (closed magnetic geometry) structures or helmet streamers near the equator and coronal holes (open magnetic geometry) near the poles. Hence, these techniques cannot be applied in case of transient phenomena

such as CMEs, when the hypothesis of axy- or spherical symmetric density distribution is obviously no longer valid and a 3-dimensional reconstruction of corona is needed. Recently Moran & Davila (2004) presented a technique to reconstruct from LASCO images the 3-dimensional structure of CMEs. The theoretical ratio $r = I_p/I_u$ of polarized to unpolarized electron scattered brightness is independent on the electron density (see equations 3.67, 3.68) and is a monotonically decreasing function of z along the LOS; hence, from a comparison between observed and theoretical ratio it is possible to estimate the average position z along the LOS of the emitting plasma. However, the Moran & Davila (2004) technique requires the knowledge of the observed intensities I_α , I_β and I_γ , while in some cases only the calibrated pB measurement is available and the ratio r cannot be estimated. Hence, when analyzing white light CME data (see later, § 6.7) we will describe a simple technique we used to evaluate, from the observed pB , the electron density in CMEs.

Chapter 4

Instrumentation and Data Reduction

All studies carried out for this Thesis make use of data collected by the *UltraViolet Coronagraph Spectrometer* (UVCS) aboard the *Solar & Heliospheric Observatory* (SOHO). After a brief description of the SOHO mission (§ 4.1), we review the main characteristics of the UVCS instrument (§ 4.2) and standard techniques used in the UVCS data reduction (§ 4.3). For a better and more thorough interpretation of data, we made use also of data collected by other instruments aboard the SOHO spacecraft such as the *Large Angle Spectroscopic COronagraph* (LASCO), the *Extreme ultraviolet Imaging Telescope* (EIT) and the *Magnetic Doppler Imager* (MDI) which are also briefly described in the last Section (§ 4.4).

4.1 The SOHO mission

The SOHO mission¹ has been designed to study the internal structure of the Sun, the solar corona and coronal heating processes, the origin and acceleration mechanisms of the solar wind (Domingo et al., 1995). The mission was born from a project of international cooperation between ESA and NASA; the satellite payload include twelve instruments for solar wind *in situ* measurements, and for solar corona and helioseismology *remote sensing* observations. SOHO contains the largest complex of instruments for solar physics purposes since the *Skylab* ATM was launched more than 30 years ago (see Chapter 1).

The satellite was launched on December 2, 1995 from Cape Canaveral (US) and, after a transfer trajectory, reached a stationary (i.e. three axis stabilized) halo orbit around the Earth-Sun Lagrangian point L1 (see Figure 4.1), at a distance of about $1.5 \cdot 10^6$ km sunward from the Earth. During its orbit around L1 (with a period of about 180 days) the satellite is constantly pointing to the Sun center with an accuracy of $10''$ and a point stability of $1''$ per 15 minutes interval. This

¹see <http://sohowww.nascom.nasa.gov/> for more detailed informations.

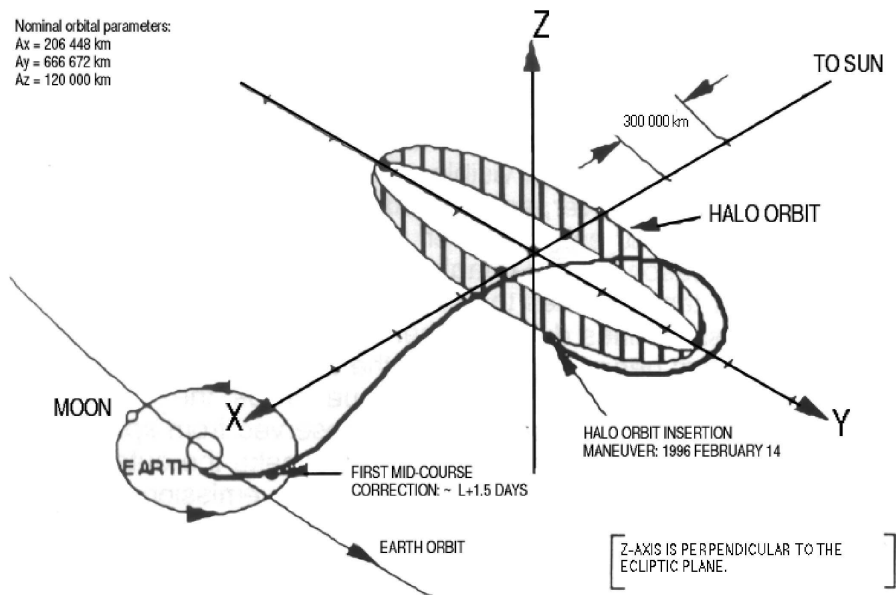


Figure 4.1: The SOHO transfer orbit to the Lagrangian point L1 and its orbit around it.

peculiar position gave many advantages to SOHO: first, while observations from Earth-based observatories and Earth satellites can be made only during “day” time, from the L1 point SOHO have the possibility to observe the Sun continuously. Second, because the L1 point is far outside the Earth magnetosphere, the *in situ* measurements of solar wind plasma properties detect solely the plasma from the Sun. Moreover, the small Sun-spacecraft velocity changes throughout the orbit are appropriate for helioseismology.

The mission, was initially designed for two years life; then, the ESA Scientific Program Committee (SPC) approved the 5 years SOHO mission extension (from May 1998 to April 2003). Finally, at the beginning of 2002, a further extension until March 2007 has been approved. This eleven years lifetime will provide coverage over a full solar cycle.

In the following we describe the UVCS experiment and other SOHO instruments whose data have been used in this Thesis.

4.2 The SOHO/UVCS instrument

4.2.1 The spectrometer UV and WL channels

The UVCS is a coronagraph spectrometer designed for UV spectroscopy and visible light polarimetry of the extended solar corona. The primary scientific objectives of this instrument are to identify and give the physical condition of the source region of solar wind, to study the wind acceleration mechanisms and the possible coronal

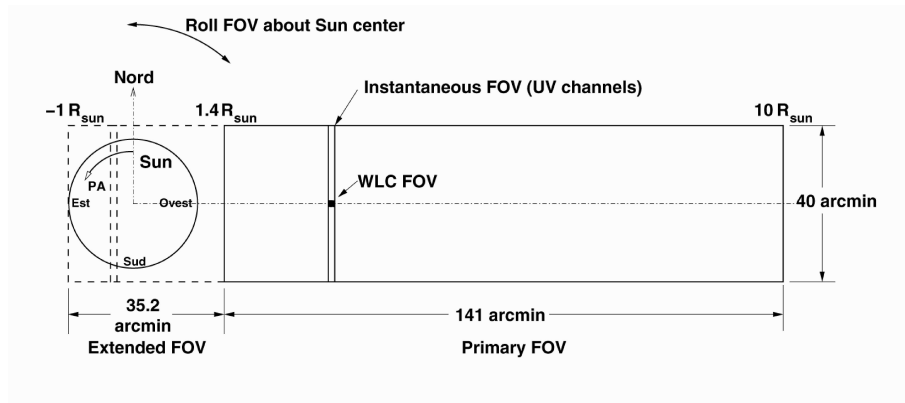


Figure 4.2: The field of view (FOV) of the three UVCS channels.

plasma heating processes.

The instrument consists of three externally and internally occulted telescopes and a high resolution spectrometer assembly. The telescopes focus co-registered coronal images onto the three entrance slits of the spectrometer assembly which consists of three channels:

- The *Lyman α channel*, which is optimized for the observation of the neutral hydrogen Lyman- α λ 1216 Å spectral line and used also for observations of other lines in the spectral range 1145 – 1287 Å (since november 1998 this channel has been turned off because it draws about 50% of the maximum current; the Lyman α line is also observed with the O VI channel)
- The *O VI channel*, which is optimized for observations in the spectral range around the O VI 1031.90 Å/ 1037.63 Å doublet and covers the interval between 937 Å and 1126 Å, in the first order and the interval from 469 to 563 Å in the second order. An additional mirror between the spectrometer grating and the detector allows observations at longer wavelengths which include the neutral hydrogen Ly α 1215.67 Å line (redundant channel).
- The *white light channel* (WLC), which is a coronagraph polarimeter measuring the polarized intensity of the K-corona in the wavelength band from 4500 to 6000 Å.

The UVCS field of view (FOV) is shown in Figure 4.2: the instantaneous FOV of the two UV channels is given by the projected length of the spectrometer slit (40 arcmin) times the selected slit width, while the FOV of the WL channel is a 14"×14" spatial field at the center of the instantaneous UV FOV. The UVCS pointing mechanism can be used to move the instantaneous FOV between 1.4 and 10 R_{\odot} ; moreover, the FOV can be rotated about the Sun-center in order to observe the full corona.

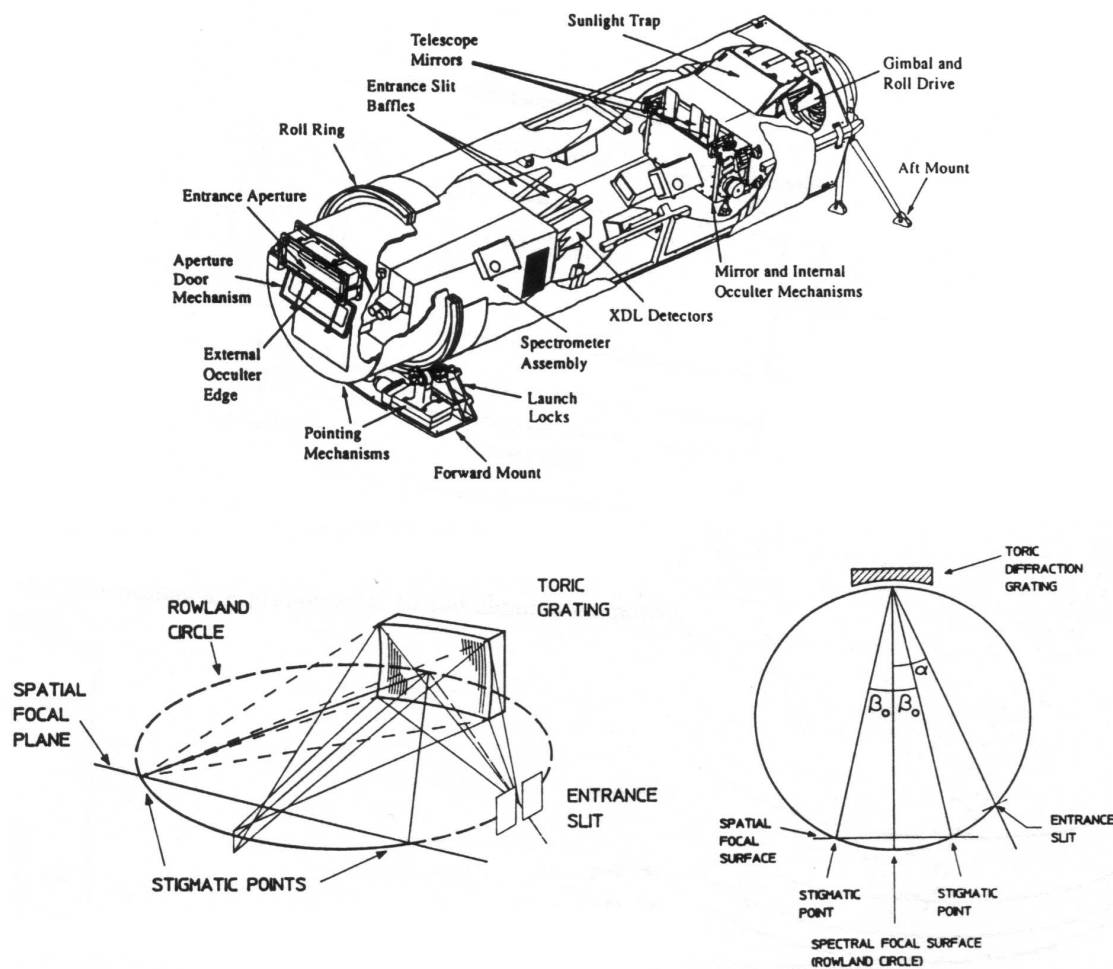


Figure 4.3: Top: UVCS diagram. Bottom left: isometric display of the imaging properties between the two stigmatic points $\pm\beta_0$. Bottom right: schematic of the spectral and spatial imaging of a single toric grating (from Kohl et al., 1995).

4.2.2 Instrument description

The UVCS instrument (Figure 4.3) consists of three very similar telescopes; the primary optical components are the rectangular entrance aperture (the external occulter), the telescope mirror, the internal occulter, the entrance slit baffle, the entrance slit and the sunlight trap. The external occulter consists of three knife edges that limit the FOV and the amount of solar disk light and shields the telescope mirrors from direct sunlight. The light from the solar disk is attenuated by a series of three baffles and a sunlight trap that reduces the stray light by multiple reflections from low reflectivity plates.

The coronal radiation is then focussed onto the spectrometer entrance slit by the spherical telescope mirror with a focal length of 750 mm; the segment of the

Channel	Ly α	O VI
Ruling frequency	2400 l/mm	3600 l/mm
Incidence angle α	12.85°	18.85°
Diffraction angle β	3.98°	2.78°
R_h	750 mm	750 mm
R_v	729.5 mm	708.9 mm
Reciprocal dispersion	5.54 Å/mm (1st order)	3.70 Å/mm (1st order)
Spectral bandwidth of pixel	0.14 Å(1st order)	0.0925 Å(1st order)
Spatial width of pixel	7" (0.025 mm)	7" (0.025 mm)

Table 4.1: UVCS channels optical parameters (from Kohl et al., 1995).

coronal image entering the slit corresponds to the UVCS instantaneous FOV and by rotating the mirror it is possible to select different portions of the solar corona. An internal occulter over the mirror intercepts the portion of light scattered and diffracted by the external occulter otherwise be reflected reflected by the mirror through the entrance slit. The width of the slit (measured with an error of $\pm 1 \mu\text{m}$) can be adjusted to optimize the spectral resolution and count rate requirements for a particular observation.

The roll mechanism can rotate the telescope assembly over a $\pm 179.7^\circ$ range with a rotational position control of $\pm 0.1^\circ$ and a baseline rotation rate of $8^\circ/\text{minute}$.

The UVCS imaging properties are shown in the bottom panels of Figure 4.3. Both spectrometers channels use toric gratings (i.e. with two curvature radius) mounted in the Rowland-circle configuration (i.e. entrance slit, grating and detector on a circle whose diameter $2R$ equal to the horizontal radius R_h of curvature of the grating). This configuration guarantees stigmatic spectral imaging and reduces the number of optical surfaces intercepted by the coronal light, an important factor because of the relatively low reflection coefficients in the UV wavelength domain. In order to reduce the aberrations, the diffraction angle β has to be near zero (measured from the grating normal) and it is necessary to keep the incidence angle α small (see Figure 4.3). The vertical (i.e. spatial) radius of curvature R_v of the grating is smaller than the horizontal one (see Table 4.1) and the vertical (i.e. the stigmatic) focal plane intersects the Rowland circle at angles $\beta = \pm\beta_0$, which define the two stigmatic points (Figure 4.3). In this geometry, provided β_0 is small, it is possible to have effective stigmatic imaging over a section of the Rowland circle on the order of $\approx 2R\beta_0 = R_h\beta_0$. In order to cover a wide spectral range, the grating can rotate around an axis nearly perpendicular to the bisector of the angle between the incident and diffracted rays (see Figure 4.3) keeping the best spectral focus on the detector. An additional grazing incidence mirror in the O VI channel between the grating and the detector allows for observations of the Ly α line; the deflected spectral range is called *redundant channel*.

The UV detectors are two dimensional photon counting microchannel plate sen-

sors with electronic readout (Siegmond et al., 1994). The detector has physical dimensions of $26 \text{ mm} \times 9 \text{ mm}$, electronically digitized to 1024×360 pixels (1024 pixels in the spectral direction and 360 pixels in the spatial direction); each pixel has physical dimensions of $25 \times 25 \mu\text{m}^2$, which correspond to a projected angular resolution of $7'' \times 7''$. Incoming photons interact with a photocatode and the subsequent photoelectron emission is followed by a charge avalanche which results in an overall charge multiplication of $\sim 2 \cdot 10^7$. A wire grid in front of the O VI detector at a distance of 9 mm from the microchannel plates (biased at +15 V) attenuates the low energy ions which enter the detector and possible electric induction effects. This grid produces a shadow on the detector reducing the intensity of some spectral lines (see § 4.3); the average distance between two adjacent wires is about $\simeq 95$ pixels (Naletto, 1996). For each observation it is possible to select a “detector mask” which defines the active area on the detector (up to 5 areas can be defined) and specifies the spatial and spectral pixel binning.

4.2.3 Stray light suppression

An important problem for an off-limb spectrometer is the suppression of the stray light, that is the percentage of the disk light that, leaking through the optics, results in an overestimate of spectral line intensities and changes in the line profiles. Stray light may reach the detector in two different ways: 1) entering the instrument directly and 2) being diffracted by the edges of the entrance aperture and/or reflected/diffracted by other optical elements. The first component is totally removed by a light trap that absorbs or reflects away this radiation. The second component includes also the radiation scattered from the light trap and/or diffracted off the external occulter, radiation from multiple non specular reflections off structural elements and other processes. This component can only be reduced by configuring the instrument optical geometry: UVCS has been designed in such a way that the level of stray light is lower than most coronal signals. As revealed by laboratory tests, the dominant stray light contribution comes from just inside the solar limb (Romoli et al., 1993), hence it decreases with the increasing observation height over the solar limb.

The percentage of stray light on the detector can be estimated using the so called *stray light monitor lines*, i.e. spectral lines which form at low chromospheric temperatures and should not be observed in corona, for example the C III $\lambda 977\text{\AA}$ line observed in the O VI channel. For each spectral line the stray light contribution I_{str} to its total intensity can be calculated for instance from the C III observed intensity $I_{obs}(C III)$ as

$$I_{str} = I_{disk} \frac{I_{obs}(C III)}{I_{disk}(C III)} \quad (4.1)$$

where I_{disk} and $I_{disk}(C III)$ are, respectively, the disk intensities of the considered and C III spectral lines. The latter have been measured for instance by Vernazza & Reeves (1978) using *SkyLab* data. With this technique it has been possible to estimate

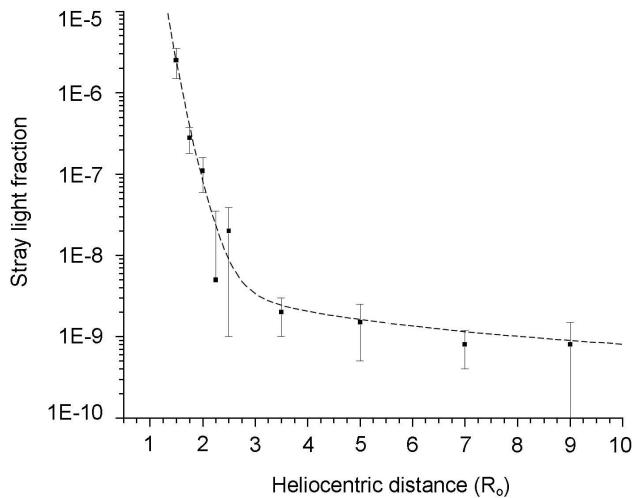


Figure 4.4: The measured fraction of stray light (see text) at different heliocentric distances and the exponential fit to the data (dashed line).

the fraction of stray light on the UVCS instrument as a function of the heliocentric distance of observation (Figure 4.4). With an exponential fit to these measurements (data from L. Gardner, personal communication) we obtain the following expression for the stray light contribution (see Figure 4.4):

$$\log(f_{str}) = -20.7 + 71.2 e^{-1.46 r/R_{\odot}} \quad (4.2)$$

where r is the heliocentric distance of observation and f_{str} is the stray light fraction ($I_{str} = I_{obs} \cdot f_{str}$).

4.3 UVCS data reduction

Before starting the data analysis, it is necessary to follow a series of standard procedures to calibrate the data; this is done using the UVCS Data Analysis Software (DAS) developed by the UVCS science team and written in IDL language. The UVCS data are stored in FITS format and the files are uncalibrated (raw data in counts/pixel). Hence, the first step is the so called “instrumental calibration” procedure, which converts all parameters used for the observations and stored in the file header (i.e. slit width, slit position, exposure time, etc...) in physical units readable for the user. The second step corrects exposures altered by cosmic ray impacts (typically no more than one or two exposures over a whole dataset of many hours). The third step is the correction for the flat field. Hence, using the DAS code, the user may perform the wavelength calibration (which converts spectral bins in \AA both for the primary and redundant channels) and radiometric calibration (which converts line intensities from counts/pixel to photons $\text{cm}^{-2} \text{s}^{-1} \text{sr}^{-1} \text{\AA}^{-1}$). From a combination of laboratory pre-flight calibrations and in flight observations it turns out that

UVCS radiometric calibration have a relative uncertainty of 20 – 22% for the first order and of 50% for the second order spectral lines. Moreover, because variations in the pixel to pixel response on the detector are (for the O sc vi channel) on the order of $\pm 5\%$ (hence much smaller than the radiometric uncertainty), for essentially all analyses the flat field correction is not made, and the above additional uncertainty is adopted (Gardner et al., 2000).

After these procedures have been completed, the data still contain instrumental effects that are not corrected by the DAS code. One of these effect is the presence of imperfections in the diffraction grating which produce a deviation of the diffraction pattern from that of pure points to blurred-out points. As a consequence, some photons of a spectral line may be scattered onto the detector at different wavelengths and create a “false” spectral line known as *grating ghost*. In UVCS, this occurs in particular for photons from the extremely bright Ly α and O VI spectral lines; these ghosts can be removed whenever their position is known.

Another instrumental effect that should be considered is the non perfect alignment of the grating grids with the columns of the detector. The consequence of this error is that the line centroids progressively shift moving along the slit from one to the other side. For instance, for the Ly α line we measured a relative line shift between profiles at the two opposite sides of the slit of about 0.25 Å. This effect can be eliminated by measuring in each spectrum only relative shifts between spectral lines.

As we already mentioned, a further instrumental effect that one has to take care is the dispersion produced by the wire grids. The result is a sharp drop of the intensity at almost equi-spaced points along the spectrum (the non perfect regularity of spacing is due to the effect of the light reflected by the mirror that generates the redundant channel and that has different incoming direction from that of the primary spectrum). If the shadow falls on a spectral line, its use becomes questionable, because both its intensity and profile are affected.

Finally, a fourth instrumental effect that has to be considered when measuring spectral line widths is the instrumental line broadening. As we mentioned at the end of § 3.2.7, the observed profile is a convolution between the line emission profile and the instrumental profile. In the particular, the FWHM of the instrumental profile (see equation 3.46) $\Delta\lambda_{inst}$ can be expressed as (Kohl et al., 1999)

$$\Delta\lambda_{inst} = \sqrt{(\Delta\lambda_{iw})^2 + \frac{2}{3} \ln 2 \left[P^2 + \left(\frac{W}{0.025 \text{ mm}} \right)^2 \right]} \quad (\text{pixels}) \quad (4.3)$$

where $\Delta\lambda_{iw}$ is the instrumental line width, P is the number of pixels per bin and W is the slit width in mm. The $\Delta\lambda_{inst}$ is the factor that has to be subtracted in quadrature from the width obtained by the line profile fitting.

FOV (r/R_{\odot})	Occulter type	Spectral bandpass	CCD array	Pixel size	Brightness range (B_{\odot})
C1 1.1 - 3.0	Internal	Fabry-Perot	1024 ²	5.6"	$2 \cdot 10^{-5} - 2 \cdot 10^{-8}$
C2 2.0 - 6.0	External	Broadband	1024 ²	11.4"	$2 \cdot 10^{-7} - 5 \cdot 10^{-10}$
C3 3.7 - 32	External	Broadband	1024 ²	56.0"	$3 \cdot 10^{-9} - 1 \cdot 10^{-11}$

Table 4.2: LASCO telescopes optical characteristics (from Brueckner et al., 1995).

4.4 Other SOHO instruments

In the following we give a brief description of the other SOHO instruments whose data have been used during this Thesis.

4.4.1 LASCO

The LASCO instrument aboard SOHO consists of three optical systems (C1, C2 and C3), each equipped with its own 1024×1024 pixel CCD camera. The C1 telescope is an internally occulted coronagraph observing the white light corona with field of view that goes from 1.1 to 3.0 R_{\odot} , while C2 and C3 telescopes are externally occulted coronagraphs observing the white light corona respectively from 2.0 to 6.0 R_{\odot} and from 3.7 to 32.0 R_{\odot} . The “synoptic” observations are made with C2 using an orange filter ($\lambda \sim 540 - 640$ nm) while C3 observes with a clear filter ($\lambda \sim 400 - 850$ nm). Typical LASCO data consist of a sequence of images taken at a rate of about 1 each 24 minutes, typically viewed as “movies”. Table 4.2 summarizes the design parameters of the three coronagraphs; for a more complete instrumental description see Brueckner *et al.* (1995).

4.4.2 EIT

The EIT (Delaboudinière et al., 1995) instrument images the solar corona in four narrow passbands centered on the He II λ 304 Å, Fe IX/x λ 171 Å, Fe XII λ 195 Å and Fe XV λ 284 Å spectral lines using multilayer filters in normal incidence to separate the wavelength bands. The corresponding peak temperatures are, respectively, $8 \cdot 10^4$ K, $1.3 \cdot 10^6$ K, $1.6 \cdot 10^6$ K and $2 \cdot 10^6$ K, hence images acquired with the He II filter refers to the chromospheric level, while the other three filters give images of corona/transition region boundaries, quiet corona and active regions. The EIT field of view is a 45 arcmin square and the disk images are focused on a 1024×1024 pixel CCD camera; the spatial resolution is limited only by the 2.6 arcsec pixel size of the CCD. As for the LASCO instrument, EIT data are typically viewed as “movies” with a time resolution of 12 min. and a pixel resolution sometimes reduced to 512×512 to keep the file size reasonable (160 - 200 Kbyte).

4.4.3 MDI

The MDI instrument measures line-of-sight motions (Dopplergrams), magnetic field (magnetograms), and brightness images in full disk. The instrument images the Sun on a 1024×1024 pixel CCD camera and can observe in either two spatial resolutions: the full disk path (FD) has a FOV of $34' \times 34'$ with $4''$ resolution, while the high resolution path (HR) is magnified by a factor of 3.2 to provide $1.25''$ resolution on a $11' \times 11'$ FOV centered about $160''$ north of the equator. These images are acquired in the spectral range $6767.8\text{\AA} \pm 190\text{ m\AA}$ (centered on the Ni I 6768\AA mid-photospheric absorption line) through a series of increasingly narrow spectral filters. Its filter system allows narrow band (94 m\AA) filtergrams to be made anywhere in the vicinity of the Ni I line using a pair of tunable Michelson interferometers; combining data from these filtergrams (typically five, 1 in the continuum, 2 on the line wings and 2 about the line core) MDI gives an estimate of the Doppler velocity and the continuum intensity. Moreover, several times each day circular polarizers are inserted and a longitudinal magnetogram is constructed by measuring the Doppler shift separately in right and left circularly polarized light: the difference between these two is a measure of the Zeeman splitting and is roughly proportional to the line of sight component of the magnetic field (average magnetic flux). For a more complete instrumental description see Scherrer et al. (1995).

Figure 4.5 shows an example of LASCO, EIT and MDI data for the same day.

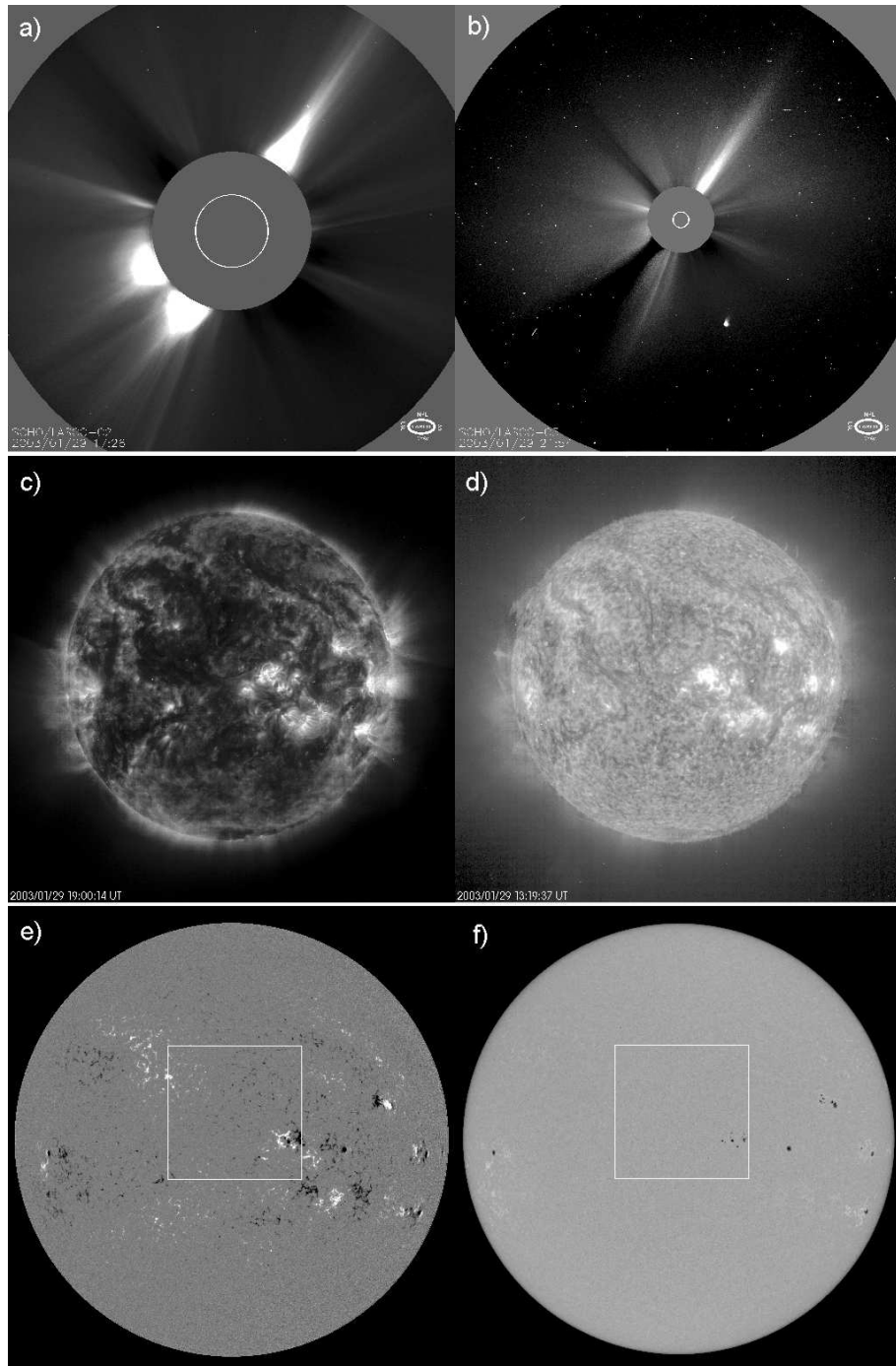


Figure 4.5: Top row: LASCO/C2 (a) and C3 (b) observations on January 29, 2003 respectively at 17:26 and 21:54 UT; the white circle gives the sun size inside LASCO occulting disk, North is up. Middle row: EIT Fe IX $\lambda 171\text{\AA}$ (c) and He II $\lambda 304\text{\AA}$ (d) on January 29, 2003 respectively at 19:00 and 13:00 UT. Bottom row: MDI magnetogram (e) and continuum intensitygram (f) on January 29, 2003 respectively at 20:48 and 22:24 UT.

Part II

Observations & Results

Chapter 5

Temporal evolution of a streamer complex

In this second Part we present the results we obtained from an analysis of UVCS datasets using the plasma diagnostic techniques described in § 3.3. In particular, these have been applied to the study of the following structures: a coronal streamer complex (this Chapter), the early evolution of a CME observed in the low corona (Chapter 6) and the coronal restructuring following a different CME event (Chapter 7). Moreover, in the last Chapter (8), we show how the UVCS instrument has been used also to observe a sungrazing comet and how, from these observations, it has been possible to derive both cometary and coronal plasma parameters.

This second Part is then organized as follows: for each of the above arguments we review the actual knowledge in the literature and the unanswered questions we want to address with our data. Then, after a concise illustration of our datasets, we discuss how the diagnostic techniques have been adapted to the different cases and we conclude with a description and discussion of our results.

5.1 Introduction

We first will show how the techniques described in Chapter 3 can be applied to quiescent structures such as coronal streamers. As we said streamers are the most prominent features of the corona and have been long observed in eclipse even before the space era started accumulating a really large amount of data on these structures. In spite of being the brightest and hence the most easily observable coronal structures, there are a number of areas where work has still to be done. Past studies focussed mainly on solar minimum streamers: the most complete set of data was collected during the Whole Sun Month campaign (Galvin & Kohl, 1999) in several experiments. Temperatures and densities given in Chapter 2 have been derived from data collected during this campaign, and refer to a streamer observed in 1996 (i.e. at the last solar minimum). Elemental abundances, kinetic temperatures and outflow velocities have been given, still for minimum structures by J. Li et al. (1998),

Feldman et al. (1998, 1999) and Strachan et al. (2002). These extensive analyses still leave areas where our knowledge of the physical parameters of streamers is incomplete. Little do we know, for instance, about profiles of density and temperature *across* streamers, about the evolution of these parameters during streamers' lifetime, or about the association of slow wind with streamers and, in particular, with streamers legs. Because the site where slow solar wind originates is still unknown, a comparison (see § 2.4) between coronal and slow wind *in situ* abundances may provide information on this issue. Raymond et al. (1997) from the apparent similarity between slow wind abundances and streamers legs, claim these regions to be sources of this component of the solar wind. However, because this conclusion has been challenged by some authors (see e.g. Marocchi et al., 2001), the problem is still open.

It is well known (see e.g. Schmelz, 1999) that the coronal to photospheric abundance ratio depends on the First Ionization Potential (FIP) of the element, the ratio for elements with low FIP (≤ 10 eV) being larger than that for high FIP elements (*FIP effect*). Measurements of the FIP effect in the wind and in the corona confirmed fast wind to originate in coronal holes, while the association between FIP effect in streamers and slow wind has not been thoroughly analyzed. Moreover, few studies addressed the problem of FIP effect in streamers at altitudes above 1.5 solar radii.

5.2 The goal of our observations

In this work, we analyze a streamer complex which has been observed by UVCS over about one week, in June 2000, close to the peak of the solar activity cycle. Purpose of the present study is: to derive temperatures, densities and elemental abundances in streamers observed close to the time of maximum solar activity - which may be useful to understand the evolution, if any, of streamers with solar cycle - and evaluate the variation of these parameters across streamers, which is poorly known and may help us understand their structure. The choice of the time interval over which data were taken has been dictated by the occurrence of a SOHO-Sun-Ulysses quadrature (see, e.g. Suess et al., 2000). This is a geometrical configuration where coronal plasma observed remotely by SOHO experiments is later sampled *in situ* by Ulysses instrumentation. Hence, taking advantage of this configuration, we plan to compare abundances in streamers with abundances measured *in situ* by Ulysses: this, as we just said, provides crucial information for the identification of the source of slow wind.

In the following Sections we first discuss the temporal evolution of the streamer complex, at altitudes above 2 solar radii, by analyzing LASCO C2 images (§ 5.3). This helps us understand which structures UVCS is sampling, when observing at lower altitudes. In § 5.4 we describe UVCS observations, while in § 5.5 we describe the electron densities, temperatures and elemental abundances we derived from our

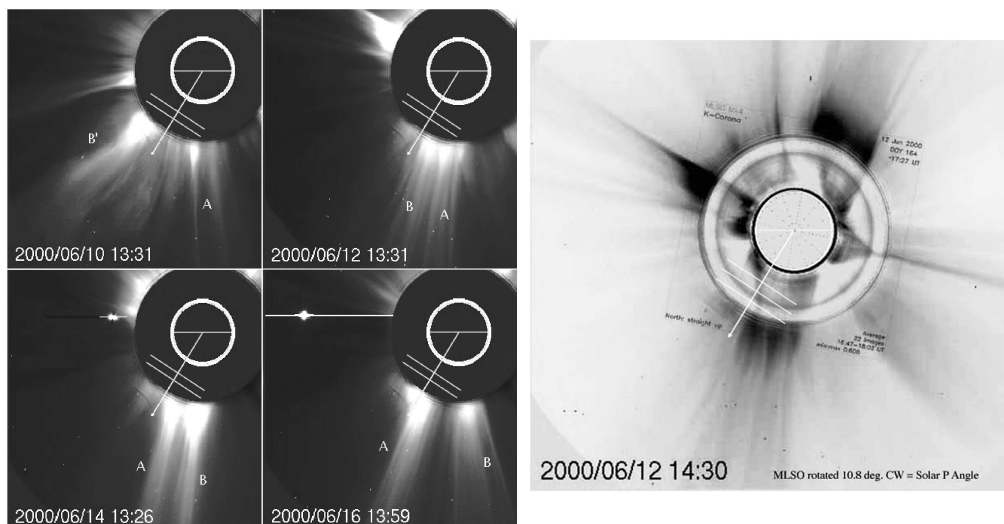


Figure 5.1: Left: LASCO C2 images from June 10 to June 16, 2000. Labels A, B, B' identify different streamers (see text), the radial to Ulysses is shown, together with the position of the UVCS slit. Right: a composite image for June 12, 2000, showing the low corona from a Mauna Loa white light image and, superposed, the outer corona from a LASCO C2 image. The Figure shows that the LASCO C2 streamers in the south-east quadrant do not extend radially inwards.

analysis of UVCS data. We give also an estimate of FIP effect in our streamers and in the next Section (§ 5.6) we compare coronal and *in situ* abundances. A discussion of our results completes the work (§ 5.7).

5.3 Streamer evolution from LASCO C2 images

In June 2000, at the time of the SOHO-Sun-Ulysses quadrature, Ulysses was at a southern latitude of 58.2° , off the eastern limb of the Sun. Hence, in the following, we consider only what's happening in the south-East quadrant of the corona.

Figure 5.1 (left panels) illustrates the coronal evolution in that quadrant, from June 10 to June 16, 2000; superposed on each image, we give also the radial to Ulysses at a latitude of 58.2° , and the position of the UVCS slit (set normal to the radius, at heliocentric distances of 1.6 and 1.9 solar radii). On June 10 the mid-latitude streamer labeled B' (Figure 5.1) is going through a disruption, which modifies the coronal morphology, over that quadrant, and makes it difficult to identify individual streamers on LASCO images of the next day (June 11). The lower latitude streamer which shows up after the streamer disappearance of June 10 will be hereafter dubbed streamer B (that is, B is a newly formed structure). Starting from June 12, it is easy to identify two streamers – labeled A, B, in Figure 5.1 – which move apart in subsequent days. On June 16 – 17, streamer B eventually slides off the UVCS slit. A and B appear to separate with time because A, rooted on the

back side of the Sun, is dragged eastward by solar rotation, while streamer B, rooted on the front side of the Sun, is dragged westwards. On June 13 the two streamers are superposed along the line of sight and are not individually identifiable. Because on June 10 the streamer A is more or less lying along the radial through the south pole and considering the time it takes to drag it by solar rotation from its polar position to the limb of the Sun, we surmise that on June 16 and/or early on June 17 streamer A is in the plane of the sky, possibly face-on, with emission from other structures contributing to the asymmetric brightness emission on its low latitude edge.

Our analysis will focus on streamers A and B, from 11 June onwards. However, because the UVCS slit is about $\approx .5$ (or $\approx .2$, when UVCS makes observations at the higher level) solar radii below the base of LASCO C2 images, the inclination of the streamer axes, with respect to the radial, is relevant for a correct interpretation of UVCS data. To this end, Mauna Loa limb images help us understand the coronal white light morphology below 2 solar radii. Unfortunately, Mauna Loa data are available only for 11 and 12 June 2000; Figure 5.1 (right panel), where composite Mauna Loa and LASCO C2 images are shown, reveals that streamers are not radial: this has been taken into account when analyzing UVCS images.

5.4 UVCS observations and data analysis

As mentioned, the UVCS slit (100 μm wide) was centered at a southern latitude of 58.2° , with its center at altitudes of 1.6 and 1.9 solar radii. Spectra have been acquired with the O VI channel using different grating positions, in order to cover a more extended spectral range and obtain lines from as many elements as possible. Typical observation times, for each grating position, are 7200 s. Table 5.1 give the list of the emission lines we observe. Data, with a spatial resolution of $70''$ and a spectral binning of 0.1986 \AA in the primary and of 0.1830 \AA in the redundant channel, have been acquired on June 10 – 13 and 16, at an altitude of 1.6 solar radii, and on June 12 – 14 and 17, at an altitude of 1.9 solar radii.

The strongest lines in the recorded spectral range are the H Lyman- α and the O VI lines. Two sample spectra at two different grating positions are shown in Figure 5.2. Other ions, like Si XII have a 10 times lower emission than O VI lines, but are still easily distinguishable. Total line intensities were computed summing over all the bins along the line profile. The background level has been estimated from spectral intervals devoid of lines and it has been subtracted from the line intensity.

Table 5.1 shows that in our data we have spectral lines which originate from ions forming at quite different temperatures: for instance, in ionization equilibrium, the O VI 1032 \AA emissivity peaks at a temperature of $3 \cdot 10^5 \text{ K}$, while the Si XII 520.67 \AA emissivity peaks at a temperature of $2 \cdot 10^6 \text{ K}$, with appreciable emission from plasmas at temperatures as high as $2 \cdot 10^7 \text{ K}$. A comparison between the observed line intensity distributions along the UVCS slit of the O VI and Si XII lines shows

λ_{obs} (Å)	λ_{ID} (Å)	Ion	Transition	$\log T_{max}$
972.51	972.54	H I	Ly γ	4.5
974.08	487.03	Fe XIII	$3s^2 3p^2 \ ^3P_2 - 3s 3p^3 \ ^5S_1$	6.2
976.99	977.02	C III	$2s^2 \ ^1S_0 - 2s 2p \ ^1P_1$	4.8
998.76	499.37	Si XII	$1s^2 2s \ ^2S_{1/2} - 1s^2 2p \ ^2P_{3/2}$	6.3
1018.77	1018.60	Ar XII	$2s^2 2p^3 \ ^4S_{3/2} - 2s^2 2p^3 \ ^2D_{5/2}$	6.3
1020.05	510.05	Fe XIII	$3s^2 3p^2 \ ^3P_2 - 3s 3p^3 \ ^5S_2$	6.2
1025.69	1025.72	H I	Ly β	4.5
1028.04	1028.04	Fe X	$3s^2 3p^4 3d \ ^4D_{7/2} - 3s^2 3p^4 3d \ ^4F_{7/2}$	6.0
1031.90	1031.91	O VI	$1s^2 2s \ ^2S_{1/2} - 1s^2 2p \ ^2P_{3/2}$	5.5
1034.50	1034.48	Ni XIV	$3s^2 3p^3 \ ^4S_{3/2} - 3s^2 3p^3 \ ^2P_{3/2}$	6.2
1037.63	1037.61	O VI	$1s^2 2s \ ^2S_{1/2} - 1s^2 2p \ ^2P_{1/2}$	5.5
1041.04	520.66	Si XII	$1s^2 2s \ ^2S_{1/2} - 1s^2 2p \ ^2P_{1/2}$	6.3
1054.87	1054.90	Ar XII	$2s^2 2p^3 \ ^4S_{3/2} - 2s^2 2p^3 \ ^2D_{3/2}$	6.3
1100.14	550.01	Al XI	$1s^2 2s \ ^2S_{1/2} - 1s^2 2p \ ^2P_{3/2}$	6.2
1115.52	557.74	Ca X	$3s \ ^2S_{1/2} - 3p \ ^2P_{3/2}$	5.8
1136.24	568.12	Al XI	$1s^2 2s \ ^2S_{1/2} - 1s^2 2p \ ^2P_{1/2}$	6.2
1174.64	1174.65	Ni XIV	$3s^2 3p^3 \ ^4S_{3/2} - 3s^2 3p^3 \ ^2P_{1/2}$	6.2
1196.11	1196.25	S X	$2p^3 \ ^4S_{3/2} - 2p^3 \ ^2D_{5/2}$	6.1
1215.70	1215.67	H I	Ly α	4.5
1219.71	609.86	Mg X	$1s^2 2s \ ^2S_{1/2} - 1s^2 2p \ ^2P_{3/2}$	6.1
1238.57	1238.82	N V	$1s^2 2s \ ^2S_{1/2} - 1s^2 2p \ ^2P_{3/2}$	5.3
1242.00	1242.03	Fe XII	$3s^2 3p^3 \ ^4S_{3/2} - 3s^2 3p^3 \ ^2P_{3/2}$	6.1
1242.80	1242.80	N V	$1s^2 2s \ ^2S_{1/2} - 1s^2 2p \ ^2P_{1/2}$	5.3
1249.90	624.95	Mg X	$1s^2 2s \ ^2S_{1/2} - 1s^2 2p \ ^2P_{1/2}$	6.1

Table 5.1: The most intense lines identified in the O VI channel spectral range. In the last column we give the temperature of maximum ion formation from the ionization equilibrium of Arnaud and Raymond (1992) for Fe ions and of Arnaud and Rothenflug (1985) for other ions.

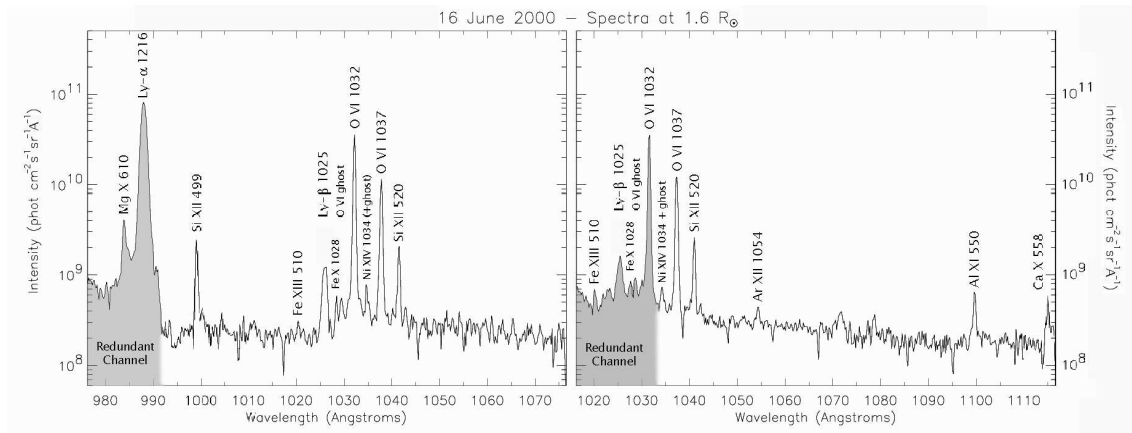


Figure 5.2: Two sample spectra at 1.6 solar radii for June 16 using two UVCS grating positions; intensities and wavelength scales refer to the primary channel.

that both intensities peak, on June 10, at the same latitude ($\approx 48^\circ$), where the white light emission is also brightest (see Figure 5.3). This emission originates from the extension of streamer B' to the lower altitudes sampled by UVCS; on the same day, a secondary O VI and Si XII intensity maximum seems to originate from the extension to lower altitudes of streamer A (latitude of $\approx 70^\circ$). However, on June 12, at the position of O VI maximum intensity, the Si XII emission is altogether negligible, while appreciable white light and Si XII emission keeps originating from streamer A. Unless there has been a dramatic drop in the abundance of Si in streamer B, this behavior can be interpreted as an indication that streamer B is a cooler structure than streamer A, because it does not reach temperatures high enough to give rise to an appreciable emission in the Si XII 499 Å line. On the contrary, streamer A emission in Si XII is approximately constant over these three days. The distribution of O VI and Si XII line intensity along the UVCS slit for the other days, and for the height of 1.9 solar radii, confirms the results obtained on June 12, that is, streamer B keeps being persistently “colder”, with respect to streamer A. This qualitative analysis shows that different streamers may have different temperatures and that white light images obviously are unable to convey any information in this respect. In the next Sections we will show that the interpretation of the Si XII behavior in terms of a temperature rather than an abundance effect is correct.

5.5 Streamers physical properties

In this section we describe the streamers' temperatures, densities and elemental abundances we derived using the diagnostic techniques we described in § 3.3. On June 10 only a limited number of spectra were acquired and data on H Lyman- α and Fe XII are missing. Because these are crucial for the determination of temperatures and elemental abundances, as shown in the following, streamer physical parameters

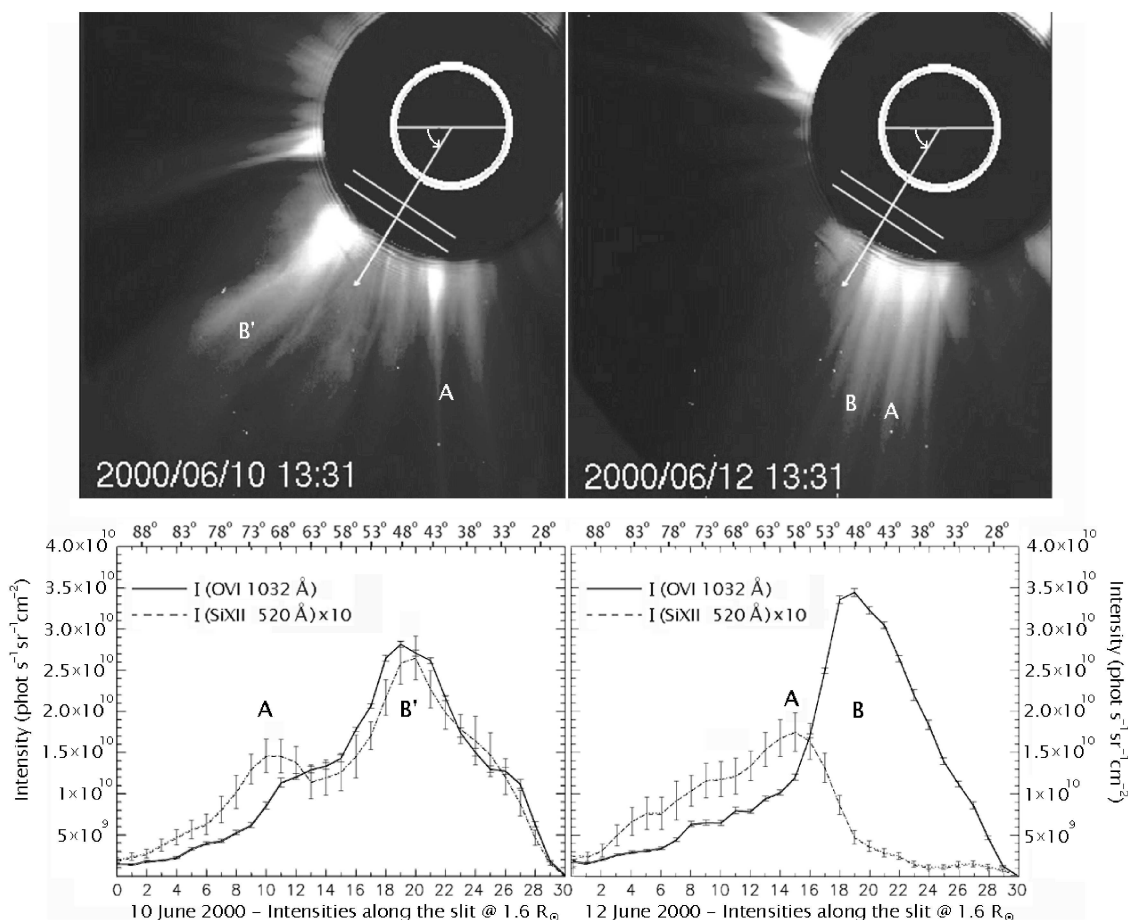


Figure 5.3: Top: LASC0 C2 images for June 10 and 12. As described in the text, streamer B' on June 10 disrupts and a streamer B is visible on June 12 images, which may, or may not, be the reformation of B'. Bottom: profiles of the O VI 1032 Å and Si XII 520 Å line intensities as a function of the UVCS slit bins. The Si XII line intensity has been multiplied by 10; the latitude corresponding to the UVCS slit bins are given at the top of the UVCS panels.

are not given on that day.

5.5.1 Electron temperatures

In this work, because we have spectra that include lines from Fe x ($\lambda = 1028 \text{ \AA}$), Fe XII ($\lambda = 1242 \text{ \AA}$) and Fe XIII ($\lambda = 974 \text{ \AA}$; see Table 5.1), we derive electron temperatures from the ratio of the intensities of these lines (see § 3.3.2), under the hypothesis of ionization equilibrium. Obviously line emission is integrated along the line of sight: we make the hypothesis that the temperatures we derive refer to streamers' regions. Hence we suppose that the background contribution is negligible. This is justified because the line emission depends on N_e^2 and N_e decreases as we

Date 2000	streamer	1.6 R _⊙	1.9 R _⊙
June 11	B	6.01 ± 0.03	
June 11	A	6.12 ± 0.04	
June 12	B	6.03 ± 0.02	
June 12	A	6.13 ± 0.04	
June 12	B		6.01 ± 0.04
June 12	A		6.14 ± 0.06
June 13	B	6.08 ± 0.03	
June 13	A	6.09 ± 0.04	
June 13	B		6.02 ± 0.04
June 13	A		6.15 ± 0.06
June 14	B		6.12 ± 0.04
June 14	A		6.14 ± 0.06

Table 5.2: Electron temperatures ($\log T$) for streamers A and B.

move out of the plane of the sky and of the streamer edges.

We note that the most intense Fe lines in our data are those from Fe X and Fe XII, the Fe XIII line being very weak and hence affected by large errors. Hence temperatures have been derived by comparing the observed Fe X/Fe XII line intensity ratio with the emissivities predicted by the CHIANTI 3 code and the ionization equilibrium of Arnaud and Raymond (1992). Then we verified that the observed Fe X/Fe XIII and Fe XII/Fe XIII ratios were consistent with those predicted for those ratios at the temperature previously obtained. We point out that different Fe ionization equilibria don't affect the temperatures values we derived. For instance, emissivities based on the Fe ionization equilibrium of Mazzotta et al. (1998) do not lead to any change in our values.

Table 5.2 gives the electron temperatures at the bin corresponding to the peak intensity of streamers A and B for June 11 through 14 at 1.6 and 1.9 solar radii, depending on data availability. We have been unable to derive the temperature vs. height variation in the 1.6 to 1.9 altitude range because of the larger statistical uncertainties in the 1.9 R_⊙ data. We can only say that the temperature vs. height profile, in this range, is flat enough to be compatible with a constant temperature. We also remind the reader that, on June 13, A and B are more or less aligned along the line of sight. Hence temperatures on that day cannot be easily ascribed to either structure and are most probably indicative of the average plasma temperature of the two streamers.

The qualitative results that lead us to identify streamer B as a cooler streamer than A are confirmed here: a difference of about 0.1 in $\log T$ seems to characterize

the two structures. Uncertainties in Table 5.2 have been calculated taking into account the statistical uncertainties in the line intensity calculations. Assuming that the high temperature streamer A is at the lowest temperature compatible with the uncertainty and that the low temperature streamer B is at the highest temperature compatible with the uncertainty decreases the $\log T$ difference between A and B to $0.03 - 0.04$, that is, to about a 10% difference. The reason why a slight temperature variation has such a dramatic effect on the Si XII line visibility lies in the shape of the emissivity curve for Si XII which, for instance, increases by a factor ~ 40 between $\log T = 6.0$ and $\log T = 6.1$ (see Figure 5.4). We will come back to this point when discussing the abundances in the streamers.

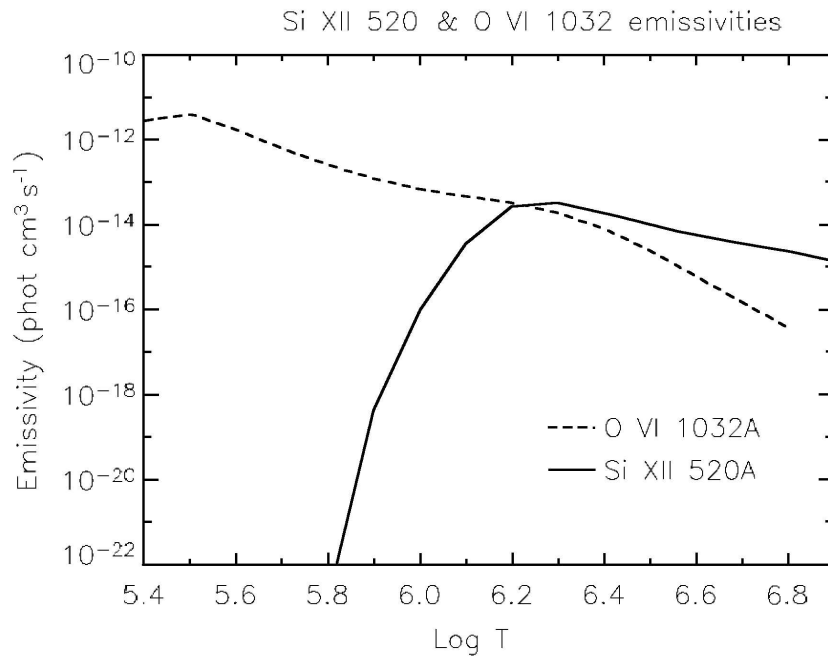


Figure 5.4: The O VI 1032 Å and Si XII 520 Å emissivities vs. $\log T$; emissivities have been calculated from the CHIANTI 3 code (Dere et al., 2001), and the ionization equilibrium of Arnaud & Rothenflug (1985).

The temperatures of A and B compare favorably with previous estimates of temperatures in streamers. In particular, the temperature of streamer A agrees with the scale height temperature given by Gibson et al. (1999) for the WSM streamer at minimum of the activity cycle (see Figure 2.2). Wilhelm et al. (2002) give a streamer temperature $T_e = 1.4 \cdot 10^6$ K, at an heliocentric distance of $1.11 R_\odot$, in the rising phase of the activity cycle, which is compatible with our estimate, since temperature is supposed to increase and reach a maximum somewhere in between 1 and 1.5 solar radii (Gibson et al., 1999). However, we did not find any evidence for plasma at $T_e = 2.2 \cdot 10^6$ K at $\approx 1.6 R_\odot$, which Foley et al. (2002) found in streamers

observed in August 1999, close to solar maximum. Foley et al. (2002) results were based on an emission measure analysis of CDS data: these showed, in streamers at maximum, the presence of a much higher percentage of plasma giving rise to emission in Fe XIII, XIV, XV than observed in streamers at minimum. In our data even Fe XIII is hardly identifiable. The reason for this discrepancy is not known: possibly individual streamers at maximum activity cover a wider range of temperatures than at minimum and Foley et al. structure belongs to a higher temperature class than streamers studied in the present work.

Data do not allow us to come to definite conclusions about the behavior of temperature with time. The temperature of streamer A is constant with time, in agreement with results from J. Li et al. (1998), who didn't find any major variation in the physical parameters of streamers observed over a 6 day time span. The temperature of streamer B possibly increases slightly with time. Its temperature is lower than most of the estimates cited above. Whether this is related to the age of the streamer, being B a newly formed structure which is slowly heating up, is an interesting hypothesis which should be checked on other streamers.

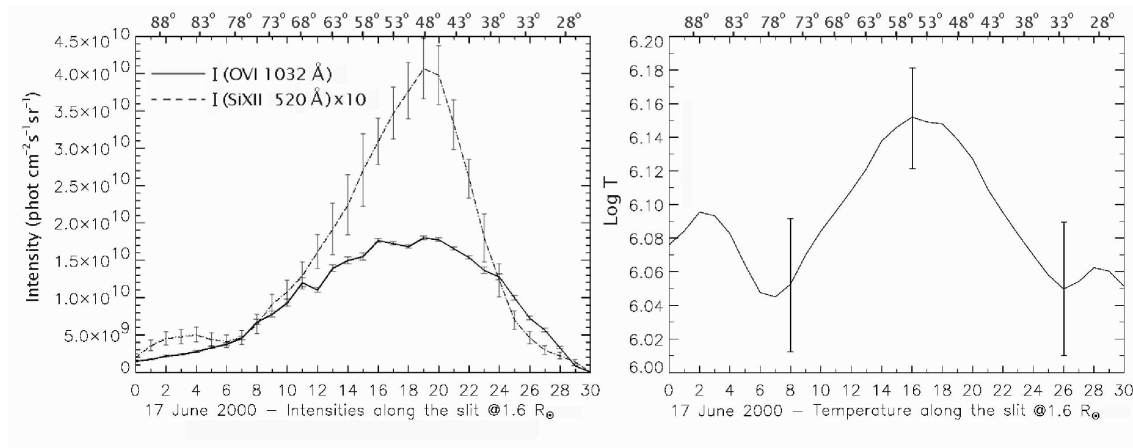


Figure 5.5: Left: profiles of the O VI 1032 Å and Si XII 520 Å line intensities along the UVCS slit, at 1.6 solar radii, for June 17. Right: electron temperature profile along the UVCS slit, showing that the electron temperature across the streamer (streamer A), peaks towards the streamer center and decreases towards its edges.

In order to derive the electron temperatures across the streamers, we applied the ratio technique at different latitudes along the UVCS slit: this has been done on June 16/17 for streamer A, when (as we mentioned) this structure is seen against the plane of the sky. The resulting temperature profile is given in Figure 5.5, right panel. We caution the reader that values at high latitudes (that is, in the coronal hole area) are only tentative, because ionization equilibrium may not hold in a plasma outflowing region. Also, because only the center of the UVCS slit (bin 15, latitude $\approx 58^\circ$) is at 1.6 R_\odot its edges extending to higher altitudes, the variation of temperature with altitude affects the temperature profile. However, the plot points

Date 2000	streamer	1.6 R _⊙	1.9 R _⊙
June 16	center	6.15 ± 0.03	
June 16	edge	6.08 ± 0.04	
June 17	center		6.12 ± 0.04
June 17	edge		6.07 ± 0.0

Table 5.3: Electron temperatures (log) across streamer A.

to a decrease of the electron temperature as we move from the center towards the edges of the streamer, in agreement with results obtained by Parenti et al. (2001). The temperature difference between the streamer peak and its (southern) edge, which we locate at the distance where the intensity drops by $1/e$ of the peak value, amounts to $\approx .05 - .06$ dex, that is, is on the order of 10 to 15%.

Table 5.3 gives temperatures at the center and at the edge of the streamer at 1.6 and 1.9 solar radii. It is worth pointing out that this result refers to a streamer which does *not* show the weak oxygen emission core that has been found in UVCS images of streamers at the minimum phase of the activity cycle (see, e.g. Kohl et al., 1997).

5.5.2 Electron densities

Once electron temperatures are known, we can make an evaluation of the electron density in streamers A and B as explained in § 3.3.3 from the oxygen lines, for a static streamer plasma, taking advantage of the N_e and N_e^2 dependence of, respectively, the line radiative and collisional components.

Using these relationships we derived densities across the UVCS slit; in the top part of Table 5.4 we give densities at the positions of the peak intensity of streamers A and B from June 11 through 14 at 1.6 and 1.9 solar radii and in the bottom part of the same Table we give the density at the center and edge of streamer A on June 16. We note that the two streamers have about the same density (which is consistent with their comparable WL brightness) and that the density is about constant until, on June 16/17, the density of streamer A increases by a factor of ≈ 2 .

Densities on 11, 12 and 13 June are about a factor 3 higher than streamer densities at minimum given by Gibson et al. (1999), as might be expected at the present phase of the solar cycle (see Figure 2.2). At the streamer center densities are larger than at the edges by a factor 1.5 – 2, depending on the heliocentric distance. A similar behavior has been found by Strachan et al. (2002) at larger heliocentric distances. Uncertainties given in Table 5.4 take into account uncertainties in temperature and statistical errors in line intensities. We also assumed a 10% uncertainty in the value of the O VI disk intensity (the value of the disk intensity affects the identification of the collisional and radiative components of the 1032 Å line).

Densities for streamers A and B			
Date 2000	streamer	1.6 R _⊙ 10 ⁷ cm ⁻³	1.9 R _⊙ 10 ⁶ cm ⁻³
June 11	B	3.0 ± 0.5	
June 11	A	2.9 ± 0.7	
June 12	B	2.2 ± 0.3	
June 12	A	1.7 ± 0.4	
June 12	B		7.5 ± 1.4
June 12	A		10.0 ± 2.7
June 13	B	3.1 ± 0.5	
June 13	A	3.1 ± 0.7	
June 13	B		7.8 ± 1.5
June 13	A		5.0 ± 1.3
June 14	B		9.4 ± 1.9
June 14	A		8.7 ± 2.3
Densities across streamer A			
Date 2000	streamer	1.6 R _⊙ 10 ⁷ cm ⁻³	1.9 R _⊙ 10 ⁶ cm ⁻³
June 16	center	5.3 ± 0.8	
June 16	edge	2.7 ± 0.4	
June 17	center		18.9 ± 3.8
June 17	edge		11.6 ± 2.3

Table 5.4: Electron densities in streamers A and B (top) and across streamer B (bottom).

5.5.3 Elemental abundances: FIP effect

The *absolute* oxygen abundance (i.e. the oxygen to hydrogen abundance ratio) is here calculated with the method described in § 3.3.5, which is independent on the knowledge of a precise value of T_e . For Hydrogen, following Raymond et al. (1997), we used the ionization rate of Scholz and Walters (1991) and the recombination rate of Hummer (1994).

This technique, however, requires disk intensities in the H Lyman- β and O-VI lines in order to evaluate the oxygen abundance from the radiative components. Unfortunately, there are no measurements of disk intensities at the time of our observations. The procedure we followed to get an estimate of disk intensities is the following: the contrast between quiet and active region intensities has been taken from Vernazza & Reeves et al. (1978); the increase of the quiet sun and/or active regions emission during the solar activity cycle has been taken from Schühle et al. (2000), Woods et al. (1998), and Tobiska et al. (1998); the area occupied by active regions during our observations has been evaluated on the basis of MDI magnetograms taken about seven days after the time UVCS data were acquired, in an attempt to consider the solar hemisphere as seen by a slit off the limb of the Sun. On this basis, and starting from UVCS disk measurements acquired around the minimum of the solar activity cycle, we made an estimate of the intensities of the full disk, taking into account the percentage of the solar disk occupied by active regions (see also Ko et al., 2002) on June 2000. We then compared the values we got for the Lyman- α disk emission with the Lyman- α disk intensity measured by SOLSTICE over our days: the predicted and measured values agree within 10%. This shows that the estimates we made are realistic. We note that Lyman- β disk values we predict are within 30% of the values given by Lemaire et al. (2002) for a couple of months before June 2000, which is reasonable because of the high variability of this line. Errors in the disk intensity evaluation lead to systematic errors in the oxygen abundances, but do not affect relative changes in the spatial variations of the oxygen abundance.

Table 5.5 (top) gives the absolute oxygen abundance for June 11, 12, 13 and the absolute oxygen abundance across the streamer A (bottom) from June 16/17 data, at 1.6 and 1.9 solar radii. Values in the Tables represent the average between the collisional and radiative estimates. Values of $[N(O)/N(H)]_{rad}$ and $[N(O)/N(H)]_{col}$ generally do not coincide, partly because of errors affecting the quantities they depend on, partly because the O VI line collisional component is proportional to N_e^2 and is thus more likely to be affected by density inhomogeneities along the line of sight than the O VI line radiative component which is proportional to N_e . While the separation of H Lyman- β line into radiative and collisional components may be affected by some uncertainties, this average is considered to be robust (see e.g. Raymond et al., 1997). The Table shows that we are unable to give the variation with height of the abundance, due to the higher statistical errors in data taken at 1.9 solar radii.

Oxygen abundance (log) in streamers A and B			
Date 2000	streamer	1.6 R _⊙	1.9 R _⊙
June 11	B	8.76 ± 0.13	
June 11	A	8.42 ± 0.22	
June 12	B	8.84 ± 0.13	
June 12	A	8.46 ± 0.22	
June 12	B		9.06 ± 0.25
June 12	A		8.31 ± 0.35
June 13	B	8.70 ± 0.13	
June 13	A	8.67 ± 0.22	
June 13	B		8.70 ± 0.25
June 13	A		8.35 ± 0.35
June 14	B		8.50 ± 0.25
June 14	A		8.48 ± 0.36

Oxygen abundance (log) across streamer A			
Date 2000	streamer	1.6 R _⊙	1.9 R _⊙
June 16	center	8.39 ± 0.13	
June 16	edge	8.49 ± 0.22	
June 17	center		8.42 ± 0.25
June 17	edge		8.67 ± 0.36

Table 5.5: Oxygen abundances in streamers A and B (top) and across streamer A (bottom).

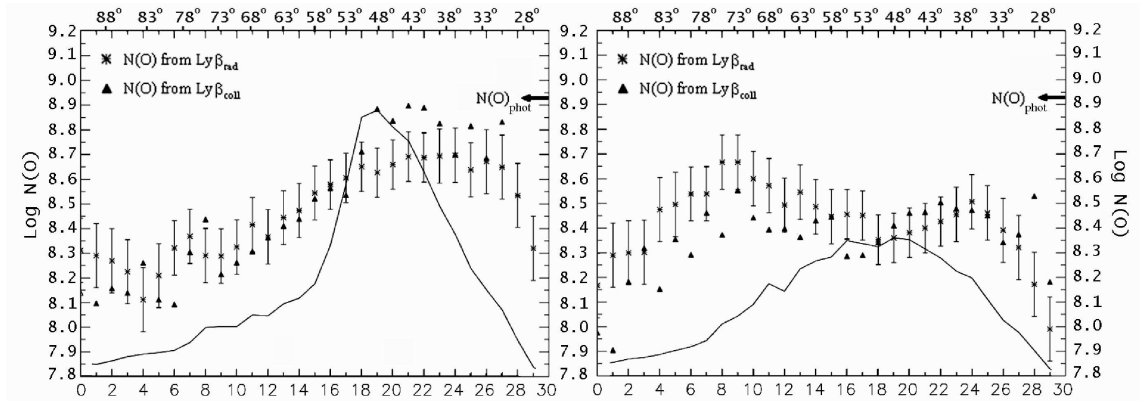


Figure 5.6: Profiles of the oxygen abundance distribution along the UVCS slit for June 12 (left) and June 16 (right), 2000. Abundances from the collisional component of O VI (triangles) and from the radiative component of O VI lines are given, together with the statistical error which affects the radiative determination. The photospheric abundance (log) of oxygen, 8.93, given by Feldman (1992) is also indicated. The O VI 1032 Å intensity profiles have been superposed onto the abundance profiles to identify the center of streamer B along the slit; on June 12 the center of streamer A corresponds to bin 14–16 (see Figure 5.3).

What appears to emerge from Table 5.5 (top) is a lack of variability in the oxygen abundance throughout our data, that is, over a one week time interval. There is a similar lack of variability across streamer A, on June 16/17 (Table 5.5, bottom), because changes in oxygen abundances are basically within error limits. However, Figure 5.6, which gives (left panel) the profile of the oxygen abundance across the UVCS slit for June 12, and (right panel) the profile of the oxygen abundance across streamer A, on June 16, challenges this conclusion: there is an obvious pattern in the variation of the abundance along the slit on both days. The values in Table 5.5 may be slightly misleading because of the large errors given there. Those numbers represent errors averaged over the (small) errors of the radiative component and the (large¹) errors of the collisional component. Focussing on calculations from the radiative component only, however, shows that the abundance of oxygen in streamer B is higher than in streamer A and that the abundance in the streamer core is lower than in the streamer’s legs. It is interesting to notice that on this day we have little discrepancy between the collisional and radiative abundance determination, as may be expected at the time the streamer is on the plane of the sky.

Our analysis suggests that there may be differences in the abundances between different streamers. The lower abundance in streamer A may be associated with a lifetime long enough to achieve a gravitationally stratified equilibrium, while in the younger B streamer dynamical inflows of new material may prevent gravitational

¹The larger error on the collisional component derives from error propagation on the relationships for the separation of the collisional and radiative components of the total line intensities.

Abundances at 1.6 R _⊙								
Date 2000	streamer	Al	Ca	Mg	Fe	Si	S	N
June 11	B	6.85	6.48	7.86	7.93	7.82	6.84	7.53
June 11	A	6.13	5.93	7.27	7.46	7.47	6.23	7.07
June 12	B	6.51	6.38	7.76	7.80	7.78	6.72	7.59
June 12	A	6.16	6.03	7.34	7.49	7.53	6.35	7.36
June 13	B	6.30	6.02	7.55	7.70	7.73	6.80	7.68
June 13	A	6.26	6.09	7.59	7.72	7.75	6.31	7.45
June 16	A	6.17	6.02	7.57	7.56	7.62	6.40	7.31
Abundances at 1.9 R _⊙								
Date 2000	streamer	Al	Ca	Mg	Fe	Si	S	N
June 12	B	6.45	6.52	7.88	7.90	7.70	6.69	7.48
June 12	A	5.72	5.89	7.50	7.45	7.21	6.26	6.98
June 13	B	6.41	6.39	7.86	7.77	7.74	6.51	7.55
June 13	A	6.16	6.33	7.25	7.54	7.25	5.84	7.32
June 14	B	6.03	6.06	7.63	7.62	7.56	6.40	7.43
June 14	A	6.19	6.22	7.66	7.67	7.24	6.35	7.37
June 17	A	6.08	6.09	7.59	7.58	7.62	6.50	7.40

Table 5.6: Elemental abundances with respect to hydrogen (log) for streamers A and B at different heliocentric distances.

stratification to set in. This suggestion is supported by the value of the oxygen abundance in streamer B, which is close to the photospheric value given by different authors (see, e.g. Feldman, 1992, 8.93, Feldman and Laming, 2000, 8.83 ± 0.06 , Holweger, 2001, 8.74 ± 0.08). Streamer A, on the other hand, has abundances similar to those found by Raymond et al. (1997) in streamers legs/core (8.5/8.4). Thus we cannot invoke projection effects to explain the higher abundances of streamer B, because they are higher than abundances found in the streamer legs by Raymond et al. (1997, 1998a).

As shown by Table 5.1, UVCS spectra include lines from many other ions. In order to find the abundances of elements responsible for the ion emission, we followed the technique described in § 3.3.4 (using emissivities from the CHIANTI 3 code with the ionization equilibria of Arnaud and Rothenflug, 1985 and the photospheric abundances of Feldman et al, 1992): any discrepancy between observed and predicted ratios has been attributed to a variation of the element abundance with respect to its photospheric value. Table 5.6 give the abundances we derived for Al, Ca, Mg, Fe, Si, S and N at 1.6 (top) and 1.9 (bottom) solar radii. For June

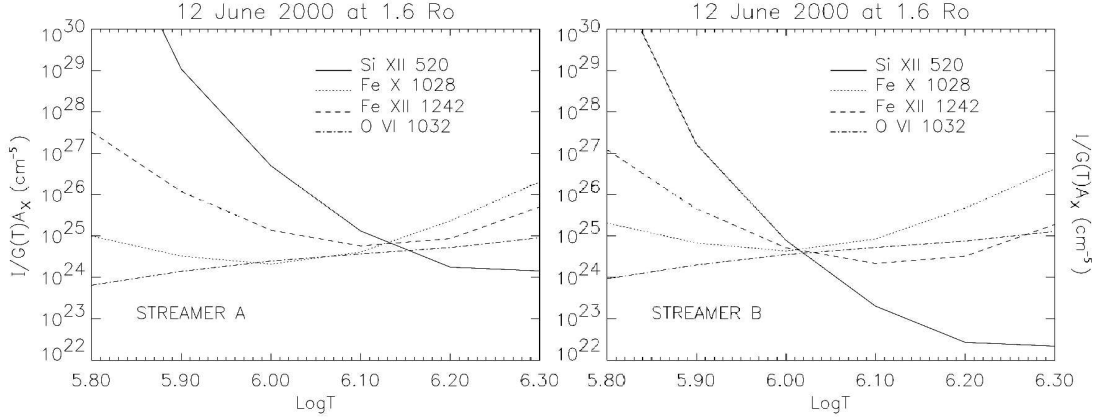


Figure 5.7: The different temperatures of streamer A and B on June 12 at 1.6 solar radii as given by an emission measure loci method (see text); abundances from Tables 5.5 and 5.6.

16/17 we give an average abundance between streamer center and edge, as we did not find any evidence for variation of abundances across the streamer. The errors in the determination of abundances are $\approx 0.1 dex$ for Fe and Si, $\approx 0.2 dex$ for Mg, Al, S and N and $\approx 0.3 dex$ for Ca. The variation of the error from element to element is due to the different intensity of the lines used in the calculations and of their background. Abundances seem to be different, in the two streamers, even if the difference is small. We warn the reader that most of the lines used in our analysis are from the Li or Na-like ions, whose ionization equilibrium may be subject to large uncertainties (see e.g. Raymond et al., 2001; Del Zanna et al. 2001; Del Zanna et al. 2002).

In order to visualize the different temperatures of streamers A and B on the basis of the elemental abundances we derived, we show in Figure 5.7 the results of an emission measure loci analysis applied to June 12 data. To this end we evaluate the upper limit to the emission measure EM (cm^{-5}) which is related to the observed line intensity I ($\text{phot cm}^{-2}\text{sr}^{-1}\text{s}^{-1}$), the electron temperature T_e , the abundance A_X of element X and other atomic factors by (see equation 3.47):

$$EM = \frac{4\pi \langle I_{col} \rangle}{\langle A_X \rangle C_{line}(T_e)}$$

where $C(T_e)$ is the contribution function (see e.g. Del Zanna et al., 2002) defined in § 3.2.6. Then we made plots of EM vs. $\log T$ for O VI, Si XII, Fe X and Fe XII lines: these are shown in Figure 5.7. The Figure shows that the EM curves intersect near a single temperature which is different for streamer A (left) and B (right) in agreement with values given in Table 5.2.

In order to discuss the behavior of elemental abundances at the coronal altitudes we analyzed, we evaluated the ratio $Y = \log[N(X)_{cor}/N(X)_{phot}]$ between the coronal and the photospheric abundance for element X as a function of its First Ionization

Potential (FIP). The present data include high FIP elements such as S, O and N and low FIP elements like Al, Ca, Mg and Fe. This allows us to build plots of the ratio between streamer and photospheric abundances (Feldman, 1992) for each of the above mentioned element vs. its FIP value. Representative plots of our results for streamers A and B, at 1.6 solar radii, are given in Figure 5.8 for June 11 and 12. The photospheric abundances are from Feldman et al. (1992). Dashed lines help visualize the pattern corresponding to a FIP bias of 4.

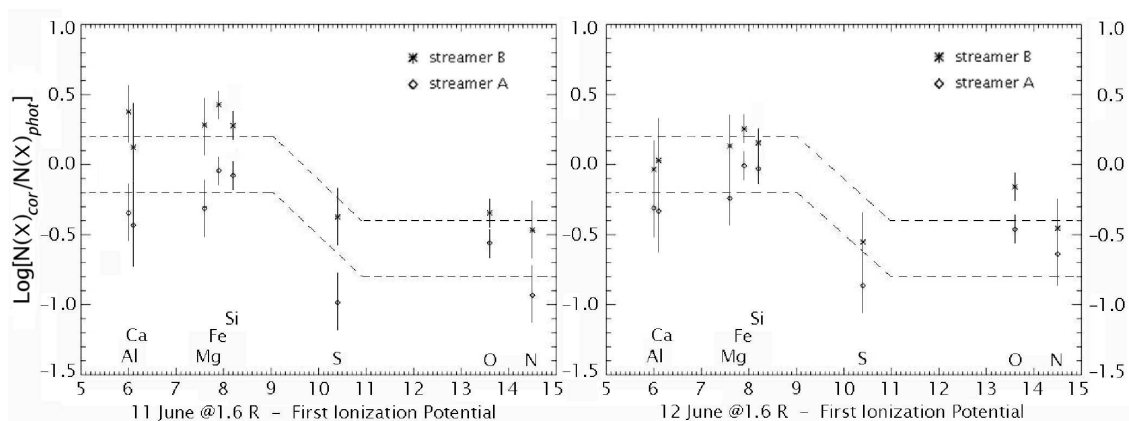


Figure 5.8: Left: coronal element abundances (log, with respect to photospheric values) against their FIP values, for June 11, 2000 data, at 1.6 solar radii, for streamer A, diamonds, and B, stars. Right: as for the left panel, but for June 12, 2000. The dotted lines correspond to a FIP bias of 4.

Figure 5.8 shows the presence of a FIP bias in streamers A and B, even if the abundances of the two streamers are different. The high FIP elements S and N, in streamer B, turn out to be depleted by as much as oxygen, even if abundances of S and N have been derived from total line intensities, while for oxygen we made an average between abundances derived from radiative and collisional line components. This strengthens the validity of our results. The two streamers show the same FIP effect, but in streamer B the low FIP elements are enhanced with respect to their photospheric values, while in streamer A the low FIP element abundance is lower than the photospheric abundance by a factor of ≈ 1.5 (and the high FIP elements are depleted by a factor of ≈ 6). We note that the 8.93 value of the photospheric oxygen abundance is larger than more recent estimates (see e.g. Feldman and Laming, 2000, Holweger, 2001). New values will shift upward the Y data point in Figure 5.8. However we keep the 8.93 value to facilitate the comparison with FIP-plots of Raymond et al. (1997, 1999) where this value was adopted. We also remind the reader that oxygen Y values are affected by uncertainties in the H Lyman- β and O VI disk intensities and these may be responsible for the discrepancy between oxygen and other high FIP elements Y values.

Plots in Figure 5.8 are constructed from absolute element abundances, while most of the FIP plots are built from relative element abundances. Usually, oxygen

is taken as reference element. However, as pointed out by Uzzo et al. (2003), the strong oxygen depletion observed sometimes in the core of streamers makes the problem of whether the FIP effect is due to an enhancement/depletion of the low/high FIP element even more complex. Our data point to an enhancement of the low FIP element abundance in streamer B, but not in streamer A. Hence, it looks like similar FIP effects can be obtained from a different behavior of the elemental abundances.

There are not many measurements of FIP effect in streamers (see, e.g., Feldman et al., 1998) and often results are contrasting (see, e.g. Schmelz, 1999). Moreover they refer to lower altitudes than examined here. At heliocentric distances comparable to ours however, Raymond (1999) found a behavior similar to that shown by streamer A in the core of the streamers he analyzed, and a behavior similar to that shown by streamer B in active regions and/or legs of streamers. In the scenario we have been pursuing so far, an explanation for the observed behavior calls for a FIP effect imposed at chromospheric levels, with gravitational settling afterwards modifying the values of the abundance ratios, but not the FIP bias. As we said, possibly, conditions in “young” streamer B have not been stable long enough for gravitational settling to reduce the abundances of low FIP elements, which, on the contrary, are depleted in the “older” streamer A. A similar explanation has been given by Raymond (1999) to interpret the difference between the abundances of the core of streamers and the abundances of active region streamers.

5.6 Abundances measured *in situ* and their coronal counterparts

During the June 2000 quadrature Ulysses was at a southern latitude of 58° , as mentioned. In spite of this rather high latitude, because of the phase of the activity cycle, Ulysses was immersed in slow wind. Data from the Solar Wind Ion Composition Spectrometer (SWICS; see Bame et al., 1992) show that the solar wind speed emanating from the Sun between 10 and 17 June 2000 was about 350 km/s, which is typical of the slow wind originating from non-coronal hole areas. Hence we expect *in situ* abundances to show a FIP effect on the order of 2–3 in contrast to high speed wind where the FIP effect is negligible (see, e.g., Geiss, 1998, Von Steiger et al., 2000, Von Steiger et al. 2001). This behavior is consistent with the FIP pattern in the corona, weak FIP effect having been found in coronal holes (Feldman & Widing, 1993, Doschek et al., 1998, Doschek & Laming, 2000), from which fast wind originates. Quadrature configurations allow us to make a direct comparison between the coronal FIP and the *in situ* FIP effect. Because only the abundances of few elements are measured *in situ*, we chose the Fe/O abundance ratio as a proxy for the FIP bias, both elements being prominent among, respectively, the low/high FIP elements.

Because UVCS data have been acquired below the altitude where the magnetic

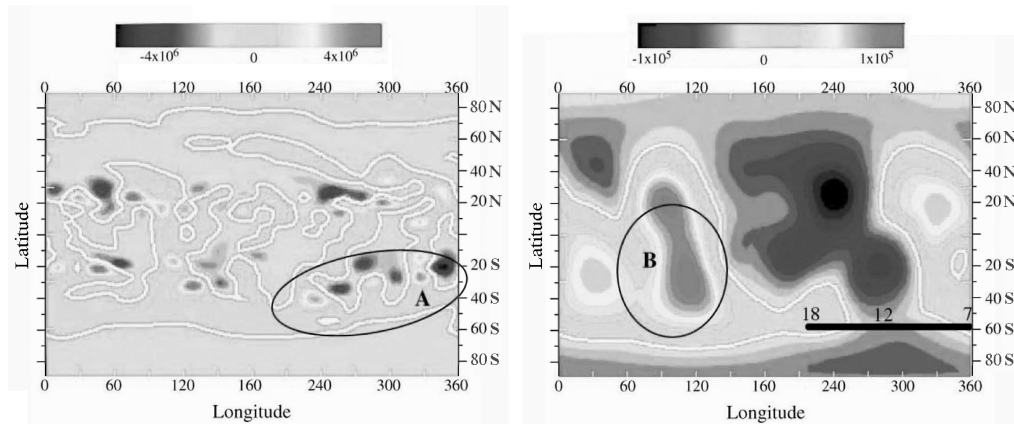


Figure 5.9: Measured magnetic field at the photosphere (left) and predicted magnetic field at 1.6 solar radii (right) for Carrington rotation 1964 (June 13 to July 10, 2000), using the MHD model of the corona described in Riley et al.(2001). Regions A and B are described in the text. Heliographic longitude is labelled at the bottom. The magnetic field intensity at the left and right gray-scales are shown in the horizontal bars. The black bar in the right panel shows the projected footpoint at Ulysses on 7 – 18 June 2000.

field is radial, we need first to extrapolate the photospheric magnetic field out to the altitude where the field is radial, reconstructing a map of the field configuration at coronal levels. Then we locate the position of the Ulysses “footpoint” on this map, and identify the location, along the UVCS slit, of the plasma which eventually reaches Ulysses. To do this, we utilize the MHD model of the corona and inner heliosphere described in Riley et al. (2001). This model uses the observed line-of-sight component of the magnetic field as the inner boundary condition for a fully three-dimensional MHD model of the corona. With this model we extrapolated the photospheric magnetic field measured at the Wilcox Solar Observatory to coronal altitudes and made magnetic field maps at several heights: these maps allowed us to infer the location of the footpoint of Ulysses with respect to the neutral line. From this we have been able to determine which side of the streamer observed by UVCS has been the source of the *in situ* measurements. The shape of the streamers correlate well with those observed by LASCO.

The photospheric field used in the model and the predicted field at 1.6 R_{\odot} are shown in Figure 5.9 (for the projection of Ulysses footpoint at 1.6 R_{\odot} see next paragraph). Region A in this Figure is the mixed photospheric polarity region that gave rise to the band of streamers lying on the limb and containing streamers A and B discussed above. Region B in this Figure was the source of the higher speed wind that followed the band of streamers. As might be expected at this phase of the solar activity cycle, the photospheric field has a complex pattern which simplifies at coronal levels in part because short length scale variations are lost in the extrapolation into the corona, but also because short time scale variations are lost in the smoothing used to estimate the field over the entire photosphere for a

UVCS Date 2000	Ulysses Date 2000	$(Fe/O)_{cor}$	$(Fe/O)_{SWICS}$	v_p (km/s)
June 11	June 29	0.12 ± 0.03	0.09 ± 0.04	365
June 12	June 30	0.14 ± 0.04	0.14 ± 0.05	352
June 13	July 01	0.15 ± 0.04	0.15 ± 0.05	339
June 14	July 02	0.16 ± 0.05	0.19 ± 0.16	333
June 17	July 05	0.11 ± 0.03	0.10 ± 0.07	309

Table 5.7: Coronal $(Fe/O)_{cor}$ vs. *in situ* $(Fe/O)_{SWICS}$ ratios: in the last column we give the speed of the solar wind stream sampled by SWICS.

full solar rotation. In Figure 5.9 it is clear that Ulysses skims along the neutral line for most of the June 2000 quadrature. From the model coronal configuration, we estimated the latitude, and hence the position along the UVCS slit, where fieldlines reaching Ulysses intersected the UVCS slit.

Values of Fe/O at these positions and the average Fe/O values measured by SWICS are given in Table 5.7. There is only one UVCS grating position, among those we used, which includes the Fe XII line. Hence, only one Fe/O value per day is available from UVCS observations. SWICS temporal resolution (see Figure 5.10) is much higher: in the Table we give the daily average over SWICS measurements. We list in the Table also a daily average of the proton velocity and the day when velocities and Fe/O ratios have been measured at Ulysses. Ulysses was, during the JOP 112 campaign, at a distance of ≈ 3.25 AU: the time taken by plasma leaving the corona to reach the Sun has been calculated using the average speed on 7 – 17 June (see Figure 5.10) and corresponds to an 18 day constant shift.

The agreement between coronal and solar wind value is remarkable. Moreover, values of the ratio compare well with Fe/O values measured by Aellig et al. (1999) in ecliptic solar wind with SOHO CELIAS CTOF for solar wind speed of the order of 300 - 350 km/s, as measured in our case. However, it is worth noticing that *in situ* values represent daily averages over widely different values, which cannot be probed by coronal measurements that provide only values of the ratio integrated along the line of sight. Figure 5.11 shows *in situ* Fe/O values, measured over a 3 hour time interval, the daily averages from these values and their 1 sigma excursion, together with the Fe/O coronal values: clearly the 1 sigma deviation is so large that the comparison between coronal and *in situ* values is meaningful only when averages over extended time intervals are considered, because individual values may agree or disagree altogether fortuitously.

The present work improved upon Aellig's work in that the quadrature configuration allows us to compare the values of the Fe/O ratio measured in the same plasma parcel first in the corona and later *in situ*. However, we point out that this is strictly true only for the June 16/17 plasma, where we surmise streamer A to be in the plane of the sky (see section 5.3). On previous days, the coronal Fe/O values have

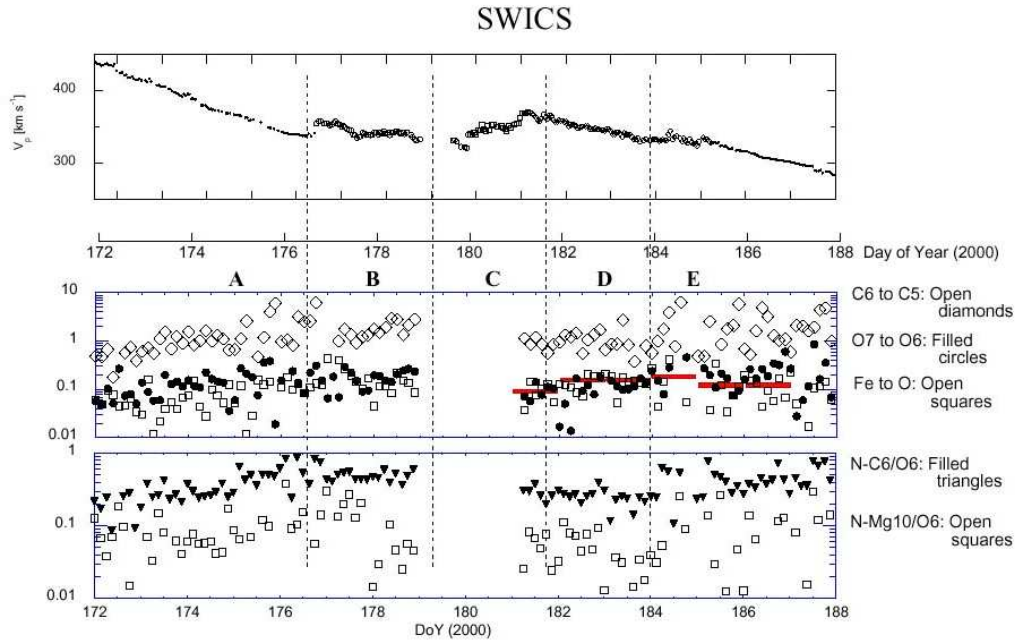


Figure 5.10: Top: plasma speed from SWICS data over the time interval which includes the JOP 112 campaign (June 20, 2000 is DoY 172). Bottom: the Fe/O ratio as observed by SWICS over the same time period. The daily average we used for comparison with coronal Fe/O values are indicated by short horizontal lines.

been evaluated on the basis of the magnetic field maps previously described – which allow us to identify the coronal latitude where plasma sampled *in situ* originates – with the additional assumption that plasma reaching Ulysses can be represented by coronal plasma which projects onto the plane of the sky, provided it originates from the same latitude. This assumption is justified by the location of the Ulysses footpoint which runs along the neutral line of the magnetic field over all the days for which Fe/O values are given in Table 5.7.

Aellig et al. (1999) also compared the Fe/O values obtained by CELIAS over an 80 day period (from DOY 150 to 229, 1996) with the value derived by Raymond et al. (1997) for the legs of streamers observed in 1996. Although there may not be a one-to-one correspondence between the streamer plasma observed by Raymond and the CELIAS plasma, the time when *in situ* data had been acquired overlaps the time when streamers had been observed, making the two values likely comparable. Aellig points out that Raymond's value of $0.13 \pm_{0.03}^{0.05}$ is consistent with slow wind *in situ* Fe/O values and provides evidence in favor of streamer edges being the site where slow wind originates. However, if we consider the values given in Table 1 of Raymond et al. (1998a), we find a Fe/O value, both in the July 25 streamer core and legs, of 0.16 and values of Fe/O = 0.08, 0.12, respectively, for July 23/24 and Aug. 21 streamers, where no distinction is made between streamer core and/or legs. Hence, there is very weak evidence, if any, in this data, favoring streamer

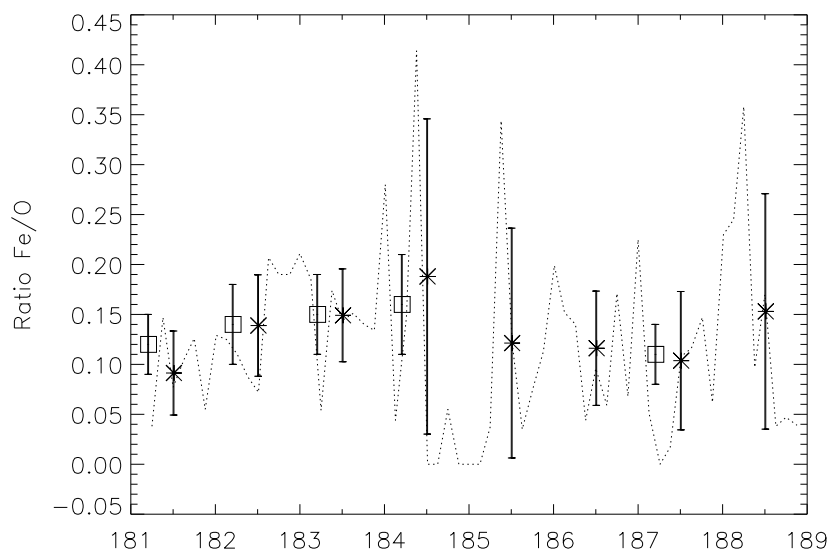


Figure 5.11: The Fe/O ratio from three hour averages, measured by SWICS (dashed line), daily averages of Fe/O calculated from the SWICS measurements, and their 1 sigma uncertainty (asterisks), coronal Fe/O ratio, calculated from the abundances derived from UVCS spectra and their 1 sigma uncertainty (squares) vs. time from June 29 (DoY 181) to July 7 (DoY 189).

legs as sources of the slow wind. We conclude that we should probably resort to a comparison between coronal and *in situ* absolute abundances, rather than to a comparison between abundance ratios.

The same conclusion has been reached by Ko et al. (2002), who analyzed data acquired by UVCS at heliocentric distances between 1.2 and 1.6 solar raddi, above an active region. The lower heights and higher line intensities considered by Ko et al. (2002) allowed these authors to measure, much better than we could, the decrease of element abundances with height. However, they point out that a similar FIP effect is present all over the range of altitudes they examined. If FIP effect is independent of absolute abundances, these are a more valid means to establish an association between coronal and *in situ* parameters than the FIP effect might be.

5.7 Conclusions

In this work we analyzed UVCS observations of a couple of streamers taken over a time interval of about one week in June 2000, during the ascending phase of the solar activity cycle. The two streamers have a higher density, but about the same temperatures, than streamers at the phase of minimum in the solar activity

cycle. Moreover, they are characterized by different temperatures. Temperature apparently decreases from the center towards the edge of streamers.

The streamers we examine do not show the dichotomy in the oxygen vs. hydrogen behavior, typically found in streamers observed by UVCS at the minimum of the solar activity cycle. This raises the problem of the behavior of the oxygen and other element abundance in these streamers. Our analysis shows that the two streamers we examined have different elemental abundances. One of them, newly formed, at the time of our observations, has higher abundances than the other: neither of them shows such a high oxygen depletion as found in streamers at minimum activity. This result apparently cannot be ascribed to projection effects, because in the only day when we are able to distinguish the streamer core and legs we still find a lower difference between center and edge of the streamer, and a higher oxygen abundance in the core, than measured in streamers at minimum activity.

We found evidence for the FIP effect in both streamers: however, the same FIP effect turns out to originate from different elemental abundances. Our results for the newly formed streamer agree with those found for the active region streamers by other authors. Hence we conclude that the process responsible for the FIP effect is at work independently of the absolute values of the abundances.

We made a comparison between coronal values of the Fe/O ratio and *in situ* measurements of the same ratio, taking advantage of the SOHO-Sun-Ulysses quadrature configuration at the time data have been acquired. Coronal and *in situ* values compare well. However, the fluctuations in the *in situ* values are so large that a comparison can be made only between time-averaged values. Moreover, we show that there is so far little evidence in the coronal data favoring an association between abundances in the streamer legs and slow wind abundances. This issue should be further pursued to find a more persuasive evidence favoring streamer edges as the site where slow wind originates.

Chapter 6

Early evolution of a CME in the low corona

6.1 Introduction

A Coronal Mass Ejection (CME) is a sporadic ejection of large plasma structures. These phenomena occur about once per day (depending on the phase of the solar cycle) carrying a mass on the order of $\approx 10^{14} - 10^{16}$ g, which corresponds to an average mass loss rate of $m_{CME}/(\Delta t \cdot 4\pi R_{\odot}^2) \approx 2 \cdot 10^{-14} - 2 \cdot 10^{-12}$ g cm⁻² s⁻¹ ($\Delta t = 1$ day), less than 1% and 10% of the solar wind mass loss, respectively, in coronal holes and streamers. CMEs involve the catastrophic loss of equilibrium of a magnetic configuration with the release of the stored energy and a subsequent reconfiguration of the disrupted fields. Projected onto the plane of the sky they have typically a three part structure (Figure 6.1, left) consisting of 1) a bright leading edge (“plasma pileup” in Figure 6.1), 2) a dark void (“cavity”) and 3) bright core (“prominence”). However, the 3D geometry of CME is still debated, and in different models these phenomena are treated as lightbulb bubbles, arcades of loops, or curved and twisted fluxtubes. Because of LOS projection effects and of the optical thinness of plasma, observations are often ambiguous and do not allow one to easily identify these features.

The evolution of a CME into the interplanetary space is in general conceived as an expansion of a magnetic flux rope (i.e. helical fieldlines wound around a curved cylinder) with the legs connected to the footpoints on the Sun (Figure 6.1, right). However, in the last few years edge-enhancing techniques applied to the LASCO difference images (Figure 6.2) revealed a complex fine structure of CMEs, which appear to be composed of numerous helical strands (see e.g. Wood et al., 1999; Dere et al., 1999; Lin et al., 2005). The real 3D geometry of these events is then still uncertain and their geometric modeling is still crude.

Over the last few years, Lin & Forbes (2000), Lin, Raymond & Van Ballegoijen (2004), Lin (2002) have thoroughly explored CME processes, from the CME initiation to its expansion through the solar corona and its manifestation at chromospheric

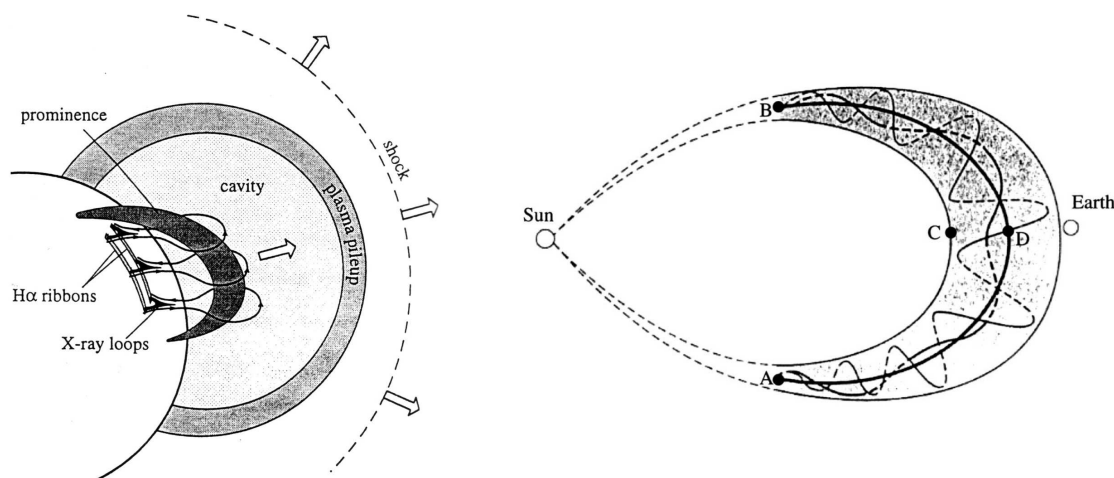


Figure 6.1: Left: the typical three part structure of a CME (from Forbes, 2000); these features are not necessarily present in all CMEs. Right: schematic of the flux rope expansion into the interplanetary space (from Lepping et al., 1997).

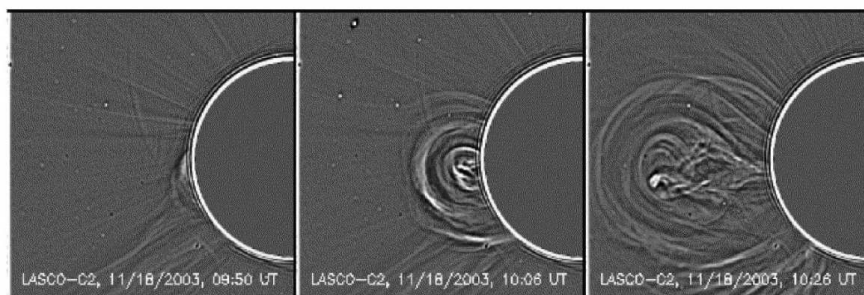


Figure 6.2: LASCO/C2 images (enhanced with the wavelet technique) of a CME showing the leading edge, cavity and core as well as the formation of the current sheet (adapted from Lin et al., 2005)

levels. During the CME, the field is stretched outwards, due to the catastrophic loss of equilibrium of the flux rope: a current sheet forms in between the reconnecting loops and the lower tip of the bubble that grows around the flux rope as reconnection progresses outward. The temporal evolution of the bubble is illustrated in the top rows of Figure 6.3, in a sequence of representative snapshots (from a numerical model of Lin, Raymond & Van Ballegoijen, 2004) that shows the magnetic configuration at different times. In this model, a flux rope is initially held in equilibrium in the corona by a balance between curvature forces, magnetic tension and compression; hence, the increase in the strength of the dipole at the base of the magnetically stable structure (i.e. a changing in the photospheric fields) leads to a sudden loss of equilibrium and the flux rope is ejected upwards, followed by the formation of a

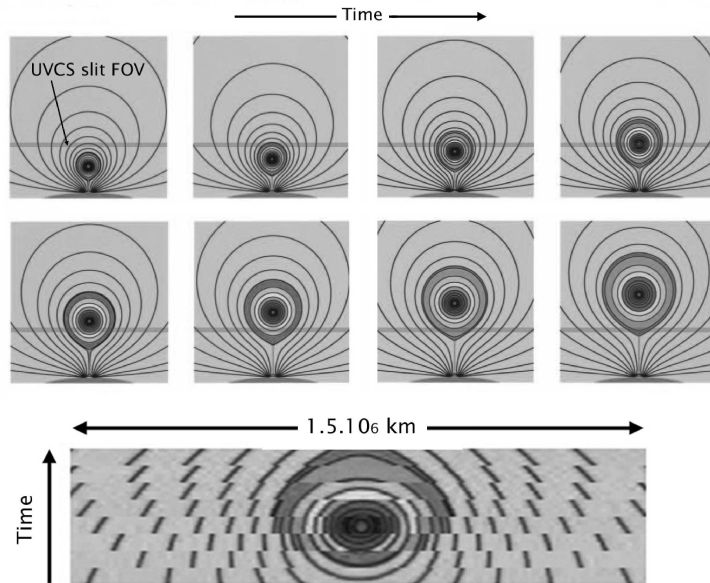


Figure 6.3: Top: a sequence of snapshots of the CME evolution showing at different times the disrupted magnetic field (from Lin, Raymond & Van Ballegoijen, 2004). Bottom: simulation of the temporal evolution of the CME topology seen through a slit at a fixed altitude, as predicted by the snapshots shown above.

current sheet. Each panel of Figure 6.3 covers an area of $\approx 2.25 \times 10^{12} \text{ km}^2$: starting from the top left panel simulations show the progressive rise of the CME core and the increasing dimensions of the CME bubble; these simulations compare favourably with the observed evolution of CMEs (Figure 6.2). At any given time a thin layer around the separatrix bubble (i.e. the outermost closed fieldline surrounding the fluxrope) is filled with hot plasma flowing out of the current sheet. Also, plasma in the outer shell is hotter than plasma in the innermost sections.

To help the reader visualize what UVCS may be expected to observe, if a CME structure happens to be sampled at a fixed altitude during its evolution, on the snapshots given in Figure 6.3 we have drawn a strip representative of the UVCS slit (width not in scale). Results from a simulation made cutting through the panels of Figure 6.3 and letting the rising CME bubble progressively enter a slit set at a constant altitude are shown in the bottom panel this Figure. This represents the temporal evolution of the topology predicted by the Lin & Forbes (2000) model, as seen by a spectrograph slit.

6.2 The goal of our observations

To our knowledge the three-part CME structure we described has been observed only above the LASCO/C2 occulter, hence at heliocentric distances higher than $2 R_{\odot}$. A first interesting question we may ask is at which heliocentric distances

these structures start forming and can be observed. Moreover, because of the very inhomogeneous distribution of plasma inside the CMEs, little information has been accumulated on electron densities and temperatures of different CME sub-structures.

To this end, in this work we analyze the early stages of a CME that occurred in the NE quadrant on January 31, 2000, for which we have data which cover the first hours of the CME evolution. Our analysis is based on Mauna Loa, LASCO and UVCS observations: unfortunately interplanetary data are not available because Ulysses was not favorably located to observe the event. We have been able to identify the CME source region and to provide evidence for the interaction between the AR where the CME originates and the large scale ambient field, which gets disrupted by the CME. The configuration of the CME is compared with that predicted by Lin & Forbes (2000) CME model which we prove to hold since the early stages of the CME development. We also provide physical parameters (N_e and T_e) of the three-part CME structure in these early stages.

6.3 The January 2000 CME scenario

On January 31, 2000, LASCO C2 and C3 coronagraphs observed a CME in the NE quadrant at an approximate latitude of $\sim 60^\circ\text{N}$, which propagated in the outer corona at a speed of ≈ 500 km/s. Extrapolating backwards in time, with a constant speed, the CME turned out to be ejected at a time $t \leq 18:43$ UT. Figure 6.4 (top left panel) shows the pre-CME corona, from a composite image made up with data taken by the Mauna Loa Mark IV Coronameter and by the LASCO C2 experiment ¹. The middle and right panel give the coronal configuration during the CME propagation. Mark IV pB images are not available after about 22:00 UT. For future reference, the positions of the UVCS slit (see § 6.4) are also shown in this Figure.

Most CMEs, independent of whether they are or are not associated with prominence eruptions, originate in Active Regions (Subramanian & Dere, 2001) and, at interplanetary distances, show a helical magnetic structure, usually referred to as “magnetic cloud”. The interaction between ARs and the background field has been recently studied by several authors (see, e.g., Luhmann et al., 2003; Leamon et al., 2004) who focussed on the relationship between the local AR field and the large scale ambient fields to get a better understanding of the origin of the helical flux ropes observed in the interplanetary medium. It turns out that an interaction between the ARs and the overlying large scale fields is crucial to the interpretation of the CME and interplanetary phenomena.

Hence, a first interesting issue we want to address is the identification of the CME source region. To this end, we analyzed MDI observations of the ARs on January 31, 2000. The most prominent AR in the NE quadrant is AR 8851 at a

¹See Mauna Loa and LASCO movies respectively at http://mlso.hao.ucar.edu/cgi-bin/mlso_datasum.cgi?2000&1&31&ACOS and http://lasco-www.nrl.navy.mil/daily_mpg/2000_01/

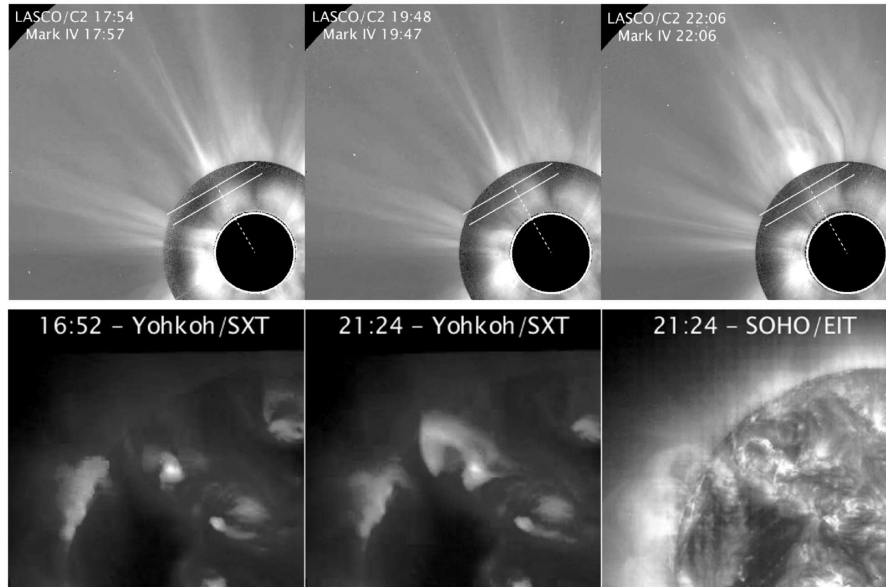


Figure 6.4: Top: Mauna Loa Mark IV and LASCO C2 images for the CME event on January 31, 2000. Bottom: Yohkoh (left and middle panel) and EIT Fe XII (right) images of the activity before and after the CME.

northern latitude of 27° and eastern longitude of 42° ; because the radial from this AR projects onto the plane of the sky at a latitude of $\sim 54^\circ\text{N}$ (which corresponds to the latitude at which the CME core is seen in UVCS and Mauna Loa data, see later Figures 6.6 and 6.9), this is a first indication that AR 8851 could be the CME source. As revealed by LASCO images, the CME is centered at a latitude of $\sim 57.5^\circ\text{N}$ at 19:48 UT (i.e. when it was at an heliocentric distance of $3.1 R_\odot$), and moved to a latitude of $\sim 67.4^\circ\text{N}$ less than 4 hours later (at $13.3 R_\odot$); this northward angular motion projects back at $1 R_\odot$ at the time of the CME occurrence at a latitude of $\sim 55^\circ\text{N}$, in agreement with the angle of the projected radial from AR 8851².

Moreover, this AR is rapidly evolving, with a total area and total sunspot number increasing in time. This rapid evolution implies flux emergence and a possibly unstable configuration that makes AR 8851 a likely candidate for the CME ejection. As revealed by images acquired by the Imaging Vector Magnetograph (IVM) at the MEES Solar Observatory³, the two sunspots within the AR are moving in opposite directions implying a shearing of the magnetic fieldlines above the AR, which is considered a likely agent to trigger the magnetic equilibrium loss.

The identification of AR 8851 as the CME source region is further supported by

²We note here that (as recently pointed out by Cremades & Bothmer, 2004) a deviation towards higher latitudes with respect to the projected radial from the source region is a systematic phenomenon for CMEs occurring around the maximum of the solar activity cycle; such deflections are probably due to the “fast solar wind flow from polar coronal holes that encompasses the CME’s expansion at the higher latitudes” (Cremades & Bothmer, 2004).

³See http://www.solar.ifa.hawaii.edu/IVM/Movie/Quick/2000/ivm_AR8851_20000131.html

EIT and Yohkoh data: Yohkoh SXT data have a gap in between 16:52 and 21:24 UT, hence there is no data coverage at the time of the CME ejection. However, in the first image available after the gap, at 21:24 UT, a prominent cusp-shaped arch is rooted in AR 8851, and an EIT 195Å loop appears to be nested within the SXT loop (see the bottom row in Figure 6.4). These newly formed structures provide strong evidence of 8851 being the source of the CME ejection and the site for reconnection of AR fieldlines, torn open by the ejection, and subsequently reforming.

The only alternative source for the CME could be AR 8858, a region which, on January 31, is behind the solar limb and, dragged by solar rotation, crosses the plane of the sky on February 3, at a latitude of 26°; however, disk activity in AR 8851 makes us favor this as the source of the CME. Note also the inclination toward higher latitudes of the SXT arch (Figure 6.4) in agreement with CME ejection northward of its AR source.

Images from the Mauna Loa Mark IV Coronameter show at the time of the CME occurrence a complex system of rising loops which are seen later in the LASCO/C2 field of view. Difference images (Figure 6.5) revealed a complex system of different loops surrounding a bright knot that we identify as the CME core. The opening CME front, the following dark void and the CME core are also visible; moreover, as revealed by a comparison with EIT Fe XII difference images, at this early stage of the event the current sheet and the neutral “Y” point are already visible. As we said, in the literature typically these structures are identified after the CME enters the LASCO/C2 field of view (see e.g. Lin et al., 2005). To our knowledge, this is the first time that the 3 part structure of CMEs has been identified at such low coronal levels. As shown in Figure 6.5, the UVCS slit is favorably located to observe the whole CME bubble; in particular we expect to observe the transit of the CME core below the UVCS slit at about 20:00 UT (see middle left panel of Figure 6.5). In the next Section we concentrate on the analysis of the UVCS data.

6.4 UVCS observations

The UVCS data of the January 31 CME were acquired in the O VI channel: observations started on January 31, 2000 at 17:05 UT and ended on February first at 02:00 UT. The UVCS slit was centered at a Northern latitude of 60° in the East quadrant (see Figures 6.4 and 6.5) and two observation heights have been used, 1.6 and 1.9 R_{\odot} : the instrument took alternatively 12 exposures at 1.6 and 3 exposures at 1.9 R_{\odot} (with an exposure time of 120 s), hence we have nearly “simultaneous” observations of the same event at two different altitudes. The slit width was 50 μm : data were acquired with a spatial binning of 6 pixels (i.e. a spatial resolution of 42”) and a spectral binning of 1–3 pixels depending on the selected wavelength interval. In particular, the five selected spectral ranges are 1063.4 – 1068.1Å, 1029.5 – 1044.4Å, 1024.3 – 1027.7Å, 987.5 – 993.4Å and 1211.8 – 1220.7 Å (redundant channel). Table 6.1 lists the lines included in these ranges, together with the tem-

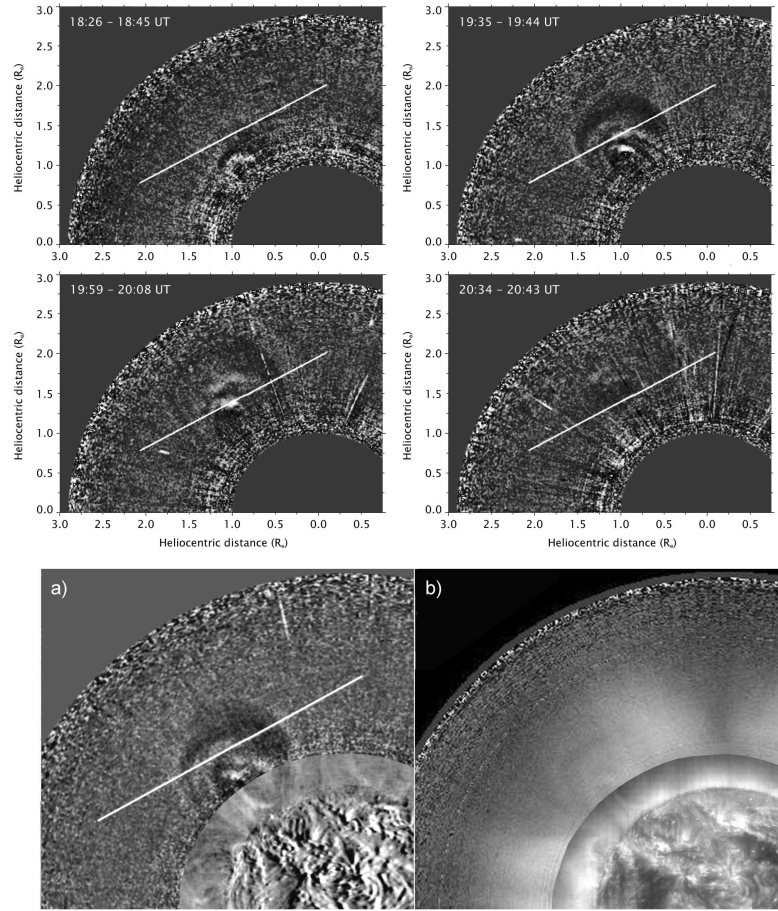


Figure 6.5: Top: a sequence of four Mauna Loa difference images (times are in each panel) showing the complex structure of the rising CME and the position of the UVCS slit at $1.6 R_{\odot}$. Bottom, a: composite image obtained by superposing a difference Mauna Loa image (19:23 – 19:32 UT) and an EIT Fe XII difference image (18:36 – 19:25 UT); b: the corresponding non-differenced images from Mauna Loa (19:23 UT) and EIT Fe XII (19:25 UT).

perature of formation of the emitting ion, from the ionization balance of Mazzotta et al. (1998).

The C II $\lambda 1065.7 \text{ \AA}$ line (absent at coronal levels) might help us correct lines for stray light contamination (see § 4.2.3); however, in our data this line is unobserved, hence the stray light contribution is negligible and the correction has not been made.

In Figure 6.6 (top and bottom left panels) we show the time evolution of the Ly α and O VI 1032 line intensities at different latitudes along the UVCS slit centered at $1.6 R_{\odot}$: in this Thesis we report only results from an analysis of data at this heliocentric distance, while data at $1.9 R_{\odot}$ are not discussed here because their analysis is still in progress. These images show the presence of some persistent

λ_{obs} (Å)	λ_{ID} (Å)	Ion	Transition	$\log T_{max}$
991.62	991.58	N III	$2s^2 2p^2 P_{3/2} - 2s 2p^2 D_{5/2}$	4.9
1025.69	1025.72	H I	Ly β	4.5
1028.04	1028.04	Fe X	$3s^2 3p^4 3d^4 D_{7/2} - 3s^2 3p^4 3d^4 F_{7/2}$	6.0
1031.90	1031.91	O VI	$1s^2 2s^2 S_{1/2} - 1s^2 2p^2 P_{3/2}$	5.5
1034.50	1034.48	Ni XIV	$3s^2 3p^3^4 S_{3/2} - 3s^2 3p^3^2 P_{3/2}$	6.2
1037.63	1037.61	O VI	$1s^2 2s^2 S_{1/2} - 1s^2 2p^2 P_{1/2}$	5.5
1041.04	520.66	Si XII	$1s^2 2s^2 S_{1/2} - 1s^2 2p^2 P_{1/2}$	6.3
1043.28	1043.29	Mg XI	$1s 2p^3 P_0 - 1s 2s^3 S_1$	6.9
1065.89	1065.89	C II	$2p^3^2 P_{3/2} - 2s 2p^2 D_{5/2}$	4.7
1215.67	1215.67	H I	Ly α	4.5

Table 6.1: Lines included in the UVCS spectral ranges.

features (visible as vertical “stripes”⁴) in the northward half of the slit, in particular at latitudes of about 56.9°N, 63.1°N and 67.8°N. By a comparison of these images with the top left panel of Figure 6.4 these three features can be identified with three radial structures observed by LASCO/C2 prior to the event at these latitudes. However it is difficult to identify in the left panels of Figure 6.6 the passage of the CME: at the CME latitudes (50 – 60°N) the data show only an approximately constant Ly α and O VI 1032 line intensity until \sim 18:30 UT, then a rapid decrease (respectively by about 30% and 40%), followed by some intensity fluctuations. Hence we do not observe, as expected, a sharp rise in the line intensities at the time the CME front enters the UVCS slit⁵. Considering that also in Mauna Loa intensity images the CME structure was hardly identifiable and we had to build difference images to enhance its visibility, we constructed “running differences” UVCS images, by subtracting, pixel by pixel, intensities of the i -th exposure from intensities of the $(i + 1)$ -th exposure. The results of this procedure applied iteratively over the whole dataset are given in the right panels of Figure 6.6 and show that UVCS is sequentially imaging the expanding CME bubble. The bright emitting knot imaged around 20:00 UT at a latitude of \approx 50 – 55° may represent the CME core, no longer visible at later times because already moved to higher levels. Around the core, the Ly α image shows the typical three part structure of the CME, and the leading edge and dark void are also clearly visible. A similar structure is observable in the O VI running difference image, but the CME core is hardly visible (we will come back later on this difference). We note also that, at later times, the Ly α CME image appears to be slightly “distorted” towards northward latitudes. This happens because, as already mentioned, the CME is deflected towards higher latitudes (i.e. moves along the UVCS slit) during observations.

The reason why the CME structures become visible only in UVCS running dif-

⁴As we discuss later, these are not due to an instrumental effect.

⁵This is better explained in the next Section.

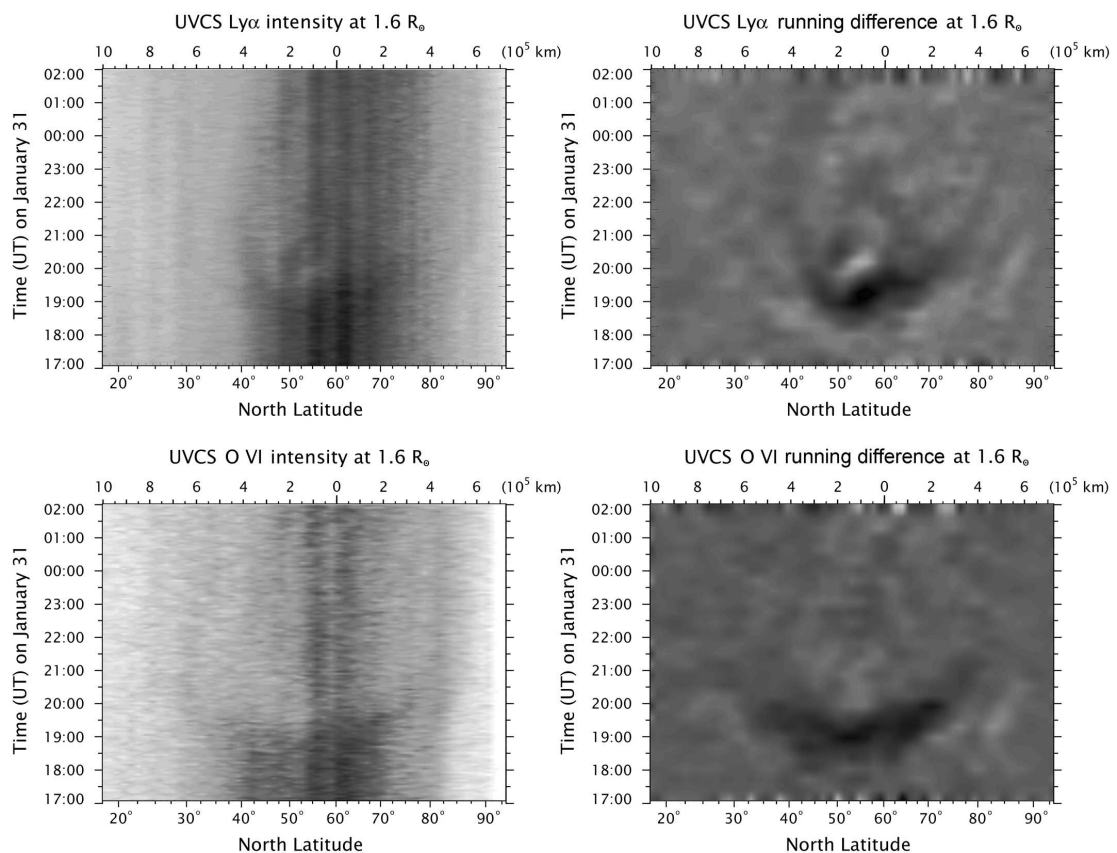


Figure 6.6: Top left: the Ly α intensity evolution along the UVCS slit (x axis) at different times (y axis) as observed at 1.6 R_{\odot} . Colors range from 0 (white) to $5.2 \cdot 10^{11}$ phot $\text{cm}^{-2}\text{s}^{-1}\text{sr}^{-1}$ (black). Top right: the Ly α running difference evolution at 1.6 R_{\odot} , colors from $-4 \cdot 10^{10}$ (black) to $+3 \cdot 10^{10}$ phot $\text{cm}^{-2}\text{s}^{-1}\text{sr}^{-1}$ (white). Bottom left: same as top left for the O VI $\lambda 1032\text{\AA}$ line, colors from 0 (white) to $3.1 \cdot 10^{11}$ phot $\text{cm}^{-2}\text{s}^{-1}\text{sr}^{-1}$ (black). Bottom right: same as top right for the O VI $\lambda 1032\text{\AA}$ line, colors from $-3 \cdot 10^9$ (black) to $+3 \cdot 10^9$ phot $\text{cm}^{-2}\text{s}^{-1}\text{sr}^{-1}$ (white).

ference images is their weak intensity: for instance, (as we show in Figure 6.7) the core structure in the Ly α line (intensity bump at about 20:00 UT) is only $\sim 10\%$ higher than the background emission, while is hardly identifiable in the O VI line. Nevertheless, in the following we will try to give an estimate of the plasma parameters in the different features of the CME from the observed UVCS line intensities. In particular, assuming a value for the elemental abundances, we have mainly the following unknown parameters which give rise to the observed line intensity: the electron density N_e , the electron temperature T_e , the outflow speed v_{out} and the extension along the LOS L of the emitting plasma. In the selected spectral intervals there are neither two lines from different ionization state of the same element nor two different lines emitted from the same ion (see Table 6.1), hence the line ratio techniques for the estimate of T_e (described in § 3.3.2) cannot be applied. Moreover,

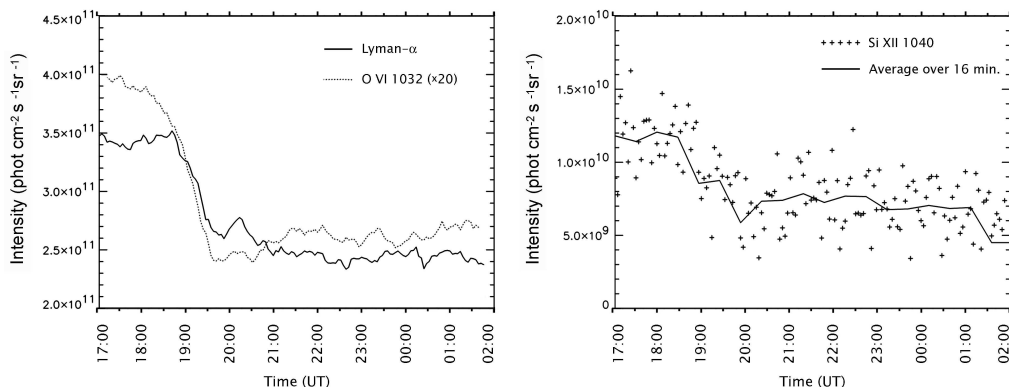


Figure 6.7: Left: the $\text{Ly}\alpha$ and O VI 1032 intensity evolution averaged over 10° around a latitude of 50°N . Note that both spectral lines show an intensity decrease (which correspond to the transit of the CME void), but only the $\text{Ly}\alpha$ line has a significant emission at the CME core (around $\sim 20:00$ UT); this is interpreted as a combination of temperature and Doppler dimming effects (see later). Right: the time evolution of the Si XII 1040 line (plus signs) and the average over 16 minutes (solid line) showing possibly a minimum at the time of the CME core transit.

the standard technique used to derive the electron density from the ratio between the O VI doublet lines (§ 3.3.3) holds only for negligible outflows, which is not the case for CMEs. Hence, in order to solve the problem, we resort to Mauna Loa pB measurements (as we describe in the next Section) to derive the CME electron density.

An estimate for the outflow speed v_{out} can be obtained from the observed ratio $R_{1032/1037}$ of the O VI $\lambda 1032$ to the $\lambda 1037 \text{ \AA}$ spectral line intensity (see § 3.3.6). However the line intensities are weak enough that errors affecting the line ratio make it impossible to distinguish between values within different CME structures. Averaging at the CME latitudes over the whole dataset we derived a value of $R_{1032/1037} \simeq 2.7$. We then built the profile of the $R_{1032/1037}$ intensity ratio vs. the plasma outflow speed v_{out} for an atmosphere with an electron density given by the GH profile (multiplied by a factor 6; this choice will be discussed in § 6.7) and a range of parallel and perpendicular temperature values (T_{\parallel} and T_{\perp} , see Figure 6.8); it turns out that a ratio $R_{1032/1037} \simeq 2.7$ corresponds to an outflow speed of $\approx 70 - 80$ km/s independently of the plasma parameters (see Figure 6.8). Because the CME features are faint with respect to the coronal background, this low value may not be representative of the CME outflow speed; as a consequence we used the pB observations for a better estimate of the outflow speed in the different CME structures.

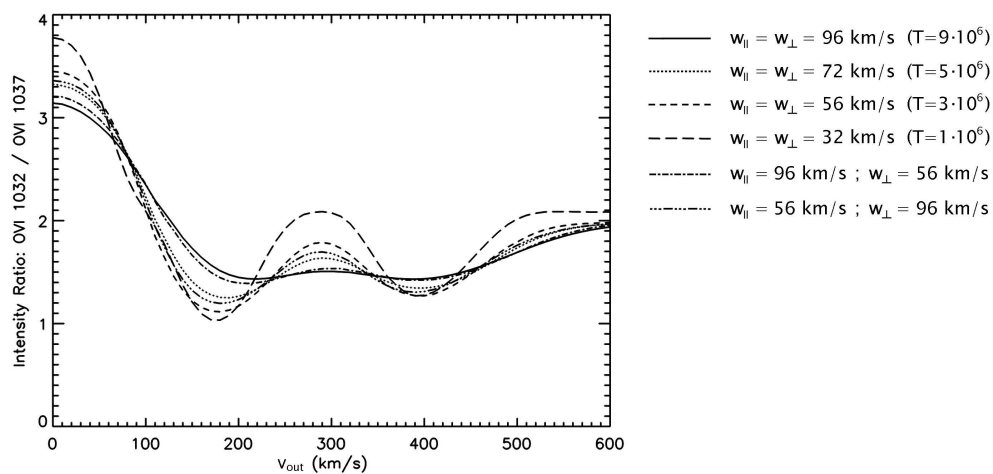


Figure 6.8: The computed ratio between O VI $\lambda 1032\text{\AA}$ and O VI $\lambda 1037\text{\AA}$ line intensities as a function of the outflow plasma speed v_{out} for different combinations of T_{\parallel} and T_{\perp} ($w = \text{sqrt}(2k_B T/m)$) obtained by computing the integral along the LOS at $1.6 R_{\odot}$ with the electron density profile of Guhatakurta & Holzer (1994) multiplied by a constant factor of 6 (see text).

6.5 Mark IV observations

The Mark IV K-Coronameter at the Mauna Loa Observatory acquires images of the low corona (700 – 1080 nm) from ~ 1.12 to $\sim 2.79 R_{\odot}$ using a 2048-element linear array (sampled to 384 pixels) aligned with the radial (projected on the plane of the sky) from the Sun center. The detector (160 pixels per solar radius) is rotated by 360° over a period of about 3 minutes acquiring data with an angular resolution of 0.5° ; from these data a 960×960 pixels image of the corona is then reconstructed. On January 31, 2000 the instrument acquired 91 exposures from 17:30 UT to 22:07 UT; the first 3 exposures are corrupted (contain negative pB values) and have not been used.

The Mark IV pB measurements are shown in Figure 6.9; in order to facilitate the comparison between data taken by different experiments, this Figure (left panel) shows the pB brightness measured at 1.6 solar radii by the Mark IV over a rectangular area that simulates the UVCS slit over the same timescale used for Figure 6.6 (UVCS observations cover a longer time interval than Mark IV data). Faint structures are better visible in the right panel of this Figure, where we show the running difference image obtained after accumulating the original data over 9 minutes (3 exposures) for a better statistics. Figure 6.9 (right panel) shows that the pB emission appears at positions along the slit which delineate branches, closely resembling the topology predicted by the Lin & Forbes (2000) model. The similarity between the pB and the $\text{Ly}\alpha$ images is not surprising: pB depends on the electron density and, for a fixed outward velocity and approximately constant electron temperature, the

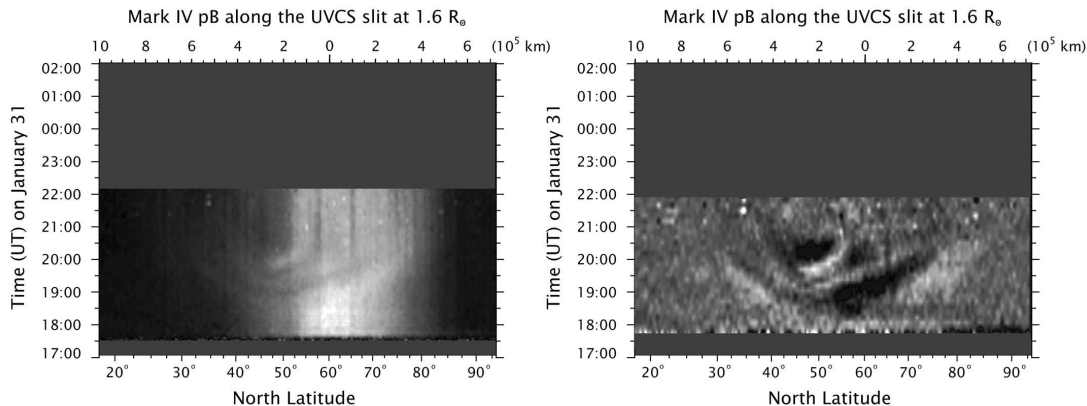


Figure 6.9: Left: the Mauna Loa Mark IV pB as measured along the position of the UVCS slit at $1.6 R_{\odot}$ (x axis) at different times (y axis). To facilitate a comparison between Mark IV pB and $\text{Ly}\alpha$ images (see Figure 6.6), pB data have been plotted on the same scale as the UVCS data; colors range from 0 to $8 \cdot 10^{-8}$ (in units of B_{\odot}^{-1}). Right: running difference image.

$\text{Ly}\alpha$ intensity is dictated by the electron density as well. Both pB and UVCS data show, until $\approx 18:30$ UT, a bright emission (between a northern latitude of ≈ 45 and 65°) which disappears after $\sim 19:00$ UT that (as we discuss later) we identify as the CME front material being ejected at later times. Moreover, we note that the pB image shows the same three background persistent structures we observed also in UVCS data (confirming us that these are not an instrumental effect) which represent the streamer structures visible in the pre-CME composite Mark IV and LASCO images of Figure 6.4.

In the next Sections we describe how, taking advantage of the Mark IV pB data, we evaluate the CME electron density N_e (§ 6.6 and 6.7) and the outflow speed v_{out} (§ 6.8); given N_e and v_{out} (which is used to derive the Doppler dimming factor), from a comparison of the predicted and the observed UV line intensities, we derived an estimate for the electron temperature T_e in the CME core, front and void (§ 6.9). Finally, from the density measurements, we derived an estimate for the mass of different CME features (§ 6.10).

6.6 Density diagnostics from white light observations

As we described in § 3.4, assuming a profile for the electron density $N_e(r)$, it is possible to compute from Equation 3.69 a value for the expected $pB(\rho)_{exp}$ at a given heliocentric distance ρ of observation; the latter has to be compared with the observed value $pB(\rho)_{obs}$. Because the Thomson scattering is more efficient at the angle of 90° , the main contribution to $pB(\rho)_{obs}$ arises from the coronal plasma close

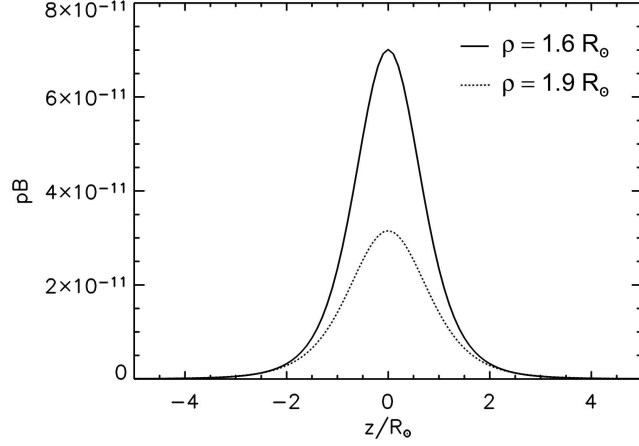


Figure 6.10: The contribution to the observed pB (assuming the Guhathakurta & Holzer, 1994 $N_e(r)$ profile) along the LOS at 1.6 (solid line) and 1.9 (dotted line) R_\odot .

to the plane of the sky. In particular, in Figure 6.10 we show the contribution from different regions along the LOS to the observed pB , as computed with equation 3.69 by assuming for $N_e(r)$ the Guhathakurta & Holzer (1994) profile (hereafter GH):

$$N_e(r)_{GH} = (1.4 \cdot 10^6) r^{-2.8} + (8.0 \cdot 10^7) r^{-8.45} + (8.1 \cdot 10^7) r^{-16.87} \quad (6.1)$$

In the computation we used the following expressions for the $A(r)$ and $B(r)$ functions (Altschuler & Perry, 1972):

$$\begin{aligned} A(r) &= \frac{1}{r^2} \sqrt{1 - \frac{1}{r^2}} \\ B(r) &= r [-B_1(r) + 3B_2(r)] \end{aligned} \quad (6.2)$$

where

$$\begin{aligned} B_1(r) &= \frac{1}{2} \left[\frac{1}{r} - \left(1 - \frac{1}{r^2}\right) \ln \left(\frac{1 + 1/r}{\sqrt{1 - 1/r^2}} \right) \right] \\ B_2(r) &= \frac{1}{8} \left[\frac{1}{r} + \frac{1}{r^3} - \left(1 - \frac{1}{r^2}\right)^2 \ln \left(\frac{1 + 1/r}{\sqrt{1 - 1/r^2}} \right) \right] \end{aligned} \quad (6.3)$$

and r (R_\odot) is the heliocentric distance. Figure 6.10 shows that, at distances z along the LOS from the plane of the sky larger than $\sim 1 R_\odot$ the contribution to the total pB becomes negligible. As a consequence, the main differences between the expected value $pB(\rho)_{exp}$ and the observed value $pB(\rho)_{obs}$ are due to changes in the electron density in a region close to the plane of the sky.

The above considerations led us to use the following method to evaluate the N_e in transient coronal structures. First, analyzing the pB coronal images, we choose a

region where no significant bright structures are visible and we evaluate the constant multiplier k of the $N_e(r)_{GH}$ profile we need to reproduce the observed pB . Then, we assume that, in coronal regions where isolated structures (e.g. streamers and/or CMEs) are present, the electron density profile along the LOS is:

$$\begin{aligned} N_e(z) &= k \cdot N_e(z)_{GH} & , \text{ if } |z| > L/2 \\ N_e(z) &= k \cdot N_e(z)_{GH} + \bar{N}_e & , \text{ if } |z| \leq L/2 \end{aligned} \quad (6.4)$$

where \bar{N}_e is the additional electron density that allows us (in a region centered on the plane of the sky with a length L (cm) along the LOS) to reproduce the observed pB . The length L is a free parameter that can be evaluated from the dimension projected onto the plane of the sky of the considered structure assuming an a priori geometry. The additional density \bar{N}_e is, in first approximation, inversely proportional to L , so that the product $\bar{N}_e L$ is nearly independent of the choice of L . This method yields an average electron density $\langle N_e \rangle$ in the structure given by:

$$\langle N_e \rangle = \frac{1}{L} \int_{-L/2}^{+L/2} [N_e(z)_{GH} + \bar{N}_e] dz \quad (6.5)$$

We note that, because the observed pB depends solely on N_e , no further assumptions are needed about the plasma physical parameters. In the next Section we describe results from applying this method to the pB data of our event.

6.7 Estimate of the CME electron density

The procedure described in the last Section has been applied pixel by pixel (along the position of the UVCS slit) to the region occupied by the CME, throughout the time interval covered by our observations. Before describing the results we obtained from this technique, we qualitatively discuss what can be inferred from observations. As we have shown in Figure 6.9, pB data reveal the presence of the bright knot CME core: because, in first approximation, the observed pB is proportional to the electron density, we may expect the core region to correspond to a plasma denser than the surrounding regions. However, after the transit of the CME front, the Ly α , O VI and Si XII line intensities decrease and a significant emission from the core is seen only in the Ly α line (see Figures 6.6 and 6.7). The radiative component of the O VI line can be Doppler dimmed, but its collisional component and the intensity of the Si XII line can be reduced (despite an increasing in electron density density) only by temperature effects. In particular, because the O VI and Si XII emissivities peak, respectively, at temperatures of $\log T = 5.5$ and $\log T = 6.3$ (see Figure 5.4), a decrease of the collisional component of both lines can be justified only by a temperature increase above $\log T = 6.3$; hence we may expect the core region to be denser and hotter than the surrounding plasma. In the following we will show how this conclusion is confirmed by our analysis.

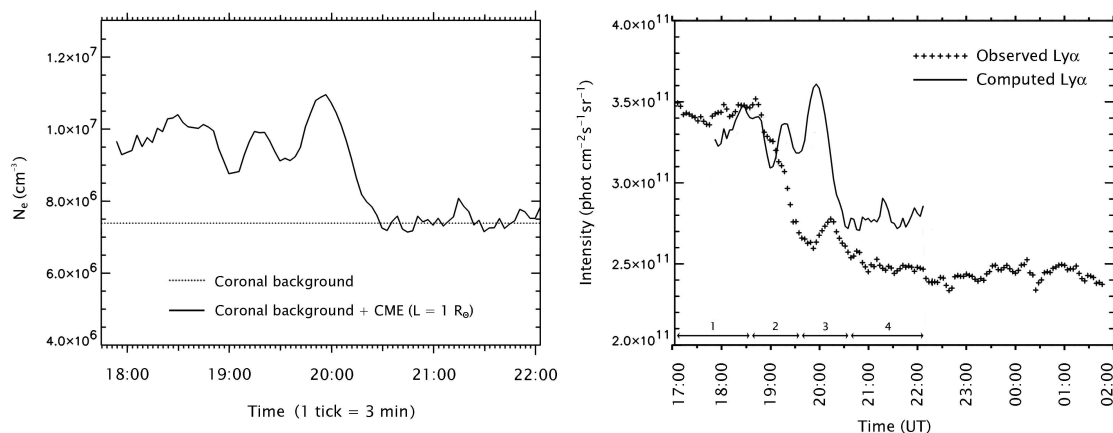


Figure 6.11: Left: the background plus additional electron density (solid) as computed (assuming an extension L along the LOS of $1 R_{\odot}$) from the Mark IV pB data as a function of time averaged over the CME latitudes. Values of \bar{N}_e can be obtained by subtracting to the solid curve the background constant density of $7.4 \cdot 10^6 \text{ cm}^{-3}$ (dashed line). Right: a comparison between the evolution of the observed Ly α intensity (cross signs) and the Ly α intensity as computed from the densities shown on the left, by assuming negligible outflows and a coronal plasma temperature of $T_e = 10^{6.15} \text{ K}$ (see text). Numbers at the bottom refer to what we identified as the CME front (1), void (2), core (3) and post-core (4) regions.

In Figure 6.11 (left panel) we show the results from the technique described in the last Section; in particular, in this Figure we give the coronal background electron density and the additional density \bar{N}_e we computed at the latitudes of the CME core as a function of time. The background pB has been reproduced by multiplying the GH density profile by a factor $k = 6$ (see equation 6.4), while the CME density has been derived by assuming an increased density \bar{N}_e over an extension along the LOS $L = 1 R_{\odot}$ centered on the plane of the sky. This assumption has been suggested by the average dimension projected onto the plane of the sky of the CME bubble (see Figure 6.9), which supposedly moves on that plane because we do not observe any significant line Doppler shift (we will discuss in § 6.11 the errors deriving from these assumptions). The computed \bar{N}_e values strongly depend on the selected L values; however, we note that the average Ly α emission (proportional to $N_e L$) does not significantly change, because a decrease in L is balanced by an increase in the computed \bar{N}_e and viceversa; hence the assumption of the L value does not significantly affect (in first approximation) the computed Ly α line intensity (uncertainties in this technique are discussed in § 6.11). The right panel of Figure 6.11 shows a comparison between the observed Ly α intensity and the intensity computed from the pB derived densities shown on the left panel of the same Figure: this will be discussed in § 6.9. We anticipate that the lack of agreement between the observed and reconstructed Ly α intensities in this Figure will be ascribed to the evolution of

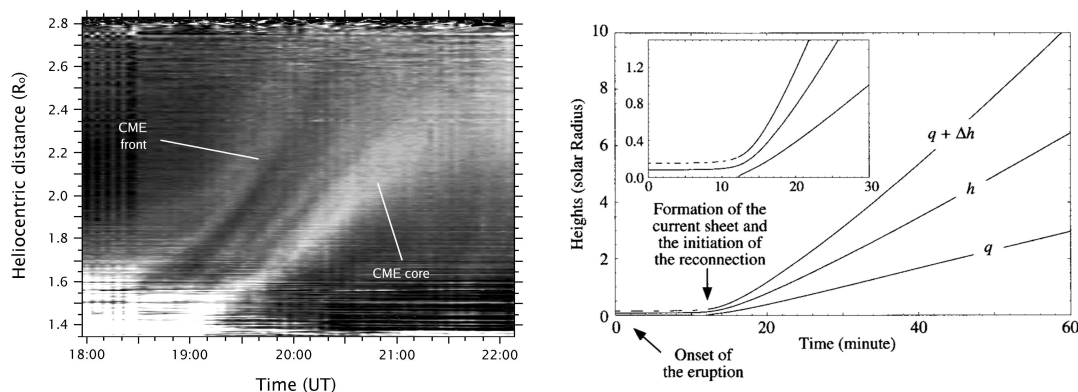


Figure 6.12: Left: altitude vs. time profile of the CME intensity (from Mauna Loa Mark IV data) integrated around the CME latitudes (see text). Right: altitude vs time plots of the CME front ($q + \Delta h$), core (h) and neutral rising point (q) in the Lin et al. (2004) CME model; note that this simulation refers to a fast CME ($v \simeq 1000$ km/s), hence rising speeds of different CME features are higher than those of our slow event.

plasma parameters throughout the CME (§ 6.9).

6.8 Estimate of the CME outflow speed

As we mentioned above, from the Doppler dimming technique we cannot distinguish between the outflow speeds v_{out} of different CME structures because these are relatively faint with respect to the coronal background. However, when trying to reproduce the line intensities observed by UVCS, an estimate for v_{out} is mandatory because both Ly α and O VI line intensities may have been significantly Doppler dimmed. Hence, we assumed the outflow speed to be the same as the CME rising speed; this has been derived from the pB data by integrating in each exposure the observed intensity over the CME latitudes and subtracting the average coronal intensity in the whole dataset. The resulting image (Figure 6.12, left panel) shows the presence of different CME substructures expanding at different speeds. Analogous variations in the rising speed of different parts of a CME has been found, e.g., by Lin et al. (2005). We note that the speed of the CME front increases from ~ 30 km/s at $1.6 R_{\odot}$ (18:30 UT) up to ~ 160 km/s at $2.6 R_{\odot}$ (20:00 UT), while the speed of the brighter CME core (possibly after slightly accelerating below $1.6 R_{\odot}$) shows a large spread of values between 70 – 100 km/s, but no significant acceleration. The secondary substructures in between the accelerating CME front and the core seem to move at intermediate speeds. We point out that the CME front seems to start rising at a heliocentric distance of about $1.6 R_{\odot}$ (i.e. the height of the UVCS slit). This may explain why we do not see the arrival of the CME front onto the UVCS slit (i.e. a sudden increase in the line intensities) and we see only an intensity decrease preceding the arrival of the CME core: at the beginning of our observations the

front material is probably “in equilibrium” at the height of the UVCS slit. Hence, this material is ejected outward and we see an intensity decrease because of the plasma electron density decrease at this height. We note that some CME models predict that the front material has to be at an heliocentric distance of $\leq 1.2 R_{\odot}$ before it starts accelerating (Figure 6.12, right panel); however, because we have no Mauna Loa observations before 17:30 UT (or before 17:42 UT, taking into account the poor quality of the first exposures), we cannot definitely provide the height of the front material at earlier times.

6.9 Estimate of the CME electron temperature

Given the a priori chosen L value and the electron density N_e and plasma outflow speed v_{out} , we may compute the expected Ly α , O VI and Si XII line intensities as a function of T_e : a comparison of the predicted and the observed intensities allows us to infer the electron temperature of the plasma. However, the Si XII is a second order line and, because of the large uncertainties in the estimate of its intensity (see Figure 6.7, right panel), cannot be used to infer temperatures, while the Ly α and O VI line intensities have a better signal to noise ratio. Both these spectral lines may have a radial and a collisional component; however, at typical coronal temperatures ($T \sim 10^6$ K), collisional excitation would give a ratio between the Ly β and Ly α intensities on the order of ~ 0.13 – 0.14 , while for resonant scattering a much lower ratio (~ 0.001 – 0.002) is expected (see e.g. Raymond et al., 1998a). Because in our data the observed $I(Ly\beta)/I(Ly\alpha)$ ratio is on the order of ~ 0.004 and ~ 0.002 , respectively at the beginning and at the end of UVCS observations, we can safely assume that the observed Ly α emission arises almost entirely from radiative excitation, making it easier to estimate the expected Ly α intensity $I_{exp}(Ly\alpha)$. Moreover, possible uncertainties in the v_{out} values do not sensibly affect the computed $I_{exp}(Ly\alpha)$ for $v_{out} \leq 100$ km/s (see Figure 3.7). Hence, the computation of the Ly α intensity is easier than that of the O VI line, for which we have to compute both the radiative and collisional components and the estimate of the Doppler dimming factor is more critical. For these reasons we infer temperatures from the Ly α intensity, while we use the O VI and Si XII line intensities for a consistency check.

In order to compare the observed line emissions with those computed from the CME region, we need to evaluate the contribution from the external corona behind and in front of it along the LOS. To this end, it is necessary to assume a background density profile, electron temperatures, outflow speeds and disk intensities. In agreement with the results from the technique we used to derive N_e , we assumed the electron density profile given by equation 6.1 and multiplied by a factor 6; the electron temperature has been assumed to be constant along the LOS and equal to the kinetic temperature of $10^{6.15}$ we derived from Gaussian fits to the Ly α line profile (see later); as a typical outflow speed we assumed a value of ≈ 100 km/s constant along the LOS and for the disk intensities we used the same values estimated for

CME region	front (1)	void (2)	core (3)	post-core (4)
	Observed line intensities (phot cm ⁻² s ⁻¹ sr ⁻¹)			
I(Ly α) (10 ¹¹)	3.5 \pm 0.1	2.6 \pm 0.1	2.8 \pm 0.1	2.5 \pm 0.1
I(O VI 1032) (10 ¹⁰)	1.9 \pm 0.1	1.2 \pm 0.1	1.2 \pm 0.1	1.2 \pm 0.1
I(Si XII 1040) (10 ¹⁰)	1.2 \pm 0.2	0.8 \pm 0.1	0.7 \pm 0.1	0.8 \pm 0.1
	Computed line intensities (phot cm ⁻² s ⁻¹ sr ⁻¹)			
I(Ly α) ^{CME}	1.8 \cdot 10 ¹¹	1.1 \cdot 10 ¹¹	1.2 \cdot 10 ¹¹	9.5 \cdot 10 ¹⁰
I(Ly α) ^{TOT}	3.4 \cdot 10 ¹¹	2.7 \cdot 10 ¹¹	2.8 \cdot 10 ¹¹	2.6 \cdot 10 ¹¹
I(O VI 1032) _{rad} ^{CME}	3.8 \cdot 10 ⁹	2.0 \cdot 10 ⁹	6.0 \cdot 10 ⁸	7.6 \cdot 10 ⁸
I(O VI 1032) _{col} ^{CME}	7.2 \cdot 10 ⁹	2.7 \cdot 10 ⁹	1.9 \cdot 10 ⁹	1.7 \cdot 10 ⁹
I(O VI 1032) _{tot} ^{CME}	1.1 \cdot 10 ¹⁰	4.7 \cdot 10 ⁹	2.5 \cdot 10 ⁹	2.5 \cdot 10 ⁹
I(O VI 1032) ^{TOT}	1.9 \cdot 10 ¹⁰	1.2 \cdot 10 ¹⁰	1.0 \cdot 10 ¹⁰	1.0 \cdot 10 ¹⁰
I(Si XII 1040) ^{CME}	8.4 \cdot 10 ⁹	6.5 \cdot 10 ⁹	4.7 \cdot 10 ⁹	3.9 \cdot 10 ⁹
I(Si XII 1040) ^{TOT}	1.0 \cdot 10 ¹⁰	9.0 \cdot 10 ⁹	7.0 \cdot 10 ⁹	6.0 \cdot 10 ⁹
	Plasma parameters			
N_e (cm ⁻³)	1.0 \cdot 10 ⁷	9.4 \cdot 10 ⁶	1.1 \cdot 10 ⁷	7.4 \cdot 10 ⁶
log T_e	6.30	6.40	6.45	6.40
v_{out} (km s ⁻¹)	30	50	80	80

Table 6.2: Ly α , O VI 1032 and Si XII 1040 line intensities observed and computed in the CME front, void, core and post-core (see text). For a discussion of the uncertainties in the computed values see later §6.11.

the June 2000 quadrature observations (see discussion in § 5.5.3). We then assumed that the measured intensities derive from a background coronal emission plus a CME emission, originating from a region centered on the plane of the sky and extending over a length $L = 1 R_{\odot}$ along the LOS. The Ly α , O VI 1032 and Si XII 1040 line emissions we computed (by using equations 3.47 and 3.51) from the background corona along the LOS at 1.6 R_{\odot} turn out to be respectively $1.6 \cdot 10^{11}$, $7.7 \cdot 10^9$ and $2.0 \cdot 10^9$ phot cm⁻²s⁻¹sr⁻¹. In order to reproduce the observed intensities, these values have to be added as a constant background to the line intensities estimated for the CME region.

We started our computations at the CME front: in this region, by assuming an outflow speed of ~ 30 km/s (as suggested by the Mauna Loa pB observations, see Figure 6.12) and by using values for the fraction of neutral hydrogen atoms as a function of temperature given by the CHIANTI spectral code (v. 5.0), the

observed Ly α intensity of $3.5 \cdot 10^{11}$ phot cm $^{-2}$ s $^{-1}$ sr $^{-1}$ is reproduced provided the average electron temperature in the CME region is $\log T_e = 6.3$. At later times, the right panel of Figure 6.11 shows that the Ly α intensities computed from the electron densities we derived, assuming the same temperature and outflow speed we assumed in the CME front, are significantly different from the observed values. Hence, it is necessary to assume different values of T_e and v_{out} in order to reproduce the intensities observed at later times. Taking advantage of the outflow speeds measured from Mauna Loa data, we infer the electron temperature we need to reproduce the observed Ly α intensities after the transit of the CME front.

Results from this computation are given in Table 6.2; the outflow speed of the plasma in the CME void is assumed to be an average between the front and core speeds (see Figure 6.12, left panel), while for the post-core region the value is uncertain because there are no visible pB structures in this region and we assumed the same speed as that of the CME core. In this Table, errors in the observed intensities (derived from the number of observed counts by taking into account the averages we made over spatial bins and exposures) are on the order of 2%, 5% and 18% respectively for Ly α , O VI and Si XII intensities starting from $\sim 20:00$ UT throughout the whole dataset, while we derived slightly smaller errors at earlier times when all the line intensities are larger (errors in the derived plasma parameters are discussed later in § 6.11). Numbers (1) – (4) in the first row of Table 6.2 correspond to the regions given at the bottom of Figure 6.11 (right panel); segments in this Figure also show the time intervals over which we computed the average observed intensities and plasma parameters given in Table 6.2. Once the Ly α intensities have been reproduced with the appropriate plasma temperatures, we computed as a consistency check, the O VI and Si XII line intensities using the line emissivities given by the CHIANTI spectral code. As a free parameter we have the oxygen and silicon abundances, that we assumed to be equal to the value we derived in coronal streamers (observed only five months later) of $\log N(O) \sim 8.7$ and $\log N(Si) \sim 7.7$ (see Tables 5.5 and 5.6). Values in Table 6.2 show a good agreement (i.e. within the errors of the observed intensities) between the computed and observed O VI and Si XII intensities. Temperatures in Table 6.2 point towards higher values in the CME structures with respect to the surrounding coronal plasma; in particular, the core region turns out to have a temperature of about $2.8 \cdot 10^6$ K, hence a factor 2 higher than the $1.4 \cdot 10^6$ K background corona and $\sim 40\%$ higher than the plasma temperature in the CME front. This corresponds to the temperature increase we expected from the observed time evolution of the O VI and Si XII line intensities, as we qualitatively discussed at the beginning of § 6.7.

We note that the temperature increase at the CME void and core is further supported by an analysis of the O VI 1032 line profiles: the kinetic temperatures we derived from the line profile Gaussian fits are on the average $\sim 25\%$ larger in the CME void and core regions than in the CME front (see Figure 6.13); larger temperature variations in the CME regions may be hidden in the average coronal plus CME line profile. This Figure shows also that we do not observe significant variations

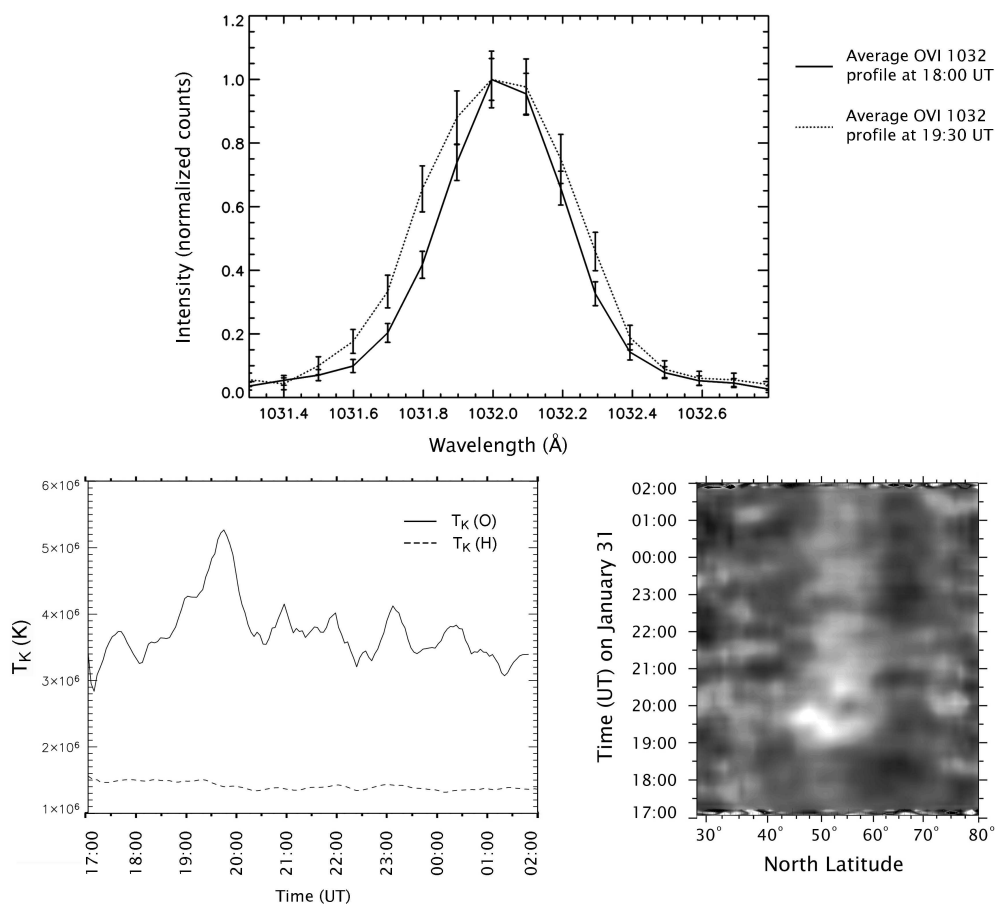


Figure 6.13: Top: a comparison between the normalized O VI 1032 line profiles at two different times (averaged over 4 spatial bins around the latitude of $\simeq 50^\circ\text{N}$ and 4 exposures) showing a $\sim 25\%$ line broadening between the CME void and core. Bottom left: the evolution at the CME latitudes of the hydrogen (dashes) and oxygen (solid) kinetic temperatures as derived from Gaussian fits of the O VI 1032 and Ly α line profiles. Bottom right: the evolution along the UVCS slit (i.e. at different latitudes) of the oxygen kinetic temperatures; colors range from 3 (black) to $5 \cdot 10^6$ K (white).

in the average hydrogen kinetic temperature, which keeps nearly constant around $1.4 \cdot 10^6$ K. This can be interpreted as follows: as we discussed above, the Ly α emission is due only to the radiative excitation, while (partly because of the larger O VI Doppler dimming), the O VI emission arises mainly from collisional excitation⁶. Because the collisional and radiative components are crudely proportional to N_e^2 and N_e respectively, the O VI line profile is much more affected than the Ly α profile by the larger density regions, such as those of the CME.

⁶For instance, our calculations (see Table 6.2) show that the radiative component of the O VI intensity in the core region is only $\sim 24\%$ of the total intensity.

6.10 Mass of the CME

The mass of the different parts of the CME can be estimated by assuming that the additional electron density \bar{N}_e derived from the pB data is representative of the CME density. Because the CME 3D geometry is unknown, the derived values will give only the order of magnitude of the real CME mass and depend on the assumed geometry.

From Figures 6.6 and 6.9 we see that (projected onto the plane of the sky) the bright CME core has a typical radius on the order of $r_{core} \simeq 0.1 R_\odot \simeq 7 \cdot 10^4 \text{km}$. In order to infer the mass of the core we assumed either a) a high density spherical blob of plasma with radius r_{core} , or b) a cylindrical structure with base surface πr_{core}^2 extending over a depth of one solar radii along the LOS and crossing the plane of the sky. In the spherical geometry the core extends along the LOS over $0.2 R_\odot$ and the additional electron density \bar{N}_e we computed to reproduce the observed pB is in this case about five times larger than density previously computed (Figure 6.11), so that the product $N_e L$ keeps approximately constant; in this geometry we estimate a core mass of $\sim 4 \cdot 10^{13} \text{g}$. In the cylindrical geometry ($L=1 R_\odot$) the additional density is on the order of $\bar{N}_e = 3.5 \cdot 10^6 \text{cm}^{-3}$ (see Figure 6.11 and Table 6.2); hence, in this second geometry, the core turns out to have a mass of $\sim 6 \cdot 10^{13} \text{g}$.

In order to derive the mass of the CME front we assumed either a) an hemispherical shell surrounding the core with thickness and internal radius of $2 \cdot 10^5 \text{km}$, or b) a semicircular sheath with thickness and internal radius of $2 \cdot 10^5 \text{km}$ extending along the LOS over $1 R_\odot$ (see Figure 6.6 and 6.9). Starting from an additional density $\bar{N}_e \simeq 2.7 \cdot 10^6 \text{cm}^{-3}$ (see Figure 6.11 and Table 6.2), the front mass in the two geometries turns out to be respectively (a) $\sim 5 \cdot 10^{14} \text{g}$ or (b) $\sim 6 \cdot 10^{14} \text{g}$.

As for the CME void in between the front and the core, by assuming the shape of an hemispherical shell with internal radius of $7 \cdot 10^4 \text{km}$ and thickness of $1.3 \cdot 10^5 \text{km}$, with an additional density of $2 \cdot 10^6 \text{cm}^{-3}$ we derive a mass of $\sim 5 \cdot 10^{13} \text{g}$, while with a semicircular sheath with the same thickness extending along the LOS over $1 R_\odot$ the mass turns out to be $\sim 1 \cdot 10^{14} \text{g}$. In conclusion, the total CME mass we estimate is on the order of $6 - 8 \cdot 10^{14} \text{g}$ depending on the adopted geometry; this mass resides mostly in the CME front surrounding the core, while the mass of the core is less than 10% of the total CME mass.

6.11 Uncertainties in the CME parameters

In this Section we give an estimate of the uncertainties which may affect the values we inferred for the plasma density and temperature. In the technique we used to derive densities from the observed pB there are two major unknown parameters: the extension L along the line of sight of the region with an additional density \bar{N}_e and the position with respect to the plane of the sky where this region is centered. All the results we have shown (except for the core mass in spherical geometry) have been derived by assuming $L = 1 R_\odot$ and $\theta_{CME} = 0$ (where θ_{CME} is the angle,

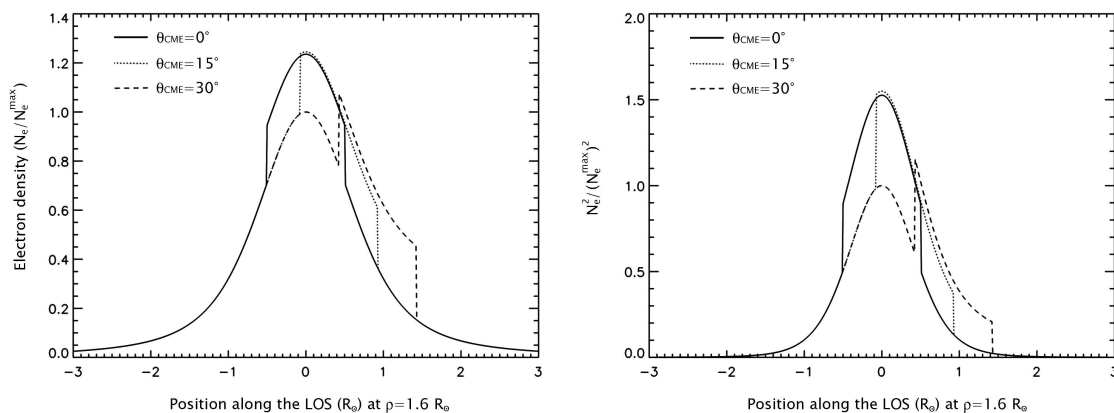


Figure 6.14: Left: typical electron density profiles (normalized to the maximum density value N_e^{max} on the plane of the sky at the position 0 on the x axis) along the LOS at $1.6 R_\odot$ computed with the region of additional density ($1 R_\odot$ long) centered on the plane of the sky (solid line), and centered at angles θ_{CME} of 15° (dotted), 30° (dashed) from this plane. Right: typical squared electron density profiles (same symbols as in the left panel) used to compute the emission measure $EM = \int_{LOS} N_e^2 dz$; these curves show that the EM value does not significantly change for different θ_{CME} values.

measured from the plane of the sky, where the region with additional density \bar{N}_e is centered along the LOS); in the following we discuss how changes in L and θ_{CME} affect the derived parameters.

As we mentioned, the assumption $\theta_{CME} = 0$ has been suggested by the observation of no significant Doppler shifts in the UVCS Ly α line profiles (i.e., the wavelength shift, if any, is $\leq 0.1 \text{ \AA}$, which is the spectral binning of our data). However, if the region with the enhanced density is centered at angles $\theta_{CME} = 15^\circ$ and 30° from the plane of the sky we find (along the LOS at $1.6 R_\odot$) an increase in the \bar{N}_e value respectively by 4% and 28%. Hence, the value $\bar{N}_e = 2.7 \cdot 10^6 \text{ cm}^{-3}$ for $\theta_{CME} = 0$ (see Figure 6.11, right panel) increases to $\bar{N}_e = 2.8 \cdot 10^6 \text{ cm}^{-3}$ and $= 3.5 \cdot 10^6 \text{ cm}^{-3}$ respectively at $\theta_{CME} = 15^\circ$ and 30° . However, the change in the background plus CME density is small, as shown in the left panel of Figure 6.14: as a consequence, the $\int_{LOS} N_e dz$ changes from the value computed with $\theta_{CME} = 0^\circ$ only by $\sim 0.3\%$ and $\sim 3\%$ respectively with $\theta_{CME} = 15^\circ$ and 30° , while at these angles the $\int_{LOS} N_e^2 dz$ changes by $\sim 3\%$ and 9% . We conclude that variations in the θ_{CME} value do not sensibly affect the computed values of the line intensities (hence the derived temperatures), at least in the simple approximation we made that the CME plasma is isothermal along the LOS and the background atmosphere has a constant temperature. On the contrary, the computed CME masses will increase with \bar{N}_e as θ_{CME} increases; in order to constrain the θ_{CME} values simulations of the overall profile originating from a superposition of the background atmosphere and a CME propagating at different angles are in progress. Because the line profiles do not show significant Doppler shift, we expect to be able to constrain the θ_{CME}

values (hence the CME mass) given the observed CME rising speed.

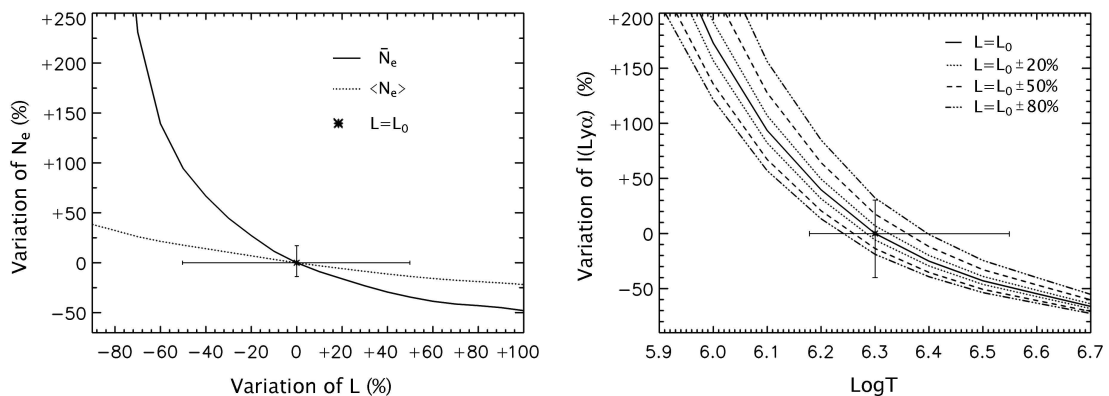


Figure 6.15: Left: the computed variations (%) of the electron density $\langle N_e \rangle$ (dotted curve, average background plus CME density along the LOS) and of the additional density \bar{N}_e (solid curve) as a function of variations (%) in the length L along the LOS of the CME region. Right: variations (%) in the computed $Ly\alpha$ intensity as a function of $\log T$ for different values of L (see text).

The assumption of $L = 1 R_\odot$ has been suggested by the observed extension (projected onto the plane of the sky) of the CME bubble (see Figures 6.6 and 6.9) which we assumed to be representative also of the CME extension in the direction perpendicular to the plane of the sky. The left panel of Figure 6.15 shows the variations in the computed electron densities as a function of the assumed length L along the LOS of the region with additional density \bar{N}_e . Let us assume, for instance, that with $L = L_0$ we derived a value of $\langle N_e \rangle = \langle N_e \rangle_0$ for the electron density, and that the computed $Ly\alpha$ intensity $I(Ly\alpha) = I(Ly\alpha)_0$ reproduces the observed value with a temperature in the CME region of $T = 10^{6.3}$ (data points in the two panels of the Figure). Hence, the left panel of Figure 6.15 shows that, by assuming for instance an error of 50% on the L value (so that $L = L_0 \pm 50\%$), we have $\langle N_e \rangle = \langle N_e \rangle_0 \pm_{20\%}^{15\%}$. The corresponding error in the estimate of the $Ly\alpha$ intensity is $I(Ly\alpha) = I(Ly\alpha)_0 \pm_{40\%}^{30\%}$ (because $I(Ly\alpha) \propto L \cdot N_e$) and from the right panel of Figure 6.15 we see that this uncertainty corresponds to $\log T = 6.3 \pm_{0.1}^{0.25}$ on the temperature value (see error bars in Figure 6.15, right panel). We note that with this uncertainty all CME temperatures may be either under or overestimated, hence temperature differences between different structures will be maintained and the general trend of higher temperatures at the CME void and core is still valid.

The a priori chosen value of L may significantly affect the derived value of the additional density \bar{N}_e , and the computed CME mass. However, as shown by the solid curve of Figure 6.15 (left panel), changes in the L value are balanced by changes in \bar{N}_e , so that the product $L \cdot \bar{N}_e$ keeps approximately constant. As a consequence, larger \bar{N}_e values correspond to smaller values of the volume occupied by the CME (because of the reduced length L along the LOS) and the variation in the computed

mass for $L = L_0 \pm 50\%$ are on the order of only $\pm 5\%$.

6.12 Discussion and conclusion

In this work we studied the early evolution of a CME which occurred on January 31, 2000, with the aim of inferring the structure of the CME in the early stage of its development. Mauna Loa white light and UVCS UV data allowed us to reconstruct the CME configuration: a comparison of the observed structure with that predicted by the Lin & Forbes (2000) CME model shows the two to be quite similar. In particular, it has been possible to identify, less than one hour after its initiation, the typical three parts of a CME (front, void and core) both in white light and UV data. From the pB data we derived the electron densities in these structures: their pB contrast with respect to the background has been reproduced by increasing the electron densities respectively by 35% and $\sim 50\%$ over the average background coronal density for the CME front and core. From these densities we tentatively derived the mass of different CME structures, by assuming some simple geometries for their 3 dimensional shape. It turns out that at $1.6 R_\odot$ the total mass we compute is $6 - 8 \cdot 10^{14}$ g. This value is on the small side with respect to more typical CME masses of $\approx 10^{15} - 10^{16}$ g; however, as pointed out by Lin et al. (2004), the mass of a CME increases with increasing heliocentric distances, because of the progressive reconnection of new fieldlines around the CME bubble. In the Lin et al. scenario, most of the CME mass ($\sim 80\%$) is added shortly after the onset of reconnection, hence it is possible that the mass value we derive is representative only of the initial mass of a CME in the early phase of its development. The total mass of this CME (as derived at higher levels from LASCO/C3 images ⁷) is about $2.1 \cdot 10^{15}$ g, hence a factor ~ 3 larger than the mass we derive at $1.6 R_\odot$. The mass of each CME measured by LASCO images increases with time also because of the partial filling in the telescope FOV and the value of $2.1 \cdot 10^{15}$ g derived by LASCO corresponds to the upper limit value reached before the CME starts leaving the LASCO field of view; hence a CME mass at $1.6 R_\odot$ of 1/3 of the total mass measured at higher levels seems to be realistic.

An interesting result we derived is the temperature variation across different CME structures, in particular a temperature higher by factors 1.4, 1.8 and 2.0 than the surrounding $1.4 \cdot 10^6$ K corona respectively in the CME front, void and core. This behaviour, also confirmed by the variations of the oxygen kinetic temperatures, is opposite to what envisaged by the Lin, Raymond & Van Ballegoijen (2004) model (see Figure 6.3 where darker colors indicate higher temperatures in the CME bubble), where plasma in the outer layers of the CME bubble, being the latter to be reconnected at the top of the current sheet, is expected to be hotter (i.e. temperatures decrease from the external bubble shells towards the CME core).

At the low heliocentric distance of $1.6 R_\odot$ we are dealing with plasma heating

⁷See LASCO CME catalog on <http://cdaw.gsfc.nasa.gov/CMEJist/>

cannot be provided by a shock as the speed of the CME front is too small. The sound speed $v_s = \sqrt{\gamma p/\rho} = \sqrt{(5/3)k_B T_e/m_H}$ in the corona at the temperature given above is about 140 km/s, while the Alfvén speed $v_A = B/\sqrt{\mu\rho} = B/\sqrt{8\pi N_e m_H}$ is on the order of 570 km/s for a 1 Gauss magnetic field and an electron density of $7.4 \cdot 10^6 \text{ cm}^{-3}$; hence the CME front moves at a sub-sonic and sub-alfvénic speed. In case of plasma heating by a simple adiabatic compression we expect the product $\Gamma = T_e N_e^{1-\gamma} = T_e/N_e^{2/3}$ to be nearly constant. Because $\Gamma_{coronal}/\Gamma_{front} \simeq 0.9$, as we computed with electron density and temperature values given in Table 6.2 for the CME front and with density and temperature given above for the external corona, we may conclude that, within the uncertainties, plasma heating at the CME front is provided in first approximation by an adiabatic compression. On the contrary, different processes have to be invoked in order to explain the observed plasma heating at the CME void and core; further analysis on this issue is at present in progress.

Chapter 7

Post–CME current sheet evolution

7.1 Introduction

In the previous Chapter we have shown that the three-part configuration of a CME can be detected in the low corona, at altitudes lower than $2 R_{\odot}$. Independently of the mechanisms that modelers invoke to explain what causes the CME events and to model the field restructuring and accompanying features, there is a general consensus about magnetic reconnection playing a fundamental role in the whole process. Models may be briefly classified either as catastrophe, or flux-rope models (see, e.g., Lin & Forbes, 2000) and non-flux-rope models, e.g. breakout (Antiochos et al., 1999) or shearing arcade models (Mikić & Linker 1994). In the latter, reconnection may be the cause of the initial instability and may eventually lead to the formation of a flux-rope. In the catastrophe models, a current sheet (hereafter CS) is envisaged, extending from the top of the reconnected loop system to the plasma bubble that surrounds the flux rope: reconnection provides for both the chromospheric/coronal features (separating bright ribbons, growing loop system) and the interplanetary phenomena (ejection of the plasma bubble). Figure 7.1 is a cartoon illustrating the flux rope model of Lin & Forbes (2000).

In the work illustrated in the previous Chapter we had no evidence for the presence of a CS: possibly at these early stages the CS was still below the UVCS observing altitudes. Direct observations of a CS during a CME event would contribute relevant information to modelers, but because a CS is supposed to be thin, its detection is quite difficult. Moore et al. (1995) infer a thickness of 800 to 8000 km for the reconnecting “wall” in a large solar flare. Ciaravella et al. (2002) and Ko et al. (2003) assume a CS depth, in a post-CME event, on the order of $\approx 10^5$ km, from the width of a bright, high temperature emitting region. This size is consistent with the thickness l that can be inferred from the Sweet-Parker relationship $l = h \times M_A$ (where M_A is the Alfvénic Mach number equal to the ratio of the inflow speed to the local Alfvén speed) assuming a sheet length h of ≈ 5 solar radii and $M_A = 0.03$, which appears to be the peak value M_A attains minutes after the CME onset (see Webb et al., 2003, and references therein). This is probably an upper limit

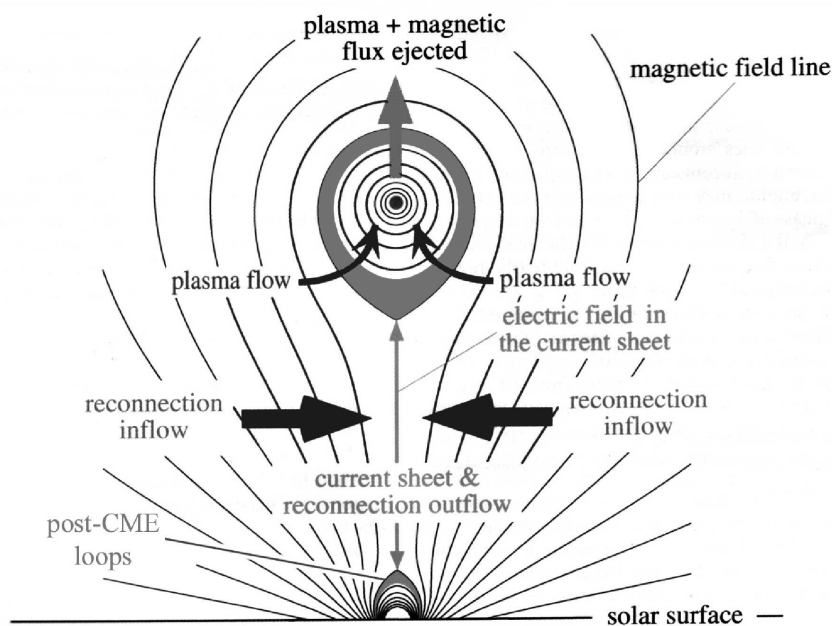


Figure 7.1: The CME/flux rope configuration from Lin & Forbes (2000). The position of the post-CME loops (see text) is also shown.

to the thickness of the CS and what is appropriate at later times cannot be easily predicted: while h is going to increase M_A decreases and these processes compete in determining the actual size. These values are much larger than those obtained by assuming that the reconnecting region has the typical size of elementary flux tubes (see, e.g., Sturrock et al., 1984) and show that the CS characteristics are still far from being identified.

Recently there have been reports of CS detections in the extended corona, from observations acquired in the wake of CME events by UVCS and LASCO (see, e.g., Ciaravella et al., 2002; Ko et al., 2003; Raymond et al., 2003). CSs have been identified in UVCS data from the presence of emission from unusually high temperature ions; typically this emission lasts for many hours, although a case for short lived (\sim minutes) has been presented by Raymond et al. (2003). In the white light LASCO images CSs correspond in general to ray like bright structures; similar ray like features have been found by Webb et al. (2003) in *Solar Maximum Mission* data in association with “disconnection events” associated with CMEs and have been ascribed to CS as well.

7.2 The goal of our observations

In the work presented here we focus on analyzing UVCS data acquired in the aftermath of a CME which occurred at \sim 17:00 UT on November 26, 2002. Because the

grating position we used allowed us to observe high temperature lines, which may form in a Current Sheet (CS), we aimed at identifying the CS and give its physical parameters. Then, because we have data for more than two days, we derived the evolution with time of the CS: this has been so far not observed and the knowledge of the temporal profile of the CS temperature, for instance, may help theoreticians develop realistic models for the behavior of the CS in the late stages of the CME event. Our observations have been taken at the time of a Sun-Ulysses-SOHO quadrature, that is at the time when the Sun-SOHO-Ulysses angle is $\simeq 90^\circ$. We have already illustrated in Chapter 5 the reason why this geometry is important (§ 5.2): instruments on Ulysses measure the properties of the solar wind plasma (Solar Wind Observations Over the Poles of the Sun [SWOOPS]) and magnetic field (Vector Helium Magnetometer and Fluxgate Magnetometer [VHM/FGM]) and, most importantly, the composition and ionization state (Solar Wind Ion Composition Spectrometer [SWICS]). Hence, this special configuration gave us the opportunity of checking whether signatures of the CME could be found in Ulysses data at ≈ 4.3 AU. As we will see, our study was successful as we have been able to identify the CS, separate its emission from that of the ambient corona, and give the evolution with time of the physical parameters of the CS. Order-of magnitude estimates of flow into the CS and the behavior of the density in the region surrounding the CS are also given. Moreover, we identified the CME signature in Ulysses *in situ* data, establishing an unambiguous correspondence between coronal and *in situ* CME parameters.

7.3 The November 2002 CME scenario

In the following, we illustrate the coronal configuration as imaged by LASCO/C2 instrument on November 26 – 29, 2002 to help the reader understand the overall scenario of the events occurring during UVCS observations. Prior to the CME the coronal configuration off the West limb shows two large streamers centered, respectively, at $\approx 10^\circ$ (hereafter streamer 1) and 50° North latitude (hereafter streamer 2). MDI and the Big Bear Solar Observatory Active Region Monitor¹ (ARM) show on November 26, 24:00 UT the presence of two active region (AR) groups: a northern group, including NOAA 10197 and 10199 ARs (located respectively at N25W84 and N28W58) and a southern group including NOAA 10198, 10201 and 10195 ARs (located respectively at S18W61, S16W78 and S16W94). This complex configuration (see Figure 7.2, top and bottom left panels) allows for topological connections within individual ARs as well as for transequatorial loops connecting active regions in the two hemispheres. With respect to the streamer locations, ARs in the northern hemisphere lie on the southern side of streamer 2 and active regions on the southern hemisphere lie on the southernmost side of streamer 1. The CME we are dealing with started around 17:00 UT on November 26, 2002 in the West hemisphere, and was mostly confined within the NW quadrant. At that time the GOES satellite does

¹see <http://www.solarmonitor.org/index.php?date=20021126> on the web

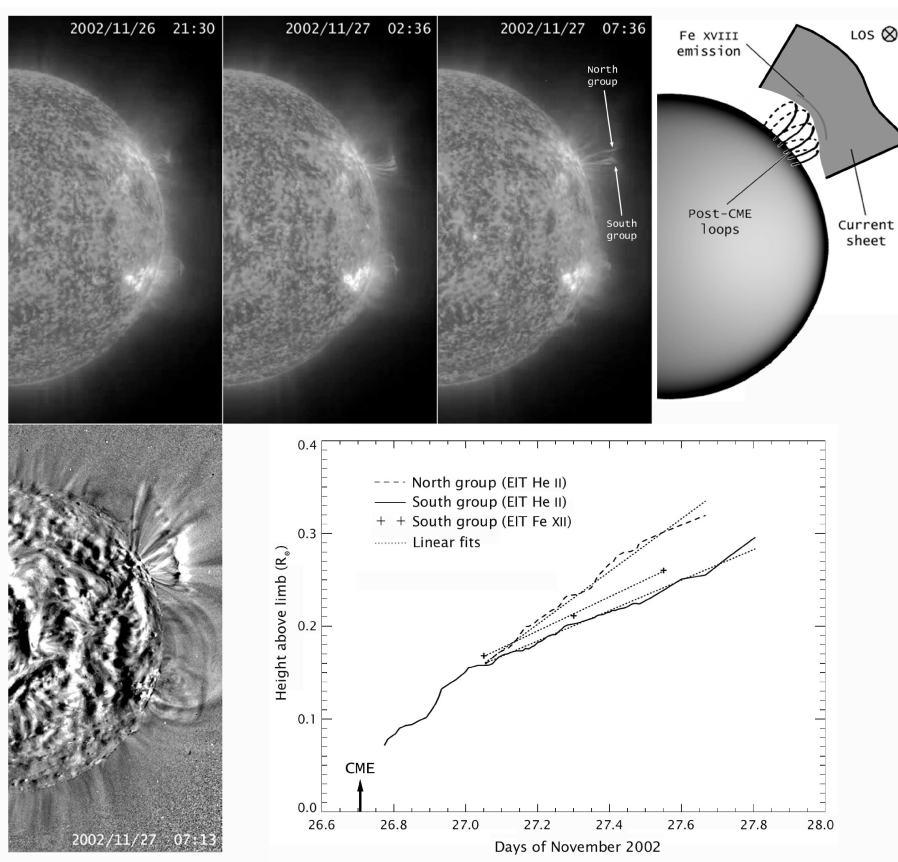


Figure 7.2: Top row: images of the loop system developing after the CME as seen in EIT He II λ 304 Å images at different times. The panel at the right of the EIT images is a cartoon depicting the scenario of the November event at the time UVCS acquired data: the line of sight is normal to a high temperature region (emitting the hot [Fe XVIII] λ 974 Å spectral line) which we interpret as a CS (see text). The EIT post-CME system consists of loops which bridge over the limb of the Sun. Bottom row, left: an EIT difference image in the Fe XII λ 195 Å emission, which better reveals the bright tops of the reconnecting loops; right: altitude vs. time profile of the top of post flare loops, as measured at different positions and in different lines. The black arrow marks the CME initiation time.

not provide evidence of any large flare event and it is difficult to identify unambiguously the CME starting time. There are no regions, behind the limb, that might contribute to the CME: NOAA 10197 and 10199 are isolated regions in the Northern hemisphere, while in the southern hemisphere the closest region to AR 10194 is NOAA 10195, 40 degrees away (and even more distant from the other regions).

In order to check for phenomena occurring in the lower corona, we examined EIT images in the He II λ 304 Å and in the Fe XII λ 195 Å spectral lines. Unfortunately, λ 195 Å data have a gap between November 26, 13:13 UT and November 26, 19:13 UT: the only available EIT data are in He II 304 Å and provide no evidence for events from the CME region at the approximate time of the CME initiation. Hence, we



Figure 7.3: LASCO images of the CME event that started on November 26, 2002 \sim 17:00 UT, at different times (time runs clockwise starting from the top left panel). Superposed onto the images we also show the radial direction to Ulysses and, normal to the radial, the UVCS slit, centered at 1.7 solar radii at a latitude of 27°N .

have no information on the CME ejection signatures. We note, however, that He II data show, from November 26 through November 29, repeated transient ejections of chromospheric material from streamer 2 (observed by UVCS as a dramatic increase of the C III intensity) unrelated to the CME event: these events will not be dealt with in this work.

Figure 7.3 illustrates the white-light coronal activity in the North-West quadrant as seen in images taken by LASCO/C2, throughout the 2.3 days observations we made. For future reference, we also show the position of the UVCS slit. As shown in Figure 7.3, the CME appears to originate from the northward side of streamer 1, in between the north and south group of ARs, and leaves initially the streamer 2 structure apparently unaffected. The relation between the CME and the two active regions complexes is not clear. Streamer 1 gets partially disrupted by the CME and deflected by $\sim 7^\circ$ towards southernmost latitudes. As time goes on, streamer 1 slowly comes back to its original position and eventually, at the end of our observations (November 29, 02:56 UT), is centered at $\approx 14^\circ$ North (that is, slightly northward of its original position), while streamer 2 shifts by $\sim 6^\circ$ northward as well. However, the multiple cusps at the top of this streamer suggest we are seeing unresolved substructures which project onto the plane of the sky within the same area. On November 28, 07:00 UT (see Figure 7.3) one of these substructures starts to rapidly shift southwards becoming clearly visible and, at the end of our observations, is centered at $\sim 30^\circ$ North. This series of events ends up tightening the “gap” area

in between streamers 1 and 2, which, on November 29, is nearly filled with emitting plasma which makes it brighter than it was prior to the CME eruption.

The CME we analyze is not a fast event: from LASCO images we derived between 16:54 and 22:06 UT the outward speed of the opening loop preceding the CME core to increase from ~ 90 to ~ 420 km/s, while, behind the dark cavity, the CME core seems to take off with an initial very low speed which increases up to a final speed that spans between ~ 130 and ~ 250 km/s depending on the different parts of the CME. Analogous variations in the rising speed of different parts of a CME have been found, e.g., by Lin et al. (2005). Here is sufficient to notice that, whatever speed is chosen, the November 26 CME is a slowly evolving phenomenon.

7.4 UVCS observations

UVCS observations started on November 26, 18:39 UT, and lasted until November 29, 02:56 UT, with 4 gaps in between. Because our observations started after the CME ejection, we expect to image the post-CME reconfiguration briefly described in the previous section.

The UVCS slit, normal to the solar radius, has been centered at a northern latitude of 27° , in the western quadrant, at a commanded altitude of $1.7 R_\odot$ (see Figure 7.3). The slit width was $100 \mu\text{m}$ and the detector masks binned the data over 6 pixels ($42''$) in the spatial direction. The mask has been selected to cover lines from ions originating in hot plasmas as well as from ions originating in cool plasma. Table 7.1 lists the lines that have been detected during the observations, together with the temperature of formation of the emitting ion, from the ionization balance of Mazzotta et al. (1998). Data have a 2 pixel spectral binning ($0.1986 \text{ \AA}/\text{bin}$) in the $1023.97\text{--}1043.23 \text{ \AA}$, $998.15\text{--}1008.87 \text{ \AA}$, $967.17\text{--}981.07 \text{ \AA}$ spectral intervals and a 3 pixel spectral binning ($0.2979 \text{ \AA}/\text{bin}$) in the $991.15\text{--}994.72 \text{ \AA}$, $943.68\text{--}965.13 \text{ \AA}$ spectral intervals.

As we mentioned in § 4.2.3, the C III $\lambda 977.02 \text{ \AA}$ emission allows to correct lines for stray light contamination. However, because in our data the C III line is usually not observed at the CME latitudes, this implies that the stray light contribution is negligible and the correction has not been made.

Figure 7.4 shows the intensity distribution along the UVCS slit, summed over ≈ 2.5 hours of observations, of four lines, H Ly β and O VI, Si XII, [Fe XVIII] representative of low, high and very high temperature plasma. These intensities are given at the beginning of our observations (Nov. 26, 18:39 UT; left column), at an intermediate time (Nov. 27, 21:30 UT; middle column) and at the end of our observations (Nov. 29, 00:20 UT; right column). The Ly β and Si XII $\lambda 499 \text{ \AA}$ lines have essentially the same intensity pattern and show brighter emitting features at the position of the northern streamer and of the disrupted southernmost streamer visible in LASCO images. The gap in between the two bright features corresponds to the dark channel in between streamers in LASCO images. Synoptic data acquired on November 25

λ_{obs} (Å)	λ_{ID} (Å)	Ion	Transition	$\log T_{max}$
943.66	943.61	Ca XIV	$2s^2 2p^3 \ ^4S_{3/2} - 2s^2 2p^3 \ ^2D_{3/2}$	6.5
944.37	944.38	Si VIII	$2s^2 2p^3 \ ^4S_{3/2} - 2s^2 2p^3 \ ^2P_{3/2}$	5.9
949.15	949.22	Si VIII	$2s^2 2p^3 \ ^4S_{3/2} - 2s^2 2p^3 \ ^2P_{1/2}$	5.9
950.09	950.15	Si IX	$2s^2 2p^2 \ ^3P_1 - 2s^2 2p^2 \ ^1S_0$	6.0
962.98	481.45	Fe XV	$3s 3p \ ^1P_1 - 3p^2 \ ^1D_2$	6.3
972.51	972.54	H I	Ly γ	4.5
974.08	487.03	Fe XIII	$3s^2 3p^2 \ ^3P_2 - 3s 3p^3 \ ^5S_1$	6.2
974.77	974.86	Fe XVIII	$2s^2 2p^5 \ ^2P_{3/2} - 2s^2 2p^5 \ ^2P_{1/2}$	6.7
976.99	977.02	C III	$2s^2 \ ^1S_0 - 2s 2p \ ^1P_1$	4.8
991.62	991.58	N III	$2s^2 2p^2 \ ^2P_{3/2} - 2s 2p^2 \ ^2D_{5/2}$	4.9
998.76	499.37	Si XII	$1s^2 2s \ ^2S_{1/2} - 1s^2 2p \ ^2P_{3/2}$	6.3
1025.69	1025.72	H I	Ly β	4.5
1028.04	1028.04	Fe X	$3s^2 3p^4 3d \ ^4D_{7/2} - 3s^2 3p^4 3d \ ^4F_{7/2}$	6.0
1031.90	1031.91	O VI	$1s^2 2s \ ^2S_{1/2} - 1s^2 2p \ ^2P_{3/2}$	5.5
1034.50	1034.48	Ni XIV	$3s^2 3p^3 \ ^4S_{3/2} - 3s^2 3p^3 \ ^2P_{3/2}$	6.2
1037.63	1037.61	O VI	$1s^2 2s \ ^2S_{1/2} - 1s^2 2p \ ^2P_{1/2}$	5.5
1041.04	520.66	Si XII	$1s^2 2s \ ^2S_{1/2} - 1s^2 2p \ ^2P_{1/2}$	6.3

Table 7.1: Lines identified in the UVCS spectra.

(hence before the CME) reveal that the O VI and Si XII line intensity distribution was very similar to what observed at the beginning of our observations.

We point out that the EIT rising loops system shows up at latitudes between 20° and 30°N matching the position of the CME ejection angle. During the same time interval, the [Fe XVIII] $\lambda 974$ Å line intensity evolution is completely different: at the beginning of UVCS observations (Figure 7.4, bottom left panel) the emission from this line, as expected, is very weak, if any, throughout the whole slit length². In the following days, an enhanced [Fe XVIII] emission, revealing a high temperature plasma ($\log T \sim 6.7$), is concentrated in a wider latitude interval between $\simeq 20^\circ$ and 30°N, hence above the EIT rising loop system. Figure 7.4 shows that at the latitudes of the [Fe XVIII] emission, the low temperature Ly β and O VI lines have a local intensity minimum, indicating that these lines are mainly emitted from the low temperature quiet corona ahead and behind the hotter region. In the O VI line this behavior is, in the November 26 and 27/28 line panel, less pronounced than in Ly β , while on November 29 no minimum appears at the position of the Ly β dip. This difference can be ascribed (see later on § 7.6) to the O VI line being entirely emitted from the background corona, while the hot region contributes to the Ly β radiation. In the days after the event, the Figure shows the appearance of a third structure in between the two streamers: this feature can be identified as the radial

²We note that we have no means to ascertain whether the [Fe XVIII] was present/absent at earlier times because the available synoptic data on the previous days do not include this line.

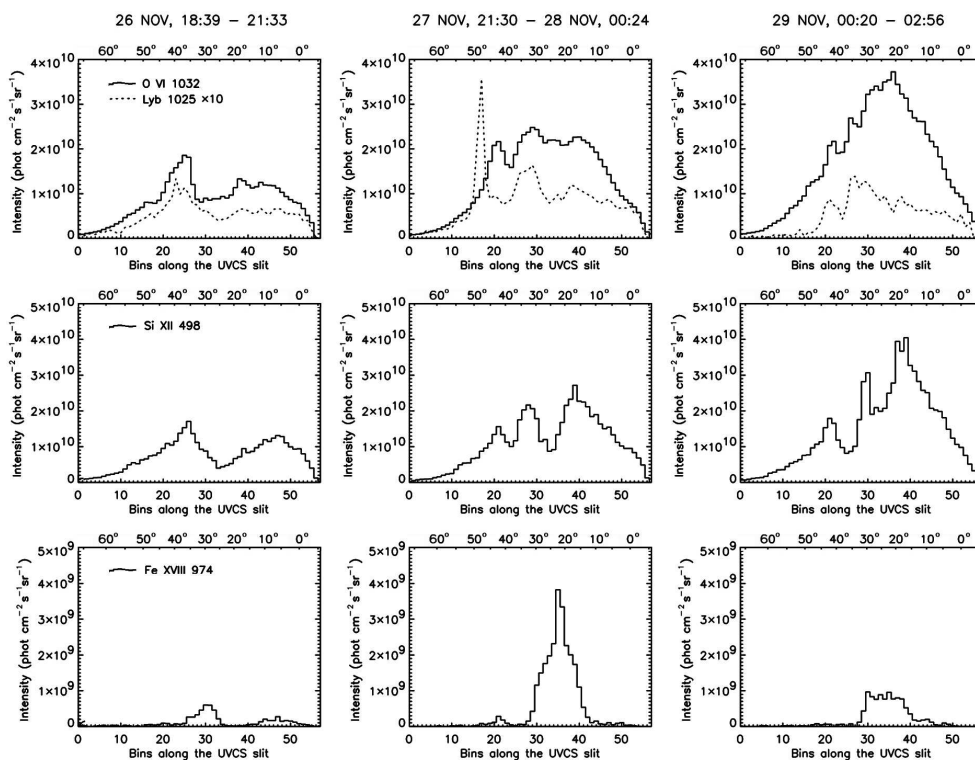


Figure 7.4: Line intensity distribution as a function of the position along the UVCS slit, at, left column, the beginning of our observations; middle column, an intermediate time; right column, the end of the observations. Intensities are given in $\text{phot cm}^{-2}\text{s}^{-1}\text{sr}^{-1}$ and have been integrated over 9600 s. Selected spectral lines are representative of plasma emitting at progressively higher temperatures (see Table 7.1 and Figure 7.7). Top row: intensity along the slit of the O VI 1032 Å and of the H Ly β (multiplied by a factor 10) lines; middle row: intensity along the slit of the Si XII 498 Å line; bottom row: intensity along the slit of the [Fe XVIII] 974 Å line.

structure observed in the LASCO/C2 data (see § 7.3 and Figure 7.3, bottom row). This implies that the hot region at a latitude of about 25°N, is included between two approaching features: the northward moving streamer 1 and the southward moving radial structure described above.

In order to better understand the evolution of the [Fe XVIII] line emission, we show in Figure 7.5 the intensity we observed along the UVCS slit during the ~ 2.3 days following the event with a time resolution of 240 s. The distribution of the line intensity varies across the 20°–30°N latitude interval, first appearing at northern latitudes and then migrating southward to occupy a wider area. Most of the time the [Fe XVIII] intensity has two emission peaks at $\approx 22^\circ$ and 28° N and these positions remain approximately constant over the 2.3 days of observations. The line intensity, however, shows an increase until the second half of November 28, when it starts decreasing. Outside the high temperature region, negligible emission in [Fe XVIII] is

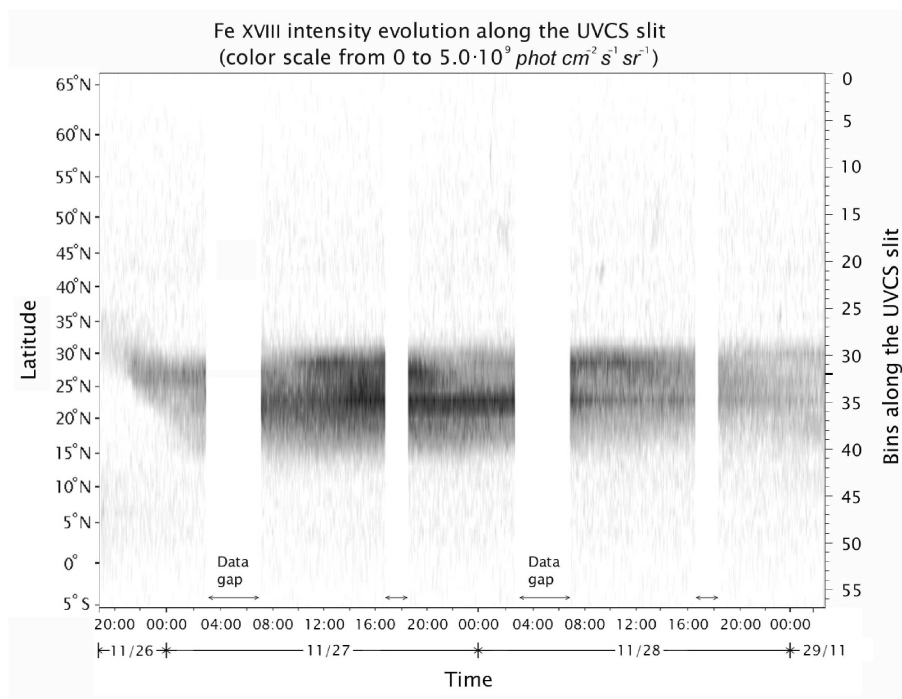


Figure 7.5: Temporal evolution of the $[\text{Fe XVIII}] \lambda 974 \text{ \AA}$ intensity along the UVCS slit.

detected.

A more quantitative view of the evolution with time of the $[\text{Fe XVIII}]$ emission is given in Figure 7.6, which shows the temporal profile of the $[\text{Fe XVIII}] \lambda 974 \text{ \AA}$ and, for comparison, of the $\text{Fe XV} \lambda 481 \text{ \AA}$ line intensities, averaged over the 20° to 30° latitude interval (bins 30 to 37). Spatial averaging allowed us to derive better Fe XV intensities, because, as Fig. 7.6 shows, the 481 \AA emission is negligible at the beginning of the observations. The $[\text{Fe XVIII}] \lambda 974 \text{ \AA}$ increases by more than one order of magnitude from November 26, 18:39 UT to November 27, $\sim 16:00$ UT, and slowly decreases afterwards. On the other hand, the weak initial emission in the $\text{Fe XV} \lambda 481 \text{ \AA}$ line continuously increases throughout the 2.3 days of observations. Qualitatively, this behavior of the line emission from different ions of the same element can be explained in terms of a temperature *decrease* with time; this is shown in Figure 7.7 which gives (left panel) the emissivities of the $[\text{Fe XVIII}] \lambda 974 \text{ \AA}$ and $\text{Fe XV} \lambda 481 \text{ \AA}$ lines (and of the $[\text{Fe X}] \lambda 1028 \text{ \AA}$ line, for future reference) vs. $\log T$.

Figure 7.7 shows that the $[\text{Fe XVIII}]$ and Fe XV emissivities peak respectively at $T \approx 10^{6.7} \text{ K}$ and $10^{6.3} \text{ K}$: hence, if plasma is cooling from a temperature higher than $10^{6.7} \text{ K}$, the $[\text{Fe XVIII}]$ line emissivity first increases, until that temperature is reached, to decrease afterwards, while the Fe XV emissivity continuously increases up to a temperature of $10^{6.3} \text{ K}$.

UVCS data have thus revealed the presence of a wide ($\sim 6 \cdot 10^5 \text{ km}$) region with anomalously high temperature plasma, which overlies the post-CME loop system

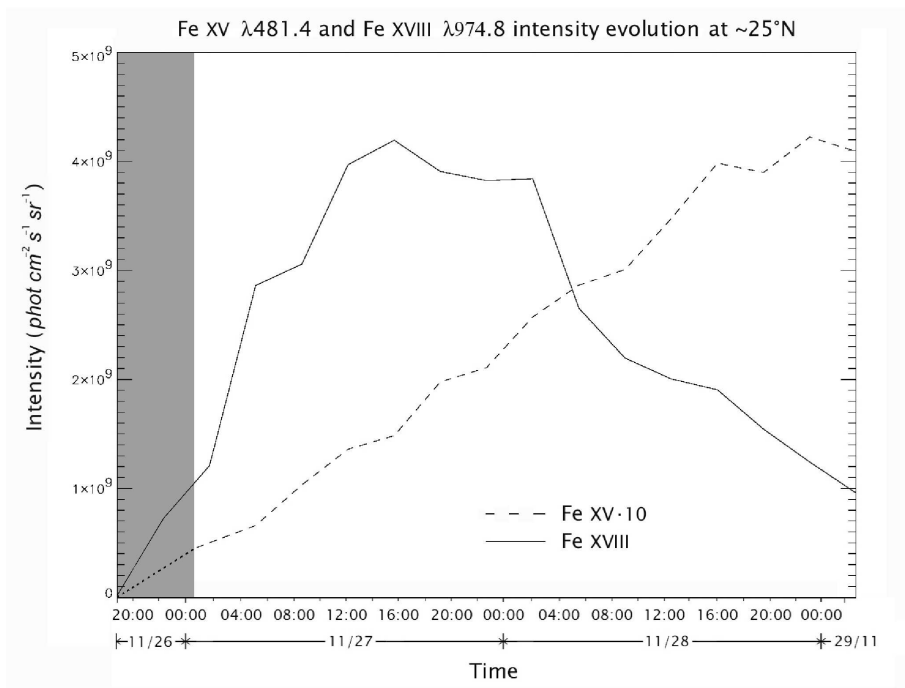


Figure 7.6: Intensity vs. time of the [Fe xviii] $\lambda 974$ (solid) and Fe xv $\lambda 481$ Å (multiplied by a factor 10, dash) lines at the position of the CS. The Fe xv intensity before November 27, $\sim 00:30$ UT (gray region) has been extrapolated back from later times (dotted line) because the line is too weak (and statistical errors too high) to be measured.

imaged by EIT and persists for more than two days in the aftermath of the CME. This might possibly originate from the top of the newly reconnected post-CME loops or in the CS formed after the event. Following Ciaravella et al. (2002), Ko et al. (2003) and Raymond et al. (2003) we identify this high temperature region with the CS that develops in the restructuring corona, as predicted by, e.g., the flux rope/CME model of Lin & Forbes (2000). From here onwards, we refer to the bright [Fe xviii] region as to the CS region and we will justify this assumption in § 7.6. In the following we concentrate on the temporal evolution of the CS physical parameters, averaged over the $\sim 20^\circ$ to 30° N latitude interval.

7.5 Physical parameters in the corona and the CS

In order to derive the plasma physical parameters we used the techniques described in Chapter 3. Here, writing the approximated expression for the intensity of a collisionally excited spectral line (equation 3.47) we defined the average contribution function (equation 3.48) in the hypothesis the plasma electronic temperature to lie in an interval $\Delta T_e \ll T_e$, hence the plasma to be nearly isothermal along the line of sight.

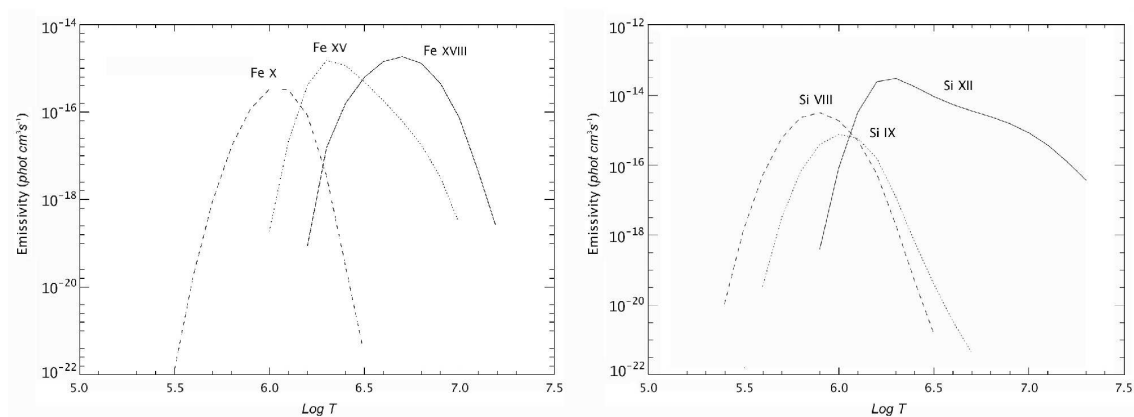


Figure 7.7: The emissivities of [Fe x] $\lambda 1028 \text{ \AA}$, Fe xv $\lambda 481 \text{ \AA}$, [Fe xviii] $\lambda 974 \text{ \AA}$ lines (left panel) and of [Si viii] $\lambda 944 \text{ \AA}$, [Si ix] $\lambda 950 \text{ \AA}$, Si xii $\lambda 499 \text{ \AA}$ lines (right panel) from the Chianti Spectral Code (v. 4.2), based on the ionization equilibria of Mazzotta et al. (1998).

However, we note that post-CME loops (as shown in Figure 7.2) seem to bridge over the solar limb: hence, we expect to see the CS, which lies approximately in the plane of the sky (Figure 7.2, top right cartoon), face-on. In this geometry, emission along the LOS originates both in the CS and in the “quiet” coronal plasma ahead and behind it, and the temperatures, densities, element abundances of the CS and of the intervening quiet coronal regions may be different; the hypothesis of nearly isothermal plasma is no longer valid. As a consequence, in order to derive the CS parameters it is mandatory to separate the CS and the coronal contribution along the LOS: at the latitude of the CS, both regions contribute to the observed line intensities, while at the latitudes besides the CS only the quiet coronal emission is present.

This has been done as follows: Table 7.1 shows that in our case the line-ratio technique (§ 3.3.2) can be applied to the [Fe x] 1028 \AA , Fe xv 481 \AA and [Fe xviii] 974 \AA lines and to the [Si viii] 944 \AA and [Si ix] 950 \AA lines. However, the emissivity curves of Fig. 7.7 show that plasma emitting in the [Fe x] 1028 \AA line has too low a temperature to account for the [Fe xviii] 974 \AA line, which forms only at high temperatures, while the Fe xv 481 \AA line originates from an intermediate regime to which both the low and high temperature plasmas may contribute. At the position of the CS, where the [Fe xviii] emission is detected, emission from a quiet, low temperature corona, superposes along the LOS onto the high temperature emission from the CS. Hence, temperatures cannot be derived simply from the observed Fe line intensities, because, independently of the pair of lines we choose ([Fe x] 1028 \AA and Fe xv 481 \AA or [Fe xviii] 974 \AA and Fe xv 481 \AA), we end up mixing contributions from different plasmas.

In order to derive the electron temperature of the quiet corona along the LOS, we then resort to [Si viii] 944 \AA and [Si ix] 950 \AA line emission, as their peak emissivities

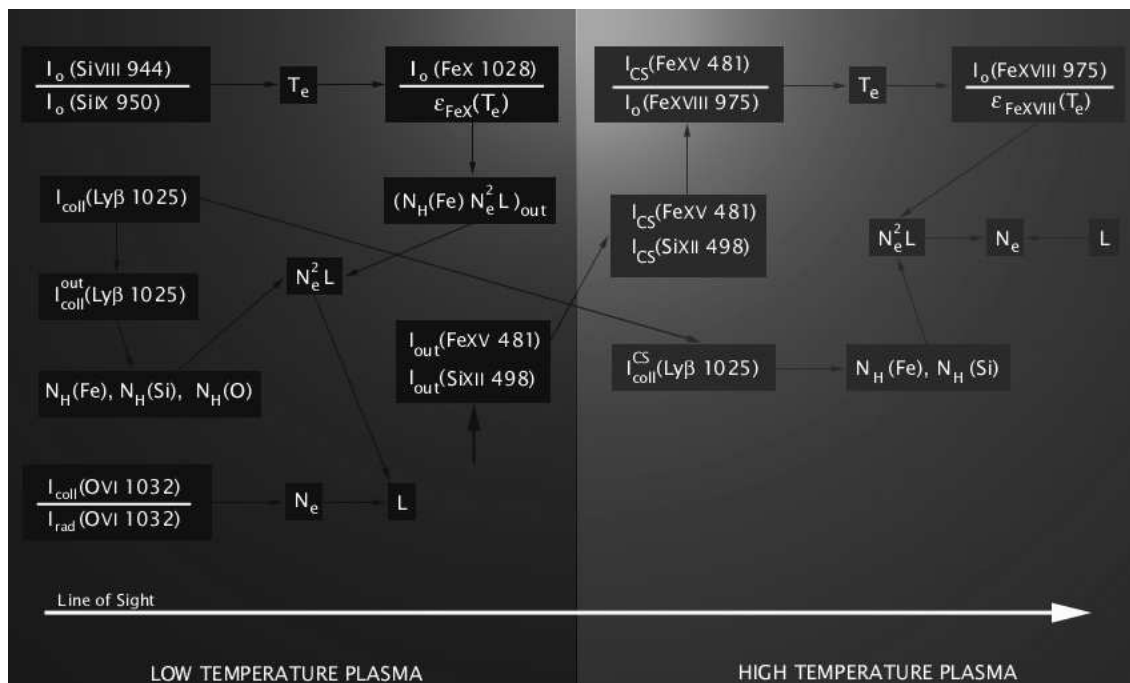


Figure 7.8: Block diagram showing the procedure used in the paper to separate the contributions along the LOS of the high temperature CS and the quiet corona to the line intensities and to determine the plasma physical parameters of both regions.

are in the $5.9 \leq \log T \leq 6.0$ temperature range, typical of the quiet corona (see right panel of Figure 7.7 and Table 7.1). Once the value of the electron temperature of the quiet corona is determined from the Si lines intensity ratio, we derive with this value and the observed [Fe x] line intensity the factor $E_{\text{Fe}} = A_{\text{Fe}} N_e N_H L$, where L is the thickness of the emitting low temperature plasma along the LOS. Knowing T_e , E_{Fe} , we can calculate the contribution $I_{\text{FeXV}, \text{QC}}$ to the Fe xv line emission originating from the quiet corona and, by subtracting this contribution from the observed line intensity, derive the contribution from the CS region $I_{\text{FeXV}, \text{CS}}$ to the total line emission. Because the [Fe xviii] is emitted only from the high temperature plasma in the CS, the ratio between the intensity of the [Fe xviii] 974 line and the $I_{\text{FeXV}, \text{CS}}$ line component gives an estimate of the CS electron temperature. Note that this procedure avoids making any hypothesis on the value of the Fe abundance in the CS, possibly different from the Fe abundance in the quiet corona; however we made the simplifying assumption that the quiet corona and the CS plasma are both isothermal.

To help the reader follow the procedure we are describing we built a flow-chart diagram (see Figure 7.8) that illustrates the links among different steps. The left part of the figure refers to the “quiet”, low temperature plasma, the right part of the figure refers to the CS, high temperature plasma. At the latitude of the CS, both regions contribute to the observed line intensities; at the latitudes beside the CS only the quiet coronal emission is present.

Having derived the electron temperatures of the quiet, low temperature corona and of the high temperature CS which contributes to the LOS emission, we proceed to determine element abundances in both regions. Absolute element abundances A_X can be derived from the collisional components of lines, provided the collisional component of a Hydrogen line is also known (see § 3.3.4). In this case, under the assumption that the collisional components of both lines originate in the same region, we may write

$$A_X = \frac{E_X}{E_H} \quad (7.1)$$

In the present data set, we detected both the H Ly β and the Ly γ lines; in order to identify the collisional and radiative components of the Hydrogen lines from their observed intensities we followed the standard procedure (see § 3.3.1). Usually, this procedure is applied to the Ly α and Ly β lines: in our case, because Ly α is not included in our data, we used the Ly β and Ly γ lines. Then, from the known electron temperatures of the CS and of the quiet corona, the percentage contribution of these regions to the collisional intensities has been inferred (as done for the $I_{Fe_{XV}}$ line), their E_H factors estimated and abundances A_X have been calculated from equation 7.1.

We still need to know the values of the quiet corona and CS thickness along the LOS (respectively, L and l), in order to derive densities. Conversely, knowing abundances and densities, it is easy to derive L values from the $E_X = A_X N_e N_H L$ relationship. Because in the CS we do not have a means to derive separately l or N_e , we assume the CS thickness to be on the order of $\approx 10^4$ km, an error of a factor 10 implying a factor 3 error in the derived densities.

We have determined the quiet corona densities from the ratio between the collisional and the radiative components of the O VI 1032 Å line intensity (see § 3.3.3). Emissivities from the O VI line decrease by about two order of magnitudes as T_e increases from $\log T = 6$ to $\log T = 6.6$, hence densities derived with this method are representative only of the quiet corona and the evaluation is not affected by the presence of the CS. Knowing densities, we calculated the quiet corona thickness L .

The separation between the radiative and collisional components of the O VI doublet lines has been performed using the same standard procedure followed for Ly β and Ly γ lines. As mentioned in § 3.3.3, densities derived with this technique are crudely evaluated as a static plasma is assumed and the emission is supposed to originate in the plane of the sky. Plasma along the LOS appears to be static, or to have a negligible speed, because spectral lines do not show evidence of any shift in λ - that is no motion along the LOS has been revealed - and the ratio between the 1032 and 1037 O VI line intensities is, throughout our data set, on the order of 2.8 to 3.5. This ratio is indicative of motions in the radial direction (see § 3.3.6): crudely we can say that a ratio of order ≈ 2 points to an outflow speed on the order of 100 km/s (Noci et al., 1987). Higher ratios, like those in our data-set, indicate negligible outflow speeds and justify the technique used to derive densities in the quiet corona. In the CS the O VI emission is undetectable, hence we can not infer

outflows in the CS from the Doppler dimming of oxygen lines.

As shown in Figure 7.7 the Si XII $\lambda 499$ Å line is emitted (analogously to the Fe XV $\lambda 481$ Å line) both from the low temperature plasma at $\approx 10^6$ K and from the high temperature plasma beyond 10^6 K. To separate the two contributions, we followed the same procedure described for the Fe XV line and shown in Figure 7.8.

In closing this section we like to remind the reader that ionization equilibrium has been implicitly assumed to hold throughout our calculations. The validity of this assumption will be discussed at the end of § 7.8.

7.6 Results

We illustrate now the results obtained by applying the technique described in the previous Section to our data set.

Electron temperatures in the CS and adjacent regions

We first examine the electron temperature evolution in the quiet corona. Figure 7.9 shows the behavior of the electron temperature along the UVCS slit at different times. Scatter between individual points is due to uncertainties in the [Si VIII] and [Si IX] line intensities (both are blended with other lines, see later), which has been minimized by averaging over 9600 s. In spite of the uncertainties, however, a value of $\log T \sim 6.25$, for regions at either side of the CS, is clearly defined. The regions which border the CS, hence the regions beside the area where the CME occurred, are occupied by streamers. Because $\log T \sim 6.25$ is the temperature of maximum formation of the Si XII ion (see Figure 7.7), we expect each streamer to correspond to a peak in the [Si XII] emission; this is confirmed by Figure 7.4.

A temperature of $\approx 10^{6.2}$ K is in agreement with estimates of temperatures in streamers at comparable heights. For instance, Uzzo et al. (2004), from UVCS data, found T_e ranging between $6.1 \leq \log T \leq 6.3$, for active region streamers observed in 2001. Electron temperatures we derived in Chapter 5 and derived (still from UVCS data) by Parenti et al. (2000) for streamers observed, respectively, in 1998 and 2000 are on the order of 10^6 – $10^{6.15}$ K at altitudes ranging between 1.5 and 1.9 R_\odot . Foley et al. (2002) from CDS data derived a slightly higher temperature of $\approx 10^{6.34}$ K at 1.6 solar radii for streamers observed near solar maximum.

Over the latitude interval where the high [Fe XVIII] emission shows up, the temperature from the [Si IX] to [Si VIII] ratio has a minimum which reveals the quiet corona beside the CS latitudes to have different physical properties than the corona along the LOS ahead and behind the CS. Lower temperatures along the LOS at the CS position can be ascribed to plasma left over by the CME rather than to the streamer plasma either side of the CS.

This temperature dip at the CS latitude originates in the observed [Si VIII] and [Si IX] line intensity variation in the transition from the CS ($\sim 25^\circ$ N) to adjacent

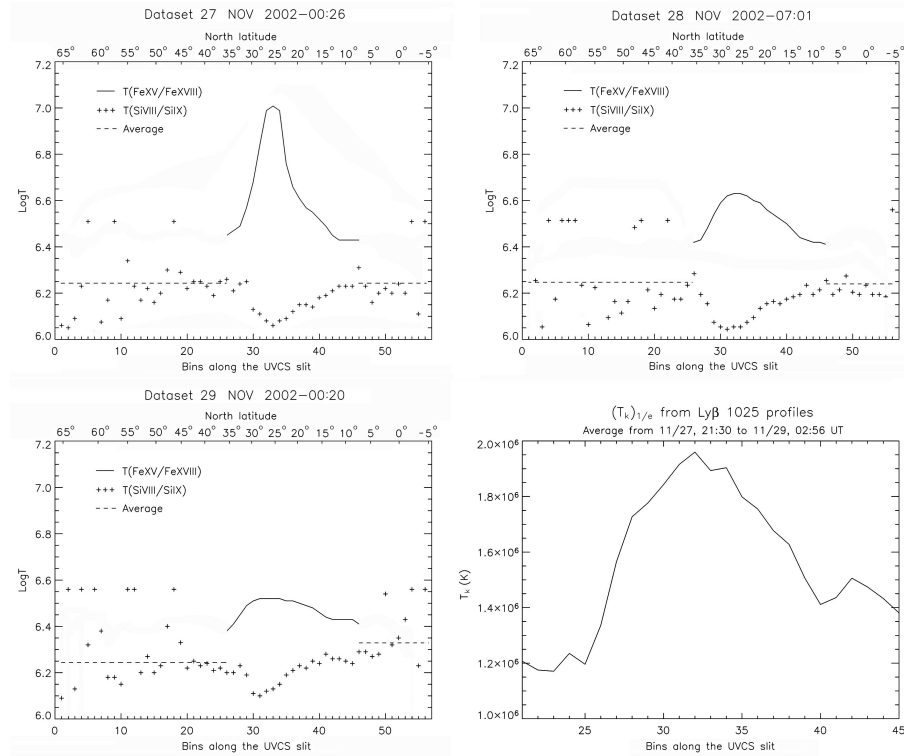


Figure 7.9: Top row and bottom left panel: electron temperatures (crosses) along the UVCS slit from the ratio between lines from Si VIII and Si IX ions at representative times on November 27, 28 and 29. Bins along the UVCS slit are given in the abscissa: corresponding heliographic latitudes appear at the top of each panel. The solid line gives the CS temperature from the ratio of [Fe XVIII] to the fraction of the Fe XV line emission which originates from the CS. Outside the CS, where [Fe XVIII] emission is missing, the average temperature from individual determination is indicated by the dashed line. Bottom right: kinetic temperatures from the Ly β line profiles along the UVCS slit (at CS latitudes) averaged over ~ 30 hours of observation.

latitudes (see Figure 7.10, left panel). Although the Si line intensities reach maximum at the CS latitudes, it is their ratio that indicates the temperature dip. Moving away from the CS, the Si VIII/Si IX ratio decreases; this implies higher temperature because the T_e increase we derived from the CS to adjacent latitudes corresponds to a decrease in the [Si VIII] and [Si IX] line emissivities (see Figure 7.7) respectively by a factor of ~ 40 and ~ 8 ³. The low value in correspondence of the CS does not show any appreciable change over the 2.3 days of our observations. This is illustrated by the right panel of Figure 7.10: because the electron density increases with time (as we show in the next Section), the [Si VIII] and [Si IX] line intensities increase, but their ratio keeps approximately constant, giving a constant quiet coro-

³This is not the case for the O VI $\lambda 1031.91$ Å line whose emissivity decreases by only a factor ~ 2 , see Figure 7.4.

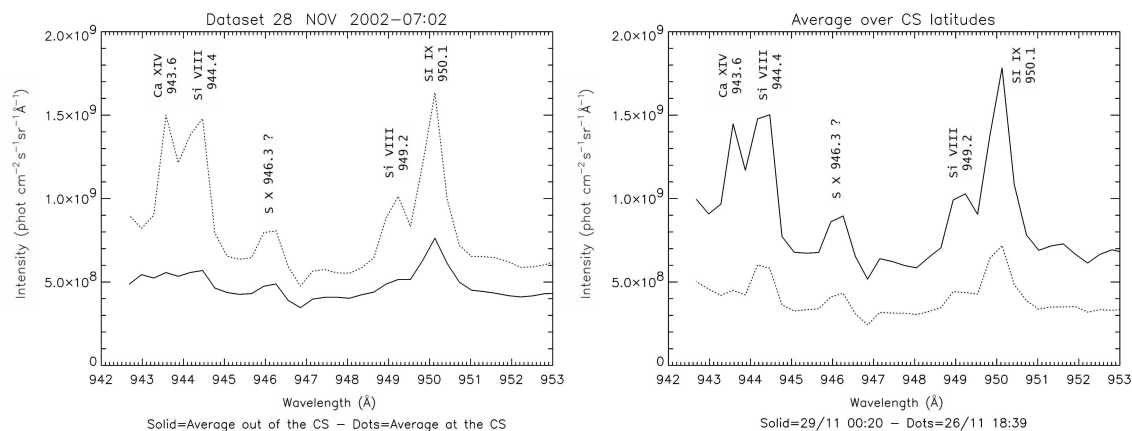


Figure 7.10: Left panel: representative behavior of the [Si VIII], [Si IX] and [Ca XIV] spectral lines at (dots) the CS and (solid) out of the CS. Data have been averaged over ~ 2.6 hours starting on November 28, 07:02 UT and over bins 30–37 for the CS latitudes and over all the residual bins for the adjacent region. Right panel: representative spectra at the CS latitude (bins 30–37) integrated over ~ 2.6 hours at the beginning (November 26, dots) and at the end (November 29, solid) of our observations.

na temperature. Figure 7.10 also shows that the [Si VIII] $\lambda\lambda 944.4$ – 949.2 Å doublet lines are blended, respectively, with the [Ca XIV] $\lambda 943.6$ Å and [Si IX] $\lambda 950.1$ Å lines, leading to uncertainties in the line intensity determination. The ensuing errors in the temperature evaluation are discussed at the end of the Section. We point out that emissivities from the O VI lines decrease by about two orders of magnitude as T_e increases from the $\approx \log T = 6.0$ of the quiet corona to the $\approx \log T = 6.6$ of the CS, hence the CS has too high a temperature to contribute to the O VI emission.

Figure 7.9 (solid line) shows the evolution along the UVCS slit of the CS temperatures as derived from the ratio between the [Fe XVIII] and the component of the Fe XV line originating in the CS. A comparison between Figure 7.5 and Figure 7.9 shows that a single peak in the CS temperature often corresponds to two peaks in the [Fe XVIII] line intensity at latitudes of $\sim 22^\circ$ and 28° N. This is a consequence of the [Fe XVIII] emissivity changes along the slit as temperature decreases northward and southward of the latitude of $\sim 25^\circ$ N. The occasional disappearance of one of the [Fe XVIII] 974 Å intensity peaks may be ascribed to reconnection processes involving at different times loops located at different latitudes. Although the altitude and time difference in between EIT and UVCS observations does not allow us to establish a close correspondence between what is seen by the two instruments, EIT images show a spatially intermittent brightening of loop tops, indirectly supporting UVCS evidence.

The bottom right panel of Figure 7.9 gives the kinetic temperatures T_k of the Ly β line along the UVCS slit and is consistent with the CS temperature profiles shown in the other panels. Kinetic temperatures have been crudely evaluated from gaussian fits of the observed Ly β profiles. Because the Ly β line originates from

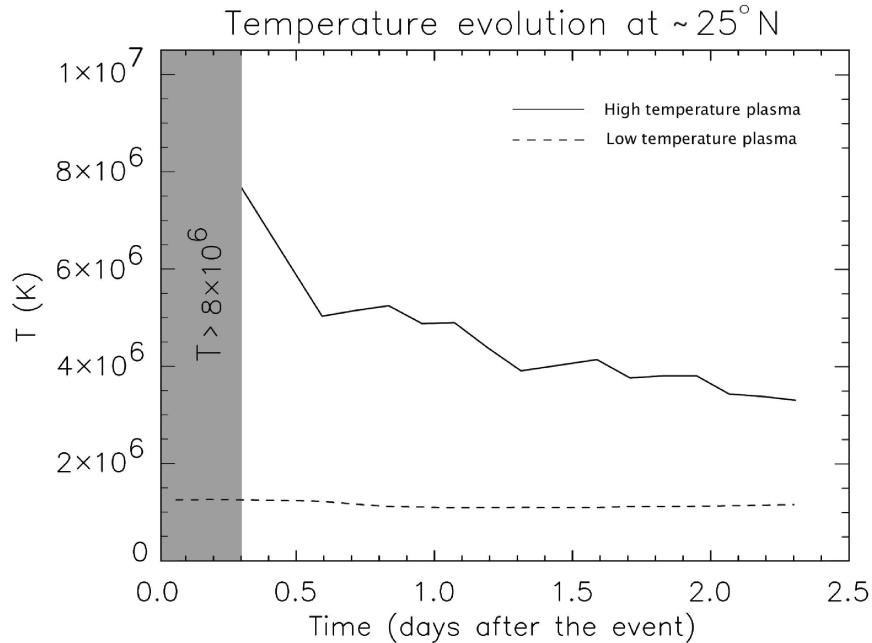


Figure 7.11: Evolution of the CS temperature (solid line) over ≈ 2.3 days from the ratio between the observed [Fe XVIII] line intensity and the calculated CS intensity of the Fe XV line. Because the latter is negligible and cannot be evaluated in earlier data (gray area), temperatures can only be assumed to be higher than $8 \cdot 10^6$ K. Temperatures from the Si VIII/Si IX line ratio at the CS latitude are also shown (dashed line).

both the CS and the quiet corona along the LOS, we expect at CS latitude a $\text{Ly}\beta$ T_k increase weaker than the temperature increase inferred from the Fe XVIII / Fe XV ratio. This is confirmed in Figure 7.9 (bottom right panel) by the factor ~ 2 variation in the $\text{Ly}\beta$ T_k .

Figure 7.11 presents the temporal evolution of the average CS temperature: data have been accumulated over the CS latitude interval (bins 30 to 37). Initially (gray area in the figure), because the observed intensity of the Fe XV line is negligible (see Fig. 7.6), we cannot give a reliable estimate of the CS temperature. The weak Fe XV emission can be explained by the quiet corona temperature behind and in front of the CS ($\log T \sim 6.05\text{--}6.10$), and the CS temperature ($\log T \geq 6.9$), being at either side of the temperature maximum ($\log T = 6.3$) of the Fe XV line emissivity.

A $\geq 50\%$ decrease in the temperature of the sheet occurs over the 2.3 days of observations, hinting at the CS cooling. The increase with time of the [Ca XIV] 943.6 Å line intensity (see right panel, Figure 7.10) supports this conclusion, because the CS cools down approaching the temperature of maximum [Ca XIV] line emissivity (see Table 7.1). There have been previous detections of [Ca XIV] in CSs: for instance, Ko et al. (2003) observed both the [Fe XVIII] and [Ca XIV] lines, but could not reproduce their intensities other than invoking the CS to spread over a range of temperatures ($6.46 \leq \log T \leq 6.66$). Possibly this depends on the different

orientation of the Ko et al. (2003) CS, which was seen edge-on: hence, different temperatures could align along the LOS. A multitemperature CS can be envisaged if either reconnection is going on with different characteristics at different positions (for instance, the reconnecting magnetic field strength varies along the reconnection region) or the reconnection process started at different times at different positions along the reconnecting arcade. In both cases, integrating along the CS implies integrating through a dishomogeneous CS.

The CS temperature evolution described above allows us to check the assumption we made that the high temperature [Fe XVIII] emission seen by UVCS originates from the CS and not from the cusps of the post-CME rising loops. Order of magnitude estimates of the conductive and radiative cooling time for a semi-circular loop of height of $0.7 R_{\odot}$ show that the loops cool mainly by conduction over times on the order of 1h. This short time is clearly incompatible with the very slow temperature decrease shown in Figure 7.11. Moreover, with the low rising speeds derived from EIT images, the post-CME rising loops would arrive at the UVCS slit height of $0.7 R_{\odot}$ over the solar limb only 2–3 days after the event. This led us to conclude (in agreement with Ciaravella et al., 2003; Ko et al., 2002; Raymond et al., 2003) that the high temperature plasma we detected originated from the CS.

Before concluding this Section, we discuss the errors in the procedures described above. As we anticipated, both [Si VIII] and [Si IX] spectral lines are blended with other lines and this may affect the determination of the quiet corona temperature: in particular, the [Si VIII] $\lambda 944.37 \text{ \AA}$ is blended with the [Ca XIV] $\lambda 943.61 \text{ \AA}$. Because the emissivity of [Ca XIV] peaks at a temperature of $\log T = 6.5$ (see Table 7.1), its emission is usually negligible outside the CS. Hence, outside the CS, the [Si VIII] line intensity is not blended with the [Ca XIV] line. At the CS latitudes the temperature of $\log T = 6.5$ is reached only at the end of our observations: at these late times the increased [Ca XIV] emission may lead to an overestimate of the [Si VIII] intensity by $\leq 40\%$. Taking into account this error the derived temperature may increase by no more than 0.1 dex , possibly indicating that ~ 2 days after the CME the dip in the quiet corona temperature, visible in Fig. 7.9 at the CS position, starts disappearing.

A further problem we need to solve is the blend of the [Si IX] $\lambda 950.15 \text{ \AA}$ and the [Si VIII] $\lambda 949.22 \text{ \AA}$ spectral lines. However, we solved this problem taking into account that the ratio between the intensities of the [Si VIII] $\lambda\lambda 944.38\text{--}949.22 \text{ \AA}$ doublet lines is 2. We then subtracted from the observed [Si IX] $\lambda 950.15 \text{ \AA}$ and [Si VIII] $\lambda 949.22 \text{ \AA}$ blend $1/2$ of the [Si VIII] $\lambda 944.38 \text{ \AA}$ intensity.

Errors in the CS temperature determination depend mainly on the [Fe XVIII] and Fe XV observed intensities and on the separation between the fraction $I_{Fe_{XV},CS}$ of the Fe XV intensity emitted from the CS and the fraction $I_{Fe_{XV},QC}$ emitted by the quiet corona. The latter depends on the quiet corona electron temperature $T_{e,QC}$ derived from the Si VIII/Si IX ratio and we said this might possibly be underestimated by up to 0.1 dex . However, the error in the temperature of the quiet corona ahead/behind the CS needs to be lower than 0.1 dex because an increase that large yields a Fe XV line emission larger than observed. Assuming, for instance, $T_{e,QC}$ to be higher by

0.02 *dex* does not sensibly modify the CS temperatures beyond November 27, 07 UT. At earlier times, because this higher $T_{e,QC}$ results in a higher $I_{Fe_{XV},QC}$ fraction (i.e. a lower $I_{Fe_{XV},CS}$), the CS temperature would be higher than shown in Figure 7.11. Statistical errors in the observed Fe xv intensity go from $\geq 90\%$ at the beginning of our observations down to $\sim 10\%$ on November 29 (because of the continuous increase in the Fe xv intensity), while statistical errors in the observed [Fe xviii] intensity are comprised between 5% and 15%. In conclusion, the CS temperature is accurately inferred after November 27, 07 UT, while at earlier stage only a lower minimum to the real T_e can be given.

7.6.1 Elemental abundances in the CS and adjacent regions

We examine here the behavior of O, which is a high First Ionization Potential (FIP) element, and of Fe and Si, which are low FIP elements; abundances of these elements are given in Figure 7.12. The Oxygen abundance can be derived only for the regions external to the CS, because, as already mentioned, the CS has too high a temperature to contribute to the O vi emission. Errors in the abundance values are easily on the order of ± 0.1 *dex* for O abundances and of ± 0.2 *dex* for Fe and Si abundances; this error can be ascribed mainly to uncertainties in the identification of the Ly β collisional component (which affects all abundances in the same way) and in the estimate of line intensities (more difficult for second order lines). Hence the apparent increase in the Oxygen abundance with time, seen in the top left panel of Figure 7.12, is within the uncertainties of the measurements and cannot be confirmed. Even so, oxygen appears to be depleted with respect to its photospheric abundance ($\log N(O)_{phot} = 8.82$; Allen et al. 1973), an effect that can easily be explained if we envisage the quiet plasma ahead/behind the CS to be the remnant of the streamer that has been partially disrupted by the CME event. An oxygen depletion in streamers has been found in the observations we described in Chapter 5 and also by many authors (see, e.g., Raymond et al. 1997; Uzzo et al. 2003), hence we may interpret the present underabundance to be a signature of the streamer origin of the plasma which is being sampled.

We note that the oxygen abundance can be derived also from the ratio between the O vi and Ly β radiative components (see § 3.3.5). Because of the different dependence of the radiative and collisional components of the line on N_e , abundances derived from radiative/collisional components tend to be different (see e.g. Raymond et al., 1997). In particular abundances derived from radiative contribution are systematically higher (by a factor ~ 1.5 – 2.0) than those derived from collisional contribution, because of the different weight ascribed to denser regions along the line of sight. Hence, our radiative oxygen abundances are closer to the photospheric value. Moreover, we note that more recent oxygen photospheric abundances tend to be lower than older estimates (see e.g. $\log N(O)_{phot} \simeq 8.65$; Asplund et al. 2004): in this case our oxygen CS underabundance may disappear. Hence the presence of a FIP-effect can not be unambiguously established for the high FIP element oxygen.

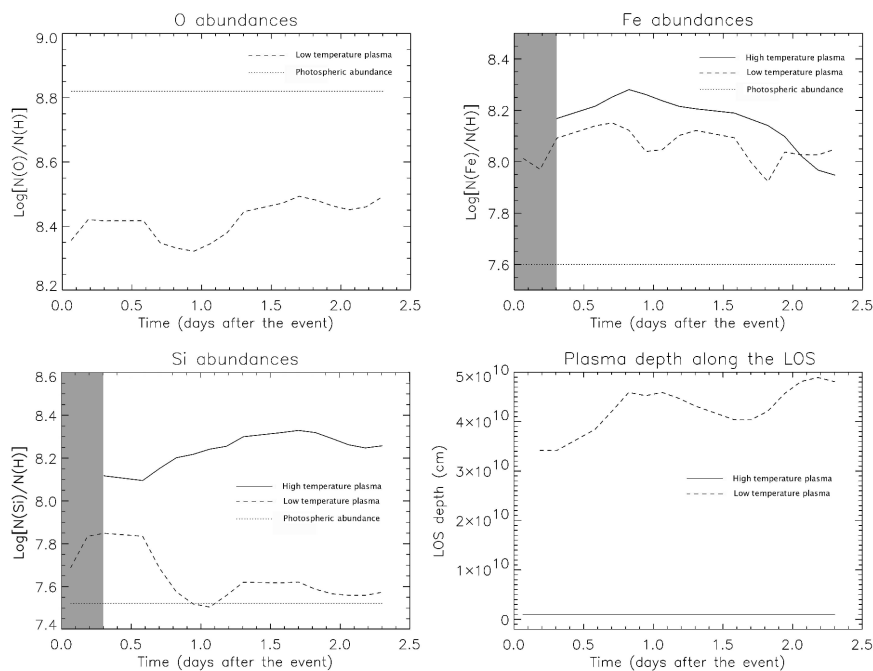


Figure 7.12: Top left panel: oxygen abundance in the quiet corona at the location of the CS vs. time (dashed line) over the 2.3 days of observation. The straight dotted line gives the assumed photospheric abundance. Top right panel: same as for the top left panel, the solid line gives the Fe abundance in the CS. Bottom left panel: same as the above panels, for Si. Bottom right panel: the assumed CS thickness l (solid line) and the computed quiet corona thickness L (dashed line) along the LOS. A gray area covers times when uncertainties are too high to give reliable CS elemental abundances.

On the contrary, the abundance of low-FIP elements like Fe and Si can be evaluated both in the quiet corona and in the CS, because a significant fraction of the total line emission originates in the CS itself. The top right panel of Fig. 7.12 shows Fe to be overabundant, with respect to its photospheric value, both in the quiet corona and in the CS. The CS Fe abundance is only slightly higher than the quiet corona abundance, hence this difference is within the error bars. However, because this seems to be a persistent feature throughout the data sets until $\sim 18:00$ UT of November 28, it is likely to represent a property of the CS plasma, possibly disappearing with time. This overabundance of low-FIP elements is better seen in the bottom left panel of the figure, where the CS Si abundance turns out to be about a factor 5 greater than its photospheric value. Also the CS Ca turns out to be overabundant by a factor ~ 2 with respect to its photospheric value. An enhanced abundance of low FIP elements in the CS has been found also by Ciaravella et al. (2002) and Ko et al. (2003) and appears to be one of the distinctive properties of CS plasmas.

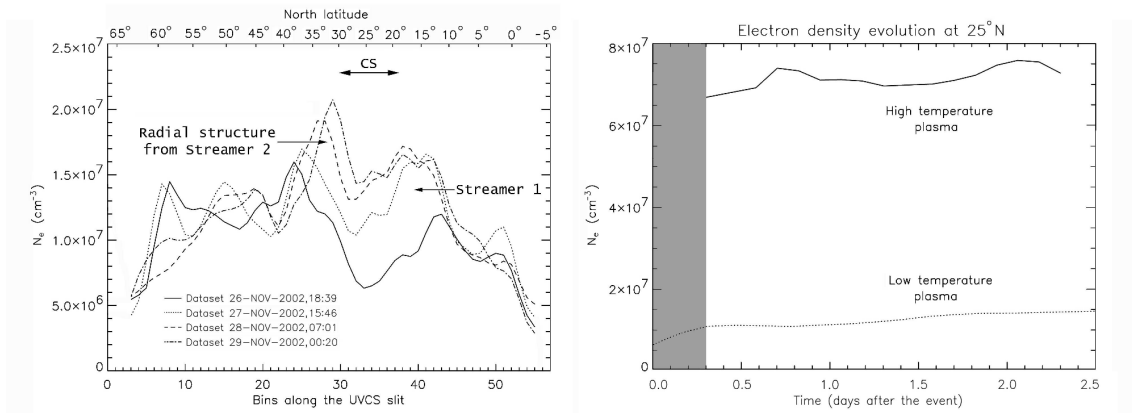


Figure 7.13: Left panel: densities of the quiet corona along the UVCS slit at different times. Right panel: temporal evolution of the density at the CS position. The solid line refers to the CS density, the dotted line refers to the density of the low temperature plasma in front/behind the CS (see left panel). A gray area covers times when uncertainties are too high to give reliable CS densities.

7.6.2 Densities in the CS and ambient corona

Figure 7.13 (left panel) shows the behavior of electron densities along the UVCS slit at different times. As we said, these have been derived from the ratio between the collisional and radiative components of the O VI $\lambda 1032 \text{ \AA}$ line. Because the CS plasma does not contribute to the O VI line emission, densities derived with this method refer to the quiet corona plasma; in particular, at the CS latitudes, these are indicative of the plasma densities along the LOS external to the CS itself. Densities are of the order of 10^7 cm^{-3} , and are consistent with values we found in Chapter 5 and a little higher than those of Gibson et al. (1999) (Figure 2.2) which, however, refer to streamers at solar activity minimum. We note that abundances inferred from the O VI line components, depend on the O VI disk intensity, for which we do not have, at the time of our observations, any measurement. Hence, densities can be affected by a systematic error, should our disk estimate be inaccurate. The O VI disk intensity has been estimated assuming a value $I_{disk}(OVI) = 1.94 \cdot 10^{13} \text{ phot cm}^{-2}\text{s}^{-1}\text{sr}^{-1}$ measured by UVCS in 1996, as representative of the disk intensity at the last minimum of solar activity. Taking into account that on November 26, 2002 the solar activity was in the descending phase, after the solar maximum of 2000, we used a value of $I_{disk}(OVI) = 3.34 \cdot 10^{13} \text{ phot cm}^{-2}\text{s}^{-1}\text{sr}^{-1}$, from an estimate of the number of ARs at that time using typical quiet Sun to AR ratio given by Vernazza & Reeves (1978).

At the CS latitudes, densities have a minimum, as expected from a corona emptied by the CME ejection. As the CS volume fills up in time, because of the corona restructuring, of the northward motion of streamer 1 and of the superposition, from northern latitudes, of a bright, dense structure onto the CS location (mentioned in

§ 7.3), the minimum region decreases in width and tends to disappear. This is more clearly shown in the right panel of the figure, where the temporal evolution of the quiet corona in correspondence of the CS is given (dotted line). Densities appear to increase by a factor ≈ 2.5 , over the 2.3 days of observations.

Figure 7.13 shows (right panel, solid line) that the CS density remains constant in time (or possibly increases by no more than 10%) and is 6 to 8 times greater than in adjacent corona. We will discuss later on the behavior of the pressure in the CS; however, it is worth reminding the reader that the CS densities of the figure are only indicative, both because the CS thickness may be greater/smaller than we hypothesized and because we assumed it to be constant in time. As already mentioned, if the thickness of the CS is one order of magnitude greater/lower than 10^4 km, densities would be a factor ~ 3 lower/higher. Moreover, if the CS is disappearing in time, its thickness l and, as a consequence, its computed densities, will change as well. In conclusion, we can safely assume only that, in the CS, $2 \cdot 10^7 \leq n_e \leq 2 \cdot 10^8$ cm^{-3} .

We note that, even if the ratio between the quiet corona and CS density is on the order of 0.14, the ratio of order 40 between the quiet corona and the CS emitting length along the LOS justifies the absence of a CS counterpart in the LASCO/C2 and C3 white light images.

7.7 Ulysses observations

The measurements by UVCS during and following the 26 November CME showed the creation of high ionization state Fe at $1.7 R_{\odot}$ in the aftermath of the CME. Interpreting this in the context of the model illustrated in Figure 7.1 suggests that the Fe ions will flow both up and down along the current sheet. The upward flowing ions will fill a shell inside the boundary of the CME. The question here is whether these Fe ions can be detected at Ulysses and, if so, whether the measurements are consistent with the model in Figure 7.1 and the measurements made by UVCS, LASCO, and EIT described in § 7.3 and 7.4. Of particular interest are the Ulysses/SWICS measurements of Fe and its ionization state since unusually high ionization state Fe will presumably have been produced in the current sheet between the post-CME loops and the CME that was remotely detected with UVCS. The Ulysses/SWICS instrument is able to detect Fe from Fe^{6+} through Fe^{16+} (Fe VII - XVII). On November 2002 Ulysses was 90° to the west of SOHO with respect to the Sun, in quadrature, at a northern heliographic latitude of 27° . This direction is shown by the radial outward line in Figure 7.3, placing Ulysses directly in line with the observed CME, assuming the CME was at or near the solar limb. The results discussed in sections 2-3 present a strong argument that the CME was on the limb.

SWICS measurements for several days around 13 December 2002 (day-of-year 347, or DoY 347) are shown in Figure 7.14. The top panel is a color plot of flux in individual Fe charge states versus time, normalized to a total flux of unity for

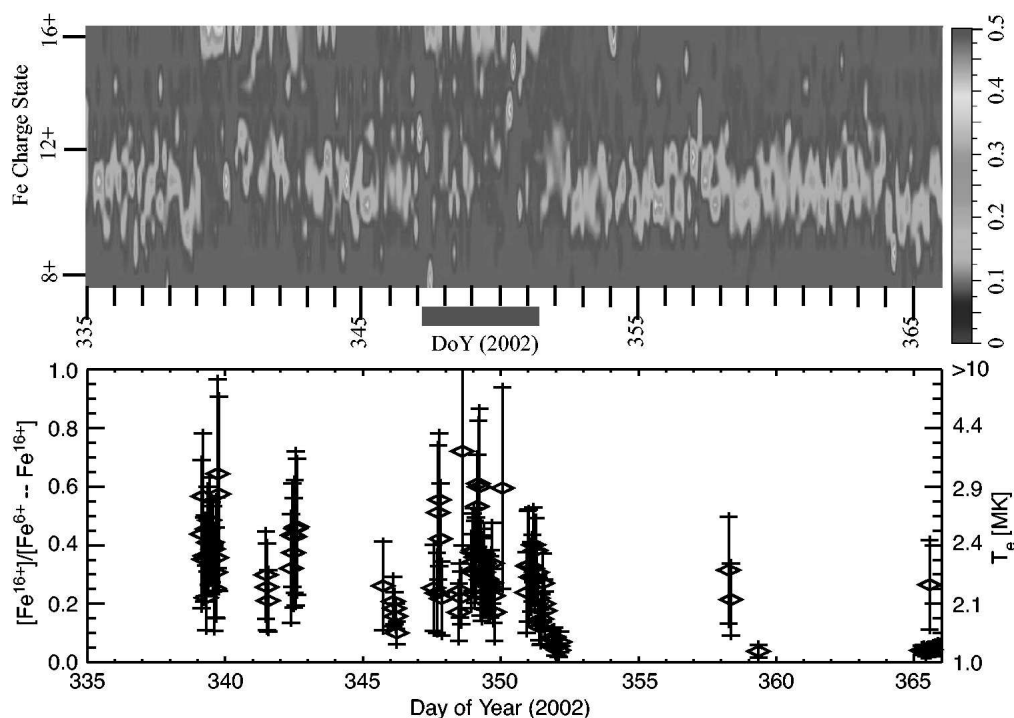


Figure 7.14: Iron charge state versus day of year (DoY) in 2022 from Ulysses/SWICS. Top: Colors give the relative abundance of each charge state from 6+ to 16+, with the total abundance normalized to unity for each three hour data sample. Bottom: The abundance of Fe 16+ relative to the total abundance of Fe over the range 6+ to 16+. The gray bar below the top panel indicates the interval of enhanced Fe16+ that was produced by the 26 November and 2 December CMEs.

each 3 hour data sample. It is important to note that the normal charge state of Fe in the solar wind is ~ 10 (Fe XI) and this is precisely what was observed over most of the displayed 30 day period in the top panel. However, there are also two obvious intervals of high ionization state Fe roughly on day of year (DoY) 339-344 and DoY 347-352. These intervals cover interaction regions formed by the merging of ICMEs, commonly known as merged interaction regions (MIRs) (Burlaga & Ness 1994). High ionization state Fe is observed in at least one-third of all ICMEs (Lepri et al., 2001; Lepri & Zurbuchen 2004), and these are obvious examples of a positive detection.

The bottom panel of Figure 7.14 gives the ratio of flux in Fe XVII to total Fe flux in Fe VII - XVII. All data with Poisson error greater than 65% have been rejected; the Arnaud & Rothenflug (1985) ionization equilibria have been used to infer temperatures. Because of the ion freezing-in we may expect these to provide information on the temperatures of the source region of Fe¹⁶⁺ ions. As usual, the charge composition data of our event are, however, not isothermal, because unusually high temperatures mix with lower temperatures. This highly structured behavior

suggests that we are observing at any given time plasma from many different source regions.

Poletto et al. (2004) extrapolated Ulysses measurements back to the Sun using the *in situ* flow speed measured by SWOOPS, the solar wind plasma detector. This gave a rough estimate of the origin time for the plasma. Then, a positive identification of the plasma resulting from the 26 November CME was made by comparing features in the solar wind with phenomena directed towards Ulysses in the corona. This was aided by there being additional CMEs on 19 and 24 November and 2 December. Ejecta from the four CMEs was easily identified at Ulysses using the results shown in Figure 7.14 and several other standard markers, including bi-directional streaming of 100 keV electrons, the presence of magnetic clouds, and enhanced α particle abundance. The ICME from the 26 November CME is the first of two CMEs that resulted in the MIR marked with the gray bar at the bottom of top panel in Figure 7.14, on DoY 347-352.

Figure 7.15 shows several solar wind parameters on DoY 330-365 which will be used to separate the 26 November ejecta from that from the following CME and for comparison with the SOHO observations and Figure 7.1. The panels are, respectively, proton number density scaled inversely with the square of heliocentric distance to 1 AU, proton flow speed, proton temperature, ratio of alpha to proton number density, total magnetic field strength, the north-south (θ) and east-west (ϕ) magnetic field angles, the total plasma β , the Fe/O abundance ratio, and the average Fe charge state. These are from the SWOOPS (1-hour data), VHM/FGM (1-minute data), and SWICS (3-hour data) instruments. Of these, only the flow speed and the proton density are not used as identifiers of ICMEs and this is because well inside 2-3 AU dynamic interactions reduce flow speed and density differentials and shift speed patterns with respect to the actual ejecta.

The MIR containing the 26 November CME is bracketed by vertical lines (shaded region in Figure 7.15). The MIR has the typical ICME properties of low proton temperature, enhanced relative alpha abundance, smooth magnetic field intensity, rotations of the magnetic field vector, low β , enhanced Fe/O, and enhanced Fe average charge state through at least some portion of DoY 347-352.

The rotation of the magnetic field vector, accompanied by low β and a smooth magnetic field intensity, is a clear indication of a magnetic cloud (Klein & Burlaga, 1982). In the shaded region there is one magnetic cloud between the first vertical solid line and the vertical dashed line. At the dashed line, the rotation changes its behavior and this probably marks the beginning of the second ICME. Within the second ICME, there is another change at DoY 351 but this is due to the presence of a shock (see the proton flow speed) and is of no significance. There is a drop in Fe/O at DoY 350 which seems to accompany the boundary between the two ICMEs.

Interpreting this in the context of Figure 7.1 is straightforward. There are two important properties of this model to look for in the data. The first is the presence of Fe XVII at both the back and the front of the ICME, even though it has been generated in the corona in the aftermath of the CME. Here we see there is not only Fe

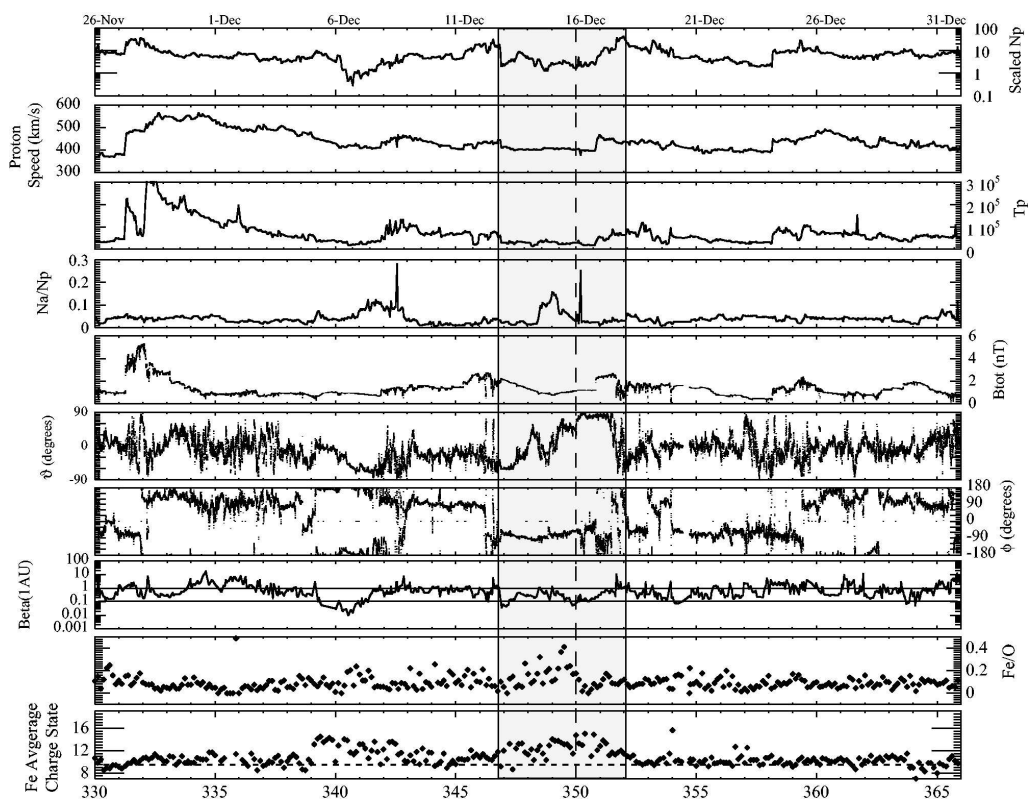


Figure 7.15: Stack plot of the indicated solar wind parameters versus time over the interval day of year (DoY) 330-365 in 2002. The proton number density (cm^{-3}) has been scaled with the inverse square of heliocentric distance to 1 AU. Beta is the ratio of thermal to magnetic pressures. θ is the north-south magnetic field angle and ϕ is the east-west angle. Btot is the total magnetic field strength in nT. Na is the alpha particle number density and Tp is the proton temperature (K). The gray region bracketed by vertical lines delimits the MIR containing the 26 November CME.

XVII at the front and back of the ICME, independent of where we pick the boundary between the two ICMEs, but also more-or-less throughout the ICME. In the context of Figure 7.1, this could mean that Ulysses did not pass through the center of the ICME/magnetic cloud, but rather off-center, so that its trajectory missed the void. Alternatively, the void could have been very small or absent. The first interpretation is supported by the magnetic field rotation in the cloud, which is not either a simple $90^\circ \rightarrow 0^\circ \rightarrow -90^\circ$ rotation in θ or a $180^\circ \rightarrow 0^\circ \rightarrow -180^\circ$ rotation in ϕ . Instead, the rotation is less than a full circle. Thus, we believe the field rotation in the magnetic cloud and the observed enhanced Fe ionization state throughout the magnetic cloud are support for the conclusion that the observed ICME had the properties predicted from Figure 7.1 and that Ulysses passed through the edge of the ICME.

The SWICS data at the bottom of Figure 7.14 exhibits strong fluctuations in ionization state that are not being resolved. This explains why inferred temperatures are less than the > 6 MK inferred in the corona using UVCS. This apparently

filamentary structure is not present in the magnetic field, which has the typical relatively smooth structure of a magnetic cloud. Figure 7.15 shows this point by the strong field strength fluctuations outside the ICME in comparison to the near absence of such fluctuations inside the ICME. The explanation for the charge state fluctuations in the absence of magnetic field fluctuations is, as stated above, that the Fe must come from many different source regions. The reconnection between the CME and the post flare loops that forms the outer shell around the CME shown in Figure 7.1 must be patchy, bursty, and localized, as is often the case in reconnection observed elsewhere in space plasmas. The different ionization Fe states, which flow up and around the CME, have been created by reconnection in different source regions at different times. In this scenario, essentially all field lines reconnect to form the smooth outer shell of the magnetic cloud but the structured history of each field line is reflected in the structure of the Fe ionization state.

In a recent paper Grigis & Benz (2005) report RHESSI direct observations of reconnection along an arcade of magnetic loops similar to the EIT arcade previously described here. They interpret their data, which show many distinct x-ray emission peaks at different times, as evidence of “elementary flare bursts”, that is, as evidence of reconnection processes which progress irregularly along the arcade. Ulysses observations of highly fluctuating Fe ionization states may represent the interplanetary imprint of such reconnection pattern, even if we are obviously unable to trace individual data back to the precise location where reconnection is occurring in the corona. EIT data, however, support this interpretation, as the location of the brightest loop changes in time.

7.8 Discussion and conclusions

The propagation of a CME in the solar atmosphere has been studied by Lin (2002), who found that the average Alfvén Mach number for the inflow into the reconnection site (i.e., the velocity of plasma flowing into the reconnection site in units of the local Alfvén speed) needs to be larger than 0.013, in order to allow the flux rope to escape into the interplanetary space. Direct measurements of the plasma inflows are extremely scanty. Yokoyama et al. (2001) gave an upper limit of 5 km/s for the inflows around an X-type neutral point over flare loops, while Lin et al. (2005) gave values ranging between $10.5 \leq v_{in} \leq 106$ km/s for inflows near the CS in a fast CME event (velocities on the order of 1500 to 2000 km/s for the leading edge/core of the CME). The latter values refer to measurements taken over 10 minutes at the beginning of the CME event and are likely to decrease as the event evolves.

There is no possibility to detect in our spectra such low velocities, because the corresponding Doppler shift is too small. Nevertheless, we tried to get some information about inflows and magnetic fields in the reconnection region by parametrizing inflow values and identifying those which give reasonable magnetic field B_{in} in the corona adjacent to the CS. To this end we write the equations (in *cgs* units) for

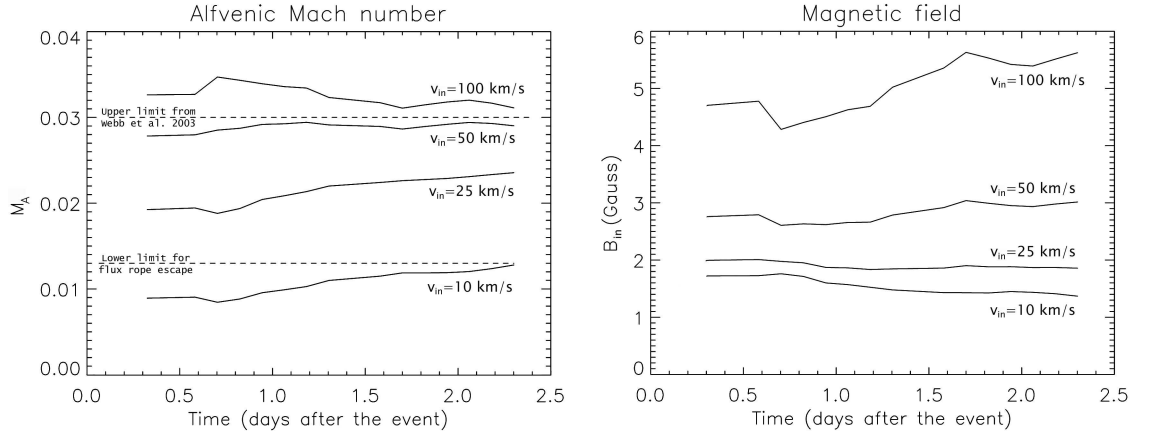


Figure 7.16: Left panel: temporal profile of the Alfvénic Mach number M_A , for different values of inflow velocities. The dotted horizontal line gives the threshold value of M_A which still allows the CME to escape from the solar atmosphere. Right panel: temporal profile of the magnetic field B_{in} in the inflow region for the inflows adopted in the left panel. No values are given for times when physical parameters have not been evaluated (gray areas in Fig. 7.13, Fig. 7.11).

pressure equilibrium and mass conservation across the CS. If the external plasma (p_{in}, ρ_{in}) is flowing into the CS with a speed v_{in} carrying in a magnetic field B_{in} , we can write:

$$p_{in} + \frac{1}{2}\rho_{in}v_{in}^2 + \frac{B_{in}^2}{8\pi} = p_0 + \frac{1}{2}\rho_0v_0^2 \quad (7.2)$$

$$\rho_{in}v_{in}h = \rho_0v_0l \quad (7.3)$$

where p_0 and ρ_0 are, respectively, the plasma pressure and density of the CS, where B_0 is negligible, and v_0 is the speed of the plasma flowing out of the top and bottom of the CS towards, respectively, the interplanetary space and the chromosphere. The CS is assumed to have a width l along the LOS and to extend radially over a characteristic length h .

Assuming v_{in} to take values between 10 and 100 km/s, h to have a characteristic value of \approx one solar radii and l to be on the order of 10^4 km, as previously assumed, we can solve Eq. 5 and 6 for B_{in} and v_0 , as all other quantities have been derived from observations. Hence, we prescribed constant values of v_{in} and solved the equations for the unknown quantities over the whole time interval of our observations. Results for M_A and B_{in} vs. time are shown in Figure 7.16.

The figure shows that inflow speeds ≤ 10 km/s correspond to M_A numbers that are too low to allow the CME to be ejected into the interplanetary space, hence they are seemingly not realistic. On the other hand, inflows as high as 100 km/s give magnetic field values increasing with time, a tendency shown very mildly also in the B_{in} vs. time profile for v_{in} of 50 km/s. Considering that the CS is eventually disappearing, as revealed by the fading emission in [Fe XVIII], an increase of B_{in}

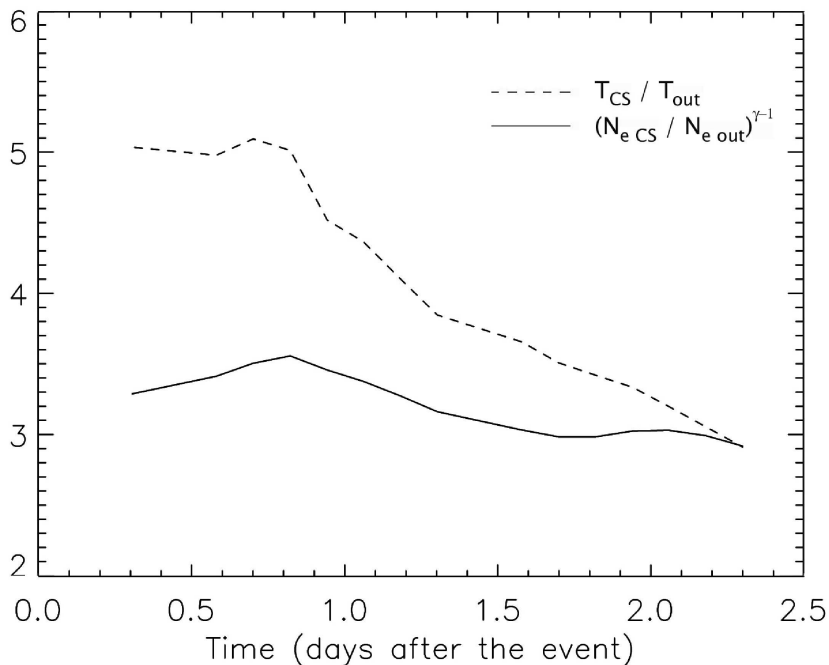


Figure 7.17: Temporal profile of the observed ratio of the CS to the quiet corona temperature (dotted line) compared to the ratio inferred from the observed densities under the assumption of an adiabatic compression of the plasma (solid line).

seems unrealistic and we are drawn to discard solutions for which this happens. Moreover, we point out that the M_A curve shown in Figure 7.16 with $v_{in} = 100$ km/s is above 0.03, which seems to be the M_A peak value reached tens of minutes after the event (Webb et al., 2003). We conclude that inflows towards the reconnection region should be higher than 10 km/s, but lower than 50-100 km/s. This result points to slightly higher values than those found by Yokoyama et al. (2001) and indicates that the inflow pattern should persist over the whole lifetime of the CS, as might be expected.

From the previous inflow values, the speed of the plasma outflows from the CS turns out to vary from $v_0 \approx 100$ km/s, for inflows of 10 km/s, to outflows ten times larger, for inflows of 100 km/s. These values give lower and upper limits for outflows: if we had the possibility of observing Doppler dimming effect, we might test our conclusions. However, Ko et al. (2003) and Lin et al. (2005) gave estimates of the outflow speed by measuring the height vs. time profile of LASCO blobs seen at altitudes larger than $2 R_{\odot}$. These authors give speeds of 500 to 1000 km/s, which are consistent with our values, considering that our CME was a slower event than the CMEs analyzed by Ko et al. (2003) and Lin et al. (2005).

Inflows towards the CS region may provide for heating the CS by adiabatic compression. However, no conclusion has been reached, yet, on whether this process

or ohmic heating by reconnection (not to mention other heating mechanism, as, for instance, slow-mode shocks) can account for the high temperatures in the CS. On the basis of the plasma parameters we derived, we have the possibility of checking on this issue by comparing the quiet corona with the CS plasma. In case the external plasma undergoes an adiabatic compression flowing into the CS, we expect:

$$\frac{T_0}{T_{in}} = \left(\frac{N_{e,0}}{N_{e,in}} \right)^{\gamma-1}$$

where T_0 and T_{in} are, respectively, the CS and quiet corona temperature, while $N_{e,0}$ and $N_{e,in}$ are the corresponding electron densities. The plot in Figure 7.17 appears to indicate that, at a late stage of the event, adiabatic compression can provide for the high CS temperatures, while at earlier times other processes should be invoked. This is not unreasonable, as the current sheet erosion is likely to result in a reduced ohmic heating. This result holds as long as the CS thickness of 10^4 km, assumed so far, is constant in time.

Figure 7.17 shows that, ≈ 2 days after the event, temperature and density in the CS are still higher than ambient values. This is obviously confirmed by Figure 7.5 where emission from the [Fe XVIII] ion, typical of the CS, has not faded, yet, at the end of UVCS observations. This evidence points to a CS lifetime longer than 2 days. This duration is not uncommon for CS detected by UVCS: for instance, in Ciaravella et al. (2002) and Ko et al. (2003) CS are observed to last for ≥ 1 day. Prior to these observations, the duration of reconnection processes was usually inferred from either the time over which chromospheric ribbons kept separating or the time over which hot loops kept rising to higher altitudes. From the time history of the H_α ribbon separation and of the hot loop heights for the July 29, 1973 flare that was considered to be an ideal example for a case study (see e.g. Moore et al., 1980; Svestka et al., 1982), reconnection was recognized to go on for at least ≈ 10 hours. Hence, UVCS data considerably extended the time interval over which reconnection was observed to operate.

It is interesting to check on the duration of reconnection processes in theoretical models. Lin (2002) has pointed out the influence of the ambient corona in the evolutionary behavior of the CS. The isothermal atmosphere he first used in his model was superseded in his later simulations by the Sittler & Guhathakurta (1999) empirical atmosphere, based on Skylab White Light coronagraph observations and *in situ* Ulysses data. Because in the Sittler & Guhathakurta atmosphere the Alfvén speed keeps decreasing with height, the CS is not rapidly eroded and its persistence over \approx one day is easily predicted. Also, Lin (2002) showed how a weak background field slows down the rise of the CME and how the morphology of the field, whether it is compacted in a small region or not, sensibly affects the motion of the flare ribbons. Hence, while qualitatively we may say that the lifetime of the CS inferred in our work can be consistent with predictions from the Lin & Forbes (2000) model, observations of the magnetic field and a better knowledge of the ambient atmosphere is needed to be able to simulate theoretically results inferred from UVCS observations. To our

knowledge, this is a relevant issue that has not been fully explored, yet.

Throughout this work we have been assuming ionization equilibrium. To check whether this is a realistic assumption, we computed collisional ionization and autoionization rates, radiative and dielectronic recombination rates, as a function of time, for transitions between Fe XIV and Fe XV and between Fe XVII and Fe XVII-I. We selected these ions, because are those from which we calculated the electron temperatures and, as a consequence, the other parameters in the CS. Over the range of temperature covered by our data, the highest rates are those for dielectronic recombination processes, which are on the order of a few units $\times 10^{-11} \text{ cm}^3\text{s}^{-1}$. At the beginning of our observations, with $T_0 \approx 8 \cdot 10^6 \text{ K}$, $N_{e,0} \approx 6.5 \cdot 10^7 \text{ cm}^{-3}$ recombination times are on the order of 500 s. Plasma flowing into the current sheet at $\approx 20 \text{ km/s}$ crosses a 10^4 km CS in about $\approx 500 \text{ s}$: hence we can roughly assume that atomic processes occur over characteristic times comparable with the time the plasma takes to cross the CS. Analogously, at the end of the observations, when inflows are, say, ten times slower than at the beginning of the event, the plasma crossing time is ten times longer and dielectronic recombination times (for $T_0 \approx 4 \cdot 10^6 \text{ K}$, $N_{e,0} \approx 7.5 \cdot 10^7 \text{ cm}^{-3}$) are on the order of 300 s. We conclude that ionization equilibrium seems to hold throughout the CS lifetime: we also point out that the CS cooling seems to occur on a longer time scale than the $\approx 5\text{--}10$ minutes time scale of atomic processes.

With regard to Ulysses measurements, the ICME resulting from the 26 November CME was already identified by Poletto et al. (2004). Here, a closer examination of that ICME was carried out by examining the full set of measurements made by SWOOPS, VHM/FGM, and SWICS. These data were shown in Figures 7.14 and 7.15. The data permitted separating the two ICMEs in the MIR on DoY 347-353 through examination of magnetic field rotations in the magnetic cloud. This separation was not unique, but the interpretation was independent of this. The interpretation led to the conclusion that the Fe ionization state was elevated, with strong fluctuations, from $\sim 10+$ to $\sim 16+$ throughout the entire ICME produced by the 26 November CME. This implies both that the model shown in Figure 7.1 fits the *in situ* observations and that Ulysses passed through the edge of the resulting ICME rather than the center. The fluctuations in the Fe ionization state, together with a smooth magnetic field, suggest the reconnection in the coronal current sheet that produced the Fe XVII was filamentary and bursty.

Chapter 8

Coronal & cometary parameters from sungrazer observations

8.1 Introduction: sungrazer observations

Sungrazing comets have a perihelion distance of a few solar radii and typically never survive after the perihelion passage. Before the launch of SOHO not many sungrazers had been identified ($\approx 25\text{--}30$), but with the LASCO coronagraphs the number of discovered sungrazers increased very quickly. Only one month after the launch of the SOHO mission, on January 1996, the first Kreutz sungrazer has been discovered in the LASCO/C3 coronagraph images and in the following months several more comets have been found, revealing the potential of the SOHO mission as a comet discoverer: between the launch of SOHO and August 2005, LASCO has detected 1000 sungrazing comets!

Before the SOHO mission only one sungrazer (the Ikeya-Seki comet) has been spectroscopically observed, from the ground, when it was at an heliocentric distance of $\sim 15 R_{\odot}$. The SOHO/UVCS spectrometer aboard the SOHO satellite, with its slit set along the comet trajectory, has been able, over the past few years, to observe a few sungrazers mostly in the Hydrogen $\text{Ly}\alpha$ and $\text{Ly}\beta$ lines. From these observations it is possible to derive coronal parameters along the comet trajectory and cometary characteristics, like the nucleus size and the outgassing rate (Raymond et al., 1998b; Uzzo et al., 2001).

In this work we focused on the C/2001 C2 sungrazing comet (SOHO-294 in the SOHO-team's numbering), a member of the Kreutz family observed on February 7, 2001 by UVCS between the projected distances (on the plane of the sky) of 7.41 and 1.78 R_{\odot} . As shown by LASCO images (see Figure 8.1), the comet approached the Sun from the South-East quadrant at a position angle (i.e. the angle measured counterclockwise from the celestial North through East) of about 100° , projected onto the plane of the sky. In Figure 8.1 we show the visual appearance of the comet C/2001 C2 as seen by the LASCO/C3 coronagraph on February 7, 2001; as C/2001 C2 approached the Sun, it progressively disappeared from the LASCO images and

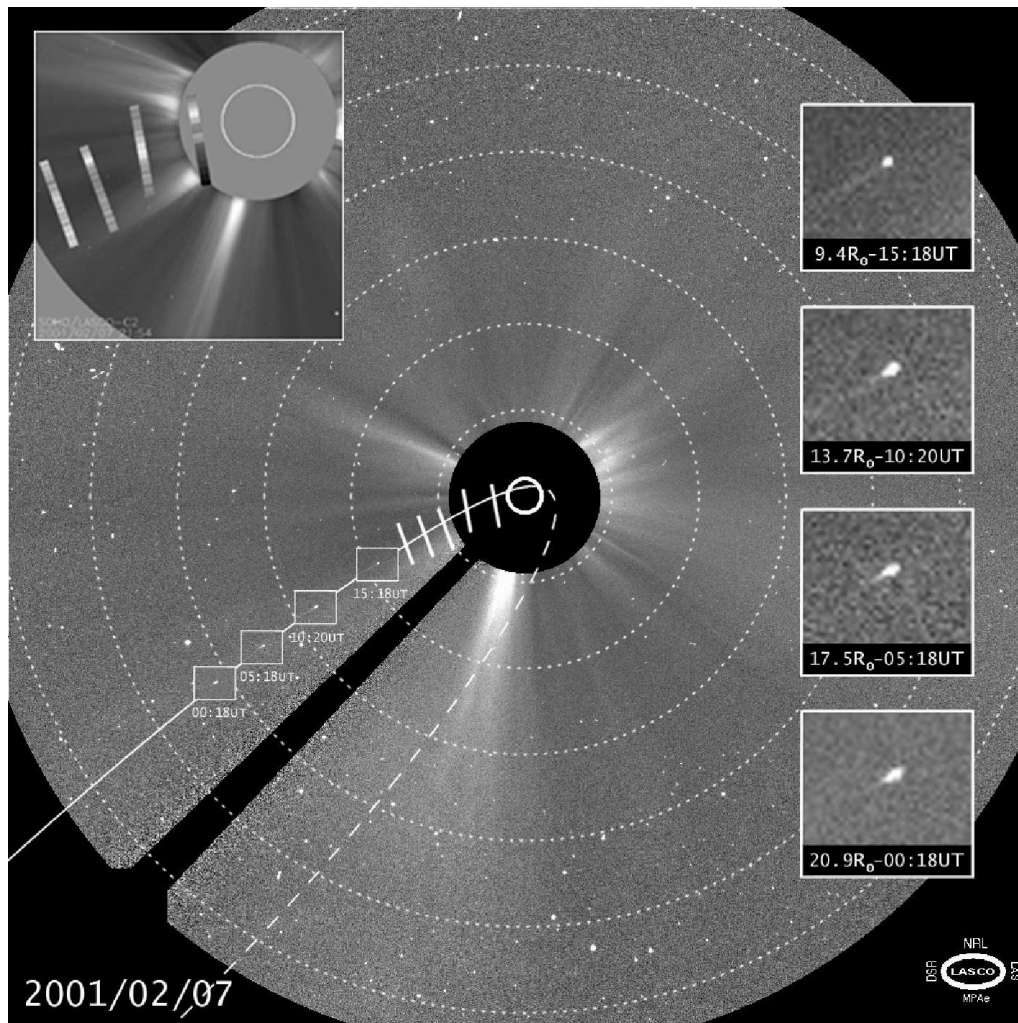


Figure 8.1: The C/2001 C2 comet as observed by LASCO/C3: in this panel we superposed onto the 7 February 2001, 10:42 UT LASCO/C3 frame the cometary LASCO/C3 images at 00:18, 05:18, 10:20 and 15:18 UT; the different UVCS slit heliocentric distances are also shown. The dotted circles are drawn at 5, 10, 15, 20, 25 and 30 R_{\odot} . In order to compare the orbit of the comet with the positions of the UVCS slit we plotted also the pre-perihelion (solid line) and expected post-perihelion (dashed line) C/2001 C2 trajectory as computed from the orbital parameters. In order to show the coronal morphology at lower levels, we superpose onto the LASCO/C2, 21:54 UT image (upper left panel) the UVCS Ly α coronal intensity before the comet arrival at the projected heliocentric distances of 1.78, 3.44, 4.94 and 6.17 R_{\odot} (the UVCS Ly α at 7.41 R_{\odot} has not been plotted because it is out of the LASCO/C2 field of view).

completely sublimated before perihelion. Superimposed onto the LASCO images we show also the orbit of the comet, computed from the orbital parameters given in the Minor Planet Electronic Circular (MPEC) 2001 – C09 and projected onto the plane of the sky.

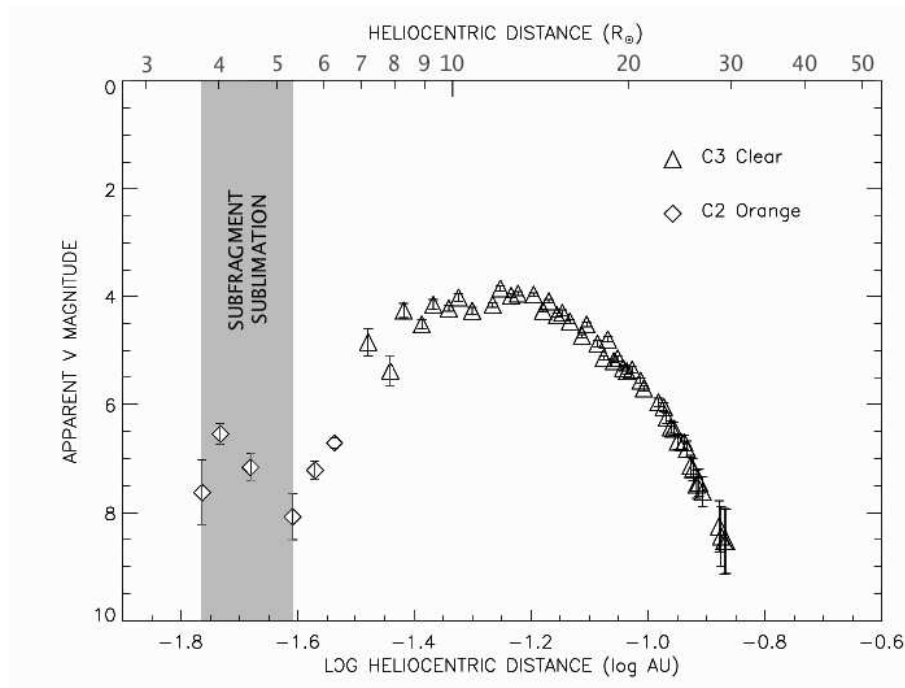


Figure 8.2: The C/2001 C2 lightcurve as measured from LASCO/C2 and LASCO/C3 apparent visual magnitude. The secondary brightening after the main peak ($\sim 12.1 R_{\odot}$) has been interpreted like a possible fragmentation event which probably occurred farther from the Sun: if the fragment has a lower erosion rate than the main nucleus it can be exposed in the final stage of the sublimation of the comet (grey zone).

Figure 8.2 gives the C/2001 C2 lightcurve (i.e. the variation of the sungrazer magnitude with the heliocentric distance of observation) built from LASCO/C2 and C3 data. The Figure shows that, after the main peak of the lightcurve at $\sim 12.1 R_{\odot}$, C/2001 C2 brightens again, starting from $\sim 5.3 R_{\odot}$. The presence of a maximum in the lightcurve is typical of sungrazers: due to the increase in solar flux, the sungrazer lightcurves show a rapid increase in intensity as the comet approaches the Sun. Because the visual magnitude is dominated by light scattered by dust, this increase corresponds to an increase in the total cross-sectional area of dust particles exposed to the solar flux, related in part to an increase in the rate of gas and dust production. Then, after a peak in intensity, the lightcurves rapidly decrease, probably because coma dust grains sublimate at a rate which exceeds the production rate. In every case, however, the fading after the main peak stops at about $7 R_{\odot}$ and is followed by different kinds of lightcurves: in some cases the lightcurve flattens, while in others there are some secondary increases in brightness. The latter have been explained by Sekanina (2003) with the introduction of an erosion model that predicts the existence of subfragments with a lower than average susceptibility to erosion. The subfragments, given the large pixel size of the coronagraph detectors, are in general optically unresolved; however the author showed that, introducing one

or more nearby companions with a slower erosion rate, it is possible to reproduce the observed lightcurves of many sungrazers.

Hence, following Sekanina (2003), a possible explanation for the C/2001 C2 secondary brightening is that a fragmentation of the cometary nucleus occurred farther from the Sun: if the fragment traveling with the comet has a lower erosion rate than the main nucleus, it can survive after the disintegration of the main part and can be observed in white light below $\sim 5.3 R_{\odot}$ (grey zone in Figure 8.2). An alternative explanation is that the comet fragments at about $5.3 R_{\odot}$, exposing more surface area to sunlight and increasing its outgassing rate for a short time until the fragments sublimate.

A first question on the UVCS observation of comets we want to address is how and why does the UVCS spectrum change, when a comet enters the field of view of the experiment. Physical processes leading to the formation of the observed cometary UV emission are different from those (typical of the coronal plasma) we described in Chapter 3. Hence, it is necessary to introduce here different plasma diagnostic techniques which apply only in this peculiar case, when a cool cometary plasma interacts with the hot corona. In the next sections we first describe UVC-S data, to show how they changed at the time of the comet transit through the instrument slit (§ 8.2.1) and we make a comparison between the observed coronal and cometary line profiles (§ 8.2.2). We then illustrate the physics of cometary line formation (§ 8.3) and the origin of a secondary component observed in the Ly α line profile. Hence, we describe a model we used to derive both cometary and coronal parameters from our observations (§ 8.4). Finally we give our results (§ 8.4.1) and we show how UVCS data have been used also to estimate the cometary dust grain number density (§ 8.4.2).

8.2 UVCS data

Observations of comet C/2001 C2 were made when the comet was at heliocentric distances of 7.42, 6.17, 4.98, 3.60 and 2.20 R_{\odot} , as shown in Figure 8.1. At each heliocentric distance we acquired a series of spectra with an exposure time of 200 s for a total observing time of about 70 minutes. In order to follow the comet orbital motion, the position angle of the slit center was set equal to 110° for the first three heliocentric distances and 100° for the last two observations (see Figure 8.1). The slit width was 150 μm wide, giving a field of view of $42''$ (projected slit width) times $40'$ (projected slit length); data have been acquired with a spatial resolution of $21''$ (which corresponds to a projected distance on the plane of the sky of $\simeq 15200$ km) and a spectral resolution of 0.595 \AA (0.549 \AA for the redundant channel) given by the 150 μm slit width. The selected spectral windows covered ranges between 1024.3 – 1039.4 \AA , 997.2 – 1000.4 \AA , 989.3 – 992.9 \AA and 975.8 – 986.8 \AA (1211.1 – 1221.1 \AA for the redundant channel). These windows allow observations of coronal plasma in the lines of the O VI $\lambda\lambda 1032, 1037$ \AA doublet, of Si XII $\lambda 499$ \AA line (second order)

and of H I Ly α and Ly β lines. The 975.8 – 986.8 Å window includes the C III λ 977 Å line, which allows us to estimate the amount of scattered light in coronal spectra, and it may possibly be present in cometary spectra as well. Moreover the 989.3 – 992.9 window (1205.4 – 1208.7 Å for the redundant channel) includes a blend of the N III λ 991.6 Å and Si III λ 1206.5 Å lines, possibly present in comet spectra.

The UVCS line emission at the time of the comet passage originates from a superposition of the cometary signal, the coronal and interplanetary emission (which might be important for the Ly α line) and the detector dark counts. The intensity of the Ly α line increases by up to a factor ≈ 8 with respect to the background coronal emission when the comet enters the UVCS field of view (see later, Table 8.1). Hence the identification of the cometary signal was made by calculating the average emission over exposures taken before the comet entered the UVCS field of view (UVCS sungrazer observations begin at each heliocentric distance 15–20 minutes before the comet transit into the slit) and subtracting this background from the following exposures. The comet gave a signal only when it was at the heliocentric distances of 4.98 and 3.60 R $_{\odot}$ (UVCS slit respectively at the projected altitudes of 4.94 and 3.44 R $_{\odot}$); moreover in the above spectral ranges the cometary emission is mainly observed in the H Ly α line. A transient weak emission was also detected in the Ly β line and in the N III – Si III window. Unfortunately the Ly β intensity was very low and has been used only to estimate the Ly α and Ly β percentage due to radiative and/or collisional excitation (see below). In the N III – Si III window we identify the observed emission as Si III λ 1206.5 Å rather than N III λ 991.6 Å or O I λ 990.8 Å, which falls somewhat off the wavelength observed. As we show in Figure 8.3, shortward of the Ly α peak we see an intensity of about 7 times the background, that we ascribe to the Si III λ 1206.5 Å line. This emission is not a fluctuation in the Ly α wing intensity as it rises above background by more than 3σ . This interpretation is possibly supported by the presence, in our data, of a background Ly α emission (see § 8.4.2) which is due to interaction between cometary silicate dust grains and coronal plasma: hence it is likely that the detected counts are due to Si III ions coming from sublimation of silicate grains.

Because in our data no C III signal was recorded, no correction has been made for scattered light from the solar disk. We note that the C III λ 977 Å line was observed by UVCS in spectra of the Comet Kudo-Fujikawa (Povich et al. 2003) and has been ascribed to carbon atoms evaporated from the dust and then photoionized. This process may be analogous to the process we invoke to account for the Si III λ 1206.5 Å line on our spectra. In the following we focus on the cometary emission at 4.98 and 3.60 R $_{\odot}$ in the Ly α line.

8.2.1 The observed emission

In Figure 8.4 we show composite images of the integrated Ly α intensity, from all the available exposures at the two heliocentric distances. These images have been scaled in arcsec in the direction normal to the slit taking into account the cometary

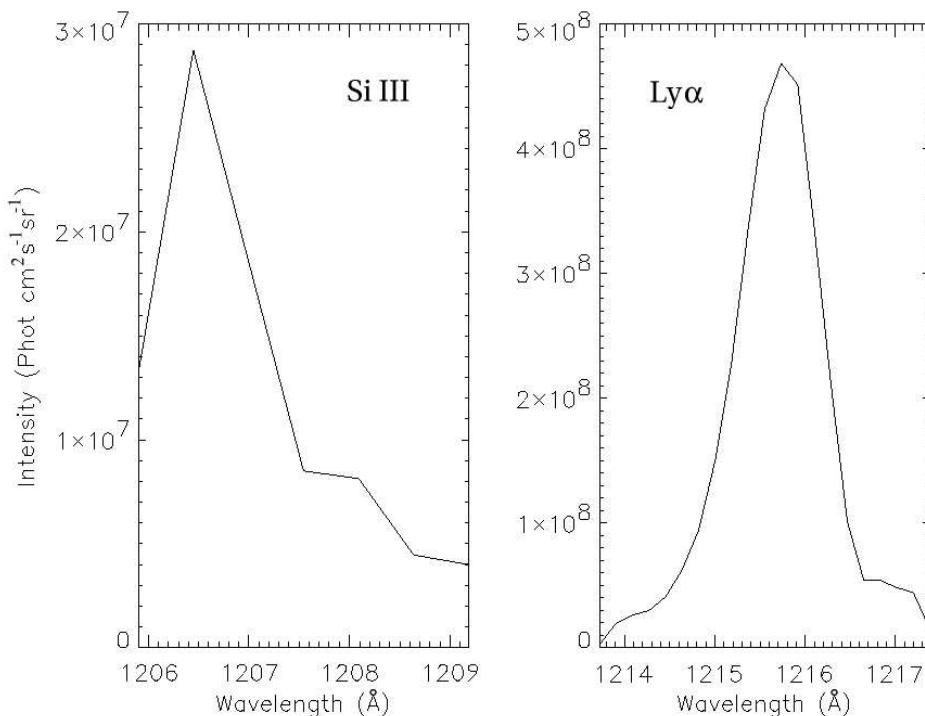


Figure 8.3: Line profiles for the Si III (left panel) and the Ly α lines (right panel) at 4.98 R_{\odot} (average over 3 exposures).

velocity component perpendicular to the slit v_{\perp} and the duration of each exposure. They give a realistic representation of the comet's appearance provided there are no major changes in the comet during the time it takes to cross the UVCS slit. The left panels (i.e. before the subtraction of background Ly α) show that at 4.98 R_{\odot} the comet is adjacent to a weakly emitting coronal structure, which is crossed by the comet at 3.60 R_{\odot} . This very small coronal feature was observed in the UVCS Ly α intensity at 2.20, 3.60 and 4.98 R_{\odot} , but is hardly detectable in the LASCO/C2 image (see Figure 8.1). In the 3.60 R_{\odot} panels in Figure 8.4 (top), because of the low intensity of the coronal background with respect to the cometary signal, the Ly α intensity has been plotted in logarithmic scale in order to show both the coronal and cometary emission.

A comparison between the top and bottom panels of Figure 8.4 reveals a very interesting difference between the comet structure at 4.98 and 3.60 R_{\odot} : at the greater heliocentric distance the image shows the presence of two tails, only one of which is observed at the lower altitude (we hereafter refer to the northernmost and brighter tail as tail 1, tail 2 being the weaker structure). Also, at 4.98 R_{\odot} the main tail intensity seems to decrease with time (or distance) more slowly than does the single tail at 3.60 R_{\odot} . A first interpretation of the data could be that

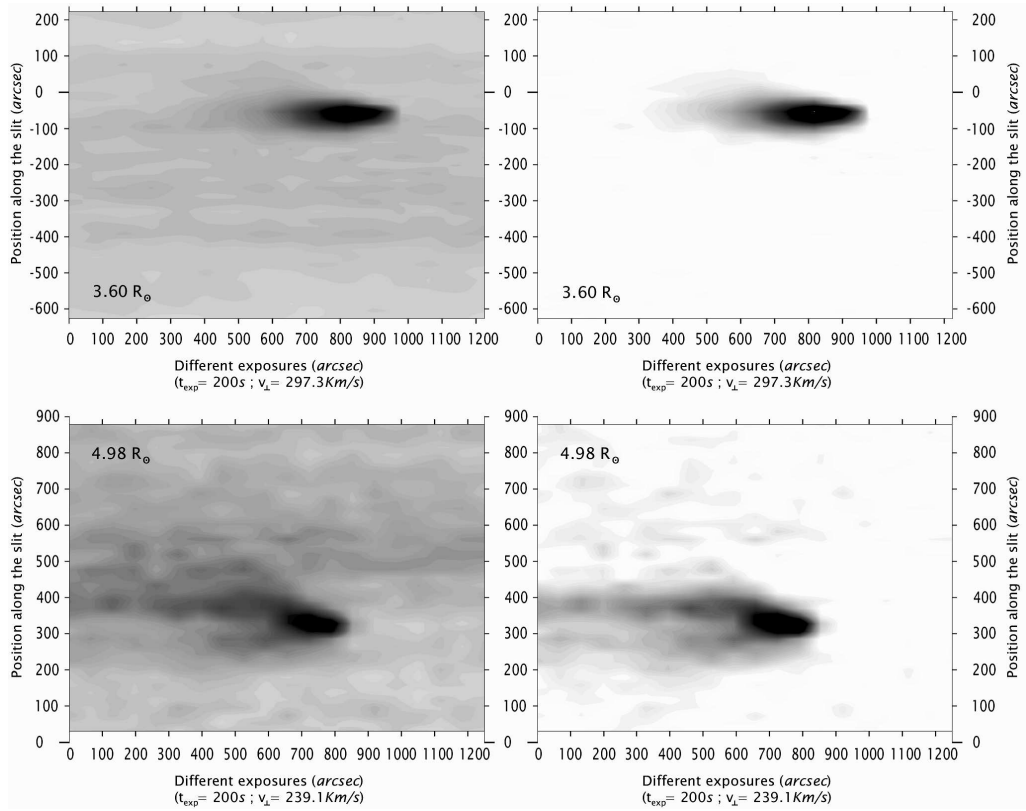


Figure 8.4: Composite Ly α images of C/2001 C2 observed at 3.60 (top panels) and 4.98 R_{\odot} (bottom panels). At both heliocentric distances we give the Ly α images before (left) and after (right) the subtraction of the background Ly α . note at 4.98 R_{\odot} the presence of two tails and the longer Ly α signal persistence after the comet passage with respect to the 3.60 R_{\odot} observation. In the y axis 0 marks the UVCS slit center position; North is up. These images have not been corrected for the cometary motion along the slit.

the comet is composed of two fragments at 4.98 R_{\odot} and of a single object at 3.60 R_{\odot} . Nevertheless three other interpretations for the origin of two tails are possible: first the two tails could be generated by a single object, if one hypothesizes that on the nucleus surface there are two emitting regions from which plasma and dust are ejected. However we have to consider that, for sungrazing comets, due to the small heliocentric distances, the nucleus is exposed to an extremely high solar flux ($\sim 2.5 \cdot 10^9$ erg $\text{cm}^{-2}\text{s}^{-1}$ at 5 R_{\odot}), hence it is difficult to imagine a nucleus with only two emitting regions: probably the whole nucleus surface is active and this interpretation can be excluded. A second possible interpretation is that cometary dust particles have been ejected from a single object at two different times: model computations (Z. Sekanina, personal communication) show that the sector in which dust ejected from the comet at different times should lie is between latitudes of 1 $^{\circ}$ S and 15 $^{\circ}$ S and the two tails in Figure 8.4 are located about between 4 $^{\circ}$ S and 12 $^{\circ}$ S, hence exactly in the same sector. In this case, tail 1 would be the younger

emission, made up mostly of tiny, sub-micron sized grains, while tail 2 would be the older emission, containing (at the observed distances of up to $\sim 200''$) relatively large particles. In principle we cannot exclude this second interpretation for the origin of the two tails: However, under this interpretation it is not easy to explain why the comet shows 2 tails at $4.98 R_{\odot}$ and only one tail \sim one hour later at $3.60 R_{\odot}$ (see Figure 8.4). A third interpretation of the origin of two tails could be that the enhanced $\text{Ly}\alpha$ emission close to the small coronal streamer (tail 1) originates from interaction between cometary plasma and the streamer itself: we rule out this possibility in § 8.4. In conclusion, in this study we will concentrate only on the two fragment interpretation assuming that the 2 observed tails are the signatures of 2 separate fragments.

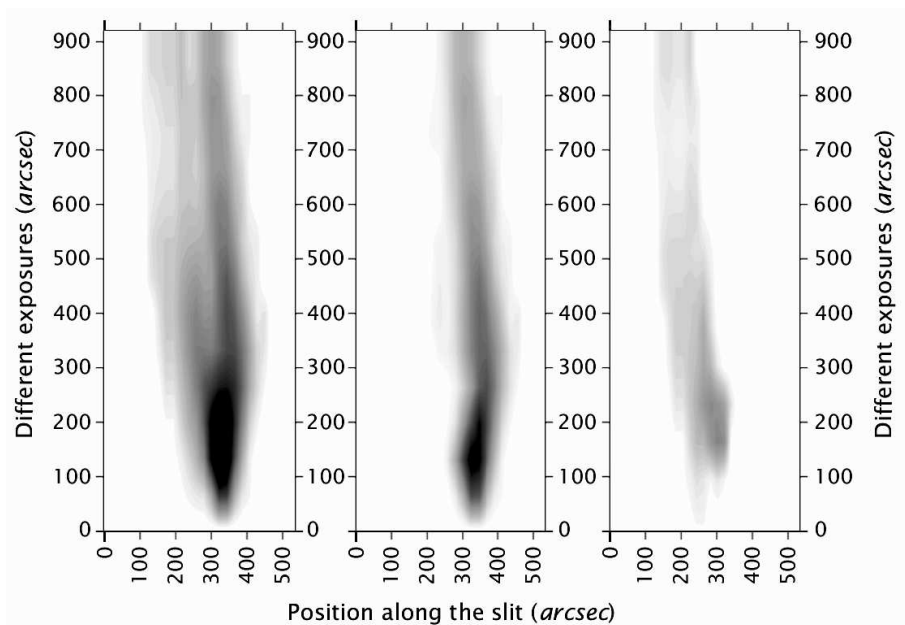


Figure 8.5: Left panel: composite $\text{Ly}\alpha$ image of C/2001 C2 observed at $4.98 R_{\odot}$ and shifted for the cometary motion along the slit (North is on the right). Middle and right panels: tail 1 and tail 2 $\text{Ly}\alpha$ images obtained respectively by symmetric reflection of the northward half of tail 1 and by subtraction of the tail 1 isophotes from the observed image (see text).

In order to separate the contribution of the two tails, we assumed that the cometary $\text{Ly}\alpha$ intensity distribution along the slit is symmetric around the peak, as suggested by the image at $3.60 R_{\odot}$. After correcting the $\text{Ly}\alpha$ images for the cometary motion in the direction parallel to the slit (using the computed values of the cometary velocity component v_{slit} along the UVCS slit of $v_{slit} = 58.2$ and 107 km/s, respectively at 4.98 and $3.60 R_{\odot}$), we assumed that tail 1 intensities northward of their peak values are, at each time, unaffected by tail 2 and we built the intensity distribution of tail 1 by simply mirroring its northern isophotes (Figure 8.5, middle panel). The secondary tail isophotes have been obtained by subtracting from the

original Ly α image (Figure 8.5, left panel) the contribution of tail 1 (Figure 8.5, right panel). We note here that, with this procedure, the number of Ly α counts we attribute to tail 1 and/or to tail 2 depends also on the subtraction of the coronal background: in particular, the intensity of the small coronal streamer mentioned above can slightly change during the observation. For instance, an underestimate of the streamer intensity, which lies northward of tail 1, could lead to an overestimate of the tail 1 Ly α counts, hence, by reflection and subtraction, an underestimate in tail 2. However, as we verified performing the same analysis with different values of the streamer intensity, this indetermination can lead to a systematic error of about 30 % over all the derived parameters. Hence the errors we give in the following sections are only statistical errors from the fit (see later), but all parameters may be affected by the systematic error mentioned above.

8.2.2 Ly α line profiles

We now proceed to analyze the Ly α line profiles for the coronal and cometary signals. To this end we made a Gaussian fit to the Ly α profiles obtained at the position along the slit where the line intensity peaks. Average coronal profiles have been obtained by summing over all the exposures prior to the comet arrival and over all the bins where we later observed a cometary signal: this coronal background has been subtracted from the cometary signal before fitting the comet line profiles.

Table 8.1 gives the parameters derived from the gaussian fits to the cometary and coronal Ly α profiles. As we mentioned, the Ly β line signal was too weak to allow us to derive a statistically significant profile. The FWHM from the gaussian fit has been corrected for the instrumental profile (see § 4.3); from the corrected FWHM (i.e. FWHM_c in Table 8.1) we derived the kinetic temperature T_k . As observed also by Uzzo et al. (2001) for comet C/2000 C6, at 4.98 R $_{\odot}$ the shift $\Delta\lambda$ between the cometary and coronal profile (or, more precisely, the shift $\Delta\lambda = (\lambda_c^{com} - \lambda_c^{cor})$ between the centroids of the coronal and cometary line profiles) is, in the first exposure, significant. This shift can be ascribed to partial filling of the UVCS aperture by the comet, which results in a profile shifted towards longer wavelengths.

Table 8.1 shows that at 3.60 R $_{\odot}$ the width of the Ly α profile from the comet is the same as the coronal width. This means that the coronal plasma and the plasma emitting the cometary signal have the same temperature, an effect which will be discussed in the next Section and agrees with the results obtained by Uzzo et al. (2001), in his observations of the C/2000 C6 sungrazing comet. Because at 3.60 R $_{\odot}$ we are sampling coronal plasma from a weakly emitting filamentary structure, we may compare the temperature we derived with typical streamer values: for instance Strachan et al. (2002) found at 3.60 R $_{\odot}$ a perpendicular kinetic temperature for Ly α of $1 - 2 \cdot 10^6$ K along the streamer axis, in agreement with our value.

At 4.98 R $_{\odot}$, Table 8.1 suggests that the cometary Ly α profile is wider than the coronal profile at that heliocentric distance, but, as shown by a more sophisticated study, there are two components to the profile. For a detailed analysis of the line

Cometary Ly α profile						
h (R_{\odot})	t_{exp} (UT)	$\Delta\lambda$ (\AA)	$FWHM$ (\AA)	$FWHM_c$ (\AA)	T_k (10^6 K)	$I(Ly\alpha)$ (phot/cm 2 s sr)
4.98	19:18	0.260	1.166	1.016	1.37	$3.35 \cdot 10^9$
	19:22	0.131	1.119	0.9611	1.23	$3.09 \cdot 10^9$
	19:25	0.123	1.123	0.9661	1.24	$2.40 \cdot 10^9$
	19:28	0.121	1.034	0.8602	0.983	$1.16 \cdot 10^9$
3.60	20:18	0.114	1.087	0.9231	1.13	$3.84 \cdot 10^{10}$
	20:21	0.0621	1.001	0.8211	0.896	$5.12 \cdot 10^{10}$
	20:25	0.0402	1.045	0.8740	1.01	$2.49 \cdot 10^{10}$
	20:28	0.0561	1.032	0.8587	0.980	$1.31 \cdot 10^{10}$
Coronal Ly α profile						
h (R_{\odot})	t_{exp} (UT)	$\Delta\lambda$ (\AA)	$FWHM$ (\AA)	$FWHM_c$ (\AA)	T_k (10^6 K)	$I(Ly\alpha)$ (phot/cm 2 s sr)
4.98	18:54–19:18	–	0.9325	0.7356	0.719	$9.71 \cdot 10^8$
3.60	20:04–20:18	–	1.042	0.8706	1.01	$4.84 \cdot 10^9$

Table 8.1: Ly α line profile parameters from gaussian fits

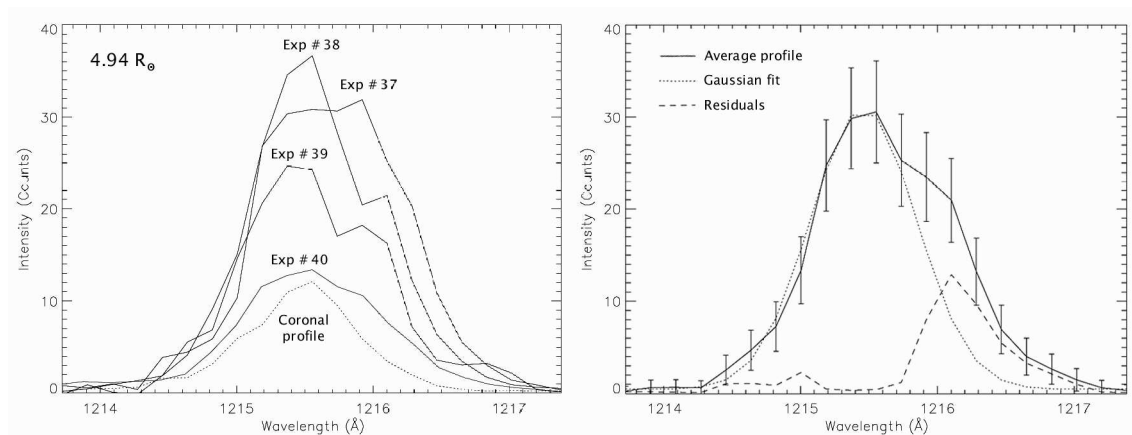


Figure 8.6: Left: cometary Ly α line profiles at 4.98 R_{\odot} (solid line, coronal profile subtracted) for the first four exposures after the comet entered the UVCS slit. The shape of the Ly α profile in first exposures may be interpreted as a superposition of two profiles (see text): the red – shifted one disappears after the fourth exposure and the cometary line approaches the coronal profile (dotted line). Right: cometary profile averaged over the first three exposures (solid), gaussian fit over the main component (dots) and the secondary profile (dashes).

profiles at this heliocentric distance, we built the Ly α profiles for tail 1 over the bin with peak Ly α intensity from each of the first 4 exposures after the comet entered the UVCS slit. These are given in Figure 8.6 (left panel). The Figure shows that a secondary Ly α peak, red – shifted with respect to the main component, and weakening progressively with time (it can hardly be identified after the 4th exposure), may be present in the first exposures. In order to increase the statistical significance of the secondary profile - if any - we averaged the Ly α profile over the first three exposures (see Figure 8.6, right panel). Superposed onto this we also show a gaussian fit to the main component: the fit has been constructed taking into account only the blue side of the line and assuming the profile to be symmetric around its peak. The profile of the secondary component, calculated from the difference between the observed and the gaussian predicted intensities is also shown. Bars on the Figure represent the 1σ error bars: intensities of the secondary component are above the 1σ uncertainty level. We conclude that a possibly significant secondary, red–shifted, Ly α component is present in the first four exposures after the comet entered the UVCS slit. The identification of two components in the Ly α line profile has been possible only in tail 1, because of the lower intensity measured in the secondary tail profiles; however, the Ly α profiles observed in tail 2 also appear to be wider than the coronal profile, suggesting that this secondary Ly α component is present in both tails. In the following, we consider the Ly α profile at 4.98 R_{\odot} as the sum of two components: the origin of the secondary component and the 0.6 Å relative Doppler shift are discussed in § 8.3.

The FWHM of the main component of the Ly α profile (Figure 8.6, dotted profile

in the right panel) is about 0.9 \AA , hence consistent with the coronal width evaluated from the pre-comet exposures (see Table 8.1). Because at this heliocentric distance we are in a low latitude open field region, we should compare the value we found with values given in the literature for the $\text{Ly}\alpha$ width in low latitude coronal holes. However, there are no $\text{Ly}\alpha$ width values for low latitude coronal holes in the literature and, since at $4.98 R_{\odot}$ the field lines of coronal streamers are probably open, we can compare our values with those of Kohl et al. (1997) and Frazin et al. (2003) who found in an equatorial coronal streamer at $5 R_{\odot}$ a $1/e$ $\text{Ly}\alpha$ width corresponding to $1.5 \cdot 10^6 \text{ K}$, in agreement with our value given in Table 8.1 of $\sim 1.2 \cdot 10^6 \text{ K}$. Polar coronal hole measurements give $T_k \sim 3.8 \cdot 10^6 \text{ K}$ above $4.0 R_{\odot}$ (Cranmer et al. 1999), which is larger than what we observed in the comet.

8.3 Physics of cometary and coronal $\text{Ly}\alpha$ emission

We illustrate briefly here the mechanisms by which the interaction between the cometary and coronal plasmas results in an enhanced $\text{Ly}\alpha$ emission (Raymond et al., 1998b; Uzzo et al., 2001). First we have to check whether the observed $\text{Ly}\alpha$ line is radiatively excited or has a significant collisional component. As we described in § 3.3.1, for $\text{Ly}\alpha$ and $\text{Ly}\beta$ lines it is possible to separate radiative and collisional components by solving a simple linear system (see equations 3.52) which requires the collisional and radiative $\text{Ly}\beta/\text{Ly}\alpha$ ratios to be known ($R_{\beta\alpha,c}$ and $R_{\beta\alpha,r}$, respectively). These ratios depend on well known atomic factors and on the $\text{Ly}\alpha$ and $\text{Ly}\beta$ disk intensities. At the high temperatures typical of coronal plasma ($\log T_e \sim 6.0$) $R_{\beta\alpha,c} \simeq 0.14$, while using $I_{disk}(\text{Ly}\alpha) = 6.678 \cdot 10^{15} \text{ phot cm}^{-2}\text{s}^{-1}\text{sr}^{-1}$ from SOLSTICE (*SOLar STellar Irradiance Comparison Experiment*) data and $I_{disk}(\text{Ly}\beta) = 9.947 \cdot 10^{13} \text{ phot cm}^{-2}\text{s}^{-1}\text{sr}^{-1}$ from SUMER (*Solar Ultraviolet Measurements of Emitted Radiation*) data both measured on 14 May, 2001 (the Sumer observation closest in time to our observations), we computed a $R_{\beta\alpha,r} \simeq 0.0021$. From these values it turns out that both at 3.60 and $4.98 R_{\odot}$ about 100% of cometary $\text{Ly}\alpha$ originates from radiative excitation of neutral hydrogen, while the $\text{Ly}\beta$ radiative component is only $\sim 30\%$ of the total emission.

Hence, because the cometary $\text{Ly}\alpha$ line is only radiatively excited (as is usually the case in the corona, see e.g. Raymond et al., 1997) and, as we showed in the previous section, its width is not larger than the coronal line width, we can invoke two possibilities to explain its origin: either the enhanced $\text{Ly}\alpha$ intensity originates from photons scattered by hydrogen atoms created in the photodissociation of the water molecules ejected by the comet, or else the products of water dissociation interact with coronal protons and, by charge transfer processes, create the neutral hydrogen atoms with the kinetic temperature of the coronal protons, which then scatter $\text{Ly}\alpha$ line photons.

However, we point out that the $\text{Ly}\alpha$ signal from the products of dissociation of water would have a profile narrower than the coronal one and would disappear

shortly after the comet leaves the UVCS slit (Raymond et al., 1998b). Because the cometary profiles have the same width and the same centroid position as the average coronal profile, the second-generation neutral hydrogen atoms have the same bulk speed and kinetic velocity distribution as the coronal H atoms. We conclude that H atoms responsible for this emission formed from the interaction (charge exchange) of coronal protons with neutral atoms that are secondary products from the comet ejection of H₂O; because in the process $p^+ + H \rightarrow H + p^+$ the momentum transfer is very small (McClure, 1966), the newly formed H atoms have about the coronal proton velocity distribution. This conclusion is in agreement with previous findings by Uzzo et al. (2001) from the analysis of the C/2000 C6 sungrazer.

We can now discuss the origin of the secondary component observed at 4.98 R_⊙ in the Ly α profiles of tail 1, which we described in § 8.2.2. The secondary profile is observed only in the first 4 exposures, which amount to a total time of 800 seconds, which (see later) is very close to the characteristic time τ_{cx} for the charge exchange process discussed above. Hence, while the main profile is due to Ly α photons scattered by H atoms created by charge transfer with coronal protons (which are “at rest” with respect to coronal H atoms), we suggest that the secondary profile originates from those H atoms, created by H₂O photodissociation, which did not have enough time for charge exchange and, moving with the comet along the LOS, give a red – shifted profile. This hypothesis is supported by the narrow width (~ 0.5 Å) of the secondary profile shown in Figure 8.6: because the cometary material is “cooler” than the coronal plasma, the line has a smaller width¹.

In this scenario we may also explain why this secondary component is unobservable at 3.60 R_⊙: at 4.98 R_⊙ the comet is crossing a coronal hole region, hence the secondary Ly α intensity due to the H atoms moving inward with the comet ($v_r \sim 250$ km/s) and the main component due to the H atoms moving outward with the solar wind ($v_{out} \sim 170$ km/s; see Poletto et al., 2002) are both Doppler dimmed. On the contrary at 3.60 R_⊙ the comet is crossing a coronal streamer, hence only the secondary Ly α component due to the H atoms from water photodissociation is Doppler dimmed, while the main component comes from coronal H atoms with $v_{out} \sim 0$. As a consequence the expected ratio between the intensities of the two components is ~ 20 , making the secondary component unobservable. A possible objection to this interpretation comes from the kinetic temperature we derived from the secondary profile ($T_k \sim 2.5 \cdot 10^5$ K), higher than expected for cometary material.

An alternative explanation for the secondary Ly α component must be considered: the O atoms from the H₂O photodissociation have a cross section for the charge exchange process with coronal protons which is about the same as the H atoms charge exchange cross section (see e.g. Kimura et al., 1997), because the H and O First Ionization Potential are approximately equal. This means that H atoms

¹We note that the shift of about 0.6 Å between the main and the secondary Ly α profile in Figure 8.6 (corresponding to about 150 km/s) is larger than implied by the component $v_{LOS} \sim 80$ km/s of the cometary velocity derived from the orbital parameters. This inconsistency may be due to the uncertainty in separating the two components of the Ly α profile.

could form also by charge transfer with cometary O atoms; but, because O is about 16 times heavier than H, there may be some momentum exchange in the process. This might explain the red shift of the secondary component: because of the near equality of the cross sections for the two processes, we can assume that the number N_{Hp} of H atoms created by charge transfer between cometary H atoms and coronal protons is about twice the number N_{HO} of H atoms created by the same process with cometary O. Hence, assuming that these atoms are responsible for the secondary Ly α emission, we estimated that, in order to reproduce its intensity, each H atom scatters $\bar{g} = 0.62$ Ly α chromospheric photons per second. At $4.98 R_{\odot}$ in a static plasma we have $\bar{g} = 4.50 \text{ phot s}^{-1}\text{H}^{-1}$, hence we need a Doppler dimming factor of 0.14 to bring \bar{g} down to the value 0.62 we estimated. This corresponds to a plasma speed of $\simeq 260 \text{ km/s}$ (see Kohl et al., 1997), which agrees with estimates of the radial velocity v_r of the comet.

The explanation we gave above for the absence of the secondary component at $3.60 R_{\odot}$, holds also for this alternative explanation. However, an objection to this interpretation comes from Lindsay et al. (1996) who seem to imply that very little momentum transfer occurs in the charge exchange between O atoms and coronal protons.

A third possibility is that the comet produces enough gas to dynamically affect a small region of the corona it passes through. This can take the form of a bow shock (e.g. Raymond et al., 1998b). The comet produces about 10^{28} atoms per second at $4.95 R_{\odot}$, which is comparable to the number of atoms swept up per second in a cylinder of 10^{10} cm radius (which is \approx the mean free path for charge transfer), and length equal to the distance covered by the comet in one second, if the coronal density is in the range estimated below. Thus the cometary material can dynamically affect the coronal gas, but it is not clear whether or not a bow shock will form.

We are unable to make a choice among the interpretations we outlined and we leave this point open for future work.

8.4 A model for the observed Ly α emission

After identifying the atomic processes at work in the comet-corona interaction we show how the observed intensities allow us to derive the comet outgassing rate, the cometary nucleus dimension and the coronal density. To this end we need to establish a relationship between the unknown number \dot{N} of neutral H atoms produced by cometary outgassing per second and the observed Ly α intensity.

The mean lifetime τ_H of H atoms produced by photodissociation may be written as:

$$\tau_H = (\tau_{cx}^{-1} + \tau_{ion}^{-1})^{-1} \quad (8.1)$$

where the charge transfer rate τ_{cx}^{-1} and the ionization rate τ_{ion}^{-1} depend on the plasma conditions and are in general unknown; these rates increase as the comet approaches the Sun. However, at plasma conditions at $3.60 R_{\odot}$ (temperature of $\sim 10^6 \text{ K}$ and

relative velocity between coronal gas and cometary H atoms of about 250 km/s), it turns out that (Scholz & Walters, 1991; Uzzo et al., 2001):

$$\tau_{cx} = \tau_{ion} \simeq (3.1 \cdot 10^7 \text{ cm}^{-3}\text{s})/N_e \Rightarrow \tau_H = \frac{\tau_{ion}}{2} \quad (8.2)$$

At 4.98 R_\odot the relative velocity between coronal plasma and cometary H atoms increases because of the coronal plasma outflow velocity: for a low latitude coronal hole outflow velocity $v_{out} \simeq 170$ km/s (Poletto et al., 2002) we have a relative velocity of about 420 km/s and $\tau_{cx} \simeq 1.8 \cdot 10^7 \text{ cm}^{-3}\text{s}/N_e = \tau_{ion}/R_\tau$ ($R_\tau \equiv \tau_{ion}/\tau_{cx} = 1.72$). Hence in general $\tau_H = \tau_{ion}/(R_\tau + 1)$ with $R_\tau = 1$ and $R_\tau = 1.72$ respectively at 3.60 and 4.98 R_\odot .

The number N_{coma} (cm^{-3}) of neutrals moving with the comet and outgassed at a rate \dot{N} ($\text{cm}^{-3}\text{s}^{-1}$) is $N_{coma} = \dot{N}\tau_H = \dot{N}\tau_{ion}/(R_\tau + 1)$. These atoms undergo charge transfer with coronal protons at a rate τ_{cx}^{-1} , hence the comet, moving at a velocity v , leaves along its path a number $N_H = N_{coma}/(\tau_{cx}v) = \dot{N}R_\tau/[(R_\tau + 1)v]$ of neutrals per cm. This shows that N_H is independent of the electron density N_e , because an N_e increase corresponds to a greater number of neutrals created by charge transfer: these, however, have a shorter lifetime because of the increase of the ionization rate.

After the comet passage the Ly α starts decreasing with time: the number N_H of H atoms that the comet leaves along its path via charge transfer exponentially decays with a lifetime τ_{ion} and the cometary Ly α signal disappears. Changes in N_e modify only the exponential decay $e^{-t/\tau_{ion}} \sim e^{-tN_e/k}$ ($k = 3.1 \cdot 10^7 \text{ cm}^{-3}\text{s}$) giving a longer Ly α signal persistence where N_e is smaller.

As we anticipated in § 8.2, at 4.98 R_\odot the Ly α isophotes show two cometary tails (see Figure 8.4). Now from equation 8.2 we can exclude the possibility that the enhanced emission, dubbed tail 1, is due to the interaction between the cometary plasma and the enhanced density of the coronal streamer. Where the electron density N_e increases (i.e. near the streamer's edge) the charge transfer rate τ_{cx}^{-1} increases and the number of H atoms produced (hence the Ly α intensity) should increase. Nevertheless, as a consequence of equation 8.2, at locations where N_e raises, the Ly α signal duration decreases, leading to a weaker rather than a stronger Ly α emission at the location of tail 1 in Figure 8.4. Moreover, sublimation of cometary dust grains provides a better explanation for the persistence of the Ly α signal, as will be shown in § 8.4.2.

The total (i.e. summed over the slit length) number of Ly α counts C_i expected in the exposure i after the first cometary observation in the spectrograph slit is (see Uzzo et al., 2001):

$$C_i = \frac{A_{eff}}{4\pi\delta^2} \frac{\dot{N}\bar{g}}{v} \frac{R_\tau}{R_\tau + 1} \int_{i t_{exp}}^{(i+1)t_{exp}} \int_0^l e^{-[t - t_{cross}(x)]/\tau_{ion}} dx dt \quad (8.3)$$

where A_{eff} is the effective area of the UVCS instrument ($A_{eff} = 0.0075$ and 0.015 cm^2 respectively at the projected heliocentric distances of 3.44 and 4.94 R_\odot), δ and v are, respectively, the comet-Earth distance (in AU) and the orbital speed of the

comet, $t_{exp} = 200$ s is the exposure time, $l = 3.0 \cdot 10^9$ cm is the UVCS slit width projected onto the plane of the sky, $t_{cross}(x) = t_{start} + x/v$ is the time at which the comet crosses the position x on the slit (t_{start} is the unknown time at which the comet first enters the slit) and τ_{ion} is the unknown characteristic time for H atom ionization. In the equation 8.3 there are two unknown parameters (τ_{ion} and t_{start}) and a normalization \dot{N} : it is possible, given the observed C_i curve, to find the pair of values for (τ_{ion}, t_{start}) at which the χ^2 value is minimum: statistical errors in the fit are estimated from the iso - χ^2 curves (see later, Figure 8.8). The electron density N_e of the plasma encountered by the cometary nucleus can be easily inferred from the τ_{ion} value given by the fit.

The value of \bar{g} has been computed from the following parameters: at $3.60 R_\odot$ we used the average $T_k = 1.0 \cdot 10^6$ K from cometary profiles (Table 8.1) and, since the comet is passing through a small streamer, an outflow speed $v_{out} = 0$ (see e.g. Strachan et al., 2002); at $4.98 R_\odot$, we used $T_k = 7.19 \cdot 10^5$ K from the coronal FWHM (see Table 8.1) and the outflow speed estimated above from Poletto et al. (2002). For a scattering angle of $\theta_{scatt} = 90^\circ$ (the Earth-comet distance was approximately 1.004 AU at the time of our observations, hence the comet was about on the plane of the sky at both heliocentric distances) we obtained $\bar{g} = 8.62$ phot $s^{-1}H^{-1}$ at $3.60 R_\odot$ and $\bar{g} = 1.09$ phot $s^{-1}H^{-1}$ at $4.98 R_\odot$. At both heliocentric distances we used $I_{disk}(Ly\alpha) = 7.75 \cdot 10^{15}$ phot $cm^{-2}s^{-1}sr^{-1}$ from the 7 February, 2001 SOLSTICE measurement.

The outgassing rate \dot{N} derived from the model can be used to estimate the ejected mass rate Q_{H_2O} (Kg/s) by simply assuming that each water molecule gives rise to two neutral hydrogen atoms. O atoms can also neutralize protons by charge transfer, but oxygen is ionized more rapidly than hydrogen. From the \dot{N} value it is possible also to give an estimate for the cometary nucleus active surface S_{act} exposed to the solar radiation: assuming a balance between the energy supplied by the solar radiation over S_{act} and the energy required to sublime the quantity of ice derived from \dot{N} , we have

$$S_{act} = \frac{\dot{N} L}{F_\odot(1 - A) N_A} \quad (8.4)$$

where $L = 4.81 \cdot 10^{11}$ erg mol^{-1} is the ice latent heat of sublimation, $A = 0.06$ is the cometary albedo, $F_\odot = 1.37 \cdot 10^6 (215.21 R_\odot/r)^2$ erg $cm^{-2}s^{-1}$ is the solar flux scaled to the cometary heliocentric distance $r(R_\odot)$ and N_A (molec mol^{-1}) is the Avogadro number. From the S_{act} value it is possible (assuming a spherical nucleus) to estimate the equivalent radius for the cometary nucleus $R = \sqrt{S_{act}/\pi}$. This relationship holds only in absence of unobserved fragmentation events, as we discuss later.

8.4.1 Cometary and coronal parameters

The derived C_i curves for tail 1 and 2 and the observed curve at $3.60 R_\odot$ have been compared with the C_i predicted curve (equation 8.3) in order to determine the fragment parameters. Table 8.2 gives the results we obtained for the cometary

and coronal plasma parameters at 4.98 and 3.60 R_{\odot} from the model described in the previous section. An example of the observed and modeled curves of the Ly α counts vs. time is given in 8.7. We note that, before fitting the C_i profile observed at 4.98 R_{\odot} we subtracted in both tails (fragment a and b in the Table) the intensity of the secondary Ly α component (from the first exposures), because the H atoms responsible for this secondary emission are not included in the model described above.

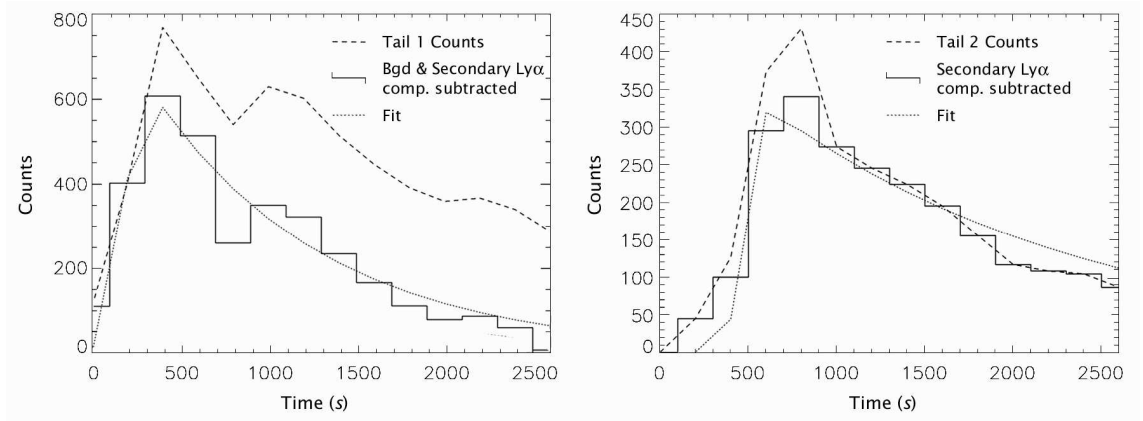


Figure 8.7: Observed (solid) and modeled (dots) Ly α counts at 4.98 R_{\odot} in the main (left panel) and secondary (right panel) cometary tail. before fitting the observed counts we subtracted in both tails the intensity of the secondary Ly α component from the first exposures; also, before fitting the counts of tail 1, a constant term of 280 counts has been subtracted from the tail 1 curve to take into account the effect of pyroxene dust grains.

Figure 8.7 shows that the C_i curve for the secondary tail (right panel) has been easily fitted yielding the parameters given in Table 8.2. On the contrary the tail 1 curve (left panel) shows a very slow decrease in time and the fit gives us a very high τ_{ion} value ($\tau_{ion} \geq 2000$ s), hence a low N_e ($\leq 1.6 \cdot 10^4$ cm^{-3}). As we mentioned in § 8.2, tail 1 is closer than tail 2 to a small coronal streamer, so in this region we expect an electron density equal or greater than the density $N_e = 1.6 \cdot 10^4$ cm^{-3} obtained from the tail 2 fit.

However the shape of the tail 1 C_i curve (dashed line in Figure 8.7) does not exponentially decay to 0, but tends to a constant Ly α emission of about 280 counts. Hence, in order to determine τ_{ion} , we subtracted a constant background of 280 counts from the measured intensities, obtaining the solid curve in Figure 8.7. From this curve, using the above model, we evaluated the main fragment parameters given in Table 8.2. From the S_{act} values given in this Table, assuming a spherical shape both for the main and the secondary fragment, we obtained respectively radii of $7.8 \pm_{0.5}^{0.4}$ and $5.4 \pm_{0.5}^{0.2}$ m; these values are similar to the nucleus diameters given by Uzzo et al. (2001) for comet C/2000 C6.

As expected, the derived τ_{ion} values in Table 8.2 decrease from tail 2 to tail 1 giving us a higher coronal electron density near the small streamer ($N_e = 3.0 \cdot 10^4$

R_{sky} (R_{\odot})	Model parameters			Derived parameters		
	t_{start} (s)	τ_{ion} (s)	\dot{N} (10^{28} s^{-1})	Q_{H_2O} (Kg/s)	R (m)	N_e (cm^{-3})
4.98 ^a	235 \pm 9 ₁₄	1020 \pm 110 ₁₅₀	0.59 \pm 0.06 _{0.07}	58.9 \pm 6.0 _{7.0}	7.8 \pm 0.4 _{0.5}	(3.0 \pm 0.5 _{0.3}) $\cdot 10^4$
4.98 ^b	505 \pm 20 ₂₄	1900 \pm 210 ₂₄₅	0.29 \pm 0.03	28.5 \pm 2.7	5.4 \pm 0.2 _{0.5}	(1.6 \pm 0.2) $\cdot 10^4$
3.60	292 \pm 12 ₂₄	430 \pm 50 ₃₀	8.2 \pm 0.8 _{0.9}	820 \pm 80 ₉₀	20.3 \pm 1.2 _{0.8}	(7.2 \pm 0.5 _{0.7}) $\cdot 10^4$

^a main fragment, ^b subfragment

Table 8.2: C/2001 C2 model and derived parameters

cm^{-3}). We give a detailed interpretation for the constant $\text{Ly}\alpha$ in the next section: here we anticipate only that this $\text{Ly}\alpha$ emission will be ascribed to the sublimation of pyroxene dust grains, a process which yields an extra number of neutrals in the coma.

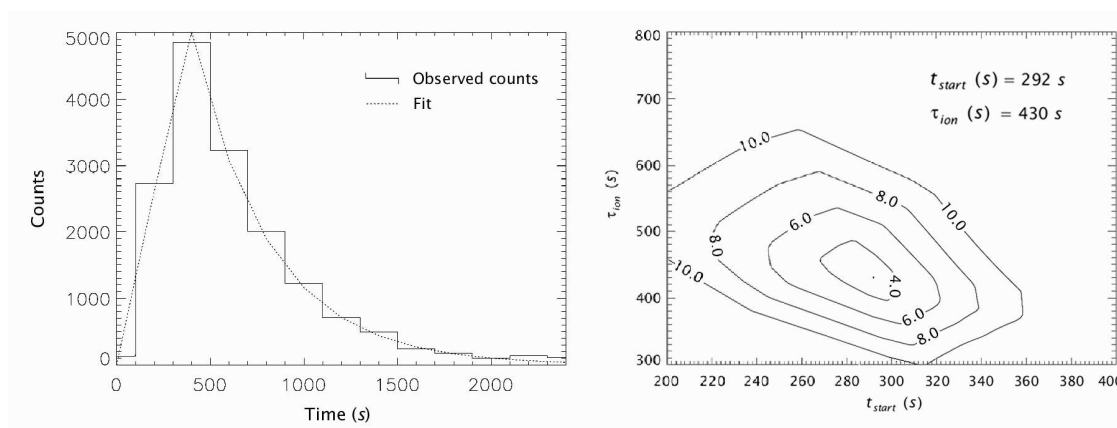


Figure 8.8: Left panel: observed (solid) and modeled (dots) $\text{Ly}\alpha$ counts at 3.60 R_{\odot} . Right panel: the iso- χ^2 curves showing the pair of values for (τ_{ion}, t_{start}) at which the χ^2 value is minimum. Errors in the parameters are determined from the iso- χ^2 curves.

At 3.60 R_{\odot} the procedure described in § 8.4 gives the results shown in Figure 8.8 and in Table 8.2. Analogously, the N_e value derived at 3.60 R_{\odot} , is at the lower edge of the profile of the streamer density band given for instance by Gibson et al. (1999) (see Figure 2.2) or by Strachan et al. (2002) at our heliocentric distances. However this low N_e value is realistic because the coronal feature crossed by the comet is a very tenuous feature, nearly unobservable in the LASCO/C3 and C2 images (see Figure 8.1). Hence the values inferred from the comet-corona plasma interaction, although rather low with respect to standard streamer densities, provide us with values describing the physical status of faint structures.

At 3.60 R_{\odot} we observe only one tail, implying that the secondary fragment disappeared by sublimation along its path between 4.98 and 3.60 R_{\odot} . This can

be verified as follows: the thickness of the sublimated layer R_{subl} may be estimated (following Iseli et al. 2002) by integrating over the cometary orbit the rate of change in radius dR/dt , which is given by

$$\frac{dR}{dt} = \frac{dR}{dr} \frac{dr}{dt} = - \frac{F_{\odot}(r) (1 - A)}{16\pi \rho_{com} L} \cdot 0.85 \quad (\text{cm s}^{-1}) \quad (8.5)$$

where r is the heliocentric distance, $F_{\odot}(r)$ and A are given in § 8.3, $\rho_{com} \sim 0.6 \text{ g cm}^{-3}$ is the density of porous ice, $L \sim 2.5 \cdot 10^{10} \text{ erg g}^{-1}$ is the ice latent heat of sublimation and 0.85 is the fraction of the solar radiation energy which, by model computations with sungrazers at small heliocentric distances (Iseli et al. 2002), goes into sublimation. Integrating this equation between the two cometary heliocentric distances of 4.98 and 3.60 R_{\odot} and taking for $dr/dt \equiv v_r$ the average value $v_r \simeq 2.6 \cdot 10^7 \text{ cm/s}$ we obtained a value $R_{subl} \simeq 2.0 \text{ m}$ which is of the same order as the subfragment estimated radius (Table 8.2). This means that at this heliocentric distance we cannot see two tails because the subfragment sublimates between 4.98 and 3.60 R_{\odot} .

We note that from the \dot{N} value in Table 8.2 we derive a radius of 20.3 m, larger than the main fragment radius at 4.98 R_{\odot} . This is a consequence of the increased surface S_{act} (see e.g. Uzzo et al., 2001): at this heliocentric distance the main nucleus is fragmented in many undetectable small pieces increasing the surface S_{act} exposed to the solar flux (hence the derived \dot{N} value) and giving an unrealistic value for the object radius. This explains also why we did not observe the comet at 2.20 R_{\odot} : the comet never reached this heliocentric distance. This scenario is confirmed by the following considerations: if the tensile strength of the cometary nucleus surface would be negligible, a lower estimate for the heliocentric distance at which the comet would break up, in a highly idealized case, is given by the Roche limit L_R :

$$L_R = 2.44 \left(\frac{\rho_{\odot}}{\rho_{com}} \right)^{1/3} R_{\odot}$$

where $\rho_{\odot} = 1.41 \text{ g cm}^{-3}$ is the average Sun density; with the density of porous ice given above, this formula yields $L_R = 3.24 R_{\odot}$. Non gravitational stresses however may fracture the comet above L_R : following Chyba, Thomas & Zahnle (1993), the nucleus fragmentation becomes most probable when the average pressure on the sunward side is about equal to its tensile strength ($\sim 10^3 - 10^5 \text{ dyn cm}^{-2}$). For typical comet material this happens around 5 R_{\odot} : we can conclude that between about 3.2 R_{\odot} and 5 R_{\odot} (hence between the heliocentric distances of our observation) the occurrence of cometary nucleus fragmentation events becomes more probable. Fragmentation processes between these two heliocentric distances increase the erosion rate (as discussed above), leading to the observed complete sublimation of the nucleus material before 2.20 R_{\odot} ; the coexistence of both fragmentation and erosion processes is needed to explain the cometary disappearance above this heliocentric distance.

In the next Section, for completeness, we show how the Ly α background we subtracted from the tail 1 C_i curve has been used to derive an estimate for the number density of pyroxene dust grains. This is an important estimate because in the literature there are no measurements for the grain density in sungrazers and our results may help modelers to better understand the shape of the observed sungrazer lightcurves. As we will see this lead us to study the interaction between coronal protons and cometary dust grains, a process that we have not described in the first part of this Chapter.

8.4.2 Effect of Pyroxene dust grains

We have shown in the last section that at $4.98 R_\odot$ a subtraction in each exposure of a constant Ly α intensity of about $I(\text{Ly}\alpha) \simeq 280 \text{ counts} = 3.93 \cdot 10^9 \text{ phot cm}^{-2}\text{s}^{-1}\text{sr}^{-1}$ from the tail 1 C_i profile allows us to determine, by the model described above, a realistic τ_{ion} value. The additional number \bar{N}_H of H atoms which produces this Ly α emission is $\bar{N}_H = [4\pi I(\text{Ly}\alpha)]/(\bar{g}L) \simeq 3.0 \text{ H cm}^{-3}$ where \bar{g} has been computed in § 8.4 and L is the extension of tail 1 along the line of sight, which we assumed to be of the same order as its extension on the plane of the sky ($L \simeq 10 \text{ bins} \simeq 1.52 \cdot 10^5 \text{ km}$, see middle panel in Figure 8.5). We need now to explain the origin of these additional H atoms.

Kimura et al. (2002) interpreted the observed sungrazer lightcurves in terms of the different characteristic timescales for sublimation of fluffy aggregates of crystalline olivine ($[\text{Mg}, \text{Fe}]_2 \text{SiO}_4$) and pyroxene ($[\text{Mg}, \text{Fe}]_2 \text{Si}_2\text{O}_6$) grains. These authors defined the dust sublimation zone as the heliocentric distance at which the timescale for grain sublimation τ_s is equal to the time $\tau_{\Delta r}$ taken by the comet to cover the distance $\Delta r = 0.1 R_\odot$. They found pyroxene aggregates in sungrazer comae to have their sublimation zone at $h \sim 5 R_\odot$, which corresponds to the heliocentric distance of our observations. Moreover Kimura et al. (2002) hypothesize that “The sublimation of pyroxene grains might account for the Ly α emission that peaks around $4 - 5 R_\odot$ if pyroxene grains act as agent to neutralize protons in the solar corona.”. Following this scenario, we ascribe the number \bar{N}_H of additional H atoms to a charge transfer process between products from pyroxene grains sublimation and coronal protons.

Tachibana et al. (2002) showed that enstatite ($\text{Mg}_2\text{Si}_2\text{O}_6$, an endmember of pyroxene) evaporates preferentially via emission of SiO_2 yielding to the formation of a forsterite (Mg_2SiO_4 , an endmember of olivine) layer on the surface of enstatite. Hence (see also Kimura et al., 2002) we assumed that the mass loss of pyroxene grains in the sublimation process occurs by ejection of SiO_2 molecules alone. The authors also showed that, during the SiO_2 evaporation from enstatite, the thickness of the forsterite layer increases with time in the early stage of evaporation and later remains constant at $\sim 4 - 6 \mu\text{m}$ depending on the external temperature. This means that, defining the equivalent grain radius $R_d = r_m n^{1/3} = 200 \text{ nm} \ll 4 - 6 \mu\text{m}$ (taking a monomer radius $r_m = 100 \text{ nm}$ and a number $n = 8$ for the monomers of the grain, see Kimura et al., 2002), all the available SiO_2 mass in the grain evaporates.

After the SiO₂ molecules have been ejected from the grain, they are photodissociated by the solar radiation. In the literature there is no estimate for the SiO₂ photodissociation rate: this molecule is likely to behave as CO₂, which has a photodissociation time of $\simeq 113s$ at 5 R_☉ (Huebner et al., 1992). Hence we assume that each SiO₂ molecule photodissociates immediately after the evaporation from the pyroxene grains; we assumed also that this process produces three neutral atoms.

From a comparison between the experimental charge transfer process rates (from Kimura et al., 1997) and the estimated ionization rates in the coronal plasma interacting with the comet ($T \simeq 7.2 \cdot 10^5$ K from the Ly α FWHM and $N_e = 3.0 \cdot 10^4$ cm⁻³ from the tail 1 fit described above), it turns out that about half of the Si atoms from the photodissociation of SiO₂ undergoes charge transfer with coronal protons, while all the produced O atoms undergo charge transfer before being ionized. Hence we have that the number density $N(Si)$ and $N(O)$ of Si and O atoms available for charge exchange traveling with the comet are:

$$N(Si) = \frac{1}{2} N_d \frac{m_d(SiO_2)}{m(SiO_2)} \quad ; \quad N(O) = 2 N_d \frac{m_d(SiO_2)}{m(SiO_2)} = 4 N(Si)$$

where $m_d(SiO_2)$ is the SiO₂ mass of the grain and $m(SiO_2) = 9.98 \cdot 10^{-23}$ g is the mass of a SiO₂ molecule. Assuming that the pyroxene composition formula is Mg_{1.8}Fe_{0.2}Si₂O₆ (see e.g. Wooden et al., 1999) and using typical bulk density and radius for the pyroxene grains estimated by Kimura et al. (2002), we have $m_d(SiO_2) = 6.42 \cdot 10^{-14}$ g. Knowing $N(Si)$ and $N(O)$, from the cross sections $\sigma_{cx}(Si)$ and $\sigma_{cx}(O)$ for inelastic processes in collisions of H⁺ ions with neutral Si and O atoms (Kimura et al., 1997), we may derive the expected number of H neutrals produced by charge transfer as a function of the unknown N_d . Equating this number to the \bar{N}_H number estimated above we find:

$$N_d = \bar{N}_H \left[N_p \frac{m_d(SiO_2)}{m(SiO_2)} v_p \left(\frac{\sigma_{cx}(Si)}{2} + 2\sigma_{cx}(O) \right) \tau_{ion} \right]^{-1} = 6.2 \cdot 10^{-10} \text{cm}^{-3}$$

where $N_p \simeq N_e$ is the coronal proton density and $v_p \simeq 420$ km/s is the proton velocity with respect to the colliding neutrals which move in first approximation with the comet. In the literature there are no dust measurements for sungrazing comets; the only estimate we found refers to the the grain number density derived by Vega 1, Vega 2 and Giotto spacecraft measurements during the comet P/Halley flyby: at a reference distance of 1000 km from the nucleus, when the comet was at an heliocentric distance between $\simeq 0.8$ and 0.9 AU, it turns out that the grains with a mass of $\sim 10^{-14}$ g have a number density of $\sim 1 - 2 \cdot 10^{-5}$ cm⁻³ (Vaisberg et al., 1987; Mazets et al., 1987; McDonnell et al., 1987), hence ~ 4 orders of magnitude greater than in our case. If the grain number density N_d decreases like $\propto 1/d^2$ (where d is the distance from the cometary nucleus), in the Halley coma $N_d = 6.2 \cdot 10^{-10}$ cm⁻³ at a distance $d \simeq 1.3 \cdot 10^5$ km from the nucleus, which corresponds to about 175'' in our observations (Figure 8.4).

8.5 Summary

In conclusion, in this work we report on UVCS observations of a sungrazing comet fragmentation: this event has been directly observed for the first time by UVCS at $4.98 R_{\odot}$ and inferred at $3.60 R_{\odot}$ from the observed apparent increase in the derived nucleus radius. The observations at $4.98 R_{\odot}$ allow us to observe two fragments whose outgassing rates and the radius have been inferred from the data; the smaller fragment radius is compatible with its total sublimation between 4.98 and $3.60 R_{\odot}$. The observed increase in the S_{act} value at $3.60 R_{\odot}$ indicates that the main nucleus breaks into many small pieces between these two heliocentric distances. The slow decrease of the $Ly\alpha$ intensity with time at $4.98 R_{\odot}$ has been reproduced by assuming that additional H atoms are created by the interaction between coronal protons and cometary pyroxene dust grains. This assumption allows us to give for the first time an order of magnitude estimate for the pyroxene dust grain number density in sungrazing comets.

Estimates of the kinetic temperature and electron density of an equatorial coronal hole at $4.98 R_{\odot}$ and of a coronal streamer at $3.60 R_{\odot}$, consistent with values given in the literature for these parameters near the last solar maximum, show an increase by a factor 2 in the density value across the coronal hole–streamer boundary. The density for a faint structure, hardly detectable in white light images, has also been inferred; this may represent a lower limit of densities for coronal streamers.

Chapter 9

Summary and Future Perspectives

After a review, in the first part of this Thesis, of the spectroscopic diagnostic techniques that allow us to infer the coronal plasma physical parameters, and, in the second part, of the works where these have been applied, we like to summarize in this last Chapter the most relevant results we obtained and to outline works in progress and/or planned for the near future.

In the first work (Chapter 5) we reported on UVCS observations of a streamer complex taken at 1.6 and 1.9 R_{\odot} (Bemporad et al., 2003), near the maximum phase of the activity cycle (June 10–17, 2000). From these observations we derived electron densities, temperatures and elemental abundances across the two observed streamers at both heliocentric distances. In particular, streamer densities at both heights (Table 5.4) are about a factor two larger than typical densities derived at the minimum of the solar activity (see Figure 2.2), and this characteristic may be ascribed to variations between the different phases of solar cycle. The variation of densities from the center to the edge of the streamer derived from our data is in agreement with other estimates (see e.g. Strachan et al., 2002; Wilhelm et al., 2002) for streamers at solar minimum, but we point out that our results apply to streamers that do not show the O VI/Ly α dichotomy observed in the same structures at solar minimum (i.e. streamer cores, where Ly α emission is highest, correspond to a weakly emitting region in the O VI radiation, an effect which is most easily interpreted as being caused by a local oxygen depletion). Electron temperatures across the streamer axis (Table 5.3) show a decrease towards the streamer edges by about 15%; however (taking into account that, for a slit centered at the streamer axis, positions along the slit at the streamer boundaries are at an higher altitude) a 7% variation can be ascribed to the altitude increase. Interestingly, we found from the ratio technique a 25% difference in temperature between the two streamers, confirmed by an emission measure loci analysis (see Figure 5.7); this effect can be related to the different “age” of the two structures, as the cooler streamer was newly formed after a plasma blowout (see Suess et al., 2004).

Our determination of the oxygen abundances first revealed the younger streamer to be overabundant with respect to the second streamer. We can hypothesize that in

the younger streamer gravitational settling had not enough time to reduce the oxygen abundance from photospheric to coronal values. This happens also with others elements, overabundant in the “younger” structure. We have been able to check the behavior of the oxygen abundance across the older (and hotter) streamer: it turns out that in the edge the abundance is higher than in the center. However, as we mentioned, we don’t observe two lobes in the O VI intensity across the streamers as observed by other authors in the minimum of the solar activity. Perhaps we can justify this apparent contradiction as a consequence of the strong density increase between streamer’s legs and center that balances the abundance effect and yields the observed single peak distribution of the O VI line intensity across the streamer. As we mentioned in § 2.4, the determination of the abundance of trace elements in different solar structures and in the solar wind may be crucial for the identification of the solar wind sources. Analyses of streamer data taken at the minimum of the solar activity cycle raised the question of whether streamers’ legs might be the site where slow wind originates, because the oxygen abundance in the lateral branches of the streamer, at coronal levels, turned out to be similar to the slow wind abundance measured *in situ*. Because our data were acquired at the time of a SOHO–Sun–Ulysses quadrature, we checked whether the behavior found at minimum is shared by our streamers at maximum of the activity cycle. Hence, in order to find some indications about the origin of slow wind, we compared coronal Fe/O values with those acquired *in situ* by the SWICS experiment aboard the Ulysses spacecraft. To this end, we need to know the geometry of fieldlines that extend from the coronal levels observed by UVCS to the distances sampled by SWICS. The magnetic field configuration has been derived via an MHD extrapolation model, which makes use of the photospheric magnetic field measurements of the Wilcox Solar Observatory. It turns out that UVCS and SWICS values are in good agreement (for example $(Fe/O)_{UVCS} = 0.12 \pm 0.03$ and $(Fe/O)_{SWICS} = 0.09 \pm 0.04$ on June 11). However the fluctuations in the *in situ* values are so large that a comparison can be made only between time-averaged values, giving little evidence in favor of an association between abundances in the streamer legs and slow wind.

In our second work we studied the early evolution of a CME that occurred on January 31, 2000, and was observed by UVCS at 1.6 and 1.9 R_{\odot} (Bemporad et al., 2005b). In the first part of our analysis we identified (from a comparison between LASCO and EIT images) the CME source region on the solar disk: it is important for CME modelers to understand how possible interactions between the magnetic field above the source active region (AR) and the overlying large scale fields may give rise to the helical flux ropes observed in the interplanetary medium. A study of magnetic configurations above this AR which may lead to the release of the observed CME is at present in progress. In particular, we plan to use MagnetoHydrodynamic codes¹ to reconstruct the coronal magnetic fields starting from fields measured

¹See <http://ccmc.gsfc.nasa.gov/models/>

at the photospheric levels. These simulations will help us understand whether the background structures observed in Mauna Loa and LASCO images played a role in the release of the CME by interacting with the dipolar field of the AR. Moreover, it will be important to study how the orientation of the magnetic neutral line on the disk gave rise to the complex structure we observed in Mauna Loa difference images.

The whole event turns out to be very faint in UV line emission: different CME structures are hardly identifiable even on the strongest spectral lines (H Ly α , O VI and Si XII), whose intensities show at most a change by about 30–40% with respect to the value at the beginning of the observations, followed by some fluctuations. These structures, however become clearly visible in the running difference images we reconstructed from UVCS data. By a comparison with the Mauna Loa white light data, we identified in the UV reconstructed CME images (Figure 6.6) the typical three parts (front, void and core) of our CME. The overall CME structure agrees with that envisaged by the Lin, Raymond & Van Ballegoijen (2004) CME model: this “loss of equilibrium” model requires changes in the magnetic fields above the source AR such that the flux rope, initially “suspended” over the AR, is destabilized. This scenario is in agreement with the variation in the AR we identified as the CME source of the sunspot number and of its total area.

Then, we estimated from the pB data the electron densities in the different parts of the CME, by assuming a priori the length L along the LOS of the CME region and the density profile of the background corona (adjusted to reproduce the background pB observed at different latitudes). It turns out that the CME core has the greatest density (see Table 6.2), while the CME front and void have a density respectively $\sim 25\%$ and 45% lower than the core. From these values, by assuming two simple geometries for the CME bubble, we derived an order of magnitude estimate of the mass of different CME parts and of the whole CME: the value we found for the total mass ($\sim 6 - 8 \cdot 10^{14}$ g) is about one third of the mass measured from LASCO images at higher levels ($2.1 \cdot 10^{15}$ g) and can be representative of the CME mass in the early stage of its development (see conclusions of Chapter 6).

With the densities we derived from the pB (hence, independently of the unknown plasma temperature), we have been able to estimate the average electron temperature in the CME region needed to reproduce the observed Ly α , O VI and Si XII line intensities. To this end, we had to estimate also the plasma outflow speeds (to compute the Doppler dimming factors of Ly α and O VI lines) from the Mauna Loa images, which turn out to be lower than ~ 100 km/s at $1.6 R_{\odot}$ (the CME accelerates at higher heliocentric distances). The resulting temperatures are about a factor 1.4, 1.8 and 2.0 higher than the surrounding $1.4 \cdot 10^6$ K corona, respectively, in the CME front, void and core. This temperature increase is confirmed also by the detection of an O VI $\lambda 1032$ Å line broadening at the CME void and core which corresponds to an oxygen kinetic temperature about 25% larger in these regions. While plasma heating at the CME front can be interpreted by a simple adiabatic compression, other processes have to be invoked in the void and core regions. In order to find

alternative explanations for the observed temperature increase and have a further confirmation of this behaviour, the analysis of the UVCS data acquired at $1.9 R_{\odot}$ will be crucial: this will be done in the next months.

We also plan to separate the contribution to the observed line profiles from different coronal and CME regions. This will help us understand the real increase in the oxygen kinetic temperature at the CME void and core, as the value mentioned above is only indicative of the behaviour of the average coronal plus CME region. Taking into account that no significant line Doppler shifts were observed, this analysis will help us constrain the values of CME ejection angle which strongly affect our estimate of the CME mass (§ 6.11).

In the third work reported in this Thesis we analyzed UVCS observations (at an heliocentric distance of $1.7 R_{\odot}$) of the coronal restructuring after a CME which occurred on November 26, 2002 (Bemporad et al., 2006). These data, acquired during a SOHO-Ulysses quadrature, gave us the unique opportunity to describe the structure of a current sheet (CS), which formed in the aftermath of the CME, from lower coronal levels out to interplanetary distances. In particular, we derived the physical parameters of this CS over 2.3 days following the event. After separating the quiet corona and CS contributions to the plasma emission along the line of sight, we derived the temporal profile of the CS temperature, density and elemental abundances. We showed that the CS temperature decreases by more than a factor two, over the observing time. This is the first time that the temporal profile of the physical parameters of a CS is given. The behavior of density is not as well defined, due to the superposition of a dense feature onto the CS location at the end of our observations.

A range of values for the plasma inflow speed towards the reconnection region has been inferred, together with values of the magnetic field in the reconnection region. Moreover, we showed that adiabatic compression of plasma cannot account for the heating of the reconnection region, other than at a very late phase of the phenomenon. The resulting Interplanetary CME observed *in situ* by Ulysses is consistent with CME models. Strong fluctuations in the high ionization Fe states detected *in situ* suggest bursty, rather than smooth, reconnection in the coronal CS and have been related to the irregular progression of reconnection events along the arcade of post-event loops. The quadrature configuration at the time data have been acquired allowed us (the first time ever) to establish a direct relationship between the high temperature plasma at the reconnection site and the high ionization stages of Fe detected *in situ* (Poletto et al., 2004).

We did not mention in the work described above that during the 2.3 days of observations, UVCS observed (Northward of the CME) repeated, sudden and short lived (30 – 60 *min*) emission peaks in the “cool” H $Ly\beta$, $Ly\gamma$, C III and O VI lines. These events are the extension at higher altitudes of recursive chromospheric ejections of plasma observed in the EIT He II images. Radial speeds of these jets, evaluated from EIT images, are strongly variable with time (~ 20 – 200 km/s) and the motion

of each jet has peculiar kinematical properties. EIT data reveal these ejections to originate from homologous compact flares whose source is an island of included polarity located just inside the base of a coronal streamer, as shown by a comparison with MDI data. Some of these ejections result in narrow CMEs that move outwards along the streamer; interestingly, the streamer is transiently “inflated” by the ejection, but it is not disrupted as it happens for typical CMEs. The study of this new type of CMEs, that we dubbed “streamer puffs” (see Bemporad et al. 2005a), will require a more thorough analysis of the UVCS and EIT data which is at present in progress. In the near future we plan to derive the temporal profiles of the electron density, electron and kinetic temperature along the axis of the jets. Preliminary results from an analysis of data point towards an higher plasma temperature at the leading edge of the jets; this effect might be a consequence of adiabatic compression and/or shock heating. A further data analysis will help us figure out how these jets interact with the background streamer plasma without disrupting the streamer itself, and will possibly lead to a more refined model for the origin of these events.

In the fourth and last work of this Thesis we analyzed UVCS data of the sun-grazing comet C/2001 C2 that was observed on February 7, 2001, at the heliocentric distances of 4.98 and 3.60 R_{\odot} (Bemporad et al., 2005c). In Chapter 8 we showed how, from these data, we derived an estimate for both cometary (i.e. outgassing rate and nucleus radius) and coronal (i.e. kinetic temperature and electron density) parameters. In particular, at 4.98 R_{\odot} the comet crossed a boundary region between a coronal hole and a streamer: from the detection and separation of the $\text{Ly}\alpha$ emission from two cometary tails we found the value of the coronal electron density of these regions which points towards an increase by about a factor two (see Table 8.2) between the coronal hole and streamer limb density. The low N_e value we derived at 3.6 R_{\odot} is representative of the tenuous coronal feature (nearly unobservable in the LASCO images) crossed by the comet at this height.

We note here that, the absence of a cometary bow shock (as revealed by an analysis of the $\text{Ly}\alpha$ line profiles), used by other authors to infer the plasma outflow speed v_{out} of the coronal plasma encountered by the comet (see Raymond et al. 1998b), led us to assume an a priori value for v_{out} at 4.98 R_{\odot} (while at 3.60 R_{\odot} the comet crossed a coronal streamer region and at this height we can assume a negligible outflow; see e.g. Strachan et al., 2002). However, the secondary H atoms travel with the solar wind, hence the sungrazers $\text{Ly}\alpha$ image strongly depends on the local magnitude and direction of the wind velocity vector. Should the comet encounter, for instance, a transition region between slow and fast wind regime, we might expect to observe an “inhomogeneous $\text{Ly}\alpha$ image” of the comet: in this sense, UVCS observations of sungrazers could be used as “tracers” of the solar wind inhomogeneities. To this end, it is necessary to better understand the relationship between the shape of the observed $\text{Ly}\alpha$ tails and the physical parameters of the coronal plasma crossed by the comet. S. Giordano and collaborators are working on a comet simulation code based on the Monte Carlo technique with the aim of reproducing the observed sungrazer

$\text{Ly}\alpha$ image as a function of both coronal (e.g. kinetic temperature, electron density, electron temperature, wind speed, etc...) and cometary (e.g. outgassing rate, velocity distribution and kinetic temperature of the outgassed, etc...) free parameters. On the basis of this work, we plan to better constrain in the next future the outflow speed values of coronal plasma as a function of the observed shape of the sungrazer $\text{Ly}\alpha$ tail. This will possibly provide a new technique to estimate v_{out} also at distances larger than $\sim 5 R_{\odot}$, where other sungrazers have already been observed and typically the Doppler dimming technique cannot be applied because of the very faint coronal UV intensities.

Acknowledgements

I like first to thank my supervisors, Dr. Giannina Poletto and Dr. Marco Romoli for their guidance and support. My special thanks go to Dr. Poletto, who followed my work in these three years step by step: I feel really lucky to have had the opportunity to work with Giannina, who constantly encouraged me and shared with me not only her time at work, but sometimes even her free time to support me with her experience and critical advice.

My thanks to Prof. John Raymond for giving me the opportunity to work with him and for his patience in answering my numerous questions: during the time I collaborated with him I started two of the four works whose results are presented here and his knowledge and experience have been very fruitful to my work. These thanks are also extended to the Harvard-Smithsonian Center for Astrophysics, Cambridge (USA) for hosting me and for the financial support it supplied.

Next, I thank Prof. Giancarlo Noci for his advice and helpful suggestions on almost every work I presented at meetings and conferences that improved the clearness and correctness of my presentations.

I thank Dr. Steve Suess, for interesting and useful discussions during his visits to the Arcetri Astrophysical Observatory which helped me becoming familiar with heliospheric phenomena.

I like also to thank Dr. Steve Cranmer, with whom I had many precious discussions during my stay in Cambridge; many thanks to Dr. Raid Suleiman for his kindness in providing answers to all my practical questions and for keeping me a good company; to Dr. Pete Riley and to all the colleagues I met during the time I spent in Cambridge who contributed to make my visit more profitable.

My thanks to Dr. Giulio DelZanna and Dr. Zdenek Sekanina for

interesting comments, suggestions and criticisms which helped me improve, respectively, the first and the last work reported in this Thesis. I thank also Dr. Gianpaolo Tozzi for enlightening discussions on cometary physics, a theme, that, at the time, was new to me.

I would like to thank also Dr. Andrew L. Stanger for useful discussions and for providing the calibrated Mauna Loa data I used in one of the works of this Thesis.

This Thesis uses data acquired by the SOHO experiments and, in particular, by UVCS. I like to thank the SOHO scientists for providing the solar community with such an extraordinary instrument assembly and to extend special thanks to the UVCS PIs (Drs. J. Kohl and G. Noci) and UVCS team, who made possible for me to analyse the data sets on which the works presented here are based.

Bibliography

- Aellig, M.R., Hefti, S., Grünwaldt, H., et al. 1999, JGR, 104, 24769
- Allen, C.W. 1973 *Astrophysical quantities*, University of London, Athlone Press, 3rd ed.
- Altschuler, M.D., & Perry, R.M. 1972, SP, 23, 410
- Antiochos, S.K., DeVore, C.R., & Klimchuk, J.A. 1999, ApJ, 510, 485
- Arnaud, M., & Raymond, J.C. 1992, ApJ, 398, 394
- Arnaud, M., & Rothenflug, R. 1985, A&AS, 60, 42
- Aschwanden, M. 2004, "Physics of the solar corona", 24
- Asplund, M., Grevesse, N., Sauval, A.J., et al. 2004, A&A, 417, 751
- Bame, S.J., McComas, D.J., Barraclough, B.L., et al. 1992, A&A SS, 92, 237
- Beckers, J.M., & Chipman, E. 1974, SP, 34, 151
- Bemporad, A., Moore, R.T., Sterling, A., Poletto, G. 2005a, ApJL, 635, 189
- Bemporad, A., Poletto, G., Raymond, J.C. 2005b, ESA SP 592, 711
- Bemporad, A., Poletto, G., Raymond, J.C., et al. 2005c, ApJ, 620, 523
- Bemporad, A., Poletto, G., Suess, S.T., et al. 2006, ApJ, in press
- Bemporad, A., Poletto, G., Suess, S.T., et al. 2003, ApJ, 593, 1146
- Brueckner, G.E., Howard, R.A., Koomen, M.J., et al. 1995, SP, 162, 357
- Burlaga, L. F., & Ness, N.F. 1994, J. Geophys. Res., 99, 21511
- Chyba, C.F., Thomas, P. J., Zahnle, K.J. 1993, Nature, 361, 40
- Ciaravella, A., Raymond, J.C., Li, J., et al. 2002, ApJ, 575, 1116
- Cranmer, S.R., Kohl, J.L., Noci, G., et al. 1999, ApJ, 511, 481
- Cremades, H., & Bothmer, V. 2004, A&A, 422, 307
- Delaboudinière, J.-P., Artzner, G. E., Brunaud, J. et al. 1995, SP, 162, 291
- Del Zanna G., Bromage B.J.I., Mason H.E. 2001, Joint SOHO/ACE workshop "Solar and Galactic Composition", AIP Conf. Proceed. v. 598
- Del Zanna G., Landini, M., Mason, H.E. 2002, A&A, 385, 968
- Dere, K.P., Brueckner, G.A., Howard, R.A., et al. 1999, ApJ, 516, 465
- Dere, K.P., Landi, E., Young, P.R., & Del Zanna, G. 2001, ApJS, 134, 331
- Domingo, V., Fleck, B., & Poland, A.I. 1995, SP, 162, 1
- Doschek, G.A., & Laming, J.M. 2000, ApJ, 539, L71
- Doschek, G.A., Laming, J.M., Feldman, U., et al. 1998, ApJ, 504, 573
- Dulk, G.A. & McLean, D.J. 1978, SP 57, 279
- Feldman, U. 1992, Phys. Scrip., 46, 202
- Feldman, U., Doschek, G. A., Schühle, U., & Wilhelm, K. 1999, ApJ, 518, 500

- Feldman, U., & Laming, J. M. 2000, *Phys. Scrip.*, 61, 222
- Feldman, U., Schühle, U., Widing, K.G., & Laming, J.M. 1998, *ApJ*, 505, 999
- Feldman, U., & Widing, K.G. 1993, *ApJ*, 414, 381
- Fischer, R.R., & Guhathakurta, M. 1995, *ApJ*, 489, L103
- Foley, C.R., Patsourakos, S., Culhane, J.L., & MacKay, D. 2002, *AA*, 381, 1049
- Fontenla, J.M., Avrett, E.H., & Loeser, R. 1990, *ApJ*, 355, 700
- Forbes, T.G. 2000, *JGR*, 105 A10, 23, 153
- Frazin R.A., Cranmer, S.R., Kohl, J.L. 2003, *ApJ*, 597, 1145
- Gabriel, A.H. 1976, *Phil.Trans.R.Soc.*, (London) 281, 399
- Galvin, A.B., Kohl, J. L. 1999, *JGR*, 104, 9673
- Gardner, L.D., Atkins, N., Fineschi, S., et al. 2000, *Proc. SPIE*, 4139, 362
- Geiss, J. 1998, *SSR*, 85, 241
- Gibson, S. E., Fludra, A., Bagenal, F., et al. 1999, *JGR*, 104, 9691
- Gonzalez, J.-F., Stehlé, C., Artru, M.-C., et al. 1998, *A&A*, 330, 1120
- Grigis, P.C. & Benz, A. O. 2005, *AA*, 434 (Issue 3), 1173
- Guhathakurta, M., & Holzer, T.E. 1994, *ApJ*, 426, 782
- Guhathakurta, M., Holzer, T.E., & McQueen, R.M. 1996, *ApJ*, 458, 817
- Harrison, R.A. & Thomson, A.M. 1992, *RAL*, 91, 092
- Holweger, H. 2001, Joint SOHO/ACE workshop “Solar and Galactic Composition”,
AIP Conf. Proceed. v. 598
- House, L.L. 1970, *J. Quant. Spectrosc. Radiat. Transfer*, 10, 909
- Huebner, W. F., Keady, J. J., Lyon, S. P. 1992, *Ap&SS*, 195, 291
- Hummer, D.G. 1994, *MNRAS*, 268, 109
- Iseli, M., Küppers, M., Benz, W., Bochsler, P. 2002, *Icarus*, 155, 350
- Kimura, H., Mann, I., Biesecker, D.A., Jessberg, E.K. 2002, *Icarus*, 159, 529
- Kimura, M., Gu, J.P., Bueker, R.J. 1997, *Phys. Rev. A*, 55, 2778
- Klein, L.W., & Burlaga, L.F. 1982, *JGR*, 87, 613
- Ko, Y.-K., Fisk, L.A., Geiss, J., et al. 1997, *SP*, 171, 345
- Ko, Y.-K., Raymond, J.C., Li, J., et al. 2002, *ApJ*, 578, 979
- Ko, Y.-K., Raymond, J.C., Lin, J., et al. 2003, *ApJ*, 594, 1068
- Kohl, J.L., Esser, R., Gardner, L.D., et al. 1995, *SP*, 162, 313
- Kohl, J.L., Noci, G., Antonucci, E., et al. 1997, *SP*, 175, 613
- Kohl, J.L., Esser, R., Cranmer, S.R., et al. 1999, *ApJL*, 510, 59
- Landi, E., & Landini, M. 1998, *A&A*, 340, 265
- Landini, M., & Monsignori Fossi, B.C. 1990, *A&A*, S82, 229
- Leamon, R.J., Canfield, R.C., Jones, S.L., et al. 2004, *JGR*, 109 Issue A5, CiteID
A05106
- Lemaire, P., Emerich, C., Vial, J.-C., et al. 2002, in “From Solar Min to Max: Half
a Solar Cycle with SOHO”, *ESA-SP 508*, 219
- Lepping, R.P., Szabo, A., DeForest, C.E., & Thompson, B.J. 1997, in *Correlated
Phenomena at the Sun, in the Heliosphere, and in Geospace*, ed. A. Wilson
(ESA-SP 415; Noordwijk: ESA), 163
- Lepri, S.T., Zurbuchen, T.H., Fisk, L.A., et al. 2001, *JGR*, 106, 29231

- Lepri, S.T., & Zurbuchen, T. H. 2004, JGR, 109, 1112
- Li, X., Habbal, S.R., Kohl, J.L., & Noci, G. 1998, ApJ, 501, L133
- Li, J., Raymond, J.C., Acton, L.W., et al. 1998, ApJ, 506, 431
- Lin, J. 2002, Chin. J. Astron. Astrophys., 2, 539
- Lin, J. & Forbes, T.G. 2000, J. Geophys. Res., 105, 2375
- Lin, J., Ko, Y.-K., Sui, L., et al. 2005, ApJ, 622, 1251
- Lin, J., Raymond, J.C., & van Ballegoijen, A.A. 2004, ApJ, 602, 422
- Lindsay, B.G., Sieglaff, D.R., Shafer, D.A., et al. 1996, Phys. Rev. A, 53, 212
- Luhmann, J.G., Li, Y., Zhao, X., & Yashiro, S. 2003, SP, 213, 367
- Mariska, J.T. 1992, "The solar transition region", Cambridge University Press, Cambridge
- Marocchi, D., Antonucci, E., Giordano, S. 2001, Annales Geophys., 19, 135
- Mazets, E.P., Sagdeev, R.Z., Aptekar, R.L., et al. 1987, A&A, 187, 699
- Mazzotta, P., Mazzitelli, G., Colafrancesco, S., & Vittorio, N. 1998, A&AS, 133, 403
- McClure, G.W. 1966, Phys. Rev., 148, 47
- McDonnell, J.A.M., Alexander, W.M., Burton, W.M., et al. 1987, A&A, 187, 719
- Mikić, Z., & Linker, J.A. 1994, ApJ, 430, 898
- Moore, R.L., LaRosa, T. N. & Orwig, L. E. 1995, ApJ, 438, 1995
- Moore, R.L., McKenzie, D.L., Svestka, Z., et al. 1980, in P.A. Sturrock, Ed., *Solar Flares*, Skylab Solar Workshop II Monograph, p. 341
- Moran, T.G., & Davila, J.M. 2004, Science, 305, 66
- Munro, R.H., & Mariska, J.T. 1977, ApJ, 211, 579
- Naletto, G. 1996, UVCS internal report.
- Noci, G., Kohl, J.L., & Withbroe, G.L. 1987, ApJ, 315, 706
- Parenti, S., Bromage, B.J.I., Poletto, G., et al. 2000, AA, 363, 800
- Parenti, S., Poletto, G., Bromage, B.J.I., et al. 2001, Joint SOHO/ACE workshop "Solar and Galactic Composition", AIP Conf. Proceed. v. 598
- Poletto, G., Suess, S.T., Bemporad, A., et al. 2004, ApJL, 613, 173
- Poletto, G., Suess, S.T., Biesecker, D.A., et al. 2002, JGR, 107, 1300
- Povich, M.S., Raymond, J.C., Jones, G.H., et al. 2003, Science, 302, 1949
- Raymond, J.C. 1999, SSR, 87, 55
- Raymond, J.C. 2001, Joint SOHO/ACE workshop "Solar and Galactic Composition", AIP Conf. Proceed. v. 598
- Raymond, J.C., Ciaravella, A., Dobrzycka, D., et al. 2003, ApJ, 597, 1106
- Raymond, J.C., Fineschi, S., Smith, P.L., et al. 1998*b*, ApJ, 508, 410
- Raymond, J.C., Kohl, J.L., Noci, G., et al. 1997, SP, 175, 645
- Raymond, J.C., Suleiman, R., Kohl, J.L., & Noci, G. 1998*a*, Space Sci. Rev., 85, 283
- Riley, P., Linker, J.A., & Mikić, Z. 2001, JGR 106 (A8), 889
- Romoli, M., Weiser, H., Gardner, L.D., & Kohl, J.L. 1993, Applied Optics, 32, 3559
- Romoli, M., Benna, C., Cranmer, S., et al. 1997, Proc. of the "Fifth SOHO Workshop", ESA SP-404, 633
- Scherrer, P.H., Bogart, R.S., Bush, R.I., et al. 1995, SP, 162, 129

- Schmelz, J.T. 1999, in Proc. of the "8th SOHO Workshop", ESA-SP 446, 585
- Scholz, T.T., & Walters, H.R.J. 1991, ApJS, 380, 302
- Schühle, U., Wilhelm, K., Hollandt, J., et al. 2000, A&A, 354, L71
- Sekanina, Z. 2003, ApJ, 597, 1237
- Siegmund, O.H., Stock, J.M., Marsch, D.R., et al. 1994, Proc. SPIE, 2280, 89
- Sittler, E.C. & Guhathakurta, M. 1999, ApJ, 523, 812
- Strachan, L., Kohl, J.L., Weiser, H., & Withbroe, G.L. 1993, ApJ, 412, 410
- Strachan, L., Suleiman, R., Panasyuk, A.V., et al. 2002, ApJ, 571, 1014
- Sturrock, P.A., Kaufman, P., Moore, R.L., & Smith, D.F. 1984, SP, 94, 341
- Subramanian, P., & Dere, K.P. 2001, ApJ, 561, 372
- Suess, S.T., Bemporad, A., Poletto, G. 2004, GRL, 31 (Issue 5), CiteID L05801
- Suess, S.T., Poletto, G., Romoli, M., et al. 2000, JGR, 105, 25033
- Svestka, Z., Dodson-Prine, H.W., Martin, S. F., et al. 1982, SP, 78, 271
- Tachibana, S., Tsuchiyama, A., Nagahara, H. 2002, Geochim. Cosmochim. Acta, 66, 713
- Tobiska, W.K., & Eparvier, F.G. 1998, SP, 177, 147
- Uzzo, M., Ko, Y.-K. & Raymond, J. C. 2004, ApJ, 603, 760
- Uzzo, M., Ko, Y.-K., Raymond, J. C., et al. 2003, ApJ, 585, 1062
- Uzzo, M., Raymond, J.C., Biesecker, D.A., et al. 2001, ApJ, 558, 403
- Vaisberg, O., Smirnov, V., Omelchenko, A. 1986, ESA SP-250 II, 17
- Van de Hulst, H.C. 1950, Bull. Astron. Inst. Netherlands, 11, 135
- Vernazza, J.E., & Reeves, E.M. 1978, ApJS, 37, 485
- Von Steiger, R., Schwadron, N.A., Fisk, L.A., et al. 2000, JGR, 105, 27217
- Von Steiger, R., Vial, J.-C., Bochsler, P., et al. 2001, Joint SOHO/ACE workshop "Solar and Galactic Composition", AIP Conf. Proceed. v. 598
- Webb, D.F., Burkepile, J., Forbes, T.G., & Riley, P. 2003, JGR, 108 (A12), 1440
- Wilhelm, K., Inhester, B., Newmark, J.S. 2002, AA, 382, 328
- Withbroe, G.L., Kohl, J.L., Weiser, H., & Munro, R.H. 1982, SSR, 33, 17
- Wood, B.E., Karovska, M., Chen, J., et al. 1999, ApJ, 512, 484
- Wooden, D.H., Harker, D.E., Woodward, C.E., et al. 1999, ApJ, 517 Issue 2, 1034
- Woods, T.N., Rottman, G.J., Bailey, S.M., et al. 1998, SP, 177, 133
- Yokoyama, T., Akita, K., Morimoto, T., et al. 2001, ApJ, 546, L69